The University of Sheffield

Sensorless Control of Dual Three-phase Permanent Magnet Synchronous Machine Drives

Ali Habib Almarhoon

A thesis submitted for the degree of Doctor of Philosophy

Department of Electronic and Electrical Engineering

The University of Sheffield

Mapping Street, Sheffield, S1 3JD, UK

December 2016

ABSTRACT

This thesis focuses on sensorless control methods for single and dual three-phase (DTP) permanent magnet synchronous machine (PMSM) drives covering both low and high-speed ranges. The sensorless control strategies for the high speed region are established based on flux-linkage observer (FO) estimator and simplified extended Kalman filter (EKF), while high-frequency carrier voltage injection based sensorless control strategies are utilised for low speed regions including standstill operation.

In the high-speed range, the influence of back-EMF and current harmonics on sensorless control performance of single and dual three-phase PMSMs is investigated by utilising FO and simplified EKF-based sensorless control strategies. The single three-phase PMSM is employed to investigate the influence of back-EMF harmonics on position estimation accuracy, while the influence of current harmonics on the accuracy of rotor position and speed estimation is studied in the case of the DTP-PMSM, which inherently exhibits harmonic currents in ST-DTC methods. By employing the simplified EKF, the sensorless control performance is significantly enhanced, since it is less sensitive to such harmonics and distortions.

When the rotor speed is low, machine saliency-based sensorless control strategies should be applied. The most commonly used conventional pulsating and rotating carrier voltage injection methods are presented for single and dual three-phase PMSMs, including measurement of the machine saliency level and analysis of cross-saturation effects. For the DTP-PMSM, both methods are applied to different machine models, i.e. the double *dq* model and the vector space decomposition (VSD) model. Both methods show decent sensorless control performances when the VSD model is employed since the mutual coupling between the two winding sets is eliminated.

The pulsating and rotating carrier voltage injections utilising zero-sequence carrier voltage for rotor position estimation are investigated for single and dual three-phase PMSMs, which differ from conventional high-frequency pulsating and rotating carrier voltage injection methods that use carrier current response to estimate the rotor position. However, for the single three-phase PMSM with both techniques, undesirable 6^{th} harmonic estimation error occurs due to multiple saliency components in the zero-sequence carrier voltage. The existing compensation schemes require time-consuming offline measurements and complex structures to solve this problem. In the case

of DTP-PMSM drives, two independent high frequency signals are proposed to be injected for the two separated winding sets thanks to the existence of additional degree of freedom. By applying the proposed optimum phase shift angle between the two injected signals, improved pulsating and rotating carrier signal injection employing zero-sequence voltage based sensorless control techniques are proposed to suppress these 6^{th} harmonic on rotor position errors. In addition, a new simple technique to measure the zero-sequence carrier voltage is proposed, in which one voltage sensor is put between the two isolated neutral points of the two stator winding sets.

In order to achieve high accuracy in terms of estimating the rotor position for a wide speed range, a combination of sensorless control strategies to achieve smooth transition between low and high speeds is introduced. The combined sensorless control methods include the flux-linkage observer method and four different high-frequency carrier signal injection techniques. Such methods are applied to the DTP-PMSM to investigate the sensorless control performance within different speed ranges. The estimation of the rotor position is obtained by using the high-frequency carrier voltage signal injection methods in the low-speed range, while the flux-linkage observer method is utilised to estimate the rotor position within the high-speed range. Furthermore, a function similar to hysteresis is applied for certain speed ranges, with optimum weighted gains for both estimated positions to achieve a smooth transition between the combined methods.

ACKNOWLEDGEMENTS

I would like to express my sincere gratitude and thanks to my supervisor Professor Z.Q. Zhu for his professional technical guidance encouragement, constructive help, enthusiastic, and valuable suggestions during my entire PhD study.

Thanks should also be given to Mr. Peilin Xu, and Dr. Yuan Ren for the technical assistance they have provided. Discussions with Dr. Kan Liu, Dr. Yashan Hu, Mr. Beomseok Lee, and Mr. Nattapong Pothi were also useful and helpful.

Also, I would like to thank other PhD students and staff members in the Electrical Machines and Drives Group at the University of Sheffield.

I am very grateful to my wife, Anwar Al Sadah, and my son Hassan for their love, encouragement, understanding, and support throughout my PhD study, which inspired me to dedicate great effort to the research work.

I warmly thank my parents, and whole family for their encouragement, support, and endless care.

Finally, I owe special thanks to the government of Saudi Arabia and the Royal Commission for Jubail for sponsoring me during the entire period of my PhD study.

CONTENT

SYMBOLS

L_{d1}	*d*-axis inductance for the first winding set
L_{q1}	*q*-axis inductance for the first winding set
L_{d2}	*d*-axis inductance for the second winding set
L_{q2}	*q*-axis inductance for the second winding set
M_d	*d*-axis mutual-inductance
M_q	*q*-axis mutual-inductance
ψ_{PM}	Flux-linkage produced by permanent magnets
T_e	Electromagnetic torque
i_d	*d*-axis current
i_q	*q*-axis current
v_d	*d*-axis voltage
v_q	*q*-axis voltage
$[T]_6$	Six dimensional transformation matrix
$\bar{V}_{s\alpha\beta}$	Stator voltage vector in $\alpha\beta$-subspace
$\bar{\psi}_{s\alpha\beta}$	Stator flux vector in $\alpha\beta$-subspace
$\bar{I}_{s\alpha\beta}$	Stator current vector in $\alpha\beta$-subspace
$\bar{V}_{sz1z2}$	Stator voltage vector in z_1z_2-subspace
$\bar{\psi}_{sz1z2}$	Stator flux vector in z_1z_2-subspace

$\overline{I}_{sz1z2}$	Stator current vector z_1z_2-subspace
L_{ls}	Leakage self-inductance
P	Pole pairs number.
P	Differential operator
R_s	Stator resistance
ω_r	electrical angular speed
ψ_d	d-axis flux-linkage
ψ_q	q-axis flux-linkage
L_d	d-axis inductance
L_q	q-axis inductance
$\Delta\theta$	The rotor position estimation error
E_{ex}	Extended back-EMF
θ_r	Rotor position
$V_{s\alpha\beta}$	Stator voltage in the stationary reference frame
$\psi_{s\alpha\beta}$	Stator flux in the stationary reference frame
$I_{s\alpha\beta}$	Stator current in the stationary reference frame
L_s	Stator self-inductance
ω_r	Rotor speed
$u(k)$	Input signal to simplified EKF
$y(k)$	Output signal to simplified EKF
$w(k)$	Process noise of simplified EKF

$v(k)$	Measurement noise of simplified EKF
$x(k)$	The state vector estimated by EKF
K_k	Kalman gain
ω_{est}	Estimated rotor position and speed
ψ_{s_ripple}	Stator flux ripple
T_{e_ripple}	Torque ripple
$T(\Delta\theta)$	Transformation matrix
L_{dh}	The high-frequency incremental *d*-axis self-inductance
L_{qh}	The high-frequency incremental *q*-axis self-inductance
L_{dqh} and L_{qdh}	The high-frequency incremental mutual-inductances
L_{sd}	The difference of *d*- and *q*-axis incremental inductances
L_{sa}	The average of *d*- and *q*-axis incremental inductances
θ_m	The cross-saturation angle
$\lambda=L_{qdh}/L_{qh}$	Cross-coupling factor
,$f(\Delta\theta)$	Input error signal to the position observer of HF injection methods
V_c	The amplitude of the injected high-frequency carrier voltage
ω_c	The angular speed of the injected high-frequency carrier voltage
Φ	The initial phase angle of the high-frequency carrier injection voltage
i_{dh}^e	carrier current of *d*-axis in the estimated synchronous reference frame

i_{qh}^{e}	*q*-axis carrier current in the estimated synchronous reference frame
v_{dh}^{e}	*d*-axis high-frequency carrier voltage
v_{qh}^{e}	*d*-axis high-frequency carrier voltage
I_p	The amplitude of positive-sequence current
I_n	The amplitude of negative-sequence current
v_{abcn1}	The phase voltages of the first winding set
L_p	The equivalent positive-sequence inductance
L_n	The equivalent negative-sequence inductance
i_{abc}	The phase currents of the first winding set
L_{aa}, L_{bb}, L_{cc}	The three phase incremental self-inductances of the first winding set
M_{ab} , M_{ac} , M_{bc}	The three phase incremental mutual-inductances of the first winding set
L_{xx}, L_{yy}, L_{zz}	The three phase incremental self-inductances of the second winding set
M_{xy} , M_{xz} , M_{yz}	The three phase incremental mutual-inductances of the second winding set
$\left\lvert i_{dqh}^{e} \right\rvert$	The amplitude of the high-frequency carrier currents
θ_r^e	The estimated rotor position
L_0	The amplitude of dc phase self-inductance

M_0	The amplitude of dc phase mutual-inductance
L_2	The amplitude second harmonic of phase self-inductance
M_2	The amplitude second harmonic of phase mutual-inductance
v_{0sn1}	The resultant zero-sequence carrier voltage for the first winding set
v_{0sn2}	The resultant zero-sequence carrier voltage for the second winding set
v_{xyzn2}	The phase voltages of the second winding set
i_{xyz}	The phase currents of the second winding set
V_{0sn1n2}	The corresponding demodulated zero-sequence carrier voltage
$v_{0sn1n2} = v_{0sn1} - v_{0sn2}$	The resultant zero-sequence carrier voltage between the two isolated neutral points

ABBREVIATIONS LIST

A/D	Analog to digital conversion
AC	Alternating current
BLAC	Brushless AC
BLDC	Brushless DC
BPF	Band-pass-filter
DC	Direct current
DTC	Direct-torque-control
DTP	Dual three-phase
EKF	Extended Kalman filter
EMF	Electromotive force
FE	Finite element
FOC	Field-oriented-control
HPF	High-pass-filter
INFORM	Indirect flux detection by on-line reactance measurements
IPM	Interior permanent magnet
LPF	Low-pass-filter
MBPC	Mode based predictive control
MRAS	Model reference adaptive system
PI	Proportional Integral
PLL	Phase locked loop
PM	Permanent magnet
PMSMs	Permanent magnet synchronous machines
PWM	Pulse width modulation
SMO	Sliding mode observer
SNR	Signal-to-noise ratio
SPM	Surface-mounted permanent magnet
SRFF	Synchronous reference frame filter
ST-DTC	Switching-table based direct torque control
SVPWM	Space vector pulse width modulation

THD	The total harmonic distortion
VC	Vector control
VSD	Vector space decomposition
VSI	Voltage source inverter

CHAPTER 1

GENERAL INTRODUCTION

1.1. Introduction

Three-phase permanent magnet synchronous machines (PMSMs) have been widely used in many industries over the last decade due to their merits of improved power density, high torque density, high efficiency, easy maintenance, and excellent control performance. Furthermore, multi-phase AC machine drives nowadays are in demand for many industrial applications especially for high-power and/or high-current applications such as aerospace applications, ship propulsion, electric/hybrid vehicles, and renewable energy generation [BOJ03]. This is due to their excellent features including reduced DC-link current harmonics, reduced torque ripples, improved efficiency, and increased reliability of the system compared to their three-phase machine drive counterparts. Recently, the dual three-phase (DTP) machine has been most widely discussed and regarded as the most common type among several types of multi-phase machines. The DTP machine involves two stator winding sets typically spatially shifted by 30 electrical degrees with two isolated neutral points and it is supplied by a six-phase inverter. Multi-phase machines are also built for fault-tolerant applications. In cases of post-fault conditions, such as a situation where one of three-phase stator winding sets is completely disconnected from the corresponding source, the redundant three-phase stator winding set can thus be put into operation to preserve the continuity of the machine drive operation, including sensorless control.

In order to achieve high performance control of PMSMs, an accurate rotor position information is required. Generally, high-resolution sensors, such as resolvers and encoders, are often utilised to obtain the rotor position information. By using such sensors, however, not only the system cost and size are increased, but also the reliability and robustness of the system are reduced. Numerous strategies have therefore been developed to obtain high sensorless control performance in industry, which will be the subject of the research in this thesis.

This chapter gives an introduction about various machine topologies of PMSMs, as well as the existing control strategies and sensorless control techniques, particularly for single and dual three-phase PMSMs. Furthermore, the research outline and contributions of this thesis are detailed at the end of this chapter.

1.2. Permanent Magnet Synchronous Machines

1.2.1. Single Three-Phase PMSM

Permanent magnet synchronous machines (PMSMs) can be categorised into several topologies, as addressed in [CHE99]. They are summarised in Fig. 1.2.

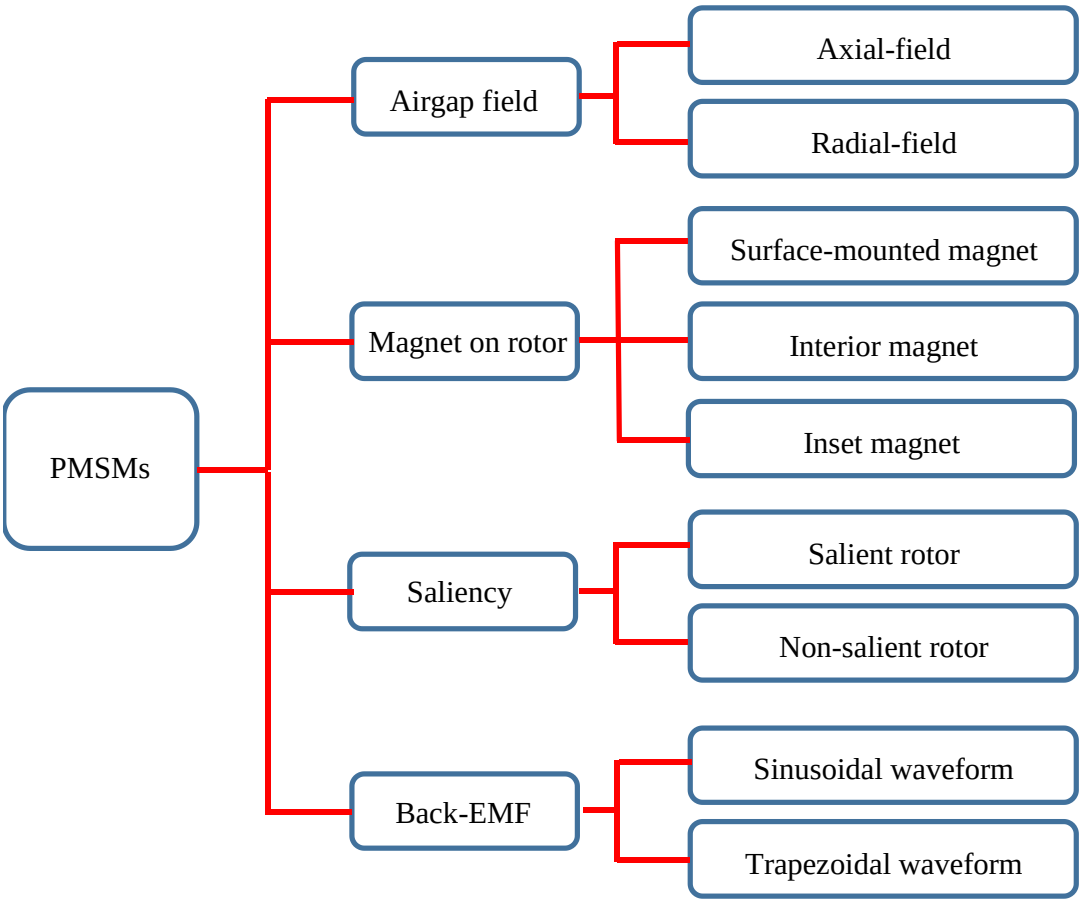

Fig. 1.1. Summary of PMSMs topologies [CHE99].

In PMSMs, the field is usually resulted from the permanent magnet (PM) on the rotor and the armature winding on the stator. With respect to the rotor structures of PMSMs, the structures of conventional inner rotor radial field PMSMs can be categorised as surface-mounted PM, inset PM, interior radial PM, and interior circumferential PM, as illustrated in Fig. 1.2:

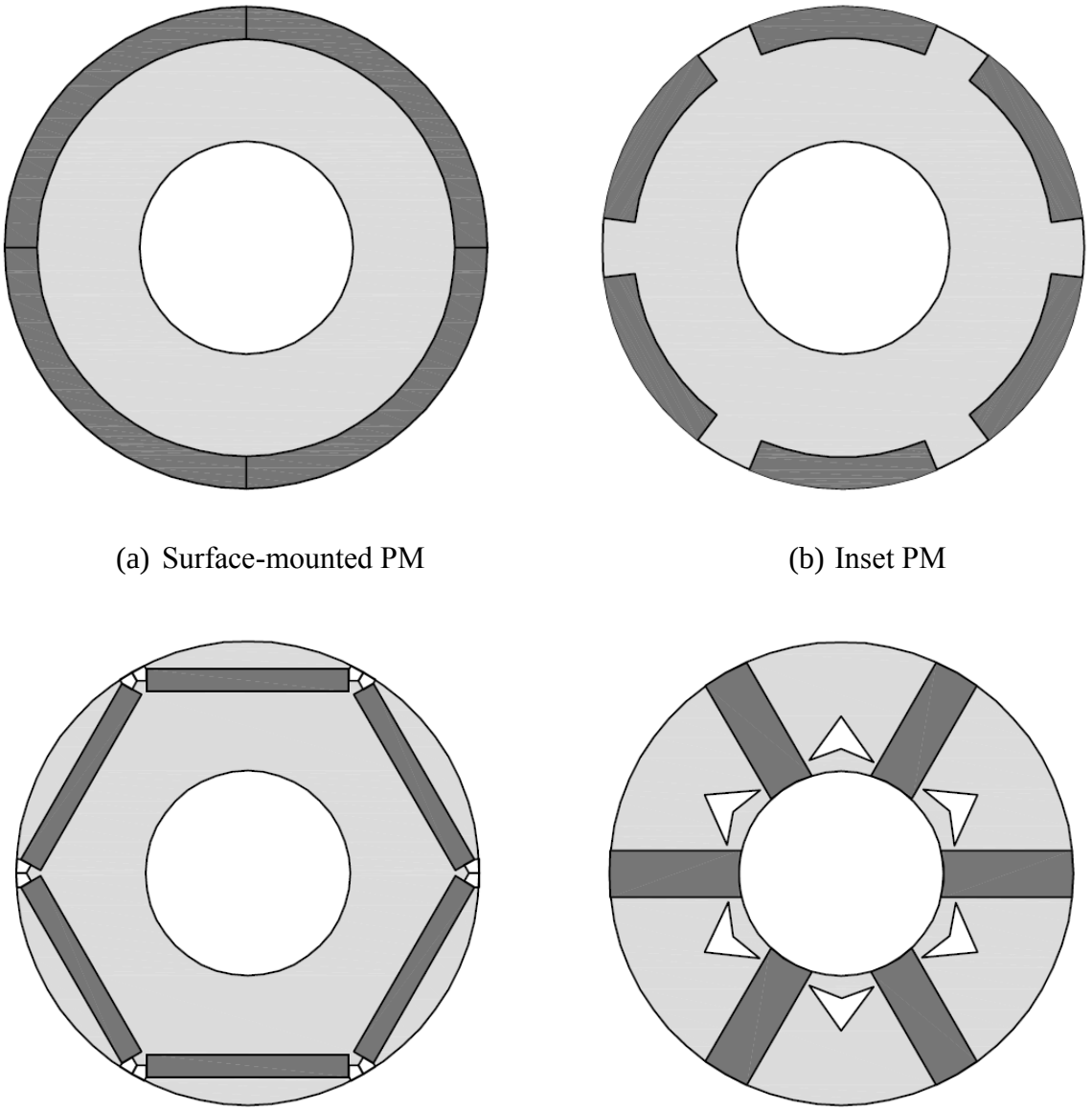

Fig. 1.2. Typical rotor structures of brushless PMSM [CHE99].

For surface-mounted PM rotor structures, the effective air-gap is large, equal to the physical air-gap between the stator and the rotor plus the PM radial thickness. Consequently, they have small winding inductances and low armature field. In addition, the variation in winding inductance and hence geometric saliency are negligible [CHE99]. On the other hand, the other three structures show significant saliency, which results from geometric anisotropy.

Brushless PM synchronous machines can be classified into two categories, as brushless DC (BLDC) machines and brushless AC (BLAC) machines depending on the type of the fundamental excitation. BLDC machines with trapezoidal back-EMF are driven by square wave current excitation, while sinusoidal current drive BLAC machines have sinusoidal back-EMF [ACA06] [LI09]. Fig.1.3 shows the waveforms of phase back-EMF and current for BLDC and BLAC machines.

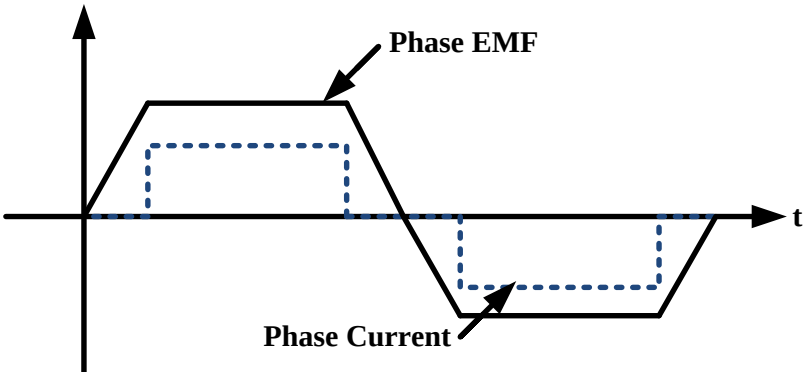

(a) BLDC

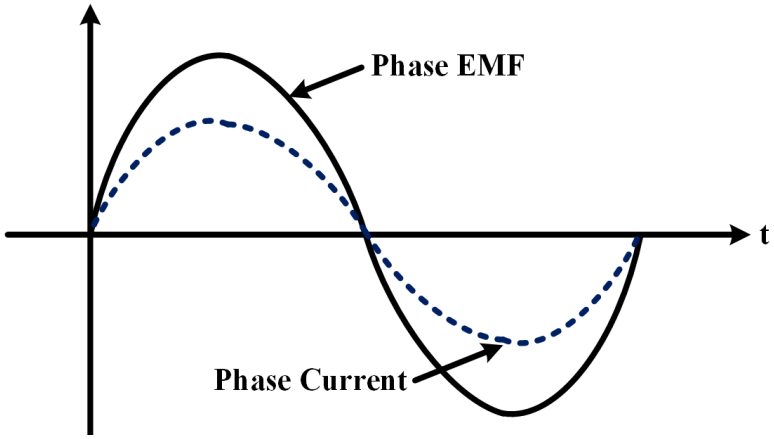

(b) BLAC

Fig. 1.3. Phase back-EMFs and currents for BLDC and BLAC machines.

1.2.1.1. Control of Single Three-Phase PMSM

The single three-phase permanent magnet synchronous machine (PMSM) has been widely considered in many industrial applications for several decades. High efficiency, low rotor inertia, high power density, efficient heat dissipation structure, small volume, accurate speed control, and robustness are the main advantageous of such machines. The control of PMSMs has therefore been of interest in recent years, with many control strategies have been developed in order to achieve high control performance. The PMSM drive includes a motor, a voltage source inverter (VSI), and a controller, as illustrated in Fig.1.4. Usually, BLDC machines only require discrete information of the rotor position with low resolution, and are often used for low cost applications. BLAC machines, on the other hand, require continuous rotor position information with high resolution, since such machines are excited by sinusoidal phase current synchronising with the PM-excited flux-linkage. In this thesis, all of the research is based on BLAC PMSM drives due to their excellent control performance.

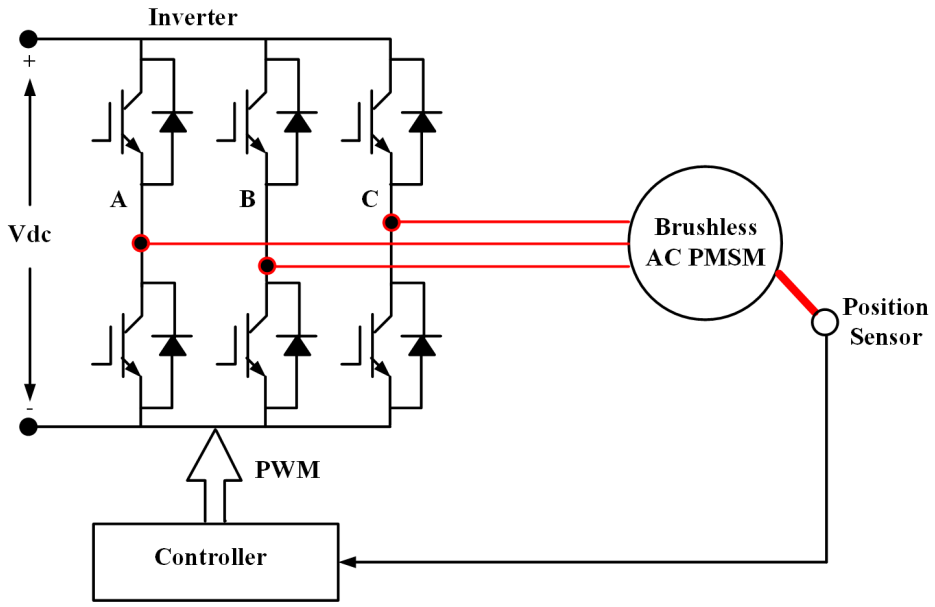

Fig. 1.4. Single three-phase PMSM drive.

The classical schematic diagrams of vector control, which is also known as field orientation control (FOC), and direct torque control (DTC) for the PMSM are depicted in Fig. 1.5 and Fig. 1.6, respectively.

The main idea of FOC is the stator flux and torque are controlled independently and indirectly by using a current control loop and PI controllers. Additionally, a proper pulse width modulation (PWM) technique, such as space vector pulse width modulation (SVPWM) or carrier-based PWM, is utilised in order to implement voltage vector references. FOC is formulated in such a way that the stator current can be decoupled into two components. This method is performed by transforming the stator currents into two-axis synchronously-rotating reference frame components. The rotor flux is controlled by the direct axis (*d*-axis) component while the quadrature axis (*q*-axis) controls the output torque [TIA11].

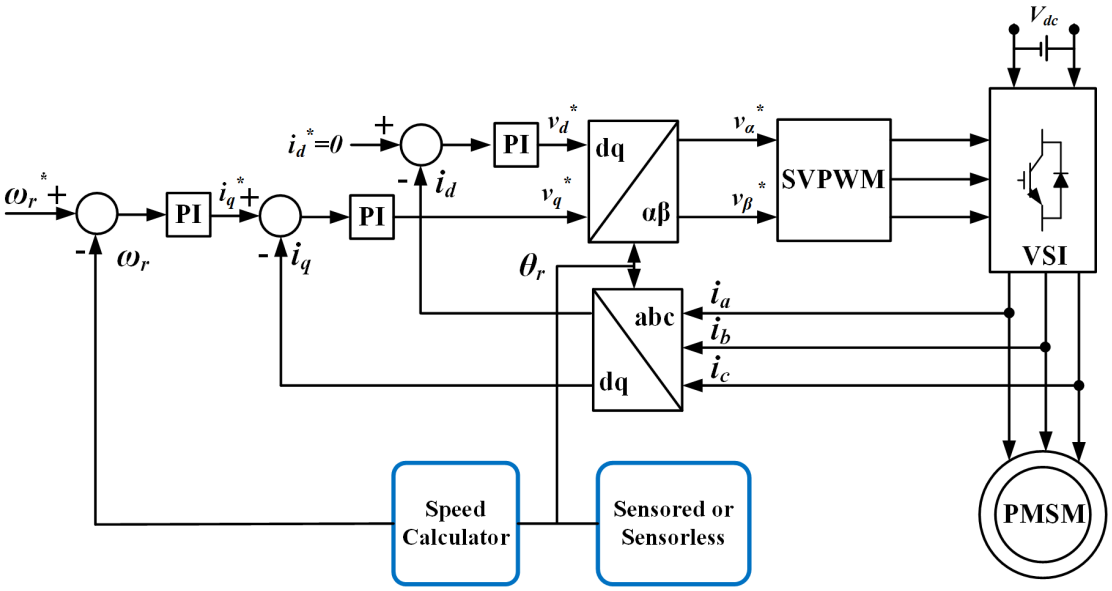

Fig. 1.5. FOC of PMSM drive.

DTC was firstly introduced by Takhashi [TAK86] and [DEP88] to be applied to induction machine drives. It is a robust control strategy due to its good robustness against machine parameters, simple structure, and outstanding transient response. DTC has also been developed and extended for PMSMs [ZHO97] [PAC05] [FOO09a] [ZHA11]. Usually, in the conventional switching table-based DTC technique, the hysteresis regulators are implemented to regulate the stator flux and electromagnetic torque. Compared to classical FOC, DTC is much simpler, as coordinate transformation, PI regulators, and position encoders are not required, which results in a significant improvement in the transient torque control performance. There are some disadvantages to DTC, however, such as fast sampling time and variable switching frequency being required due to hysteresis-based control loops.

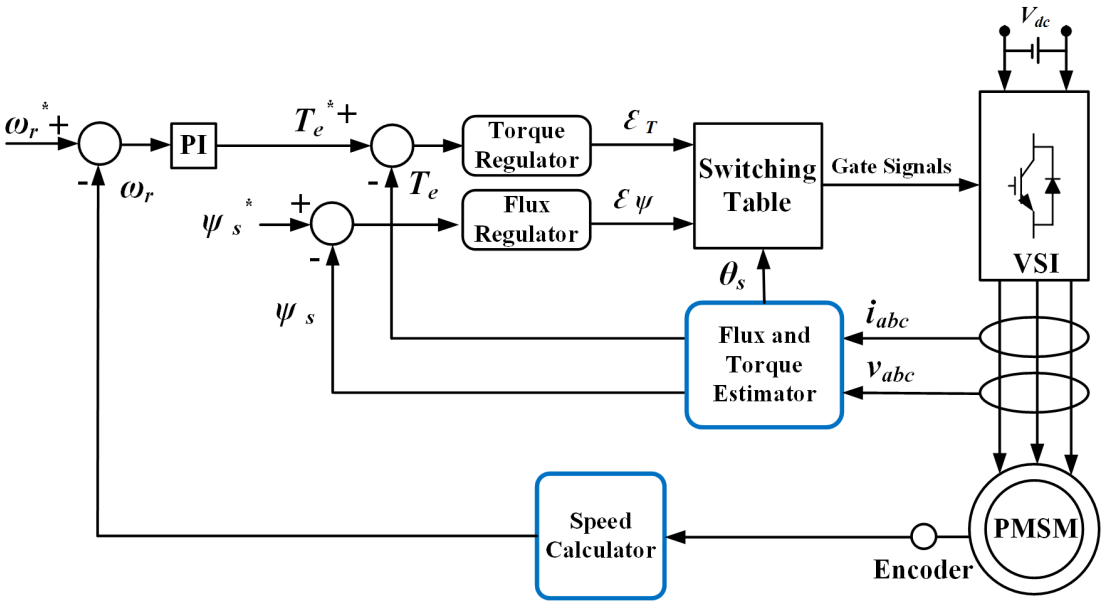

Fig. 1.6. DTC of PMSM drive.

1.2.2. Dual Three-Phase PMSM (DTP-PMSM)

Although three-phase machine drives were widely used in many industrial applications over last decades, the interest in multi-phase AC machine drives was extremely increased, particularly for high-power and/or high-current applications including renewable energy generation, aerospace applications, ship propulsion, and electric/hybrid vehicles [BOJ03]. This is because their excellent features over traditional three-phase machine drives, such as improved efficiency, reduced DC-link current harmonics, reduced torque ripples, and increased reliability of the system [BAN16] [KAR16] [LEV08] [YUA15] [ZHA95].

The basic dual three-phase structure is similar to that of single three-phase machine as presented earlier, where the windings can be categorized into overlapping windings and non-overlapping windings. The rotor can be classified as surface-mounted permanent magnet and interior permanent magnet. Due to multiphase winding structure, the displacement of three-phase winding sets can have different phase shift. In [NEL74], a multiphase machine has been analysed in which it permits an arbitrary displacement between any numbers of three-phase winding sets. The most frequently considered dual three-phase (DTP) machine drive for high power applications is the asymmetric dual three-phase machine. The choice of asymmetric dual three-phase machine with 30^o displacement between the two three-phase winding sets rather than symmetrical dual

three-phase machines with 0^o or 60^o displacement has been dictated by the need to eliminate/suppress the 6^{th} harmonic of the torque ripple, caused by the 5^{th} and 7^{th} stator current harmonics [LEV07]. In the case of 30^o displacement, the *q*- and *d*-axis rotor currents are seen to be more sinusoidal that that for other two cases, in which the associated 6^{th} harmonic torque pulsating torque is minimised.

Among different types of multi-phase machines including five-phase [GAO11], six-phase [BAN16] [BOJ05] [CHE14] [DUR11] [KAR16] [REN15a] [REN15b] [ZHA95], and nine-phase [KEL03], the most interesting and well-discussed type is the dual three-phase machine, which typically has two independent three-phase stator winding sets displaced by 30 electrical degrees as depicted in Fig. 1.7.

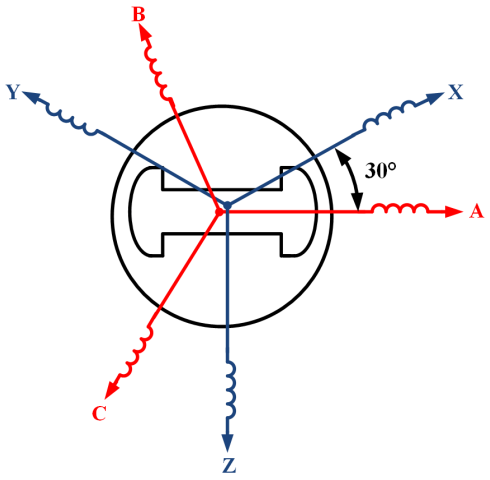

(a) Schematic

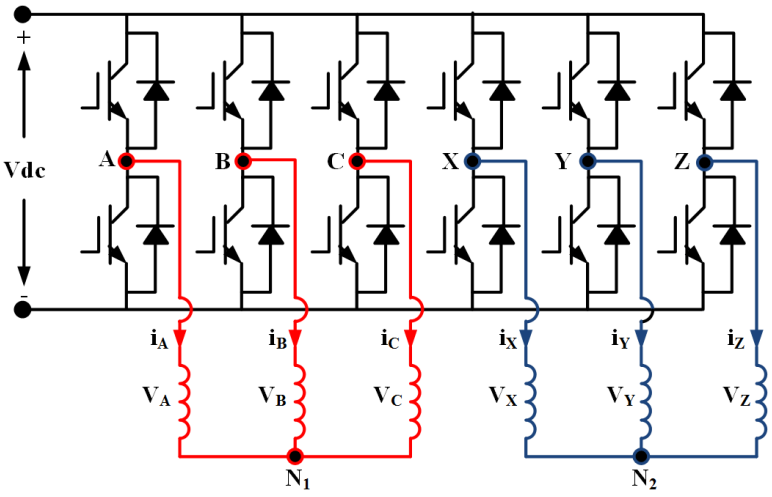

(b) Drive configuration

Fig. 1.7. Six-phase voltage source inverter (VSI) fed DTP-PMSM.

However, in the voltage-source-inverter fed dual three-phase machine, significant stator currents harmonics are observed [KLI83] [ZHA95]. Extra losses will be occurred due to theses currents harmonics [DUR11]. Thus, a higher semiconductor device ratings is required. By owning extra phases to control, additional degree of freedom is available, giving further improvement in the system drive. Usually, the dual three-phase machine is excited by a full-bridge voltage source inverter (VSI), Fig. 1.7 (b). By employing the multi-phase inverter instead of a group of devices connected in parallel, the inverter phase current is reduced, and hence the reliability of the whole system is improved [BOG06].

1.2.2.1. Modelling of Dual Three-phase PMSM

The modelling of the dual three-phase PMSM can be represented in two different approaches, i.e. the double *dq* synchronous reference frame model [HE10] [KAR12] [LIP80], and vector space decomposition [ZHA95]. In both approaches, the two zero-sequence components can be neglected since the neutral points N_1 and N_2 of the two three-phase windings are isolated as shown in Fig. 1.7 (b). Both models are described below.

A. Double *dq* Synchronous Reference Frame Approach

For this approach, the machine can be represented with two pairs of *dq* windings for the two three-phase winding sets, which could be regarded as two single three-phase machines with coupling voltage [NEL74] [LIP80].

In this modelling approach, the two stator windings are assumed to be identical. Thus,

$$L_{d1} = L_{d2} = L_d,\ L_{q1} = L_{q2} = L_q,\ M_{d12} = M_{d21} = M_d,\ M_{q12} = M_{q21} = M_q \qquad (1.1)$$

where L_{d1}, and L_{q1} are referred to as *d*- and *q*-axes inductances for the first winding set, respectively, and L_{d2}, and L_{q2} denote *d*- and *q*-axis inductances for the second winding set, respectively. The *d*- and *q*-axes mutual-inductances between the two winding sets are represented by M_d, and M_q, respectively.

Then, the voltages of both stator winding sets in *dq* reference frame can be derived as

$$\begin{cases} v_{d1} = R_s i_{d1} + L_d \dfrac{di_{d1}}{dt} + M_d \dfrac{di_{d2}}{dt} - \omega L_q i_{q1} - \omega M_q i_{q2} \\ v_{q1} = R_s i_{q1} + L_q \dfrac{di_{q1}}{dt} + M_q \dfrac{di_{q2}}{dt} + \omega L_d i_{d1} + \omega M_d i_{d2} + \omega \psi_{PM} \\ v_{d1} = R_s i_{d2} + L_d \dfrac{di_{d2}}{dt} + M_d \dfrac{di_{d1}}{dt} - \omega L_q i_{q2} - \omega M_q i_{q1} \\ v_{q1} = R_s i_{q2} + L_q \dfrac{di_{q2}}{dt} + M_q \dfrac{di_{q1}}{dt} + \omega L_d i_{d2} + \omega M_d i_{d1} + \omega \psi_{PM} \end{cases} \quad (1.2)$$

where i_d, i_q, v_d and v_q are *d*- and *q*-axes currents and voltages, respectively, ψ_{PM} is the flux-linkage resulted from permanent magnets. 1 and 2 represent the two stator winding sets.

The total electromagnetic torque is hence expressed as [KAR12]

$$\begin{cases} T_{e1} = \dfrac{3}{2} P \left(\psi_{PM1} i_{q1} + (L_d - L_q) i_{d1} i_{q1}\right) \\ T_{e2} = \dfrac{3}{2} P \left(\psi_{PM2} i_{q2} + (L_d - L_q) i_{d2} i_{q2}\right) \\ T_{e,total} = T_{e1} + T_{e2} \end{cases} \quad (1.3)$$

where *P* is pole pairs number.

B. Vector Space Decomposition (VSD) Approach

The dual three-phase machine is very complex six-dimensional electromechanical system, which makes it not suitable for the high performance control strategies. Therefore, the approach of vector space decomposition (VSD) has been introduced in [ZHA95], in which the original six-dimensional machine system can be transformed to a new six-dimensional system. The new six-dimensional system is decomposed into three orthogonal subspaces which are mutually decoupled, i.e. $\alpha\beta$, z_1z_2 and o_1o_2, with different harmonics mapped into different subspaces. According to the VSD scheme, the harmonics with order $12k \pm 1$(k=1, 2, 3,…) and the fundamental components of the machine variables are mapped into the $\alpha\beta$-subspace. On the other hand, the harmonics with order $6k \pm 1$(k=1, 3, 5,…) are located in the z_1z_2-subspace, whilst the zero-sequence component

with $3k$ (k=0, 1, 2,…) is mapped into the o_1o_2-subspace. By this decomposition, the parameters which produce rotating MMF and the parameters of zero-sequence are totally decoupled within one set. Thus, the analysis and control of the machine are simplified, and the dual three-phase PMSM can be excited by applying the conventional space vector pulse width modulation (SVPWM) generator. The surface spanned by the fundamental component vector with key importance to the electromechanical energy conversion function, i.e. $\alpha\beta$-subspace, can be controlled by applying FOC as single three-phase PMSM. The z_1z_2-subspace is orthogonal to $\alpha\beta$-subspace, and is expected that the variables on this subspace will not generate any rotating MMF in the airgap. However, stator currents of fundamental frequency will appear in z_1z_2-subspace if there is any asymmetry between the two stator winding sets or inside each winding set. Thus, they should be eliminated to avoid the inherent asymmetry effect of the dual three-phase systems [BOJ03] [HE10] [GRE10]. This decomposition can be obtained by applying the transformation matrix in (1.4) [ZHA95] to the machine variables, where x could represent the machine variables, i.e. voltage, current, and flux.

$$\begin{bmatrix} x_\alpha \\ x_\beta \\ x_{z1} \\ x_{z2} \\ x_{o1} \\ x_{o2} \end{bmatrix} = \frac{1}{3}\begin{bmatrix} 1 & \cos\frac{4\pi}{6} & \cos\frac{8\pi}{6} & \cos\frac{\pi}{6} & \cos\frac{5\pi}{6} & \cos\frac{9\pi}{6} \\ 0 & \sin\frac{4\pi}{6} & \sin\frac{8\pi}{6} & \sin\frac{\pi}{6} & \sin\frac{5\pi}{6} & \sin\frac{9\pi}{6} \\ 1 & \cos\frac{8\pi}{6} & \cos\frac{4\pi}{6} & \cos\frac{5\pi}{6} & \cos\frac{\pi}{6} & \cos\frac{9\pi}{6} \\ 0 & \sin\frac{8\pi}{6} & \sin\frac{4\pi}{6} & \sin\frac{5\pi}{6} & \sin\frac{\pi}{6} & \sin\frac{9\pi}{6} \\ 1 & 1 & 1 & 0 & 0 & 0 \\ 0 & 0 & 0 & 1 & 1 & 1 \end{bmatrix}\begin{bmatrix} x_a \\ x_b \\ x_c \\ x_x \\ x_y \\ x_z \end{bmatrix} \tag{1.4}$$

The transformation has the ability to separate the harmonics into different combinations, and to map them into each subspace. The harmonics with low order such as the 5th and 7th harmonics will be mapped in z_1z_2-subspace which leads to large stator circulating 5th and 7th currents harmonics [GOP93], when dual six-step VSI is utilized in particular [NEL74] due to the small impedance for these harmonics. Therefore, a proper current control of z_1z_2-subspace is required to avoid these kind of currents harmonics.

With considering sinusoidal distributed windings, and neglecting the magnetic saturation, core losses, and the mutual leakage inductance, the model of DTP-PMSM is expressed as [ZHA95]

$$\bar{V}_{s\alpha\beta} = R_s \bar{I}_{s\alpha\beta} + p\bar{\psi}_{s\alpha\beta} \tag{1.5}$$

$$\bar{\psi}_{s\alpha\beta} = L_s \bar{I}_{s\alpha\beta} + \bar{\psi}_{r\alpha\beta} \tag{1.6}$$

$$\bar{\psi}_{r\alpha\beta} = \bar{\psi}_{PM} e^{j\theta_r} \tag{1.7}$$

$$\bar{V}_{sz1z2} = R_s \bar{I}_{sz1z2} + p\bar{\psi}_{sz1z2} \tag{1.8}$$

$$\bar{\psi}_{sz1z2} = L_{ls} \bar{I}_{sz1z2} \tag{1.9}$$

$$T_e = 3P\left(\psi_{s\alpha} i_{s\beta} - \psi_{s\beta} i_{s\alpha}\right) \tag{1.10}$$

where $\bar{V}_{s\alpha\beta}$, $\bar{\psi}_{s\alpha\beta}$, $\bar{I}_{s\alpha\beta}$, $\bar{V}_{sz1z2}$, $\bar{\psi}_{sz1z2}$, $\bar{I}_{sz1z2}$ are stator voltage, flux, and current vectors in $\alpha\beta$- and z_1z_2-subspaces, respectively, L_{ls} is leakage self-inductance, T_e is electromagnetic torque.

From the machine model above, it can be clearly seen that the expressions of machine variables are similar to that of the single three-phase model. Since the impedance in the z_1z_2-subspace is relatively small, which only consists of the leakage-inductance and stator resistance, the voltage harmonic in the z_1z_2-subspace is the source for high current harmonics.

1.2.2.2. Control of Dual Three-phase PMSM

For dual three-phase PMSM control, the same control strategies used for the single three-phase PMSM, i.e. FOC and DTC, can be applied. However, the extension of the current control techniques from the single three-phase machine to the asymmetric dual three-phase machine is less straightforward since some machine specific aspects should be considered. Specifically, small inherent asymmetries between the two three-phase power sections could results in current imbalance between the stator three-phase winding sets, as demonstrated in [LYR02] [BOJ03] [BOJ03a]. This issue occurs when the dual three-phase machine is supplied by two independent three-phase voltage inverters. Since the dual three-phase machine system is actually regarded as a fourth order system when the two neutral points are isolated, the control scheme with only two

current controllers cannot ensure a satisfactory performance. To ensure high current control performance, four current controllers are therefore required. The existing FOC methods that utilise four current controllers can be divided into two groups based on the two modelling approaches; these are double synchronous reference frame current control techniques based on the double *dq* synchronous reference frame model, and VSD current control based on the VSD model.

With two isolated neutral points, the DTP-PMSM could be regarded as two independent sets of single three-phase PMSMs. A current control scheme utilising the double *dq* synchronous reference frame scheme is thus introduced. The reference currents in d- and q-axis are shared by two individual current controllers which correspond to the two stator winding three-phase sets. Four simple PI current regulators are employed in the double *dq* current control technique, as shown in Fig. 1.8 [BOJ03]. In this way, the scheme is able to compensate for the drive asymmetries since the currents of the two stator windings sets are independently controlled, but cannot compensate for current imbalance between the phases in each winding set.

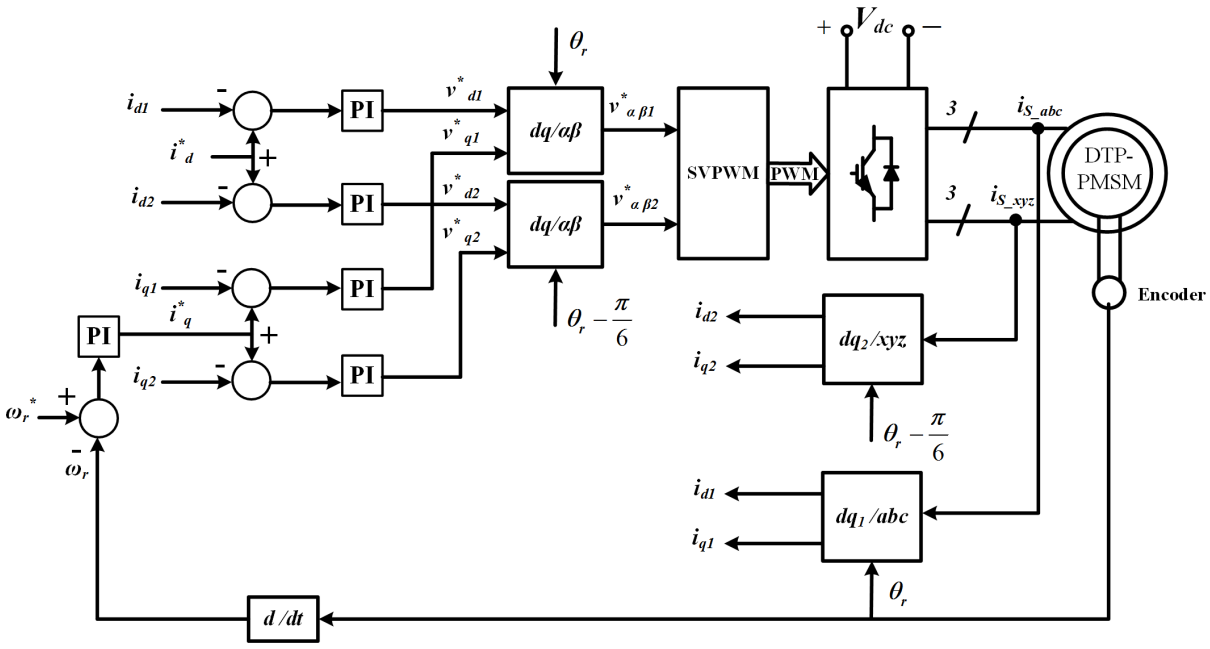

Fig. 1.8. Double *dq* current control for dual three-phase PMSM.

Alternatively, the VSD approach can provide a method to describe the machine model which is much straightforward, since different harmonic components are mapped into different subspaces. Unlike double *dq* current control technique that can be only applied in the case of dual three-phase machines, this method is applicable for multi-phase machines with any number of phases, including the dual three-phase machine. For the control techniques based on VSD model, a proper PWM method is required to ensure that the voltage components on different subspaces are properly implemented [BOJ06].

For the VSD approach, the conventional FOC for DTP-PMSM is simple, however, large current harmonics can be found, since the z_1z_2-subspace variables are not controlled. Thus, controlling of the $\alpha\beta$-subspace only is not sufficient for high performance control of dual three-phase machines. In [BOJ06], the current control strategy in the stationary reference frame was introduced, in which improved PI regulators are utilised to control the $\alpha\beta$-subspace and resonant regulators are employed for the z_1z_2-subspace. Both current controllers involve the electrical angular speed, which makes it a very complicated technique. The $\alpha\beta$- and z_1z_2-subspaces can also be controlled by conventional PI regulators, as is the case in [JON09]. By applying a rotational transformation, mixed values of DC and AC components will be found in the transformed z_1z_2 currents. The PI regulators can completely eliminate the DC components, but the AC component can be only be suppressed to some extent because the bandwidth of the PI controllers is limited. Fig. 1.9 shows the current control method based on VSD for dual three-phase machine drive. In the z_1z_2-subspace, the currents can be regarded as circulating currents between the two stator winding sets, as demonstrated in [CHE14] where the detailed characteristics of the currents in z_1z_2-subspace due to the machine/inverter asymmetries are analysed. Then, in order to eliminate harmonic currents in the z_1z_2-subspace caused by machine/inverter asymmetries, the dual PI controllers, i.e. synchronous and anti-synchronous PI controllers, are utilised to control the currents in the z_1z_2-subspace as illustrated in Fig. 1.10 (b).

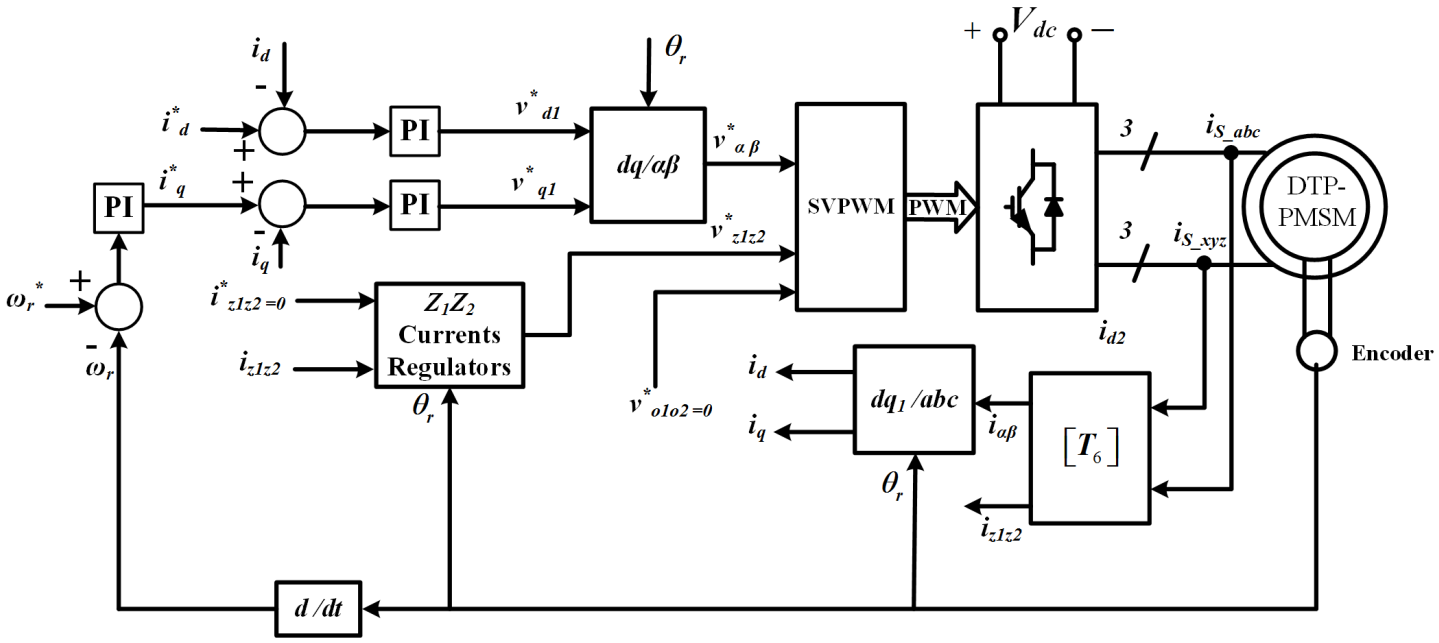

Fig. 1.9. Current control based on VSD for Dual three-phase PMSM.

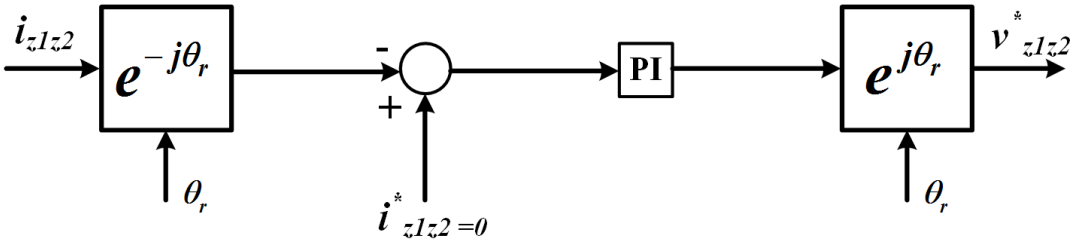

(a) Single PI regulator

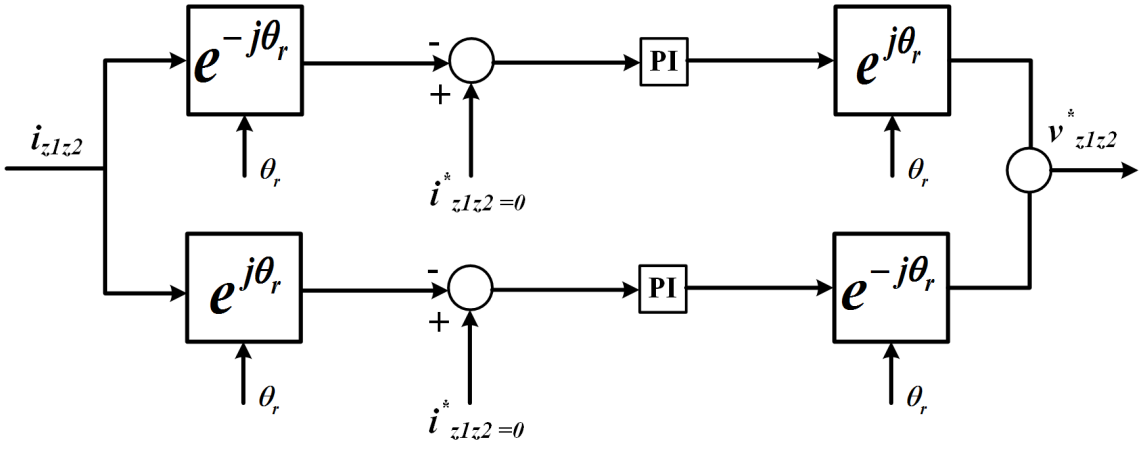

(b) Dual-PI regulators

Fig. 1.10. Two types of current controllers for z_1z_2-subspace.

When fast dynamic performance is required, DTC control is normally implemented in single three-phase PMSM drives. This control strategy can also be extended for multi-phase machines. By minimising the current components in the z_1z_2-subspace, sinusoidal phase currents could be obtained when employing DTC with a properly designed switching table (ST) [HAT05] [HOA12]. In case of asymmetric dual three-phase machines, large distortion would occur in the phase currents. Such issues can be overcome by keeping a constant switching frequency, imposing the direct mean torque control approach, and implementing the PWM-DTC technique [BOJ05] [FAR06]. In [HOA15], an optimised ST-DTC strategy has been introduced, in which a two-step strategy is involved to define the most convenient inverter voltage vector to diminish the stator current harmonics. Also, an improved switching-table including twelve new synthetic voltage vectors for the ST-DTC technique was proposed in [REN15a] to suppress the stator harmonic current and thus enhance the performance. The improved switching-table can successfully eliminate the variables contributing to the current harmonics in addition to controlling the variables related to torque production. In [REN15b], two types of synthetic vector have been introduced to reduce the current harmonics and an improved five-level torque regulator was presented to enhance the torque performance.

The dual three-phase machine has a higher reliability at the system level, since it can operate in cases where one or more inverter legs or machine phases have broken down and is thus fault-tolerant. In cases of post-fault conditions, such as a complete disconnection of one three-phase stator winding set from its corresponding source, the redundant three-phase stator winding set can be operated to preserve the continuity of the machine drive operation, including sensorless control [BAR12] and [LI11]. In [BAR10a], the control capability of the DTP-PMSM has been investigated during faulty operating conditions. The torque behaviour, thermal limits, and overload capability of a fractional-slot interior DTP-PMSM according to different winding configurations have been evaluated in [BAR10b].

1.3. Sensorless Control of PMSM

As mentioned earlier, accurate rotor position information is essential in order to achieve good performance of both BLDC and BLAC machines. Rotor position information is generally obtained from high-resolution rotor position sensors such as encoders and resolvers mounted on the machine shaft. However, such sensors result in increasing the size, cost and complexity of the entire system, and also impair the system's reliability. Numerous sensorless control methods have therefore been widely developed for both BLDC and BLAC machines to overcome such drawbacks. In this thesis, only sensorless control methods for BLAC PMSM are considered. The sensorless control strategies for BLAC machines can be categorised into two main methods; methods based on back electromotive force (EMF), and strategies based on machine saliency, as illustrated in Fig. 1.11. The former approaches provide adequate performance at medium and high speeds, but deteriorate the performance at zero speed and in low-speed range where the back-EMF is insufficient, i.e. small or even zero. On the other hand, the machine-saliency-based methods achieve decent performance in terms of estimating the rotor position at a standstill and at low speed. These methods rely on the machine saliency, which results from either geometrical rotor saliency or magnetic saturation saliency.

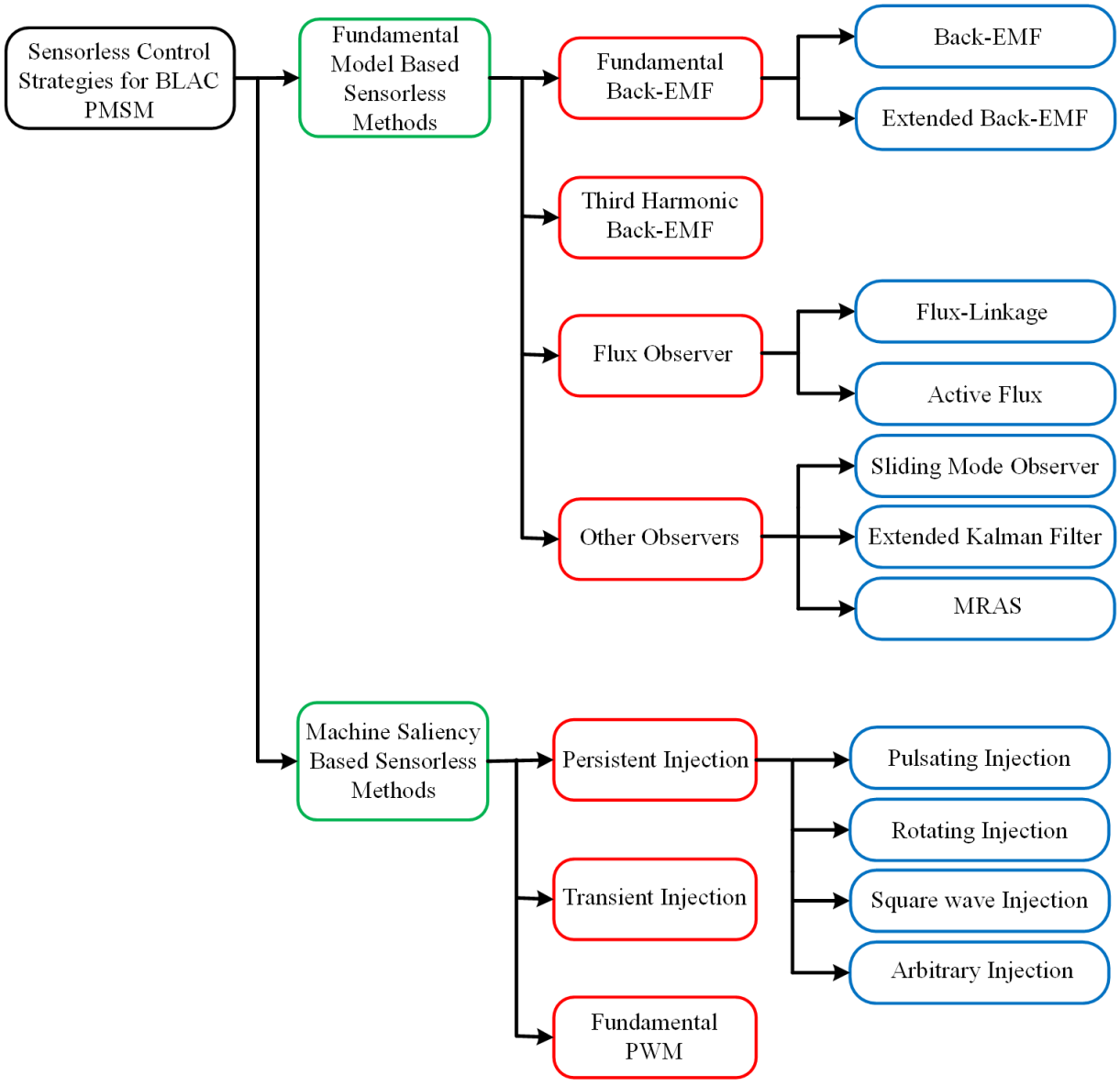

Fig. 1.11. Categories of sensorless control techniques for PMSM.

Machine-saliency-based methods include transient voltage vector injection [ROB04], PWM signal injection [RAC08], and persistent carrier signal injection methods. The most common approaches of continuous carrier signal injection strategies include rotating sinusoidal signal injection in the stationary reference frame [AND08] [DEG98] [GAR07] [BRI04] [BRI05] [CON06] [RAC10] [GAB13], and pulsating sinusoidal signal injection in the *dq* estimated reference frame [MED15] [XU15] [XU16] [RAC08] [CAR06] [ZHA13] [SIL06] [ACC12] [REI08] [LIN14].

1.3.1. Fundamental Model-Based Sensorless Control Strategies

In general, the fundamental model-based sensorless control strategies can be defined as the estimation of back electromotive force (EMF) or flux-linkage calculated from the machine fundamental model, where the rotor position could be estimated using open-loop calculation or close-loop observation. Furthermore, the rotor position can also be estimated directly from the machine's fundamental model without taking into account of the back-EMF or flux-linkage by utilising the adaptive observers, such as the extended Kalman filter (EKF), the sliding mode observer (SMO), and the model reference adaptive system (MRAS). Fundamental model-based sensorless control strategies work very well within medium and high speeds.

A. Fundamental Back-EMF Based Sensorless Control Technique

Back-EMF is produced in electrical machines when a movement between the machine armature and the air-gap magnetic field produced by the permanent magnets exists. It has direct proportion relationship with the rotor speed. Back-EMF contains the rotor position information, since the back-EMF is directly proportional to the rotor speed and varies with respect to the rotor position for brushless PM machines. The rotor position can be easily estimated when back-EMF is available, whether from measurements or indirect calculations.

Back-EMF-based sensorless control techniques were developed primarily to estimate the rotor position of non-salient PM BLAC motors, i.e. surface-mounted PMSMs, with equal *d*- and *q*-axis inductances (i.e. $L_d=L_q$). Then, these techniques were extended to estimate the rotor position of salient PM BLAC machines, i.e. interior PMSMs, with unequal *d*- and *q*-axes inductances (i.e. $L_d\neq L_q$), where the difference between inductances is merged with the back-EMF in order to obtain a symmetrical impedance matrix of *d*- and *q*-axis voltage expressions [CHE03] [MOR02] [KIM03] [LI09].

In the synchronous reference frame, the basic mathematical model of permanent magnet BLAC machines is given by

$$\begin{bmatrix} v_d \\ v_q \end{bmatrix} = \begin{bmatrix} R_s & 0 \\ 0 & R_s \end{bmatrix} \begin{bmatrix} i_d \\ i_q \end{bmatrix} + p \begin{bmatrix} \psi_d \\ \psi_q \end{bmatrix} + \begin{bmatrix} -\omega_r \psi_q \\ \omega_r \psi_d \end{bmatrix} \tag{1.11}$$

where p represents the differential operator, R_s is referred to as phase resistance, ω_r is the electrical angular speed, and ψ_d and ψ_q denote the d- and q-axes flux-linkages.

With assumption of sinusoidal distributed flux without considering the effects of magnetic-saturation and cross-saturation, (1.11) becomes

$$\begin{bmatrix} v_d \\ v_q \end{bmatrix} = \begin{bmatrix} R_s + pL_d & -\omega_r L_q \\ \omega_r L_d & R_s + pL_q \end{bmatrix} \begin{bmatrix} i_d \\ i_q \end{bmatrix} + \begin{bmatrix} 0 \\ \omega_r \psi_{PM} \end{bmatrix} \tag{1.12}$$

where L_d and L_q denote the d- and q-axes inductances, ψ_{PM} indicate the flux-linkage excited by PM. For the non-salient BLAC PMSM, the impedance matrix in (1.12) becomes symmetric since $L_d = L_q = L$.

Then, with the help of transformation matrix $T(\Delta\theta)$, (1.13), the fundamental model of non-salient BLAC PMSM in the estimated synchronous reference frame is given as (1.14) [CHE00].

$$T(\Delta\theta) = \begin{bmatrix} \cos(\Delta\theta) & \sin(\Delta\theta) \\ -\sin(\Delta\theta) & \cos(\Delta\theta) \end{bmatrix} \tag{1.13}$$

$$\begin{bmatrix} v_d^e \\ v_q^e \end{bmatrix} = T(\Delta\theta) \begin{bmatrix} v_d \\ v_q \end{bmatrix} T^{-1}(\Delta\theta) = \begin{bmatrix} R_s + pL & -\omega_r L \\ \omega_r L & R_s + pL \end{bmatrix} \begin{bmatrix} i_d^e \\ i_q^e \end{bmatrix} + \omega_r \psi_{PM} \begin{bmatrix} \sin(\Delta\theta) \\ \cos(\Delta\theta) \end{bmatrix} \tag{1.14}$$

where $\Delta\theta$ denotes the estimation error of rotor position, i.e. $\Delta\theta = \theta_r - \theta_r^e$, and $\omega_r \psi_{PM}$ represents the back-EMF. For the non-salient BLAC PMSM, it can be clearly seen that only the back-EMF involves the need for rotor position information.

However, for salient BLAC PMSM such as interior PMSM, due to asymmetric impedance matrix in (1.12), the information of rotor position can be found in the conventional back-EMF and the armature effect.

Referring to the mathematical model in (1.12) with $L_d \neq L_q$, it can be used as a mathematical model of salient BLAC PMSM. Similarly, it can be transformed into the estimated reference frame applying transformation matrix $T(\Delta\theta)$, i.e. (1.13). Since the impedance matrix in (1.15) is not symmetrical, i.e. $L_d \neq L_q$, the terms of $\Delta\theta$ cannot be cancelled when it transformed into the estimated reference frame. Consequently, it cannot be directly utilised to calculate the rotor position error ($\Delta\theta$) in the back-EMF based sensorless control. Therefore, an extended back-EMF strategies are introduced in [MOR02] [CHE03] to solve such problem.

$$\begin{bmatrix} R_s + pL_d & -\omega_r L_q \\ \omega_r L_d & R_s + pL_q \end{bmatrix} \tag{1.15}$$

To retrieve symmetry in the impedance matrix, the mathematical model in (1.12) is re-written as

$$\begin{bmatrix} v_d \\ v_q \end{bmatrix} = \begin{bmatrix} R_s + pL_d & -\omega_r L_q \\ \omega_r L_d & R_s + pL_q \end{bmatrix} \begin{bmatrix} i_d \\ i_q \end{bmatrix} + \begin{bmatrix} 0 \\ E_{ex} \end{bmatrix} \tag{1.16}$$

where E_{ex} is regarded as extended back-EMF, and it is expressed as

$$E_{ex} = \omega_r \psi_{PM} + \omega_r i_d (L_d - L_q) + p i_q (L_q - L_d) \tag{1.17}$$

Then, the modified mathematical model, i.e. (1.16), can be transformed into the estimated reference frame, and the terms of $\Delta\theta$ in the impedance matrix would be cancelled. In this way, the extended back-EMF includes full information as to the rotor position regardless of whether a salient or non-salient PMSM is used. For the surface-mounted PMSM, the extended back-EMF will be reduced to classical back-EMF [LI09a]. Additionally, the extended back-EMF has been improved in [LI07] by taking into account the cross-saturation effect, whilst [WAN12] develops a new start-up method based on current regulation in order to overcome the starting and low speed issues. Also, it can work under different load conditions and shows smooth transition from the start-up to the back-EMF based sensorless control mode.

Moreover, the back-EMF of PMSMs could also be estimated by employing a sensorless control scheme based on a disturbance voltage observer, as presented in [SEN95]. Also, this same method can be applied to the estimation of extended back-EMF of the interior PMSM [CHE03]. In order to improve the robustness against the load variation, the disturbance observer-based sensorless control has been introduced in [LEE11] to estimate the load torque and yield a compensating signal to diminish the errors in the estimated rotor position.

B. Third Harmonic Back-EMF Based Sensorless Control Strategy

Usually, the third harmonic back-EMF can be found in the phase back-EMF rather than line back-EMF when the machine windings are star-connected [MOR92] [PRO94] [MOR96]. The neutral point of the star-connected windings is therefore essential to detect the third harmonic back-EMF where the measurement of phase back-EMF is required.

The star-connected resistor network, Fig. 1.12, is required to detect the third harmonic back-EMF. From Fig. 1.12, the voltage v_{sn} between the neutral point "n" of the machine winding and the central point "s" of the star-connected resistor network represents the third harmonic back-EMF irrespective of the operational mode of the PMSM [SHE04].

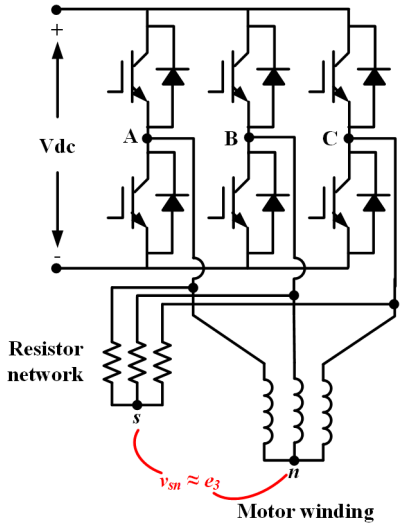

Fig. 1.12: Detection of third harmonic back-EMF.

According to [KRE94], the zero-crossings in the third harmonic back-EMF are associated with some particular positions since three cycles in terms of frequency against the fundamental back-EMF are exhibited in the third harmonic back-EMF. These specific positions are 0, π/3, 2π/3, π, 4π/3, 5π/3, 2π.

The rotor position can be simply estimated by integrating the rotor speed as [SHE06a] [LIU14]

$$\theta_r^e = \theta_o + \int_0^t \omega_r^e dt = \theta_o + \int_0^t \frac{\pi/3}{t_d} dt \tag{1.18}$$

The instantaneous current in the windings can be controlled to simplify the operation of either BLDC or BLAC once the rotor position is estimated [KRE94] [DWA08]. Some practical issues of third harmonic back-EMF based sensorless control in terms of detection and restrictions of sensorless control have been presented in [SHE06a]. Additionally, to reduce the commutation retarding and to improve the machine performance, a specific integrated circuit, ML4425, was implemented in [SHE06b], where the third harmonic back-EMF is integrated rather than the terminal voltage. Furthermore, in order to accomplish a precise switching strategy, a new software scheme of phase-looked loop (PLL) of third harmonic back-EMF detection has been introduced in [FAE09].

C. Flux-Linkage Observer Based Sensorless Control Technique

The estimation of the stator flux-linkage is essential when employed for DTC. It is also applicable to sensorless control to estimate the rotor position. Usually, the rotor position is estimated from the observed vector of the flux-linkage excited by the PM, since the position information is included in its phase angle, as shown in Fig. 1.13. Due to the complexity of directly measuring stator flux, a stator flux estimation method should be developed.

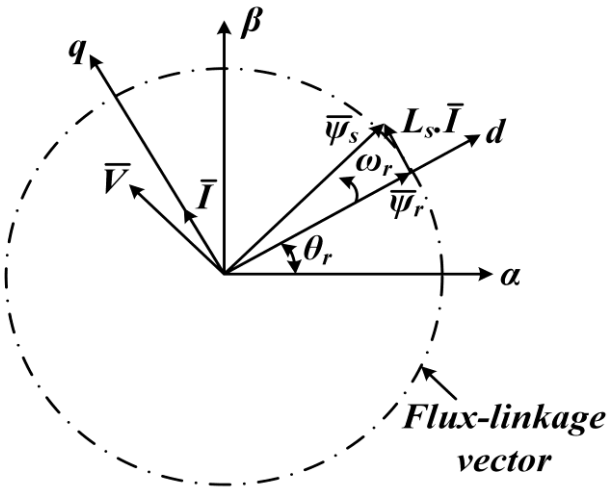

Fig. 1.13. Phasor diagram of PMSM.

The basic idea of flux-linkage observation is very simple. The stator flux-linkage vector in the stationary reference frame can be derived from the integration of the difference between the stator voltage and the voltage drop on the stator resistance, and it is expressed as

$$\bar{\psi}_{s\alpha\beta} = \int \left(\bar{V}_{s\alpha\beta} - R_s \bar{I}_{s\alpha\beta} \right) dt \tag{1.19}$$

where $\bar{I}_{\alpha\beta}$ and $\bar{V}_{\alpha\beta}$ are the stator current and voltage vectors in the stationary reference frame, respectively.

For rotor flux-linkage observation, the rotor position is obtained from the observed vector of the flux-linkage produced by PM of the machine. In the stationary reference frame, the rotor flux-linkage is calculated by subtracting the voltage drop of the inductance from the stator flux-linkage vector as [WU91] [SHE02]

$$\bar{\psi}_{r\alpha\beta} = \bar{\psi}_{s\alpha\beta} - L_s \bar{I}_{s\alpha\beta} \tag{1.20}$$

where L_s represents the stator self-inductance.

For the surfaced-mounted permanent magnet synchronous machines (SPMSMs), which are utilised in this investigation, $L_\alpha = L_\beta = L_s$. The rotor flux-linkages for SPMSM in the $\alpha-$ and $\beta-$ axes of the stationary reference frame are thus given by [CHI09] and [XU14]

$$\psi_{r\alpha} = \int \left(v_\alpha - R_s i_\alpha \right) dt - L_s i_\alpha \tag{1.21}$$

$$\psi_{r\beta} = \int \left(v_\beta - R_s i_\beta \right) dt - L_s i_\beta \tag{1.22}$$

The rotor position can hence be estimated as

$$\theta_r^e = arctan\left(\frac{\psi_{r\beta}}{\psi_{r\alpha}} \right) \tag{1.23}$$

The voltage and current vectors are obtained from the terminal voltage and phase current, respectively, but some issues can be found when measuring the voltage such as extra cost for the voltage transducer and isolation issues. The phase current is usually employed, therefore, in order to calculate the required voltage as the input reference voltage to the flux-linkage observer. However, a position estimation error may occur due to the dead-time effects between switching the devices on and off again in same inverter phase leg. Such errors have been compensated for in [HAR00].

From (1.19), the stator flux-linkage calculation is an open-loop calculation without considering some potential issues such as stator resistance variation and integration drift. In [WU91], the integration of the terminal voltage of the machine for the stator flux-linkage observation was employed in order to obtain the estimated rotor position. However, flux vector offset and drift issues can be found due to errors occurring in the winding resistance. In order to overcome such problems, a low-pass filter (LPF) can therefore be utilised instead of using a pure integrator in order to enhance the estimation of the rotor position [WU91]. On the other hand, a phase shift in the fundamental flux will occur in variable speed operation when using LPF due to its slow dynamic response.

To solve the above-mentioned problems, closed-loop methods for stator flux-linkage estimation can be utilised [HU98] [YOO09] [BOL09] [XU14]. The combination of voltage model and current model, i.e. a hybrid flux-linkage observer as shown in Fig. 1.14, could be employed over a wide speed range; the current model is predominant at low speed, whilst the voltage model is predominant within in high-speed region.

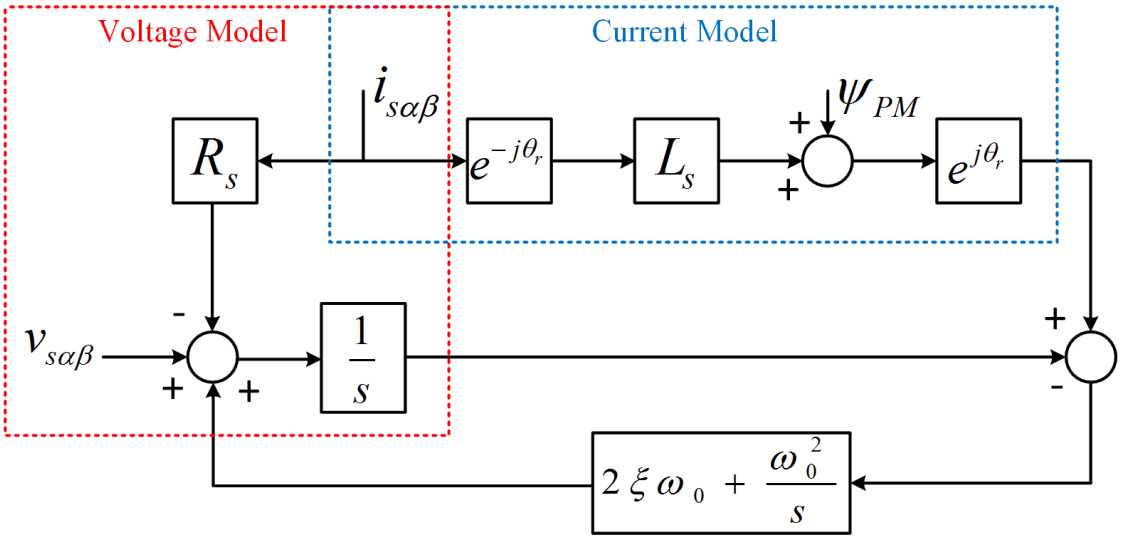

Fig. 1.14. Combined flux-linkage observer [YOO09].

D. Adaptive Observers Based Sensorless Control Technique

Depending on the fundamental model of the PMSM, some adaptive observers, including the model reference adaptive system (MRAS), sliding mode observer (SMO), and an extended Kalman filter (EKF) can also provide decent sensorless control performance. These observers have the merits of robustness, immunity to machine parameter variations, quick convergence and response, and elimination of the need to estimate back-EMF.

(a) Model Reference Adaptive System (MRAS)

The MRAS method is also a choice for providing sensorless rotor position estimation [PII08] [HE09] [GAD10]. The scheme of MRAS is illustrated in Fig. 1.15, where the real machine is represented by the reference model, whilst the adjustable model represents a fictional machine based on the mathematical model. The difference between the two responses from the reference and adjustable models with the same excitation provides an estimation error (ε), which is only small. Then, the behaviour of the adaptive model could be similar to that of the actual motor. The states of the machine involving the information of rotor position can hence be estimated from the adaptive mathematical model. By using a non-linear controller, including a 'fuzzy logic' controller [GAD10] or conventional PI regulator [MAT96] [BAE03], the correction controller can be achieved.

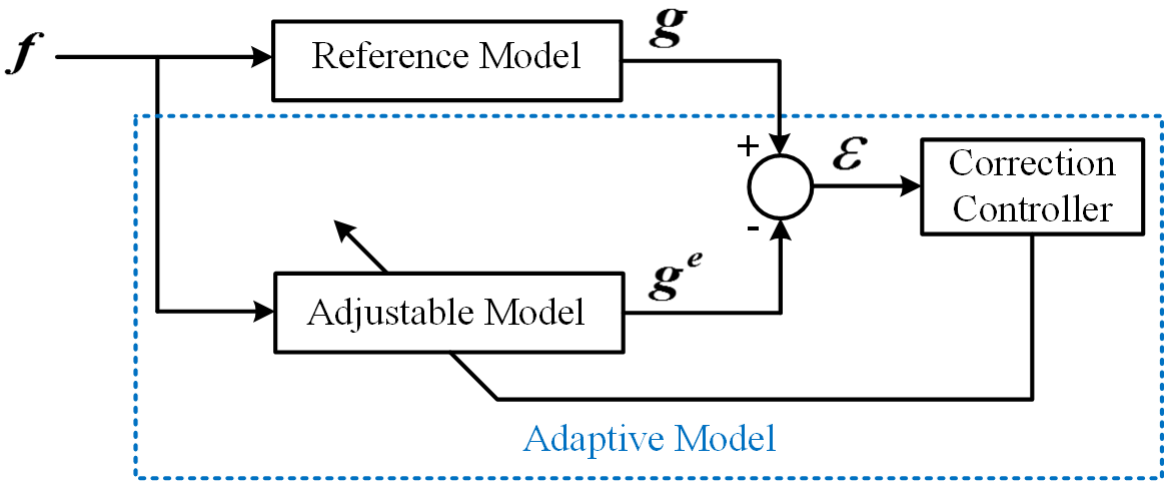

Fig. 1.15. Block diagram of MRAS [PII08].

(b) Sliding Mode Observer (SMO)

The SMO is an observer with discontinuous functions of the error between the estimated and measured machine variables, as seen in Fig. 1.16. The surfaces chosen in the state space can decide the dynamic behaviour of the control system. Such dynamic behaviour is not affected by the matched uncertainty. It therefore has the merits of disturbance rejection, strong robustness, and order reduction.

The SMO was first introduced in [FUR92] and has been utilised for sensorless control. A sensorless control based on SMO has been presented in [CHI09] for use within a wide speed range, including the flux-weakening region. Furthermore, a new SMO was introduced in [KIM11] for robust sensorless control of PMSMs, where a sigmoid as a switching function has been employed instead of the conventional sign function to overcome the problems in conventional SMO [ZHA06]. Furthermore, to improve the dynamic state performance and robustness to load disturbances, a non-linear speed controller based on SMO and high-frequency injection strategy has been proposed in [FOO10] [WAN10].

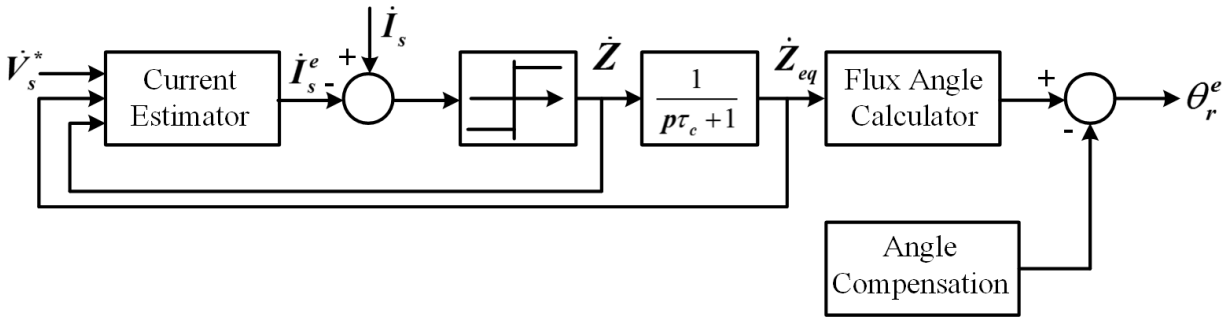

Fig. 1.16. Schematic diagram of SMO [CHI09].

(c) Extended Kalman Filter (EKF)

Generally, EKF is a recursive optimum-state estimator, which can be employed in a non-linear dynamic system by utilising noisy signals that are distributed by random noise. By using measured states in addition to the statistics of the noise, the EKF can obtain estimation of immeasurable states, including rotor position and speed [VAS03] [HAR96] [LIU06]. Unlike conventional fundamental estimation methods, EKF is less affected by parameter inaccuracy and measured noise. It does, however, require relatively complex matrix computations. A simplified EKF algorithm, which was firstly introduced in [HAR96] to estimate the rotor speed from noisy output signals of a resolver, has thus also been developed in [LIU06] to be combined with a back-

EMF estimator for accurate speed estimation. Furthermore, in [FUE11], with assuming that some of the system states will be free of noise, a reduced order EKF has been introduced in order to improve the speed of control.

1.3.2. Machine-Saliency Based Sensorless Control Techniques

Fundamental model-based sensorless control strategies can provide an adequate sensorless control performance at the medium and high speeds since the back-EMF is directly proportional to the rotor speed, but deteriorate the performance at zero speed and in low-speed range where the back-EMF is very low or even zero. To handle such limitations, machine saliency-based sensorless control techniques have therefore been developed to achieve decent performance in the low-speed range, including at standstill, since machine saliency behaviour does not depend on the rotor speed. These techniques rely on machine saliency, which results from either geometrical rotor saliency or magnetic saturation saliency, in which the winding inductance variation is an important feature to estimate the rotor position.

The measured variation of inductance according to the electrical rotor position for the PMSM is shown in Fig.1.17 [KAN10]. It shows that the position-dependant spatial saliency modulates the inductance of the machine. The information of rotor position can hence be deduced from the inductance variation.

In order to extract the information of rotor position, the saliency of the machine is essential for high-frequency carrier signal injections to derive position-dependant responses, i.e. voltage or current. Based on the types of injected signal, machine saliency based sensorless control methods could be divided into different techniques, including continuous carrier signal injection strategies, injection of transient voltage vector strategy, and fundamental PWM excitation technique.

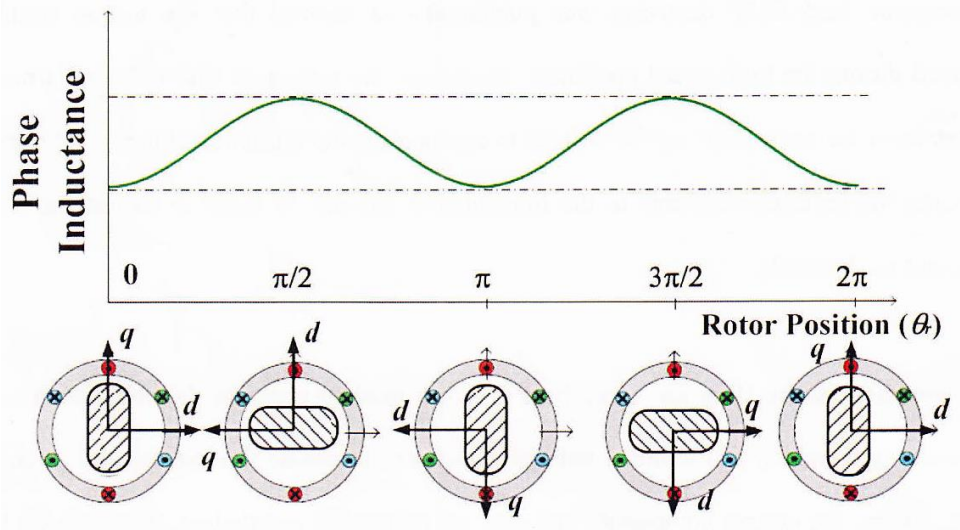

Fig. 1.17. Phase inductance variation dependant on electrical rotor position [KAN10].

(a) Persistent Carrier Signal Injection Methods

The principle idea of the persistent carrier signal injection strategies is that a high-frequency carrier signal voltage or current (usually voltage) is continuously superimposed on the fundamental excitation. A rotor position-dependent carrier signal response such as carrier current response or zero-sequence carrier voltage response, is produced from the interaction of the injected high-frequency signal with the spatial saliency of the machine. Then, the rotor position can be extracted from the position-dependent carrier signal response by using a tracking observer.

The persistent carrier signal injection can be classified as a rotating sinusoidal signal injection [JAN95] [DEG98] [BRI04] [BRI05] [CAR06] [SIL06] [GAR07] [RAC10] [GON 11b] [GAB13], a pulsating sinusoidal signal injection [COR98] [HA00] [JAN03] [LI09b] [GON11b] [ACC12] [LIU14] [LIN15b], a square-wave high-frequency signal injection method [YOO11] or arbitrary injection technique [PAU11].

For the rotating high-frequency voltage signal injection technique, a three-phase balanced voltage carrier signal is injected in $\alpha\beta$-reference frame to compose a rotating excitation superimposed into the fundamental excitation. The rotor position information could then be obtained from the phase modulated carrier current response [JAN95] [JOE05] or zero-sequence carrier voltage [BRI04] [BIR05] [GAR07] [XU16].

In the case of rotating signal injection utilising the carrier current response for position estimation, the carrier current response includes two components: a positive-sequence component in which its rotating speed is the same as that of injected carrier voltage, and a negative-sequence component where the information of rotor position is included in its phase angle. Besides, the synchronous reference frame filter (SRFF) is usually employed to deduce the position-dependent negative-sequence carrier current [DEG98] [GAR07] [RAC10]. Furthermore, the inverter non-linearity effects [GUE05] [GON11a], multiple saliencies effects [DEG98] [RAC08], and the effect of cross-saturation [GUG06] [ZHU07] [BIA07] [LI09] [GON11b] are considered, since they can cause errors in the rotor position estimation.

On the other hand, for the rotating signal injection using zero-sequence carrier voltage, it has been demonstrated that the zero-sequence carrier voltage signal can be utilised for rotor position estimation [BIR04] [BIR05] [GAR07]. The zero-sequence carrier voltage shows low total harmonic distortion (THD) and exhibits less sensitivity to the distortion of the injected carrier voltage signal compared to the carrier current response [GAR07]. Moreover, significant enhancement of the system bandwidth and rotor position estimation accuracy can be found when utilising zero-sequence carrier voltage [CON00] [BIR04] [BIR05] [GAR07] [XU16]. The measurement of the zero-sequence carrier voltage is necessary to extract the rotor position information. Usually, the measurement of zero-sequence carrier voltage is achieved based on one of the two popular measurement methods. One scheme utilises phase-to-neutral voltages [BRI04], as shown in Fig. 1.18. Another method employs the auxiliary resistor network [BRI05], as shown in Fig. 1.19. For the first method, by measuring the three phase-to-neutral voltages of the machine utilising voltage sensors, the resultant zero-sequence carrier voltage is obtained, whilst the second method measures the zero-sequence voltage by connecting a resistor network in parallel with the motor terminals.

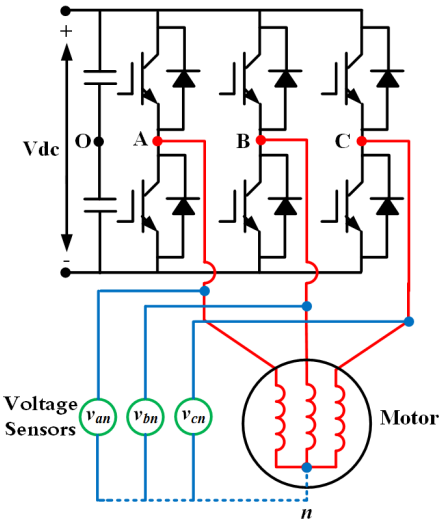

Fig. 1.18. Measurement of zero-sequence employing phase-to-neutral voltages.

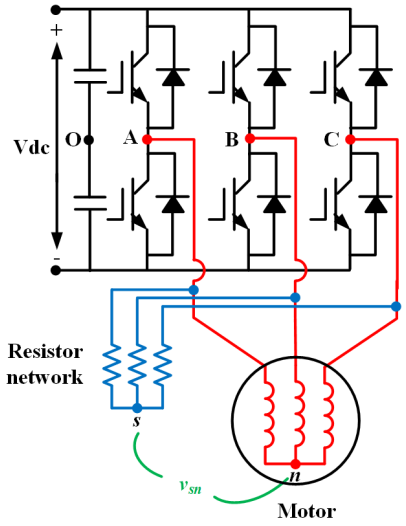

Fig. 1.19. Measurement of zero-sequence utilizing auxiliary resistor network.

For the high-frequency pulsating signal injection technique, a high-frequency pulsating voltage is injected, whether into the *d*-axis [CAR06] [HOL06] [LIN15b] [LUO16] or *q*-axis [LIN03] [JAN04] [YAN11] in the estimated synchronous reference frame as two superposed rotating carrier voltages with opposite directions. The rotor position can then be estimated through minimisation of the amplitude signal along the orthogonal axis to the injection axis. Normally, the pulsating carrier injection into *d*-axis is utilised, with the *q*-axis carrier current being employed to estimate the rotor position due to limited ripples in the *q*-axis current. Alternatively, it is also possible to use the pulsating injection into the *q*-axis, and the employ the *d*-axis carrier current response for rotor position estimation. However, more current and torque ripples will occur in this

method.

On the other hand, for the conventional pulsating signal injection employing zero-sequence carrier voltage, it has been investigated in [XU16] for the single three-phase PMSM. It has been found, however, that the conventional pulsating injection method employing zero-sequence voltage degrades the position estimation performance due to large DC and sixth harmonic in the estimation errors. This is because of large amplitudes of undesirable harmonic components in the zero-sequence carrier voltage. A new pulsating carrier signal injection strategy using zero-sequence voltage was thus proposed in [XU16]. In a departure from the conventional rotating signal injection in the stationary reference frame utilising zero-sequence carrier voltage strategy, the proposed pulsating injection is based on the estimated reference frame, which rotates anti-clockwise at twice the estimated rotor electrical angular speed. Then, the rotor position is estimated through setting the zero-sequence carrier voltage to zero. The new method is simpler for signal demodulation and more robust to signal processing delays, since the amplitude is modulated by the machine saliency. Furthermore, the phase shifts in the saliency position resulting from signal processing delays are intrinsically cancelled.

Although both conventional rotating and pulsating carrier injection techniques have been well developed, the dynamic characteristics and dynamic bandwidth of the control system are restricted in relation to the high-frequency of the injected signal. To overcome the dynamic limitation, the square waveform signal injection method is the best solution. In [YOO11], the sensorless dynamic performance has been remarkably improved by employing high-frequency square signal injection into the estimated *d*-axis, where the LPFs for signal demodulation process are not required.

All of the above-mentioned high-frequency carrier signal injection methods depend on the spatial rotor saliency, which is found in salient permanent magnet synchronous machines such as interior PMSMs. In the case of non-salient permanent magnet synchronous machines, i.e. surface-mounted PMSMs, the difficulty of obtaining the rotor position information is the main challenge, since the ratio of spatial rotor saliency is very low. However, some physical features such as eddy current loss [YAN12a] [YAN12b], and magnetic-saturation induced saliency [KOC09] [BIA08] have been exploited successfully to deduce the rotor position. In [BIA08], the magnetic saturation induced saliency was employed to obtain an appropriate saliency ratio in order to obtain the rotor position, but was not applicable for all SPMSMs. Furthermore, the stator magnetic-saturation

saliency could also be utilised to estimate the rotor position, as demonstrated in [JAN03] [FRE05] [HA08]. Based on resistance-based induced saliency due to high-frequency eddy current loss, a new sensorless control method for rotor position estimation was introduced in [YAN12a] for SPMSMs. The comparison between resistive saliency and inductive saliency has also been addressed in [YAN12b]. Additionally, the sensorless control capability of SPMSMs based on rotating and pulsating injection techniques has been investigated in [LIN15b].

(b) Transient Voltage Vector Injection Method

For the transient voltage vector injection, information concerning the rotor position could be deduced from the response of current transient against an impulse voltage vector. The typical technique is the Indirect Flux Detection by On-line Reactance Measurement scheme (INFORM) [SCH96] [ROB02] [OVR03] [ROB04], and it is designed to superimpose extra impulse voltage vectors during zero vectors for the standard PWM. However, such method might be impervious to parameter variations and measurement noise, since it detects the inductance of the machine utilising voltage signals in a short time. A compensation scheme such as a Kalman filter is required due to the injected signal being a periodic signal.

The main challenge in the classical INFORM technique is the introduced current disturbance because of the additional vectors of transient voltage. Furthermore, this method is suitable only for low speeds rather than high speeds with assumption of constant rotor position during the successive three PWM cycles. A compensation scheme employing a double transient injection is therefore introduced in [ROB04] in order to enhance the sensorless control performance at high speeds. Besides, with applying the additional vectors of transient voltage, the saliency rotor position information would be found in the zero-sequence current derivatives for the delta-connection [STA06] and the zero-sequence voltage resultant for the star-connection [HOL98]. These current derivatives and zero-sequence voltages can then also be utilised for rotor position estimation.

(c) PWM Excitation Without Injection

The voltage vectors employed in the abovementioned technique also present in the fundamental Pulse Width Modulation (PWM) from the inverter output in normal operation. Measurement of the transient current response produced by the ingrained PWM to deduce the information of rotor position should therefore be possible. Compared to transient voltage vector injection techniques, the merit of the PWM excitation is the elimination of the requirement for additional transient voltage vector injection, which results in some issues such as higher switching loss, additional current ripple, and restricted dwelling time of zero voltage vectors.

Various measured current derivative response combinations in relation to particular voltage vectors could be employed to formulate the position vector for extracting the rotor position information [HOL05] [GAO07] [BOL11] [HUA11]. An extended modulation (EM) technique has been introduced in [HOL05], where the saliency information is obtained utilising the transient current response produced by the modified PWM. The standard PWM could also be employed to estimate saliency-based rotor position, as demonstrated in [GAO07] [BOL11] [HUA11]. Additionally, the second harmonic PWM is regarded as a pulsating voltage vector because of its large amplitude. Hence, by using the second harmonic PWM voltage and current, the position-dependant impedance can be calculated to be exploited for rotor position estimation [RUA10]. Furthermore, in [LEI11], it has be proven that the zero-sequence excitation produced by fundamental PWM can be also applied to estimate the saliency-based rotor position.

The PWM excitation technique has the advantages of fast dynamic response due to wide speed range operation and high-frequency PWM. However, the measurement of the current derivative is difficult in its practical implementation.

1.3.3. Sensorless Control for Dual Three-Phase PMSM

Apparently, most of the sensorless control strategies mentioned earlier for single three-phase PMSMs could be easily be extended to be applied to dual three-phase (DTP) PMSM drives. Recently, different sensorless control methods for DTP-PMSMs have been introduced. In [HE09], the model of the DTP-PMSM was represented according to vector space decomposition (VSD) theory first, then a sensorless control strategy based on the Model Reference Adaptive System (MRAS) scheme was developed. The stability of the system has been validated by Popov's super stability theory. Furthermore, a new and very simple method for initial rotor position estimation by means of DC excitation without any sensors was also presented in [HE09].

In [BAR12], the torque components and sensorless position detection capability of dual three-phase interior PMSM have been investigated under healthy as well as faulty conditions with different configurations. To test operation under faulty conditions, an open circuit was considered and only one winding set was supplied. Sensorless control based on high-frequency carrier voltage injection was implemented to investigate the capability for rotor position detection under both conditions. In order to achieve such capability, the presence of rotor saliency has been evaluated for healthy and faulty conditions, since the position estimation for the high-frequency signal injection depends on the interaction between the signal injection and the rotor saliency. The experimental results demonstrate the presence of the rotor saliency even with a faulty configuration, as well as rotor position estimation capability. In [GRE12], sensorless speed control of asymmetric dual three-phase induction machine was investigated by utilising an inner loop of Model Based Predictive Control (MBPC), which is obtained from the mathematical model of the machine.

Furthermore, an improved third harmonic back-EMF based sensorless control method with the aid of a simplified EKF based estimator has been introduced in [LIU15], where the rotor position could be estimated without any filter and consequently can improve the frequency response and dynamic performance.

1.4. Scope of Research and Contributions of the Thesis

1.4.1. Scope of Research

This thesis focuses on the sensorless control of single and dual three-phase PMSM drives to enhance the rotor position estimation using different sensorless control methods covering both low- and high-speed ranges. The fundamental model-based sensorless control methods, i.e. flux-linkage observer (FO) scheme, and extended Kalman filter (EKF) scheme, are employed for the high speed region, and machine-saliency based sensorless control techniques, i.e. high-frequency rotating and pulsating carrier voltage injection techniques, are utilised for zero and low speed regions. Fig. 1.20 shows the scope of research of this thesis.

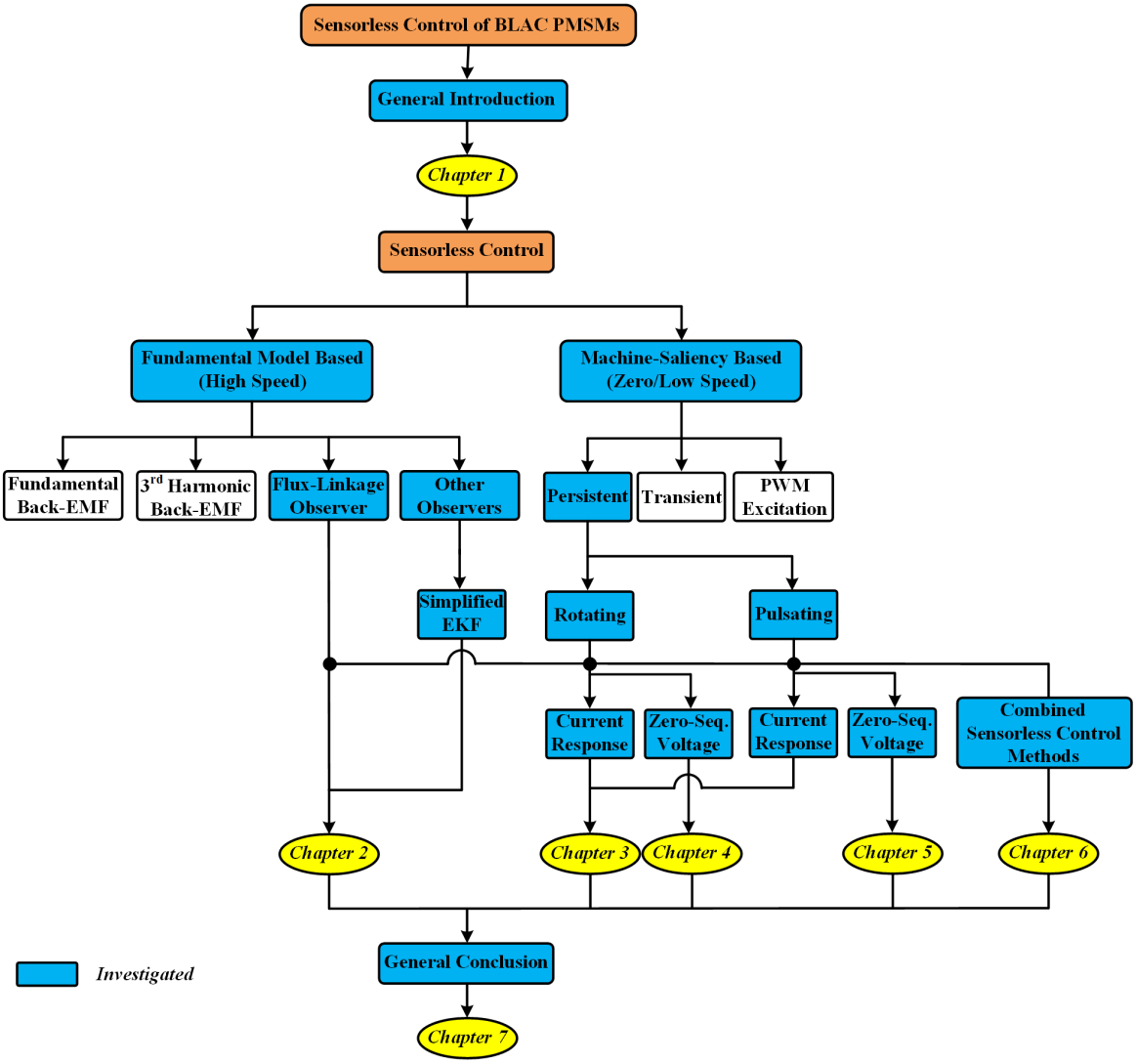

Fig. 1.20. Research of scope of the thesis.

Other chapters are summarised as follows:

Chapter 2: This chapter investigates the influence of back-EMF and current harmonics on the accuracy of rotor position and speed estimation for single and dual three-phase (DTP) permanent magnet synchronous machines (PMSMs), which are widely utilised for AC machines, with two fundamental-model-based sensorless control strategies, i.e. the flux-linkage observer (FO) method and the simplified extended Kalman filter (EKF) method. The single three-phase PMSM is employed to investigate the influence of back-EMF harmonics on the accuracy of rotor position estimation, while the influence of current harmonics on the rotor position and speed estimation accuracy is studied for the DTP-PMSM, which inherently involves harmonic currents in ST-DTC methods. The experimental results confirm that the simplified EKF shows better rotor position and speed estimation accuracy compared to the FO method, even with the existence of back-EMF and current harmonics, due to its higher noise rejection ability.

Chapter 3: In this chapter, the commonly used conventional rotating and pulsating high-frequency voltage signals injections based sensorless control strategies for single and dual three-phase PMSMs are described in detail and a comparative study between both methods is outlined. The machine saliency level, which is essential for high-frequency carrier signal injection techniques, is investigated for the test machine. Furthermore, a detailed discussion about certain practical issues concerning sensorless control implementation, including the cross-coupling saturation effect compensation and the tracking observer for rotor position, is also provided.

Chapter 4: The sensorless control performance of pulsating carrier signal injection utilising zero-sequence voltage for DTP-PMSM drives is studied in this chapter. A new simple measurement technique for zero-sequence carrier voltage is then proposed, in which only one voltage sensor is put between the two isolated neutral points of the two stator winding sets. Subsequently, an improved pulsating injection based sensorless control strategy employing zero-sequence carrier voltage is proposed, in which the undesirable 6^{th} harmonic components can be suppressed by considering an optimum phase shift, i.e. 90 degrees, between the two independent injected high-frequency signals. Consequently, the accuracy of rotor position estimation is enhanced and the experimental results validate the effectiveness performance of the proposed method under both steady-state and dynamic conditions.

Chapter 5: In this chapter, the rotor position estimation accuracy of the rotating carrier signal injection utilising zero sequence carrier voltage method for PMSM drives is investigated. For the single three-phase PMSM, undesirable 6^{th} harmonic estimation errors occur due to the additional saliency components in the zero-sequence carrier voltage. In the case of the DTP-PMSM, an improved rotating carrier signal injection using a zero-sequence voltage-based sensorless control technique is proposed, where the oscillating position estimation error can be suppressed by employing the optimum phase shift between the two injected high-frequency signals, i.e. 120 degrees, thanks to the existence of additional degrees of freedom in DTP-PMSM drives. This results in improvements in rotor position estimation accuracy. An outstanding overall performance of the proposed method for DTP-PMSM is validated by the experimental results.

Chapter 6: A combination of sensorless control strategies to derive the estimated rotor position at full speed range with smooth transition between the low and high speed ranges is presented in this chapter. The combined sensorless control technique includes the flux-linkage observer method and four different high-frequency carrier signal injection strategies, namely pulsating injection utilising carrier current response, rotating injection employing carrier current response, pulsating injection using zero-sequence carrier voltage response, and rotating injection utilising zero-sequence carrier voltage response. Such strategies are applied to the DTP-PMSM to investigate the sensorless control performance under different speed ranges. To achieve smooth transition between the combined methods, a function similar to hysteresis is applied for certain speed ranges with optimum weighted gains for both estimated positions without requiring a complex structure and time-consuming computations. A smooth transition from the high-frequency carrier signal injections techniques at low speeds to the flux-linkage observer strategy at higher speeds are achieved, with the experimental results confirming that the system stability can be ensured.

Chapter 7: This chapter summarises the research work carried out in this thesis, and discusses potential related future work.

It is worth noting that Chapters 4 and 5 represent the most significant contributions of this thesis.

1.4.2. Main Contributions

The major contributions of this thesis are:

- The new rotor position estimation methods based on pulsating and rotating carrier signal injections and zero-sequence carrier voltage sensing for DTP-PMSM are developed to significantly improve the accuracy and system robustness of rotor position estimation by injecting two high-frequency signals into both stator winding sets and employing an optimum phase shift between the two signals.

- A new simple method to measure the zero-sequence carrier voltage is proposed for the DTP-PMSM.

Other contributions include:

- To enhance the rotor position estimation for PMSMs with distorted back-EMF and currents, a simplified EKF based rotor position estimator is applied with conventional flux-linkage observer based sensorless control.

- Based on the injection of high-frequency carrier voltage based sensorless control strategies, the sensorless control performances for single and dual three-phase PMSMs are systematically investigated.

- To achieve high sensorless control performance for a wide speed range, a combination of flux-linkage observer method with four high-frequency carrier signal injection techniques is introduced. Furthermore, in order to obtain a smooth transition between the combined methods, a function similar to hysteresis is presented for certain speed ranges with optimum weighted gains for both estimated positions without needing a complex structure or time-consuming computations.

The list of publications resulting from this PhD research work is listed as follows, and also shown in Appendix III.

- **Best Paper Award**

The following paper has been selected for best paper award in *the 17th Int. Conf. on Electrical Machines and Systems, ICEMS2014, 22-25 Oct. 2014, Hangzhou, China:*

A. H. Almarhoon, and Z. Q. Zhu, "Influence of back-EMF and current harmonics on position estimation accuracy of permanent magnet synchronous machine," The 17th *Int. Conf. on Electrical Machines and Systems*, ICEMS2014, 22-25 Oct. 2014, Hangzhou, China.

Its modified version has been published in COMPEL: The International Journal for Computation and Mathematics in Electrical and Electronic Engineering.

- **Journal Papers**

[1]. A. H. Almarhoon, Y. Ren, and Z. Q. Zhu, "Influence of back-EMF and current harmonics on sensorless control performance of single and dual three-phase permanent magnet synchronous machines," *COMPEL: The International Journal for Computation and Mathematics in Electrical and Electronic Engineering*, vol.35, no.2, pp. 744-763, 2016.

[2]. Ali H. Almarhoon, Z. Q. Zhu, and P. L. Xu, "Improved rotor position estimation accuracy by rotating carrier signal injection utilizing zero-sequence carrier voltage for dual three-phase PMSM," *IEEE Trans. Ind. Electron*., in press.

[3]. Ali H. Almarhoon, Z. Q. Zhu, and P. L. Xu, "Improved pulsating carrier signal injection based sensorless control strategy using zero-sequence carrier voltage for DTP-PMSM," *IEEE Trans. on Energy Conversion*, in revision process.

- **Conference Papers**

[1]. A. H. Almarhoon, and Z. Q. Zhu, "Influence of back-EMF and current harmonics on position estimation accuracy of permanent magnet synchronous machine," The 17th *Int. Conf. on Electrical Machines and Systems*, ICEMS2014, 22-25 Oct. 2014, Hangzhou, China.

[2]. A. H. Almarhoon, Y. Ren, and Z. Q. Zhu, "Sensorless switching-table-based direct torque control for dual three-phase PMSM drives," The 17th *Int. Conf. on Electrical Machines and Systems*, ICEMS2014, 22-25 Oct. 2014, Hangzhou, China.

CHAPTER 2

INFLUENCE OF BACK-EMF AND CURRENT HARMONICS ON SENSORLESS CONTROL PERFORMANCE OF SINGLE AND DUAL THREE-PHASE PMSMS

2.1. Introduction

Three-phase permanent magnet synchronous machines (PMSMs) have been extensively applied to various industrial drives for decades due to their excellent features of high efficiency and torque density, etc. In order to achieve high performance control of PMSMs, accurate rotor position information is required, which can be obtained from high-resolution sensors, e.g. encoders and resolvers. However, such sensors may not only increase the system size and cost but also impair robustness and reliability of the system [ACA06]. Therefore, various sensorless control techniques have been proposed and developed in literature which can be classified into two categories: methods based on machine saliency [RAC10], [LIU14] and [CHE14], and methods based on fundamental model [MOR02], [SHE06], [WAN12], [WU91], [SHE02], [AND08], [CHI09], [FOO10], [LJU79], [HAR96], [TER01], [LIU06], [PII08] and [ALM14].

The former approaches have been shown to be capable of providing high performance sensorless control at low-speed and standstill operating regions. In contrast, the latter approaches provide superior performance in medium- and high-speed ranges where the machine model can be accurately established.

The main idea of sensorless control strategies based on fundamental model is to estimate back electromotive force (back-EMF) or flux-linkage, which involve the information of rotor position, according to the machine model [MOR02], [SHE06], [WAN12], [WU91], [SHE02], [AND08] and [ALM14]. Hence, the position estimation could be accomplished via open-loop calculation, closed-loop observer such as flux-linkage observer (FO) [WU91], [SHE02] and [AND08], or directly obtained from the machine model utilizing adaptive observers including sliding mode observer (SMO) [CHI09] and [FOO10], extended Kalman filter (EKF) scheme [HAR96], [TER01] and [LIU06], and model reference adaptive system (MRAS) [PII08]. Among them, the most common method is the integration of back-EMF which is stator flux-linkage observer.

In [WU91], it has been demonstrated that the pure integration of back-EMF has some issues such as flux-linkage vector drift due to the offset error resulting from the inaccurate winding resistance, measured currents and voltages. Hence, to improve the position estimation accuracy, a replacement of the pure integrator with a low-pass filter (LPF) has been presented in [SHE02]. However, in variable speed operation, a phase shift to the fundamental flux vector will occur when LPF is utilized due to its slow dynamic response.

Alternatively, EKF algorithm, which is introduced in [LJU79], can directly estimate the rotor position from the machine model. The EKF is a full-order stochastic observer for the recursive optimum state estimation of a nonlinear dynamic system in real time, which shows good position and speed estimation performance [TER01]. However, it requires relatively complex matrix computations, which makes it challenging to be implemented in practice. On the other hand, a simplified EKF algorithm, which was firstly introduced in [HAR96] to estimate the rotor speed from noisy output signals of a resolver, has been developed in [LIU06] to be combined with a back-EMF estimator for accurate speed estimation.

Ideally, both the FO and EKF approaches exhibit decent speed and position estimation performance. However, in most of the industrial applications, some issues such as distorted back-EMF and current harmonics could more or less affect the sensorless control performance for both strategies, which, based on author's knowledge, have not been investigated in literature.

Generally, the main reasons for machine variables harmonics ($k=6n\pm1$, where $n=1,3,5,\ldots$) are as follows [KAR12]:

- The construction of the machine: permanent magnets, pole shape, slotting, rotor saliency and possible magnetic saturation can produce air-gap flux harmonics, which can be calculated with finite element method (FEM) or measured from the back-EMF.
- Supplying voltage source inverter (VSI): if the supplied voltage contains harmonics of the order ($k=6n\pm1$, where $n=1,3,5,\ldots$), e.g. PWM-based VSIs, additional stator current harmonics (the 5th and 7th harmonic components in particular) might occur.

Thus, as the extended work of [ALM14], this chapter aims to provide a detailed investigation of the influence of harmonics in back-EMF and currents on the accuracy of position and speed estimation for both FO and EKF. In [ALM14], it has been demonstrated that the performance of conventional FO based sensorless control would be deteriorated when the single three-phase

PMSM suffers from distorted back-EMF. In order to overcome such issue, a simplified EKF with high-noise rejection ability has been adopted which renders a higher rotor position estimation accuracy. Furthermore, it should be noted that, in the previous work [ALM14], the harmonic components of currents are deliberately injected to the system, which is not so appropriate. Hence, in this chapter, the conventional switching-table-based direct torque control (ST-DTC) strategy for DTP-PMSM introduced in [HOA15], which inherently suffers from non-sinusoidal stator currents in addition to the distorted back-EMF, is taken as a case to investigate the effect of current harmonics on sensorless control performance. Additionally, the modified switching-table-based direct torque control (ST-DTC) method for DTP-PMSM presented in [REN15b], which exhibits more sinusoidal stator currents compared to that of conventional ST-DTC strategy is also implemented for the same investigation. The experimental results indicate that the simplified EKF exhibits better position and speed estimation accuracy in both the conventional and modified ST-DTC strategies.

2.2. Sensorless Control Based on Flux-Linkage Observer and Simplified Extended Kalman Filter

2.2.1. Conventional Flux-Linkage Observer (FO)

For rotor flux-linkage observer, the rotor position is obtained from the observed flux-linkage vector produced by the permanent magnet (PM) which could be derived by subtracting the voltage drop on the inductance from the stator flux-linkage vector in the stationary reference frame based on the phasor diagram shown in Fig. 2.1 [WU91] and [SHE02].

The stator voltage vector is expressed in $\alpha\beta$ reference frame as

$$\bar{V}_{s\alpha\beta} = p\bar{\psi}_{s\alpha\beta} + R_s\bar{I}_{s\alpha\beta} \tag{2.1}$$

and the stator flux-linkage vector in the stationary reference can be derived by the integration of the respective back-EMF as

$$\bar{\psi}_{s\alpha\beta} = \int \left(\bar{V}_{s\alpha\beta} - R_s\bar{I}_{s\alpha\beta}\right)\, dt \tag{2.2}$$

Then, the rotor flux-linkage vector produced by PM ($\bar{\psi}_{r\alpha\beta}$) can be calculated as

$$\bar{\psi}_{r\alpha\beta} = \bar{\psi}_{s\alpha\beta} - L_s\bar{I}_{s\alpha\beta} \tag{2.3}$$

where $V_{s\alpha\beta}$, $\psi_{s\alpha\beta}$, $I_{s\alpha\beta}$ are the stator voltage, flux and current vectors in $\alpha\beta$ reference frame,

respectively, p is the differential operator, R_s denotes the stator resistance while L_s represents the stator self-inductance.

In the case of surface-mounted permanent magnet synchronous machine (SPMSM), which is utilized in this investigation, $L_\alpha = L_\beta = L_s$. Thus, the rotor fluxes for SPMSM in $\alpha-$ and $\beta-$ axes are given by [SON09] and [XU14]

$$\psi_{r\alpha} = \int \left(v_\alpha - R_s i_\alpha \right) dt - L_s i_\alpha \tag{2.4}$$

$$\psi_{r\beta} = \int \left(v_\beta - R_s i_\beta \right) dt - L_s i_\beta \tag{2.5}$$

Hence, the rotor position can be estimated

$$\theta_r^e = arctan\left(\frac{\psi_{r\beta}}{\psi_{r\alpha}} \right) \tag{2.6}$$

and then, the rotor speed can be calculated as

$$\omega_r = p\theta_r = \left(\frac{\theta_{r(k)}^e - \theta_{r(k-1)}^e}{T_s} \right) \tag{2.7}$$

where θ_r is electrical rotor position, ω_r is mechanical angular speed, and T_s is the sampling period.

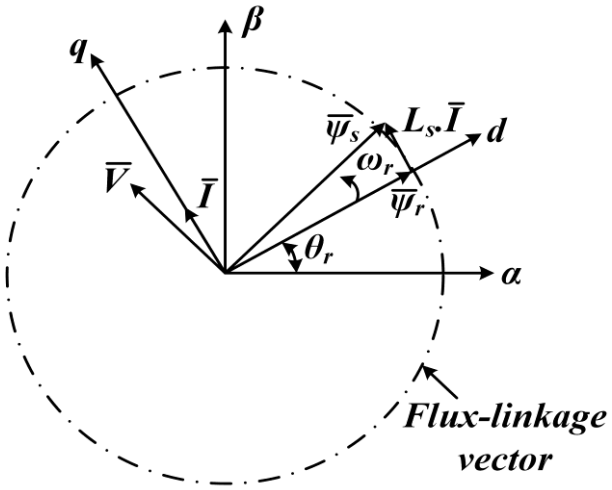

Fig. 2.1. Phasor diagram of PMSM.

As discussed in the introduction, the pure integration of back-EMF would cause the drift issue in the estimated flux-linkage vector because of the offset error in the measured currents and voltages. Usually, such offset error is a small DC value and it varies slowly. However, it can still give rise of saturation in the output value of the integrator which results in an inaccurate value. Thus, in this chapter, the pure integrator is replaced by LPF to overcome this issue [SHE02]. Additionally, the rotor position and speed estimation accuracy would also be affected by distorted back-EMF and stator currents. Hence, the simplified EKF with higher noise-rejection ability is employed to enhance the sensorless control performance, which is presented in the next subsection.

2.2.2. Simplified Extended Kalman Filter (EKF)

Generally, EKF is a recursive optimum-state estimator, and it can be employed in a non-linear dynamic system by utilizing noisy monitored signals, which are contaminated by random noise. By using measured states in addition to statistics of the noise and measurement, the EKF can obtain the immeasurable states such as rotor position and speed. Generally, it is possible to consider the modelling errors, the errors in the measurements, and computational inaccuracies due to have nosy inputs.

A discrete time, non-linear dynamic system in the state-space form can be expressed as [HAR96], [TER01] and [LIU06]

$$x(k+1) = f(x(k),\ k)+g(u(k),\ k)+w(k) \tag{2.8}$$

$$y(k) = h(x(k),\ k)+v(k) \tag{2.9}$$

where $u(k)$ and $y(k)$ are the input and output signals, respectively, and the process noise and measurement noise are represented by $w(k)$ and $v(k)$, respectively. $x(k)$ is referred as the state vector which can be estimated by EKF, and is given by

$$\hat{x}(k+1) = f(x(k),k) + g(u(k),k) + K_k\left[y(k) - h(x(k),k)\right] \tag{2.10}$$

where K_k is the Kalman gain, and it can be obtained through the Riccati difference equation. However, it requires relatively complex matrix calculations, and therefore, it takes a significant computing time [LJU79]. In [HAR96], a simplified EKF was proposed to estimate the rotor speed from noisy signals of the resolver with less computational burden. Then, in [LIU06], the same simplified EKF has been developed to be combined with back-EMF estimator for better sensorless

control performance. It is worth mentioning that the simplified EKF is regarded as two-phase PLL observer. For the same principle, in this thesis, the simplified EKF is adopted to be combined with the rotor FO for rotor position and speed estimation.

In the sensorless control with the rotor FO for SPMSM, the rotor flux-linkage in $\alpha\beta$ reference frame may be selected as the output variables of the EKF, i.e.

$$\begin{bmatrix} y_1(k) \\ y_2(k) \end{bmatrix} = \begin{bmatrix} \psi_{r\beta} \\ \psi_{r\alpha} \end{bmatrix} \tag{2.11}$$

while the state variables can be selected as the rotor position, θ_r, speed, ω, and double integration of the noise, w'.

To simplify the model in terms of the computation of the Kalman gain and the output variables, (2.11) is described in normalized form as

$$\begin{bmatrix} y_1(k) \\ y_2(k) \end{bmatrix} = \begin{bmatrix} cos\,\theta_r(k) \\ sin\,\theta_r(k) \end{bmatrix} + \begin{bmatrix} v_1(k) \\ v_2(k) \end{bmatrix} \tag{2.12}$$

Hence, the state-space model, with a state vector of $x = \left[\theta_r,\ \omega, w'\right]^T$ and input $u(k) = 0$, can be written as

$$x(k+1) = Fx(k) + w(k) \tag{2.13}$$

$$y(k) = h(x(k)) + v(k) \tag{2.14}$$

where

$$F = \begin{bmatrix} 1 & T_s & 0 \\ 0 & 1 & 1 \\ 0 & 0 & 1 \end{bmatrix} \tag{2.15}$$

and

$$h(x(k)) = \begin{bmatrix} cos\,\theta_r(k) \\ sin\,\theta_r(k) \end{bmatrix} \tag{2.16}$$

Then, the Kalman filter gain *K* can be significantly simplified as

$$K = \begin{bmatrix} 0 & k_1 \\ 0 & k_2 \\ 0 & k_3 \end{bmatrix} . \begin{bmatrix} cos\,\theta_r^e & sin\,\theta_r^e \\ -sin\,\theta_r^e & cos\,\theta_r^e \end{bmatrix} \tag{2.17}$$

where k_1, k_2 and k_3 indicate the tuning parameters. The Kalman filter gain *K*, i.e. (2.17) can be obtained by using the MATLAB's *DLQE* (A, G, C, R, Q) command (Discrete Linear-Quadratic Estimator) for the Kalman estimator design of discrete-time systems, for instant, the input variables according to [HAR96], are as follows

$$\begin{aligned} A = F &= \begin{bmatrix} 1 & T_s & 0 \\ 0 & 1 & 1 \\ 0 & 0 & 1 \end{bmatrix} \\ G &= \begin{bmatrix} 0 & 0 & 0 \\ 0 & 0 & 0 \\ 0 & 0 & 1 \end{bmatrix} \\ C &= \begin{bmatrix} 0 & 0 & 0 \\ 1 & 0 & 0 \end{bmatrix} \\ R &= \begin{bmatrix} 0 & 0 & 0 \\ 0 & 0 & 0 \\ 0 & 0 & 1 \end{bmatrix} \\ Q &= \sigma \begin{bmatrix} 1 & 0 \\ 0 & 1 \end{bmatrix} \end{aligned} \tag{2.18}$$

By choosing an appropriate tuning parameter σ to optimize the noise rejection ability of the Kalman filter, The Kalman filter gain *K* can be determined by utilizing the above Matlab command. The tuning parameter σ can be chosen by trial and errors in the experimental system. Consequently, the k_1, k_2 and k_3 can be obtained.

Finally, according to aforementioned equations, the rotor position and speed can be estimated from

$$\varepsilon(k) = y_2(k)cos\,\theta_r^e(k) - y_1(k)sin\,\theta_r^e(k) \tag{2.19}$$

$$\theta_r^e(k+1) = \left[\theta_r^e(k) + T_s\omega_{est}(k) + k_1\varepsilon(k)\right] \tag{2.20}$$

$$\omega_r^e(k+1) = \left[\omega_r^e(k) + w'(k) + k_2\varepsilon(k)\right] \tag{2.21}$$

$$w'(k+1) = \left[w'(k) + k_3\varepsilon(k)\right] \tag{2.22}$$

where θ_r^e and ω_{est} denote the estimated rotor position and speed, respectively. Fig. 2.2 shows the block diagram of the simplified EKF, which can be combined with rotor FO.

This chapter targets to provide a detailed investigation of the influence of back-EMF and currents harmonics on sensorless control performance for both FO and simplified EKF. The sensorless vector control system for single three-phase PMSM, which is employed for investigation of back-EMF harmonics influence on position estimation accuracy, is illustrated in Fig. 2.2. The switching-table-based direct torque control (ST-DTC) for DTP-PMSM, which inherently exhibits non-sinusoidal stator currents, is taken as an example to investigate the effect of current harmonics on sensorless control performance. The conventional and modified ST-DTC methods for DTP-PMSM have been presented in [HAT05] and [HOA15], and hence, only a brief description is provided here.

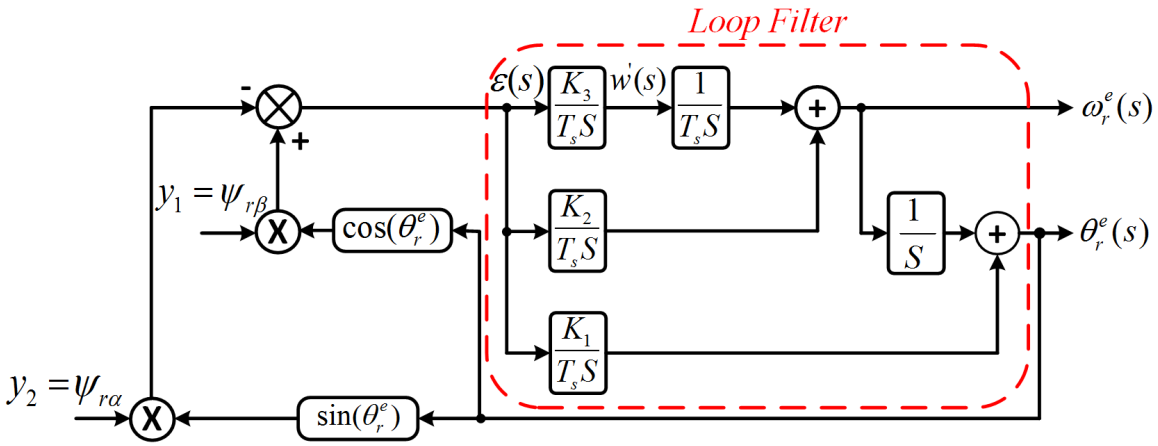

Fig. 2.2. Block diagram of simplified EKF.

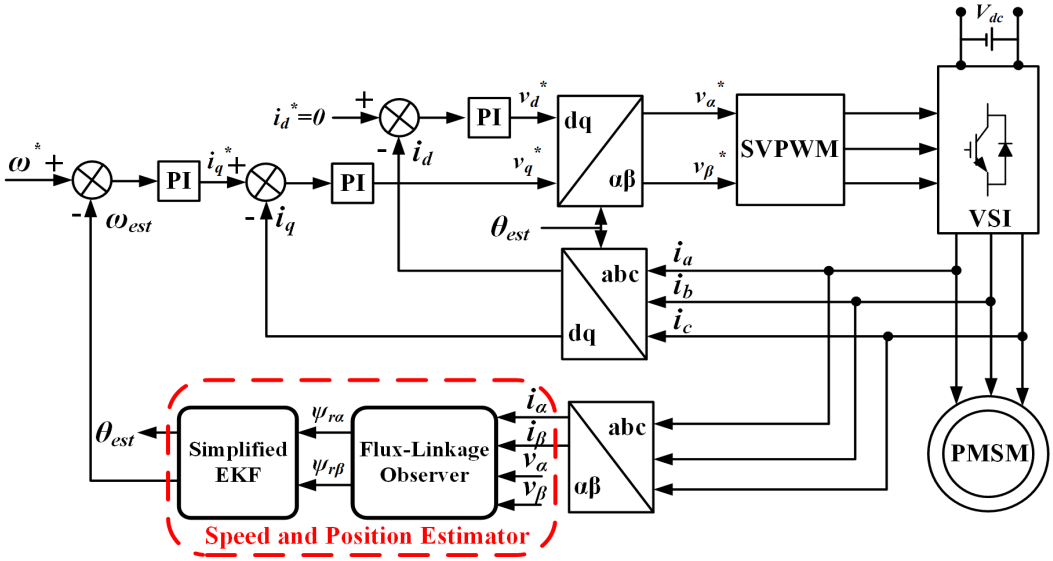

Fig. 2.3. Schematic diagram of sensorless vector control for three-phase PMSM.

2.3. Basic Principle of Conventional and Modified Switching-Table-Based Direct Torque Control (ST-DTC) for Dual Three-Phase PMSM

2.3.1. Machine Model and Voltage Vectors

By using vector space decomposition approach (VSD) [ZHA95], the final model of DTP-PMSM with isolated neutral points can be expressed in stationary reference frame as

$$\bar{V}_{s\alpha\beta} = R_s \bar{I}_{s\alpha\beta} + p\bar{\psi}_{s\alpha\beta} \tag{2.23}$$

$$\bar{\psi}_{s\alpha\beta} = L_s \bar{I}_{s\alpha\beta} + \bar{\psi}_{r\alpha\beta} \tag{2.24}$$

$$\bar{\psi}_{r\alpha\beta} = \bar{\psi}_{PM} e^{j\theta_r} \tag{2.25}$$

$$\bar{V}_{sz1z2} = R_s \bar{I}_{sz1z2} + p\bar{\psi}_{sz1z2} \tag{2.26}$$

$$\bar{\psi}_{sz1z2} = L_{ls} \bar{I}_{sz1z2} \tag{2.27}$$

$$T_e = 3P\left(\psi_{s\alpha} i_{s\beta} - \psi_{s\beta} i_{s\alpha}\right) \tag{2.28}$$

where V_{sz1z2}, ψ_{sz1z2}, I_{sz1z2} are stator voltage, flux, and current vectors in z_1z_2 subspace, respectively, L_{ls} is leakage self-inductance, T_e is electromagnetic torque, and P is number of pole pairs.

It can be seen from the above equations that the machine model could be decreased to two sets of decoupled equations identical to the machine $\alpha\beta$- and z_1z_2-subspaces [HAT05]. However, only $\alpha\beta$ components contribute to torque and flux production, while z_1z_2 components are the main sources for the large circulating current harmonics due to the small impedance in the z_1z_2-subspace.

Dual three-phase drives have many more inverter voltage vectors than a single three-phase system due to its six inverter legs. By neglecting 4 zero vectors, the $\alpha\beta$- and z_1z_2-subspaces voltage vectors are illustrated in Fig. 2.4 (a) and (b), respectively, where the voltage vector number is named with binary value of $V_i=S_ZS_YS_XS_CS_BS_A$.

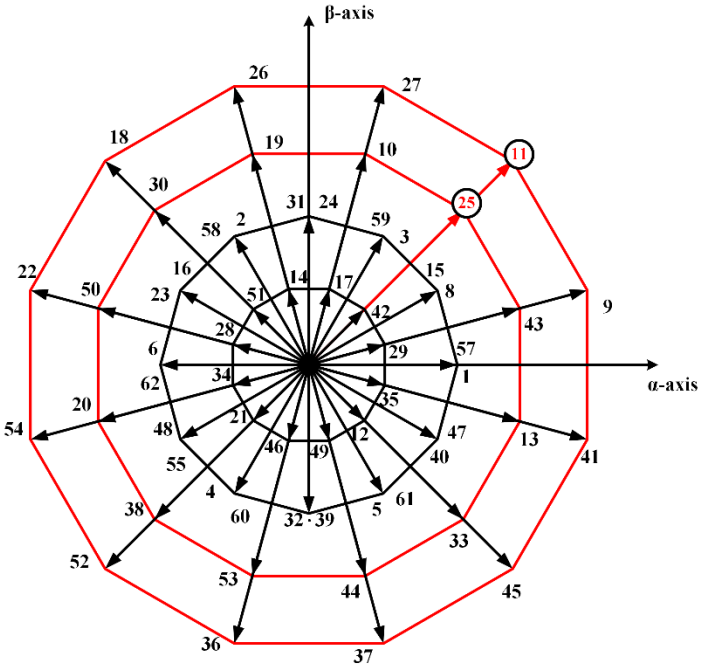

(a) $\alpha\beta$-subspace

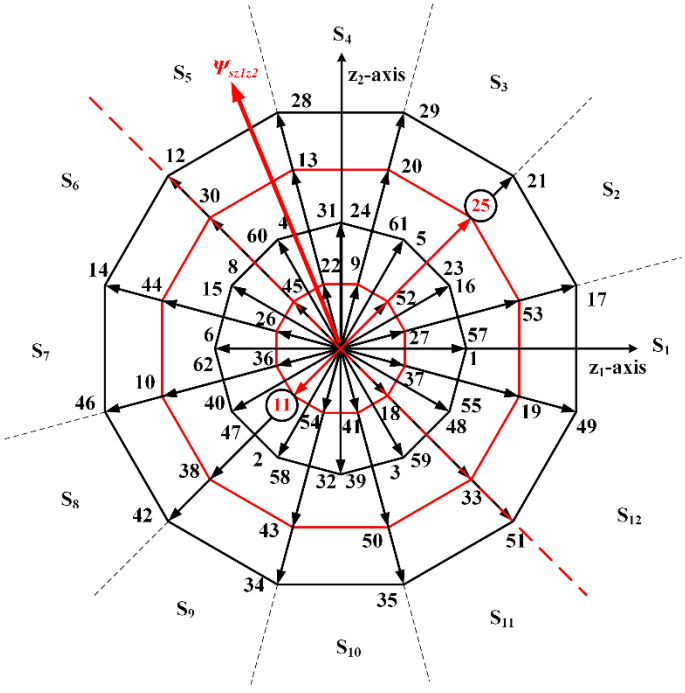

(b) z_1z_2-subspace

Fig. 2.4. Inverter voltage vectors in two subspaces.

2.3.2. Conventional ST-DTC Scheme

Conventional ST-DTC of three-phase drives can be extended to DTP-PMSM drives [HOA15]. Such method which exhibits non-sinusoidal stator currents, is utilised here to investigate the influence of stator current harmonics on the rotor position estimation accuracy. The $\alpha\beta$-subspace could be split into twelve sectors based on the estimated stator flux position, Fig. 2.5 (a). The torque response can be maximized when employing the voltage vectors from the outermost layer in the $\alpha\beta$-subspace together with the zero vectors. Generally, when the stator flux vector $\psi_{s\alpha\beta}$ lies in sector k, appropriate voltage vectors can be determined according to Table 2.1 [TAK86]. Taking voltage vector V_{k+2} for example, the torque production component is positive since it rotates at the same rotation direction, and the flux production component is positive as well. As a result, the electromagnetic torque, and stator flux will be increased.

TABLE 2.1

SWITCHING TABLE FOR CONVENTIONAL ST-DTC OF DTP-PMSM DRIVE

T_e	ψ_s	**Vector required**
Increased	Increased	V_{k+2}
Increased	Decreased	V_{k+3}
Decreased	Increased	V_{k-3}
Decreased	Decreased	V_{k-4}
Unchanged	Unchanged	V_{zero}

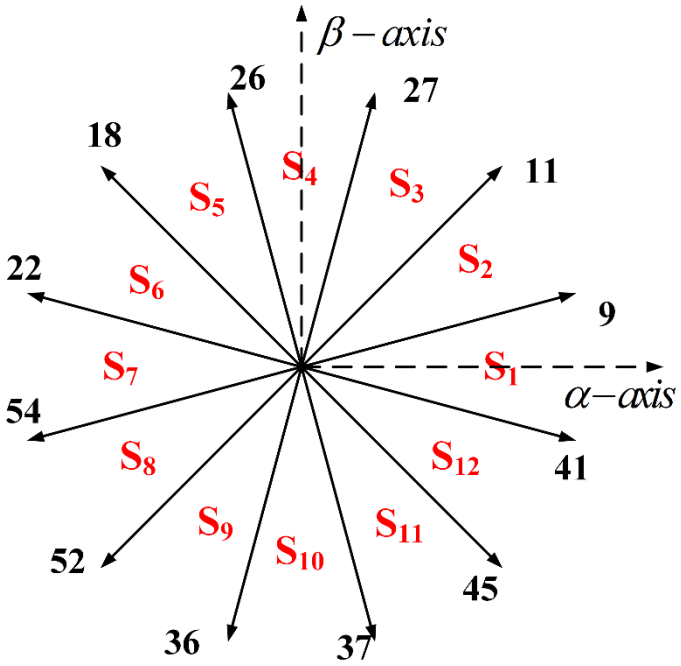

(a) Definition of twelve sectors

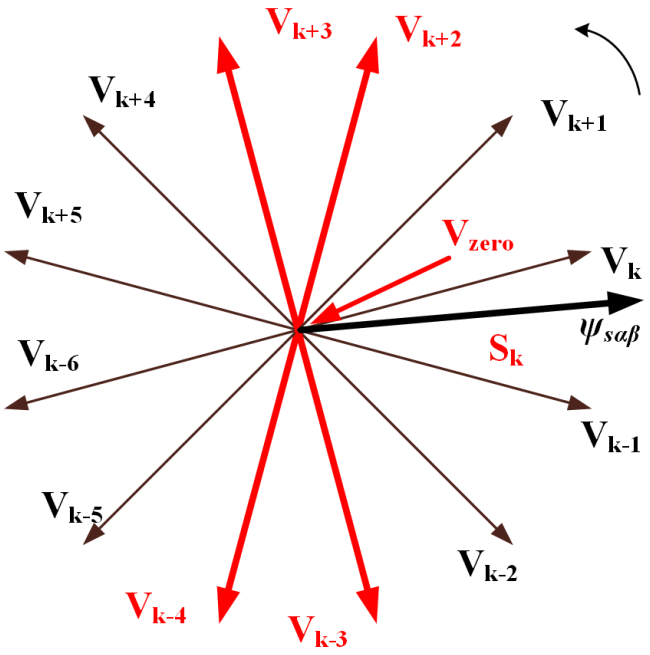

(b) Voltage vectors selection

Fig. 2.5. Principle of conventional ST-DTC scheme.

The conventional ST-DTC is easy in implementation. However, since only the components of $\alpha\beta$-subspace are involved, large harmonic currents inevitably occur. Thus, a modified strategy which controls both $\alpha\beta$ components and z_1z_2 components is required.

2.3.3. Modified ST-DTC Scheme

The modified ST-DTC of DTP-PMSM drives, which shows more sinusoidal stator currents than that of conventional ST-DTC method, is presented in [REN15b]. It is also used in this investigation to investigate the influence of stator current harmonics on the rotor position estimation accuracy. According to (2.27), minimizing the stator flux in z_1z_2-subspace ψ_{sz1z2} is an effective method to supress the current harmonics in z_1z_2, due to their proportional relationship. It can be seen from Fig. 2.4 that for each vector utilized in conventional ST-DTC, e.g. V_{11} in Fig. 2.4, there is another vector with the second-largest amplitude, e.g. V_{25}, pointing to the same direction in $\alpha\beta$-subspace, which means similar effect on torque and flux control, and simultaneously, exhibiting the opposite directions in z_1z_2-subspace which indicates opposite influence on the variation of flux ψ_{sz1z2}.

Therefore, in order to minimize the magnitude of z_1z_2 stator flux, the z_1z_2-subspace can be divided into two half circle subspaces, where the diameter is orthogonal to V_{11} and V_{25}, Fig. 2.4 (b), and if the z_1z_2 flux vector ψ_{sz1z2} lies in one half circle subspace, the voltage vector in the other half circle subspace have to be employed. For instance, when ψ_{sz1z2} locates in sector 7, as shown in Fig. 2.4 (b), the amplitude of ψ_{sz1z2} will be increased by applying V_{11}, and it will be reduced when V_{25} is utilized. Hence, V_{25} should be adopted instead of V_{11}. Similar principle can be extended to other sectors.

Consequently, based on the aforementioned concept, the two-steps approach is given:

- According to Table 2.1, one vector with largest amplitude and another vector with the second largest amplitude having similar direction in $\alpha\beta$-subspace are specified as one group;
- Depending on the position of the stator flux in z_1z_2-subspace ψ_{sz1z2}, the vector that can minimize its amplitude will be picked from the chosen group.

Since the first step is the same to the selection of vectors in the conventional ST-DTC, the vector groups can be chosen from Table 2.1. Consequently, a switching table for the second step is given in Table 2.2.For instance, if the vector group 11 is selected from Table 2.1, V_{11} will be employed only when ψ_{sz1z2} lies in sectors 1-5, and 12, otherwise, V_{25} will be adopted to decrease

the amplitude of ψ_{sz1z2}. Similar results can be easily obtained for other vector groups [HOA15]. The overall sensorless ST-DTC scheme is shown in Fig. 2.6.

TABLE 2.2

SWITCHING TABLE FOR STEP-TWO IN THE MODIFIED ST-DTC OF DTP-PMSM

Group G_i	**Sector of ψ_{sz1z2}**	**Selected vector**	**Group G_i**	**Sector of ψ_{sz1z2}**	**Selected vector**
9	7,8,9,10,11,12	V_9	54	1,2,3,4,5,6	V_{54}
	1,2,3,4,5,6	V_{43}		7,8,9,10,11,12	V_{20}
11	12,1,2,3,4,5	V_{11}	52	6,7,8,9, 10,11	V_{52}
	6,7,8,9, 10,11	V_{25}		12,1,2,3,4,5	V_{38}
27	5,6,7,8,9,10	V_{27}	36	11,12,1,2,3,4	V_{36}
	11,12,1,2,3,4	V_{10}		5,6,7,8,9,10	V_{53}
26	10,11,12,1,2,3	V_{26}	37	4,5,6,7,8,9	V_{37}
	4,5,6,7,8,9	V_{19}		10,11,12,1,2,3	V_{44}
18	3,4,5,6,7,8	V_{18}	45	9,10,11, 12,1,2	V_{45}
	9,10,11, 12,1,2	V_{30}		3,4,5,6,7,8	V_{33}
22	8,9,10,11,12,1	V_{22}	41	2,3,4,5,6,7	V_{41}
	2,3,4,5,6,7	V_{50}		8,9,10,11,12,1	V_{13}

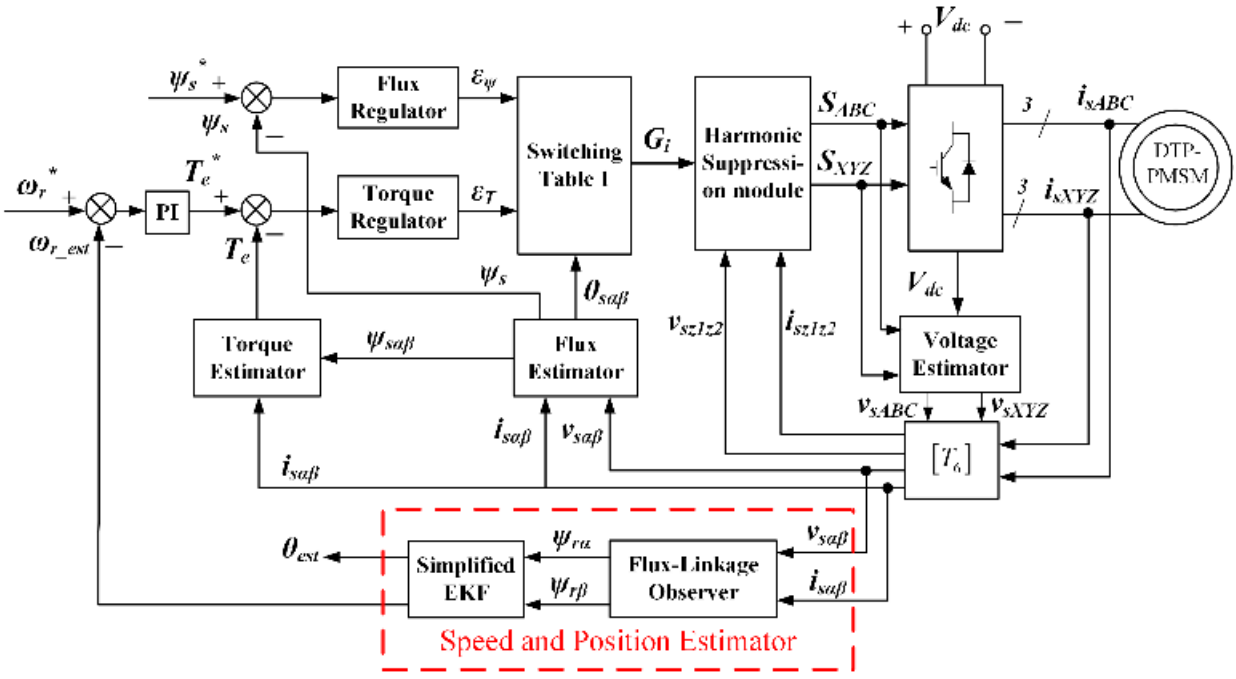

Fig. 2.6. Sensorless control ST-DTC diagram of dual three-phase PMSM drives.

2.4. Influence of Back-EMF Harmonics on Sensorless Control Performance for Vector Control of Single Three-Phase PMSM

The experiments for the influences of back-EMF and current harmonics on sensorless control performances are implemented on experimental platform which is constructed depending on a dSPACE (DS1006) control system and interfaced with Matlab/Simulink model. The hardware of the experimental rig is provided, and only the control system is applied by the author of this thesis. The detailed information about the experimental rig utilised in the thesis are presented in Appendix I. The experimental rig consists of a prototype of DTP-PMSM, and coupled with a DC machine for loading. Also, two sets of three-phase inverter, which is supplied by a DC power, is utilised for both machine drives where only one set is enabled when implementing the control of single three-phase system.

It should be noted that the DTP-PMSM can also be used as single three-phase PMSM when only one three-phase winding set is employed, which it has been employed in this thesis. The overall control system schemes shown in Fig. 2.3 and Fig. 2.6 with the scheme of simplified extended Kalman filter shown in Fig. 2.2 are implemented in the dSPACE. The investigation of the back-EMF harmonics effect on the sensorless control performance for vector control of single three-phase PMSM is fully described in the following subsections, while the investigation of current harmonics effect on the sensorless control performance for conventional and modified ST-DTC strategies of DTP-PMSM will be described in section 2.5. The the DC link voltage is set to 40V, and the sampling frequency is set to 10 kHz for both investigations.

2.4.1. Back-EMF Analysis

The vector control of single three-phase PMSM is utilized to investigate the influence of back-EMF harmonics on position estimation accuracy. The speed reference is set to 300rpm, and the load is about 1.8 Nm. The phase back-EMF has been measured as shown in Fig. 2.7 (a), and its harmonic spectrum is given in Fig. 2.7 (b). It should be noted that significant 3^{rd}, 5^{th} and 7^{th} harmonics are observed. However, the dominant harmonics are the 5^{th} and 7^{th} harmonic components since the 3^{rd} harmonic will disappear due to the star-connection of the machine windings. The conventional FO and simplified EKF are implemented to show the influence of back-EMF harmonics on the accuracy of rotor position estimation.

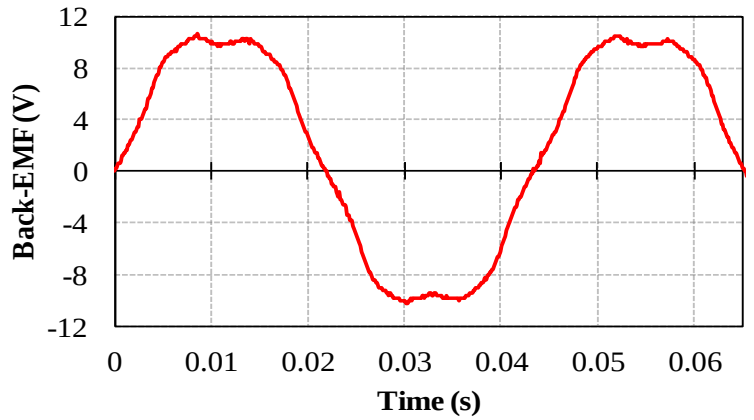

(a) Phase back-EMF

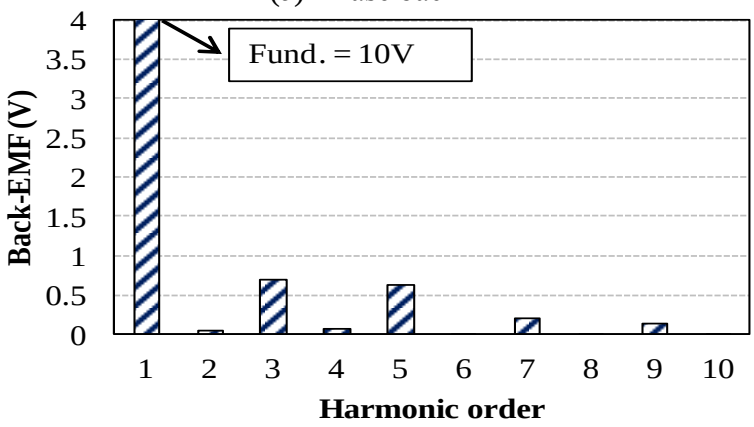

(b) Spectrum of phase back-EMF

Fig. 2.7. Phase back-EMF and FFT analysis.

2.4.2. Steady-state Sensorless Control Performance Using FO

By firstly applying FO based sensorless control, the observation of PM excitation flux-linkage vector in $\alpha\beta$ reference frame is illustrated in Fig. 2.8. It can be seen that the locus of observed flux-linkage vector is non-circle due to the back-EMF harmonic components. Then, the comparison of actual and estimated rotor positions is shown in Fig. 2.9, as well as the position estimation error. It is obvious that significant fluctuations in the position estimation error occur because of the distorted back-EMF.

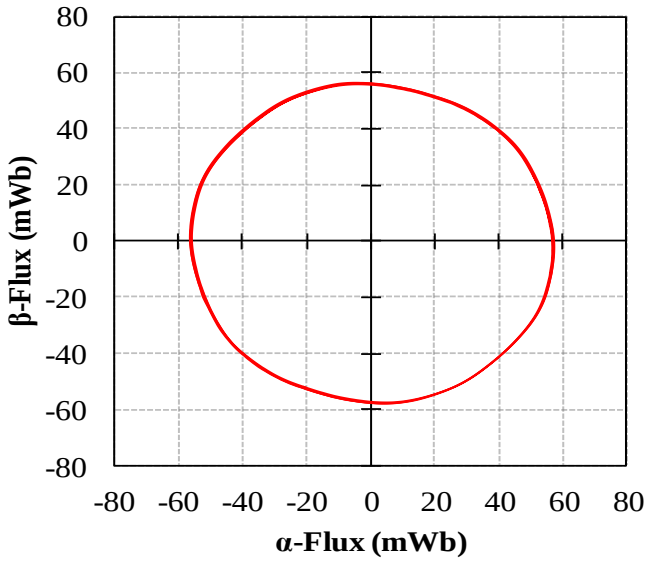

Fig. 2.8. Locus of PM excitation flux-linkage vector.

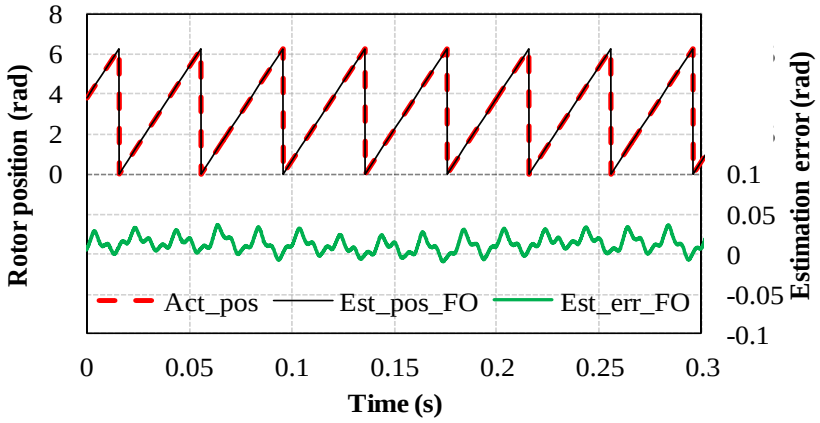

Fig. 2.9. Comparison of actual and estimated rotor position using FO.

2.4.3. Steady-State Sensorless Control Performance Utilizing Simplified EKF

After employing the conventional flux-linkage observer, the simplified EKF is applied to investigate the rotor position estimation performance when the back-EMF is distorted. The estimated rotor position of simplified EKF is compared with the actual rotor position in Fig. 2.10, in addition to the position estimation error. It is worth noting that the position estimation error of simplified EKF exhibits less fluctuations, and it is relatively small compared to that of FO. The comparison of rotor position estimation errors for both sensorless control methods is depicted in Fig. 2.11. It can be concluded that the rotor position estimation accuracy is less affected by the

back-EMF harmonics when the simplified EKF method is utilized since it is less sensitive to such harmonics.

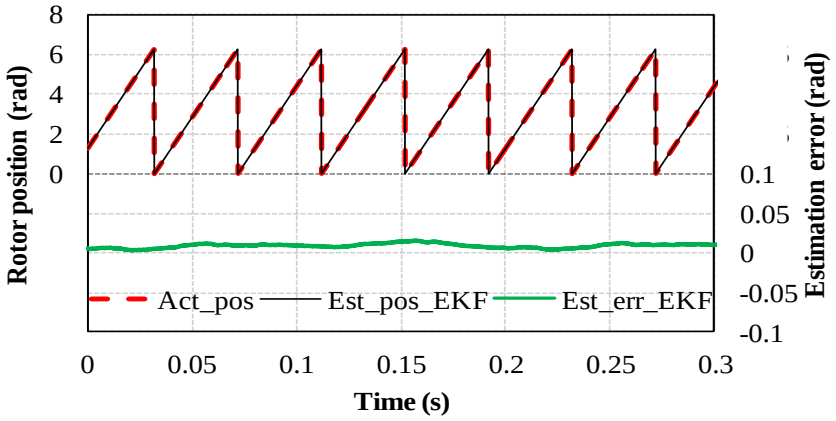

Fig. 2.10. Comparison of actual and estimated rotor position using simplified EKF.

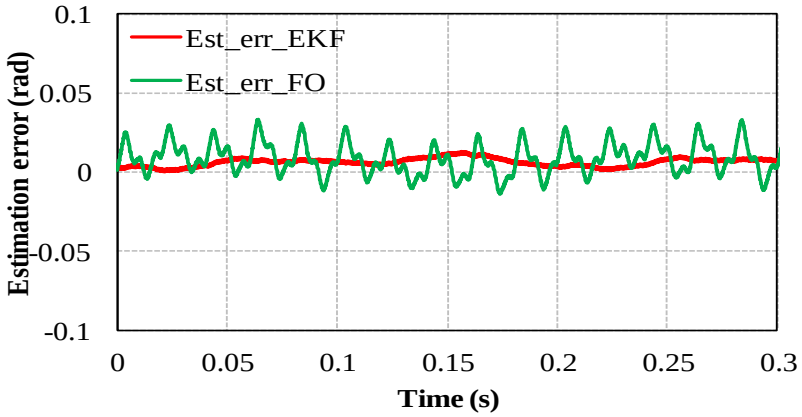

Fig. 2.12. Comparison of position estimation errors.

2.5. Influence of Current Harmonics on Sensorless Control Performance for Conventional and Modified ST-DTC Strategies of DTP-PMSM

2.5.1. Steady-State Sensorless ST-DTC Strategies Performance Applying FO

The conventional and modified ST-DTC strategies of DTP-PMSM are implemented to investigate the influence of non-sinusoidal stator currents on the position and speed estimation accuracy for conventional FO and simplified EKF. It is worth mentioning that although the testing machine exhibits distorted back-EMF, the influence of stator current harmonics is dominant in the performance deterioration in sensorless control of ST-DTC for DTP-PMSM. The machine speed

is set to 300rpm, and the stator flux reference is 0.075Wb, respectively. The load is set to about 1.8 Nm.

Figs. 2.13 shows the steady-state performances of the sensorless control for conventional ST-DTC strategy based on FO, while the steady-state performance of the modified ST-DTC based on FO is illustrated in Fig. 2.14. From Fig. 2.13 and Fig.2.14, it can be seen that both the torque and stator flux are well controlled in both the conventional and modified DTC techniques with FO. The torque ripples are slightly decreased and the steady-state error of torque is also significantly reduced when modified ST-DTC is implemented compared to its conventional counterpart, Figs. 2.13 (a) and 2.14 (a). In terms of current performance, it can be observed that the phase currents of the conventional ST-DTC strategy are severely distorted, i.e. non-sinusoidal waveforms, Fig. 2.13 (c). On the other hand, the current harmonics are significantly reduced by using the modified ST-DTC strategy, Fig. 2.14 (c).

Furthermore, the rotor position and speed estimations performances for conventional and modified ST-DTC strategies based on FO are shown in Fig. 2.15 and Fig. 2.16, respectively. It can be seen from Fig. 2.15 that significant fluctuations in the position estimation error and estimated speed can be observed due to seriously non-sinusoidal stator currents in the conventional ST-DTC. By utilizing the modified ST-DTC strategy, the fluctuations can be reduced to some extent, which, however, remain obvious since the current harmonics are still large, Fig.2.16.

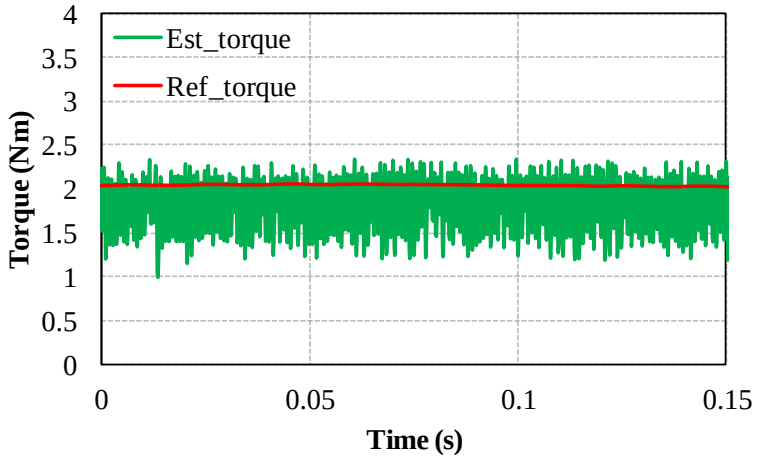

(a) Torque

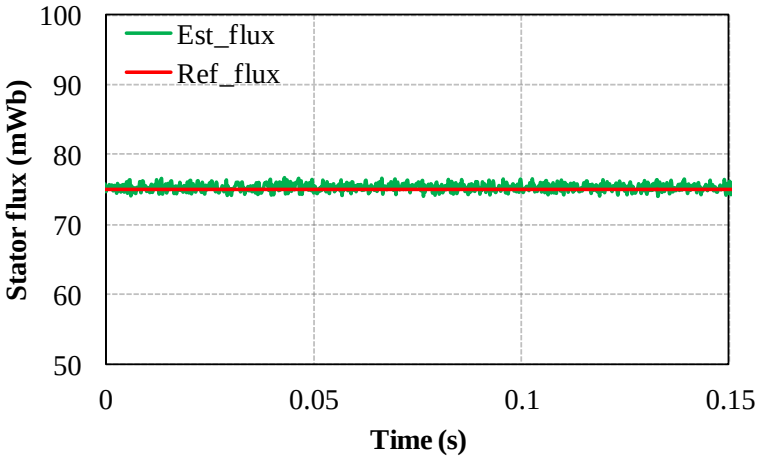

(b) Stator flux

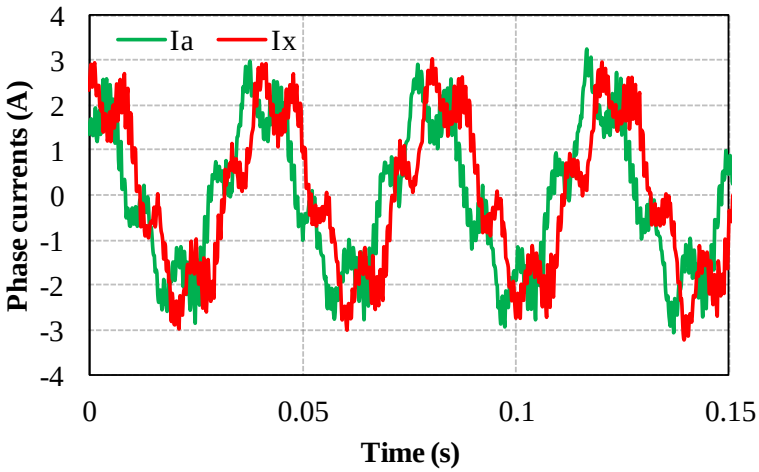

(c) Phase currents

Fig. 2.13. Steady-state performance of conventional ST-DTC, FO.

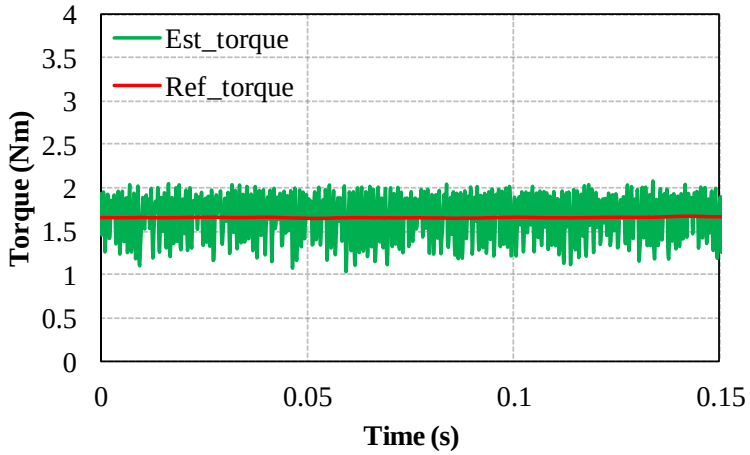

(a) Torque

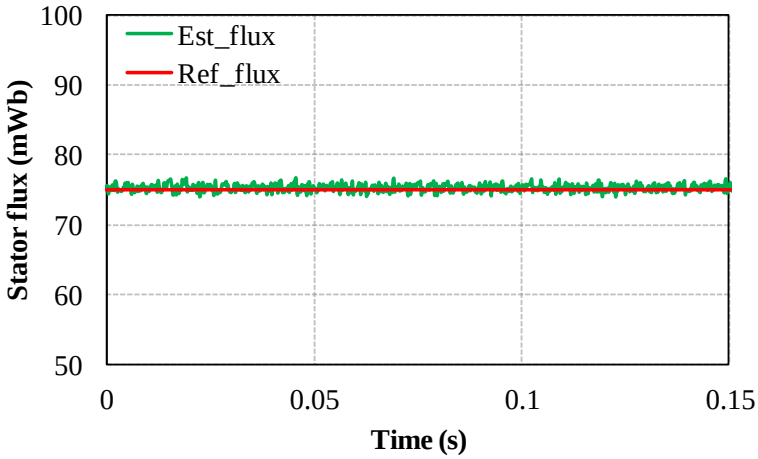

(b) Stator flux

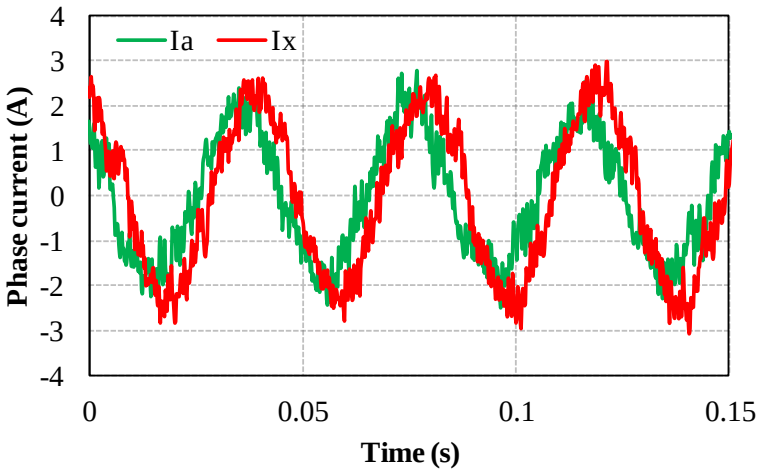

(c) Phase currents

Fig. 2.14. Steady-state performance of modified ST-DTC, FO.

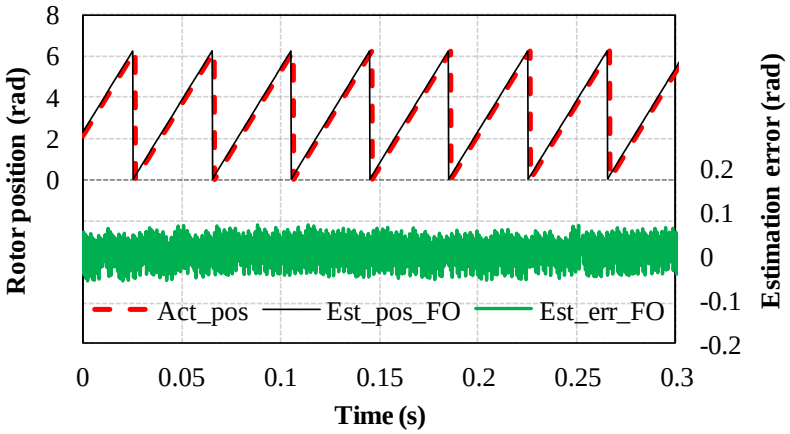

(a) Rotor position estimation

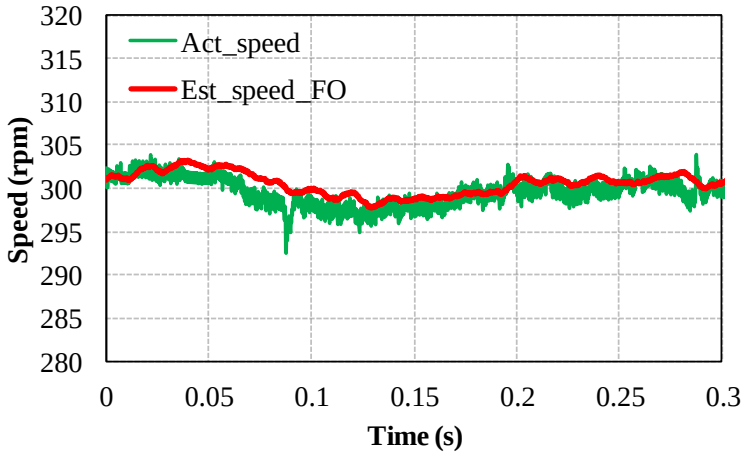

(b) Rotor speed estimation

Fig. 2.15. Sensorless control performance of conventional ST-DTC, FO.

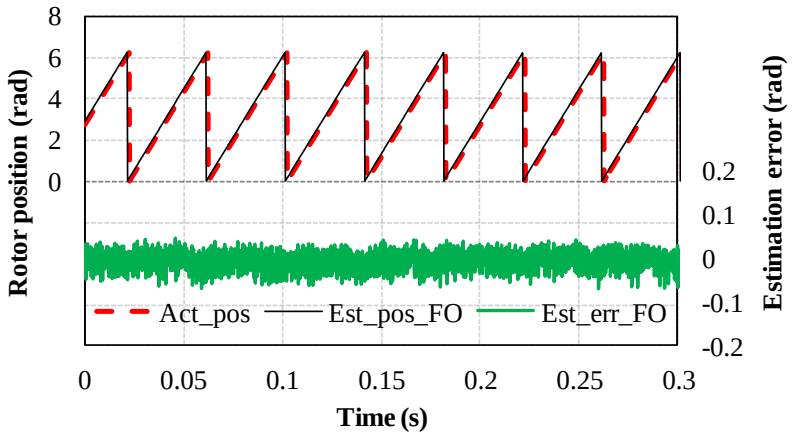

(a) Rotor position estimation

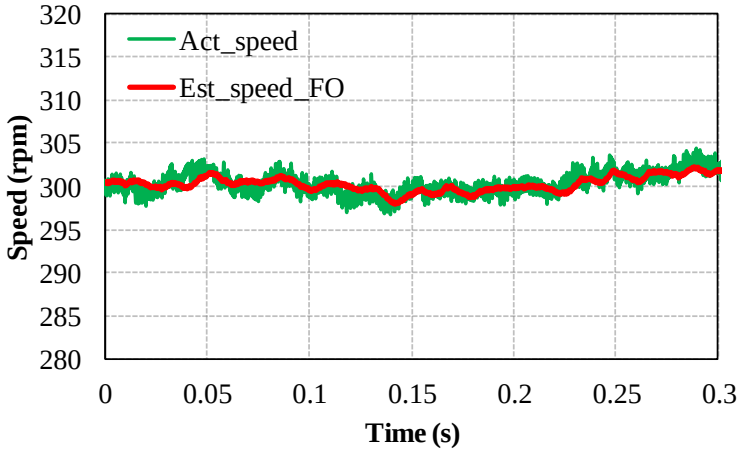

(b) Rotor speed estimation

Fig. 2.16. Sensorless control performance of modified ST-DTC, EKF.

2.5.2. Steady-State Sensorless ST-DTC Strategies Performance Employing Simplified EKF

After employing FO, the simplified EKF based sensorless control is implemented for the conventional and modified ST-DTC strategies to investigate the effect of distorted stator currents on the sensorless control performance. The steady-state performance of conventional ST-DTC strategy with simplified EKF is given in Fig. 2.17, whilst Fig. 2.18 shows the steady-state performance of modified ST-DTC strategy. For simplified EKF based sensorless control method, it can clearly be seen from Fig. 2.19 (a) and Fig. 2.20 (a) that the position estimation errors are relatively small with less fluctuations due to the higher noise-rejection capability of EKF.

Furthermore, the estimated speeds for both ST-DTC strategies exhibit less fluctuations compared to that of FO, Fig. 2.19 (b) and Fig. 2.20 (b).

Detailed quantitative results of different sensorless control ST-DTC strategies are given in Table 2.3, in which the ripples of the torque and stator flux are calculated as [HOA15]

$$\psi_{s\_ripple} = \sqrt{1/n \sum_{i=1}^{n} (\psi_{s\_i} - \psi_{s\_av})^2} \tag{2.29}$$

$$T_{e\_ripple} = \sqrt{1/n \sum_{i=1}^{n} (T_{e\_i} - T_{e\_av})^2} \tag{2.30}$$

According to Table 2.3, both of sensorless control methods can achieve significant improvement of steady-state performance when the modified ST-DTC strategies are employed, compared to their conventional counterparts in terms of flux and torque ripples, and THD of phase currents. Between them, the modified ST-DTC technique with simplified EKF exhibits better performances compared to that with FO.

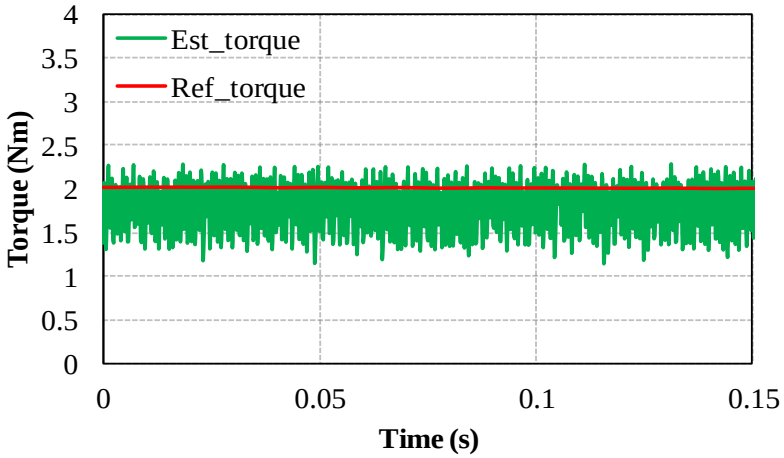

(a) Torque

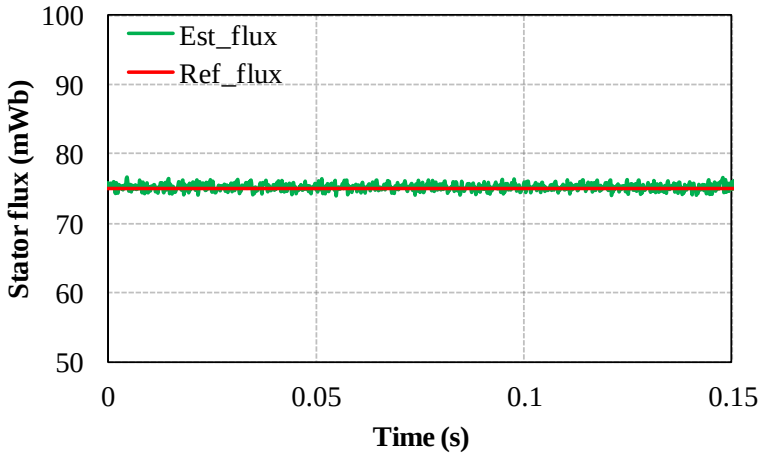

(b) Stator flux

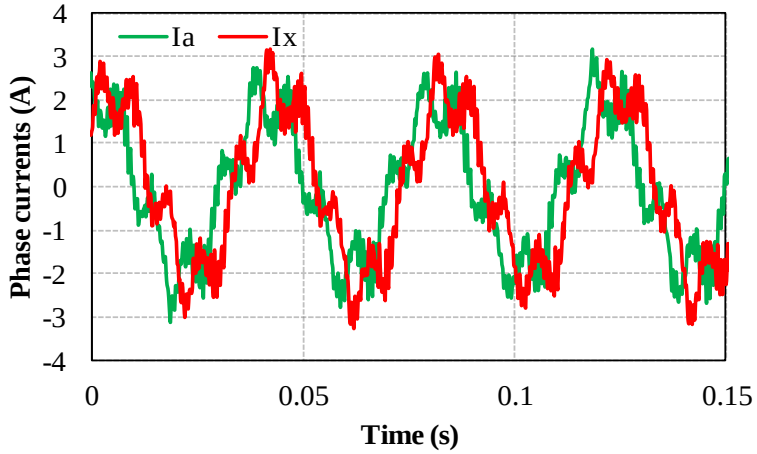

(c) Phase currents

Fig. 2.17. Steady-state performance of conventional ST-DTC, EKF.

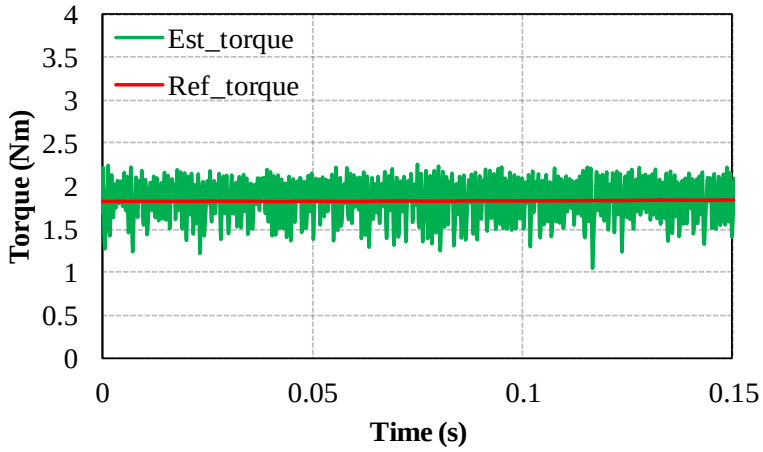

(a) Torque

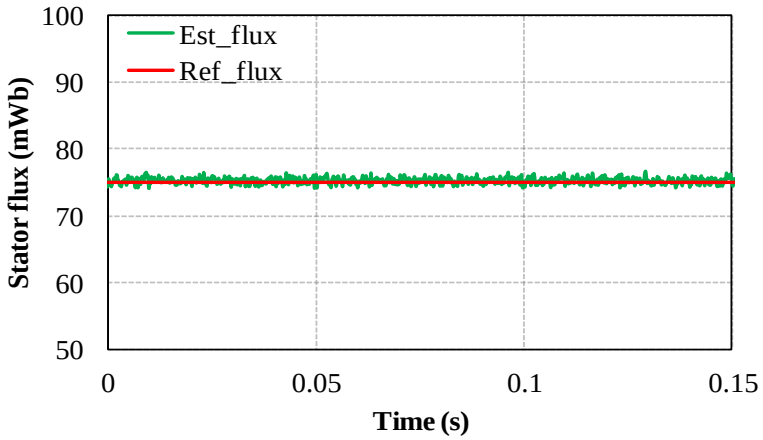

(b) Stator flux

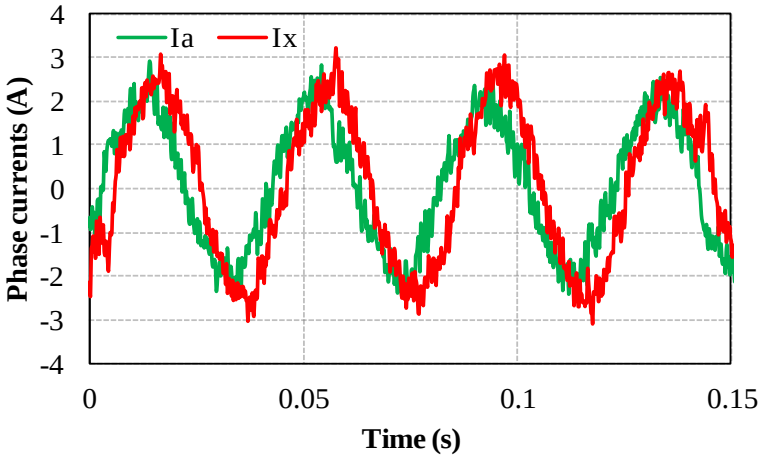

(c) Phase currents

Fig. 2.18. Steady-state performance of modified ST-DTC, EKF.

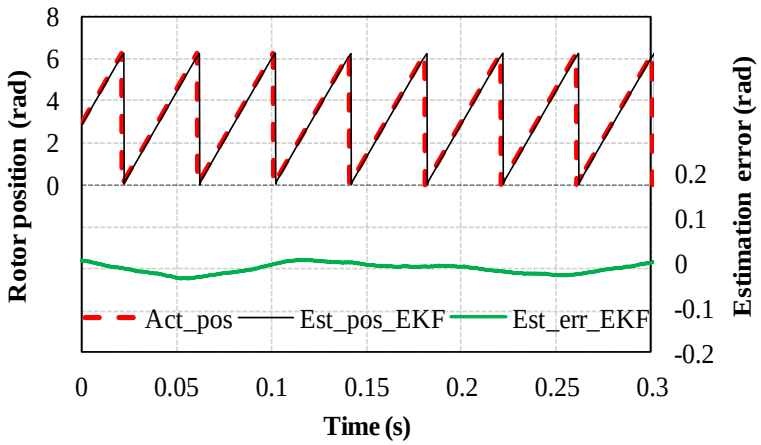

(a) Rotor position estimation

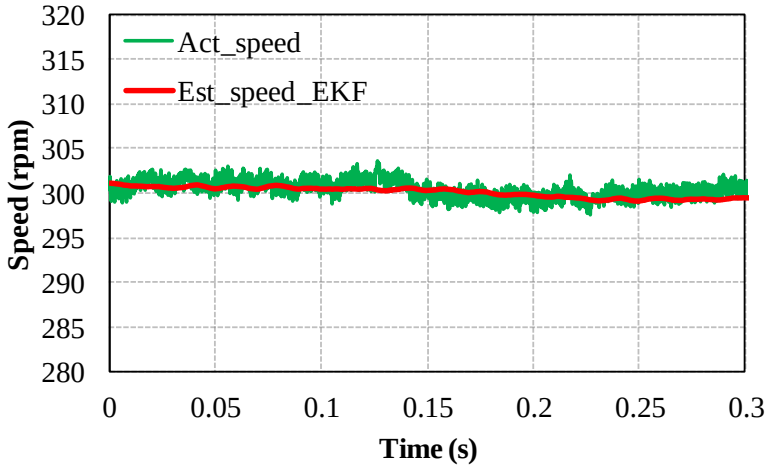

(b) Rotor speed estimation

Fig. 2.19. Sensorless control performance of conventional ST-DTC, EKF.

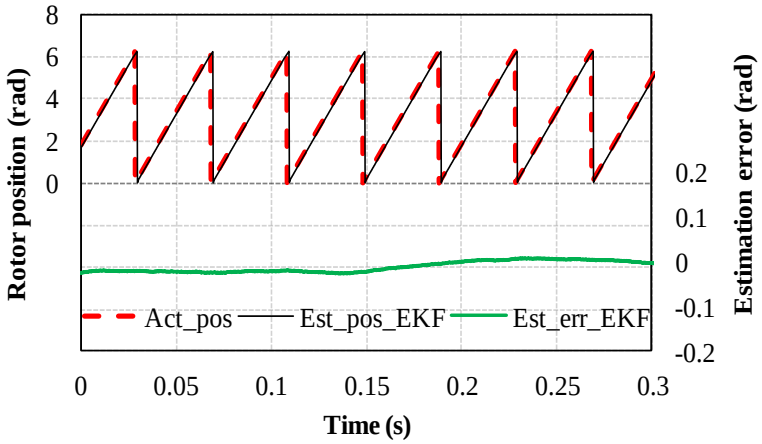

(a) Rotor position estimation

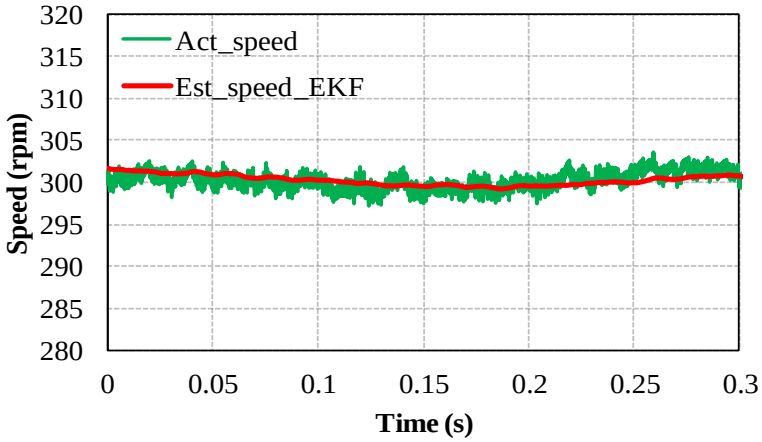

(b) Rotor speed estimation

Fig. 2.20. Sensorless control performance of modified ST-DTC, EKF.

TABLE 2.3
STEADY-STATE PERFORMANCE OF DIFFERENT SENSORLESS ST-DTC STRATEGIES

300rpm,1.8Nm	**Conventional-FO**	**Conventional-EKF**	**Modified-FO**	**Modified-EKF**
ψ_{s_ripple} *(Wb)*	7.5213e-4	7.4914e-4	5.0394e-4	4.8393e-4
T_{e_ripple} *(Nm)*	0.2958	0.2912	0.2230	0.2119
THD_I_a*(%)*	31.47	31.03	12.47	11.81

2.5.3. Dynamic-State Sensorless ST-DTC Strategies Performance for FO and Simplified EKF

By applying FO and simplified EKF based sensorless control techniques, the dynamic performances for both the conventional and modified ST-DTC strategies with FO based sensorless control are shown in Fig. 2.21 and Fig. 2.22, respectively. When the simplified EKF is employed, the dynamic performances for both ST-DTC strategies are illustrated in Fig. 2.23 and Fig. 2.24, respectively. It can be found that the estimated speed exhibits significant phase lag in FO for both ST-DTC strategies due to the low-pass filter used in the rotor flux-linkage observer. In contrast, the estimated speed tracks the actual speed with less phase lag when simplified EKF is employed thanks to its ability to suppress such noisy signals which leads to fast speed response. Furthermore, both the sensorless control techniques based on FO and simplified EKF show good dynamic torque performance for the conventional and modified ST-DTC strategies.

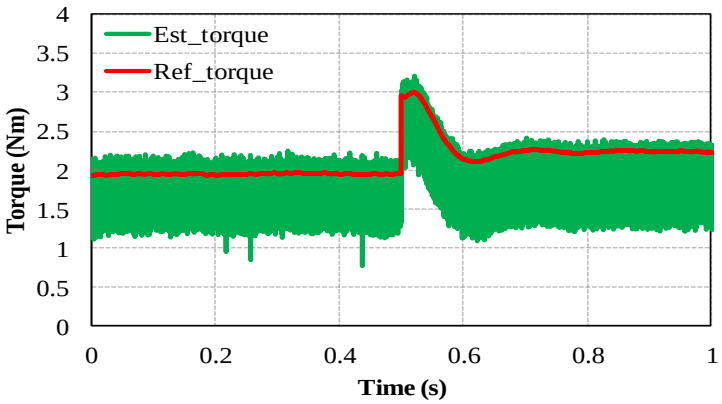

(a) Torque

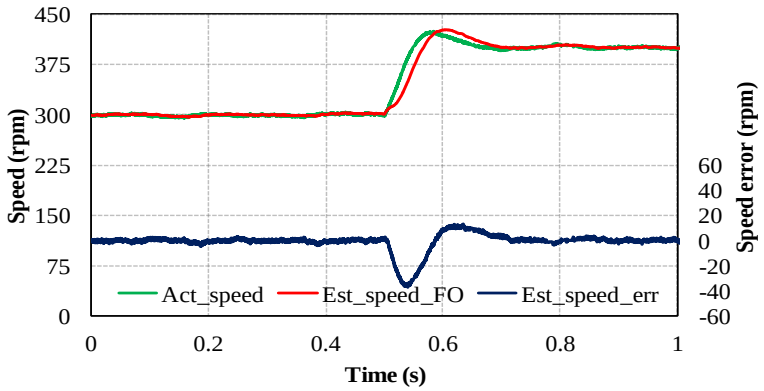

(b) Rotor speed estimation

Fig. 2.21. Dynamic performance of sensorless conventional ST-DTC, FO.

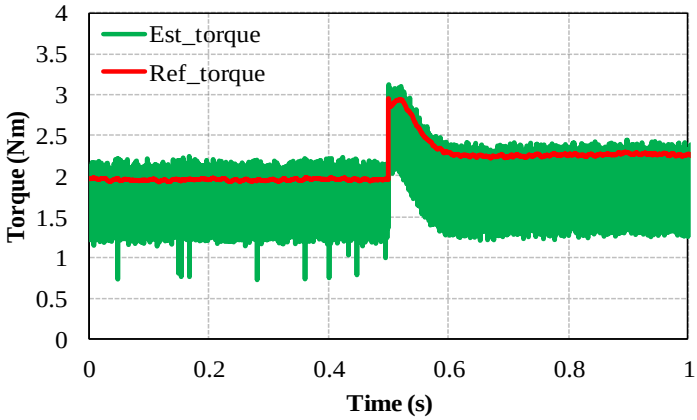

(a) Torque

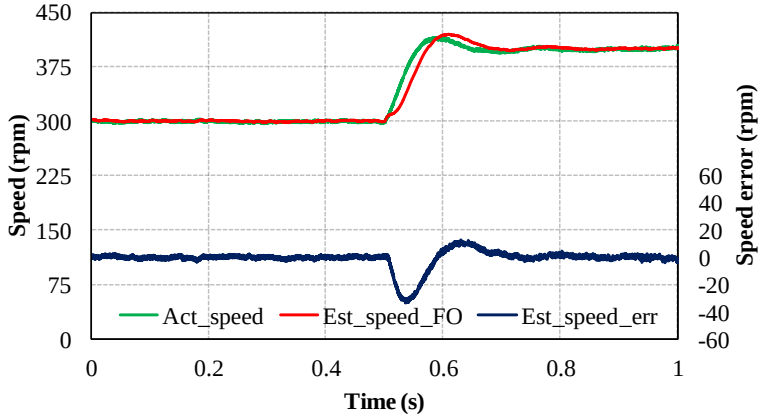

(b) Rotor speed estimation

Fig. 2.22. Dynamic performance of sensorless modified ST-DTC, FO.

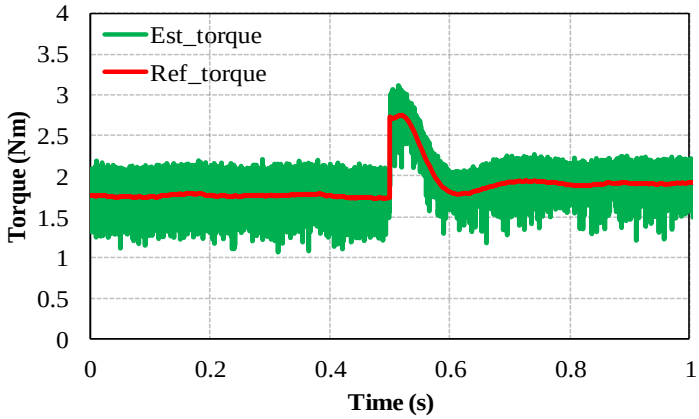

(a) Torque

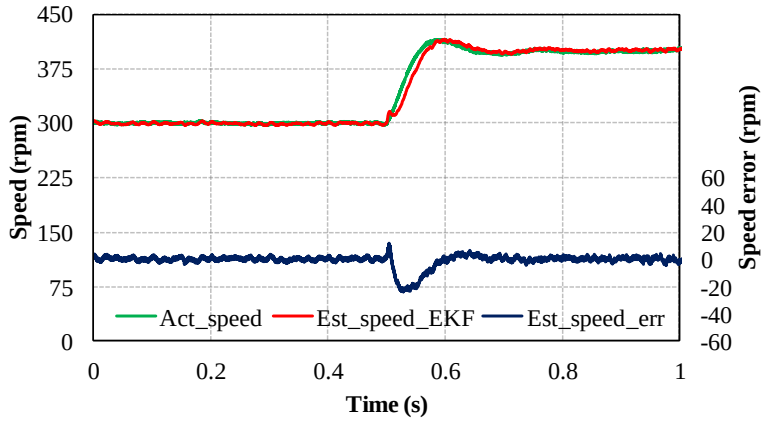

(b) Rotor speed estimation

Fig. 2.23. Dynamic performance of sensorless conventional ST-DTC, EKF.

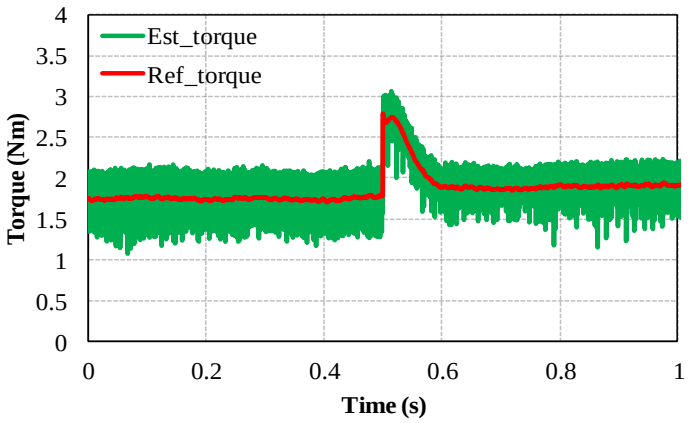

(a) Torque

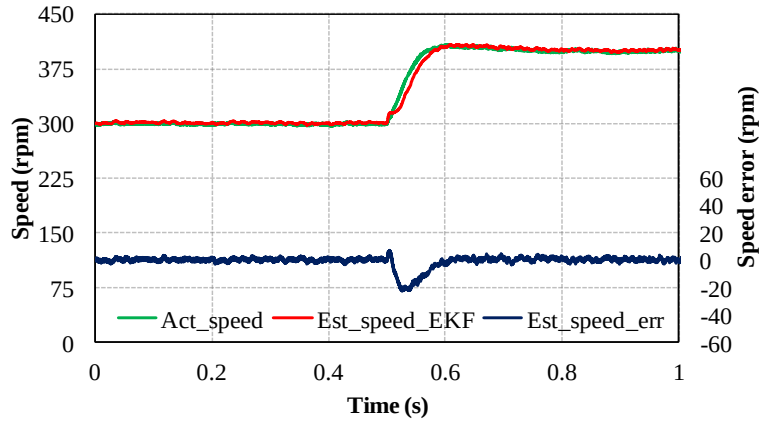

(b) Rotor speed estimation

Fig. 2.24. Dynamic performance of sensorless modified ST-DTC, EKF.

2.6. Summary

This chapter investigates the influence of back-EMF and currents harmonics on sensorless control performance of single and dual three-phase PMSMs by utilizing the most common fundamental-model-based sensorless control techniques, i.e. FO and simplified EKF. The single three-phase PMSM is employed to investigate the influence of back-EMF harmonics on position estimation accuracy, while the influence of current harmonics on the rotor position and speed estimation accuracy is studied for DTP-PMSM which inherently involves harmonic currents in ST-DTC methods.

By employing the FO and simplified EKF based sensorless vector control of single three-phase PMSM, it can be concluded that the rotor position estimation accuracy is less affected by the back-EMF harmonics when the simplified EKF method is utilized since it is less sensitive to such harmonics.

Then, the influence of non-sinusoidal stator currents together with back-EMF harmonics has been investigated for the conventional and modified ST-DTC of DTP-PMSM with FO and simplified EKF based sensorless control methods.

The experimental results indicate that the simplified EKF exhibits better position and speed estimation accuracy in both the conventional and modified ST-DTC strategies. In addition, its steady-state performance shows a slight superiority over that based on FO, in terms of flux and torque ripples, and THD of phase currents. For the dynamic performance, the estimated speed of simplified EKF shows less phase lag and fluctuations compared to that of FO.

CHAPTER 3

CONVENTIONAL HIGH-FREQUENCY CARRIER SIGNAL INJECTION BASED SENSORLESS CONTROL METHODS FOR SINGLE AND DUAL THREE-PHASE PMSMS

3.1. Introduction

Carrier signal injection based sensorless control methods are developed to achieve a high rotor estimation accuracy, both when at a standstill and when at low speed. These sensorless control methods rely on machine saliency. A high-frequency (pulsating or rotating) carrier voltage is normally superimposed in a continuous manner onto the fundamental excitation.

A rotor carrier current, which is position dependent, is produced thereafter from the interaction of the machine spatial saliency with the injected carrier voltage. The rotor position could then be extracted from the position-dependent carrier current response through the use of a tracking observer [GON11]. The two major methods of the continuous carrier signal injection are pulsating sinusoidal signal injection [COR98] [AIH99] [JAN03] [LI09b] [GON11b], and rotating sinusoidal signal injection [JAN95] [GON11b].

A high-frequency carrier current signal may also be injected and the information regarding the rotor position extracted from the carrier voltage response. The current regulator, however, is necessary to allow the carrier current injection to have high bandwidth sufficient to ensure that the high-frequency carrier current follows the reference command. The high-frequency carrier voltage signal injection is preferred because of simpler injection algorithm and simpler hardware design.

In this chapter, the two most commonly used conventional pulsating and rotating carrier voltage signal injections based on sensorless control strategies will be discussed in details. The pulsation signal is injected into *d*-axis estimated synchronous reference frame, whilst the rotating signal is injected into the stationary reference frame. Their sensorless control performances are investigated experimentally for both the single and dual three-phase PMSMs. The saliency of the testing machine is experimentally investigated under different load conditions with the aid of a position encoder for the actual rotor position. Meanwhile, in this chapter, the influence of cross saturation coupling over the accuracy of position estimation is also considered. The corresponding performances of rotor position estimation are presented with full analysis, along with

compensation of cross-saturation coupling effects. It should be mentioned that the machine used for single and dual three-phase is exactly the same. The specifications of the test machine are listed in Appendix II.

3.2. High-Frequency Models of PMSM

3.2.1. Model in Synchronous Reference Frame

The voltage of PMSM in the synchronous reference frame is expressed as

$$\begin{bmatrix} v_d \\ v_q \end{bmatrix} = \begin{bmatrix} R_s & 0 \\ 0 & R_s \end{bmatrix} \begin{bmatrix} i_d \\ i_q \end{bmatrix} + p \begin{bmatrix} \psi_d \\ \psi_q \end{bmatrix} + \begin{bmatrix} -\omega_r \psi_q \\ \omega_r \psi_d \end{bmatrix} \tag{3.1}$$

where p is referred as to differential operator, while ψ_d and ψ_q respectively denote the d- and q-axis flux linkages.

The back-EMF and resistive voltage drop can be neglected normally at zero and in low speed regions. The PMSM can be viewed as a pure inductive load when the injected carrier frequency is sufficiently higher than the fundamental excitation frequency [RAC08a]. In the synchronous frame, the high-frequency voltage of PMSM, when accounting for the cross saturation effect [LI09a], can be expressed as

$$\begin{bmatrix} v_{dh} \\ v_{qh} \end{bmatrix} = \begin{bmatrix} L_{dh} & L_{dqh} \\ L_{qdh} & L_{qh} \end{bmatrix} \begin{bmatrix} pi_{dh} \\ pi_{qh} \end{bmatrix} \tag{3.2}$$

where L_{dh} and L_{qh} represent the high-frequency incremental self-inductances of the d- and q-axes, and they are different from each other due to the machine saliency. L_{dqh} and L_{qdh} denote the high-frequency incremental mutual-inductances, and they are related with cross-saturation effect. Normally, $L_{dqh} \neq L_{qdh}$ [LI07], however, for simplifying the analysis, $L_{dqh} = L_{qdh}$ is considered in most practical applications, and it is also considered in this thesis.

3.2.2. Model of Carrier Current in Estimated Synchronous Reference Frame

The estimated rotor position is normally used in the control algorithm for the sensorless control operation. This happens because the accurate rotor position is unknown.

With the help from this transformation matrix $T(\Delta\theta)$

$$T(\Delta\theta)=\begin{bmatrix}\cos(\Delta\theta) & -\sin(\Delta\theta)\\ \sin(\Delta\theta) & \cos(\Delta\theta)\end{bmatrix} \tag{3.3}$$

where $\Delta\theta$ is the rotor position estimation error, $\Delta\theta=\theta_r-\theta_r^e$, as illustrated in Fig. 3.1, the PM BLAC machine's high-frequency voltage model can be expressed as follows in the estimated synchronous reference frame,

$$\begin{aligned}\begin{bmatrix}v_{dh}^e\\ v_{qh}^e\end{bmatrix}&=T(\Delta\theta)\begin{bmatrix}L_{dh} & L_{dqh}\\ L_{qdh} & L_{qh}\end{bmatrix}T^{-1}(\Delta\theta)\begin{bmatrix}pi_{dh}^e\\ pi_{qh}^e\end{bmatrix}\\ &=\begin{bmatrix}\cos(\Delta\theta) & -\sin(\Delta\theta)\\ \sin(\Delta\theta) & \cos(\Delta\theta)\end{bmatrix}\begin{bmatrix}L_{dh} & L_{dqh}\\ L_{qdh} & L_{qh}\end{bmatrix}\begin{bmatrix}\cos(\Delta\theta) & \sin(\Delta\theta)\\ -\sin(\Delta\theta) & \cos(\Delta\theta)\end{bmatrix}\\ &\quad\times\begin{bmatrix}pi_{dh}^e\\ pi_{qh}^e\end{bmatrix}\\ &=\begin{bmatrix}L_{sa}-L_{sd}\cos(2\Delta\theta)-L_{dqh}\sin(2\Delta\theta) & -L_{sd}\sin(2\Delta\theta)+L_{dqh}\cos(2\Delta\theta)\\ -L_{sd}\sin(2\Delta\theta)-L_{dqh}\cos(2\Delta\theta) & L_{sa}+L_{sd}\cos(2\Delta\theta)+L_{dqh}\sin(2\Delta\theta)\end{bmatrix}\\ &\quad\times\begin{bmatrix}pi_{dh}^e\\ pi_{qh}^e\end{bmatrix}\end{aligned} \tag{3.4}$$

here, L_{sd} and L_{sa} are the difference and average incremental inductances of both the *d*- and *q*-axes, and expressed as follows

$$\begin{cases}L_{sd}=(L_{qh}-L_{dh})/2\\ L_{sa}=(L_{qh}+L_{dh})/2\end{cases} \tag{3.5}$$

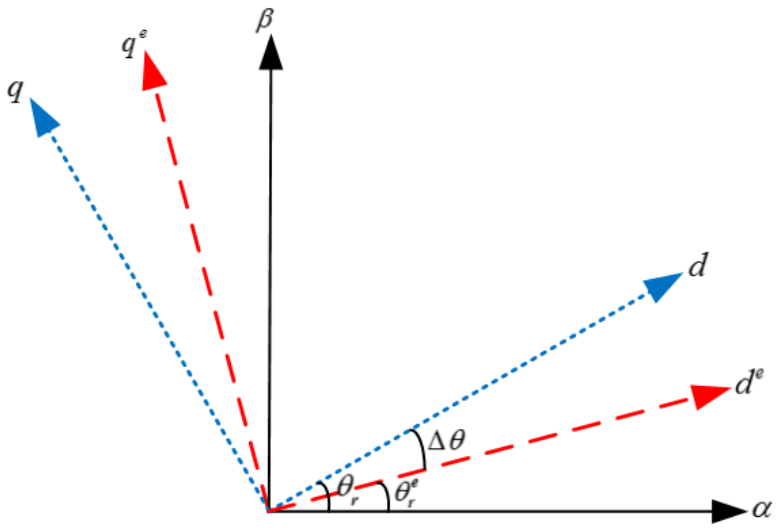

Fig. 3.1 Accurate and estimated synchronous reference frames.

The differential of the high-frequency carrier current response in the estimated reference frame can be calculated as (3.6) by solving (3.4),

$$
\begin{aligned}
p\begin{bmatrix} i_{dh}^{e} \\ i_{qh}^{e} \end{bmatrix} &= \begin{bmatrix} \dfrac{L_{sa}+\sqrt{L_{sd}^2+L_{dqh}^2}\cos(2\Delta\theta+\theta_m)}{L_{dh}L_{qh}-L_{dqh}^2} & \dfrac{\sqrt{L_{sd}^2+L_{dqh}^2}\sin(2\Delta\theta+\theta_m)}{L_{dh}L_{qh}-L_{dqh}^2} \\ \dfrac{\sqrt{L_{sd}^2+L_{dqh}^2}\sin(2\Delta\theta+\theta_m)}{L_{dh}L_{qh}-L_{dqh}^2} & \dfrac{L_{sa}-\sqrt{L_{sd}^2+L_{dqh}^2}\cos(2\Delta\theta+\theta_m)}{L_{dh}L_{qh}-L_{dqh}^2} \end{bmatrix} \\
&\quad \times \begin{bmatrix} v_{dh}^{e} \\ v_{qh}^{e} \end{bmatrix} \\
&= \begin{bmatrix} \dfrac{1}{L_p}+\dfrac{1}{L_n}\cos(2\Delta\theta+\theta_m) & \dfrac{1}{L_n}\sin(2\Delta\theta+\theta_m) \\ \dfrac{1}{L_n}\sin(2\Delta\theta+\theta_m) & \dfrac{1}{L_p}-\dfrac{1}{L_n}\cos(2\Delta\theta+\theta_m) \end{bmatrix} \begin{bmatrix} v_{dh}^{e} \\ v_{qh}^{e} \end{bmatrix}
\end{aligned}
\tag{3.6}
$$

where θ_m represents the cross-saturation angle, and

$$
\theta_m = \tan^{-1}\left(\frac{-L_{dqh}}{L_{sd}}\right),\quad L_p = \frac{L_{dh}L_{qh}-L_{dqh}^2}{L_{sa}},\quad L_n = \frac{L_{dh}L_{qh}-L_{dqh}^2}{\sqrt{L_{sd}^2+L_{dqh}^2}} \tag{3.7}
$$

3.2.3. Carrier Current Model in Stationary Reference Frame

The high-frequency voltage model of the BLAC PM machine in the $\alpha\beta$-reference frame is given as (3.9) with the help from the transformation matrix $T(\theta_r)$, i.e. (3.8).

$$T(\theta_r) = \begin{bmatrix} \cos(\theta_r) & -\sin(\theta_r) \\ \sin(\theta_r) & \cos(\theta_r) \end{bmatrix} \tag{3.8}$$

$$\begin{aligned} \begin{bmatrix} v_{\alpha h} \\ v_{\beta h} \end{bmatrix} &= T(\theta_r) \begin{bmatrix} L_{dh} & L_{dqh} \\ L_{dqh} & L_{qh} \end{bmatrix} T^{-1}(\theta_r) \begin{bmatrix} pi_{dh}^e \\ pi_{qh}^e \end{bmatrix} \\ &= \begin{bmatrix} L_{sa} - L_{sd}\cos(2\theta_r) - L_{dqh}\sin(2\theta_r) & -L_{sd}\sin(2\theta_r) + L_{dqh}\cos(2\theta_r) \\ -L_{sd}\sin(2\theta_r) - L_{dqh}\cos(2\theta_r) & L_{sa} + L_{sd}\cos(2\theta_r) + L_{dqh}\sin(2\theta_r) \end{bmatrix} \\ &\quad \times \begin{bmatrix} pi_{\alpha h} \\ pi_{\beta h} \end{bmatrix} \end{aligned} \tag{3.9}$$

The differential of the high frequency carrier current response in the stationary reference frame can be obtained as follows, in a similar way as the estimated reference frame is obtained, by solving (3.9).

$$p\begin{bmatrix} i_{\alpha h} \\ i_{\beta h} \end{bmatrix} = \begin{bmatrix} \frac{1}{L_p} + \frac{1}{L_n}\cos(2\theta_r + \theta_m) & \frac{1}{L_n}\sin(2\theta_r + \theta_m) \\ \frac{1}{L_n}\sin(2\theta_r + \theta_m) & \frac{1}{L_p} - \frac{1}{L_n}\cos(2\theta_r + \theta_m) \end{bmatrix} \begin{bmatrix} v_{\alpha h} \\ v_{\beta h} \end{bmatrix} \tag{3.10}$$

3.3. High-Frequency Carrier Signal Injection Techniques

The most common conventional high-frequency carrier signal injection techniques are pulsating sinusoidal signal injection technique [COR98] [HA00] [CAR06] [RAC08] [LI09b] [ZHA13], and rotating sinusoidal signal injection technique [JAN95] [DEG98] [BRI04] [GAR07] [GAB13].

3.3.1. Pulsating Carrier Signal Injection Technique

A high-frequency pulsating voltage is injected in the estimated synchronous reference frame into the *d*-axis or the *q*-axis in the high-frequency pulsating carrier voltage injection method. This injection is known as the superimposition of rotating carrier vectors with opposite directions and is depicted in Fig. 3.2. The rotor position can then be estimated through minimizing the modulated carrier current response amplitude orthogonal to the injection axis. If the pulsating carrier voltage injection is in *d*-axis, for instance, the *q*-axis carrier current response will be chosen to find the rotor position estimation.

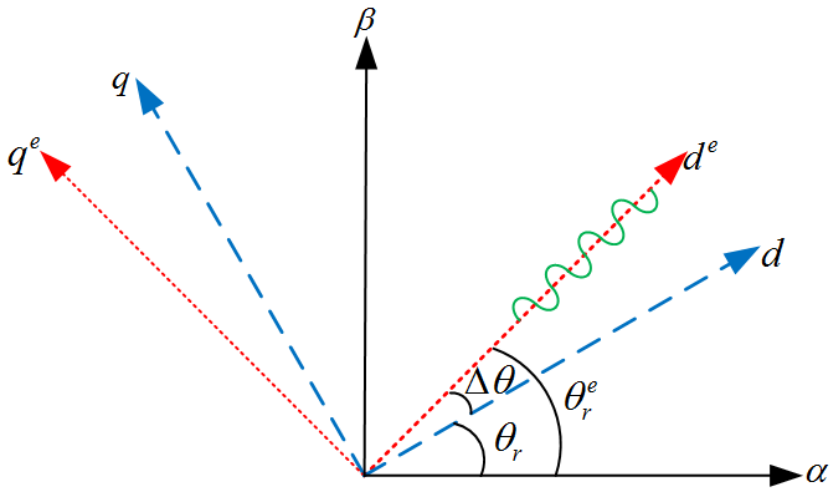

Fig. 3.2 Pulsating carrier signal injection.

The high-frequency carrier voltage is injected into the estimated *d*-axis for the *d*-axis pulsating carrier voltage injection and given by

$$\begin{bmatrix} v_{dh}^{e} \\ v_{qh}^{e} \end{bmatrix} = V_c \begin{bmatrix} \cos\alpha \\ 0 \end{bmatrix}, \text{ where } \alpha = \omega_c t + \varphi \tag{3.11}$$

where φ, ω_c, and V_c are respectively referred to as the initial phase angle, the angular speed, and the amplitude of the injected high-frequency pulsating carrier voltage.

Then, in the estimated synchronous reference frame, the differential of carrier current response is given by

$$p\begin{bmatrix} i_{dh}^e \\ i_{qh}^e \end{bmatrix} = V_c \begin{bmatrix} \frac{1}{L_p} + \frac{1}{L_n}\cos(2\Delta\theta + \theta_m) & \frac{1}{L_n}\sin(2\Delta\theta + \theta_m) \\ \frac{1}{L_n}\sin(2\Delta\theta + \theta_m) & \frac{1}{L_p} - \frac{1}{L_n}\cos(2\Delta\theta + \theta_m) \end{bmatrix} \begin{bmatrix} \cos\alpha \\ 0 \end{bmatrix} \tag{3.12}$$

In the estimated synchronous reference frame, the expression of the resultant carrier current response can thus be given as

$$\begin{aligned} \begin{bmatrix} i_{dh}^e \\ i_{qh}^e \end{bmatrix} &= \begin{bmatrix} \frac{V_c}{\omega_c L_p} + \frac{V_c}{\omega_c L_n}\cos(2\Delta\theta + \theta_m) \\ \frac{V_c}{\omega_c L_n}\sin(2\Delta\theta + \theta_m) \end{bmatrix} \sin\alpha \\ &= \begin{bmatrix} I_p + I_n\cos(2\Delta\theta + \theta_m) \\ I_n\sin(2\Delta\theta + \theta_m) \end{bmatrix} \sin\alpha \end{aligned} \tag{3.12}$$

where

$$I_p = \frac{V_c}{\omega_c L_p},\ I_n = \frac{V_c}{\omega_c L_n} \tag{3.13}$$

where I_p and I_n are respectively referred to as the amplitudes of positive- and negative-sequence currents, while L_p and L_n denote respectively the equivalent positive- and negative-sequence inductances.

It can be shown from (3.12) that the carrier current response is amplitude modulated by the information of rotor position. It also must be noted that the cross-saturation angle θ_m is constant for a given load condition. When the error of position estimation $\Delta\theta$ is small enough, the high-frequency carrier current i_{qh}^e becomes very small, which means that i_{qh}^e is commonly used in order to estimate the rotor position because of less current and torque ripples.

The carrier current response is amplitude modulated by the rotor position information, which has already been mentioned. In order to demodulate the position-dependant amplitude from the high-frequency carrier current response, the synchronous detection method is thus normally

employed [MAD95] [RAC10]. The carrier current signals in (3.12) are both multiplied by 2sinα and the signal is then applied to a LPF. The high-frequency carrier currents' amplitudes (*d*- and *q*-axes) can be obtained with noise suppression as in (3.14). The entire carrier current demodulation for pulsating carrier signal injection procedure is illustrated in 3.3.

$$\left|i_{dqh}^{e}\right| = \begin{bmatrix} \left|i_{dh}^{e}\right| \\ \left|i_{qh}^{e}\right| \end{bmatrix} = LPF\left(2\sin\alpha \begin{bmatrix} i_{dh}^{e} \\ i_{qh}^{e} \end{bmatrix}\right) = \begin{bmatrix} I_p + I_n\cos(2\Delta\theta + \theta_m) \\ I_n\sin(2\Delta\theta + \theta_m) \end{bmatrix} \tag{3.14}$$

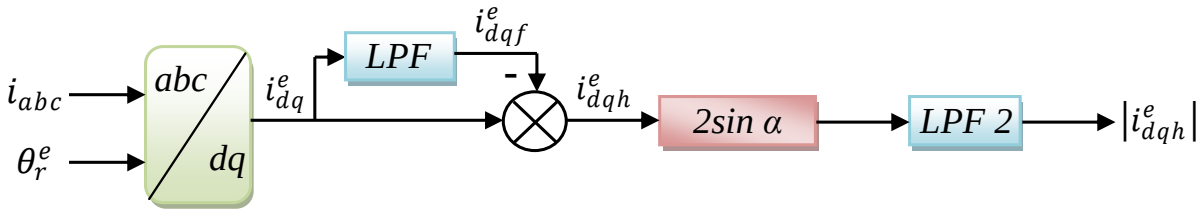

Fig. 3.3. Carrier current demodulation for pulsating injection [GON11].

The *q*-axis carrier current is utilized to be the input signal to the position observer as follows for the high-frequency pulsating carrier voltage injection in the estimated *d*-axis

$$f(\Delta\theta) = \left|i_{qh}^{e}\right| = I_n\sin(2\Delta\theta + \theta_m) \tag{3.15}$$

Due to the position observer, $f(\Delta\theta)$ is forced to be zero in the steady-state condition. The rotor position can hence be obtained with the load-dependant position estimation error ($-\theta_m/2$), which occurs due to the cross saturation effect.

Proper machine design or a compensation control method can be applied to compensate for such position estimation error. Many efforts have been made regarding the compensation control aspect. The demodulated amplitudes of the carrier current response in (3.14) can be further derived as (3.16) when the estimation error $\Delta\theta$ is small enough [ZHU11] [LI09].

$$\begin{bmatrix} \left|i_{dh}^{e}\right| \\ \left|i_{qh}^{e}\right| \end{bmatrix} = \begin{bmatrix} I_p + I_n\cos(2\Delta\theta + \theta_m) \\ I_n\sin(2\Delta\theta + \theta_m) \end{bmatrix} \approx \begin{bmatrix} I_p + I_n\cos(2\Delta\theta + \theta_m) \\ 2I_n\cos(\theta_m)(\Delta\theta) + I_n\sin(\theta_m) \end{bmatrix} \tag{3.16}$$

When defining a coupling factor as $\lambda = L_{qdh}/L_{qh}$, the input signal to the rotor position observer can be redefined as (3.17).

$$f(\Delta\theta) = \left|i_{qh}^{e}\right| + \lambda\left|i_{dh}^{e}\right| \approx 2I_n\cos(\theta_m)(\Delta\theta) \tag{3.17}$$

The position observer then forces the new input signal $f(\Delta\theta)$ to be zero. Clearly, the position estimation error due to a cross saturation effect would not be generated. The overall control system

for sensorless control method based on high-frequency pulsating carrier voltage injection is illustrated in Fig. 3.4.

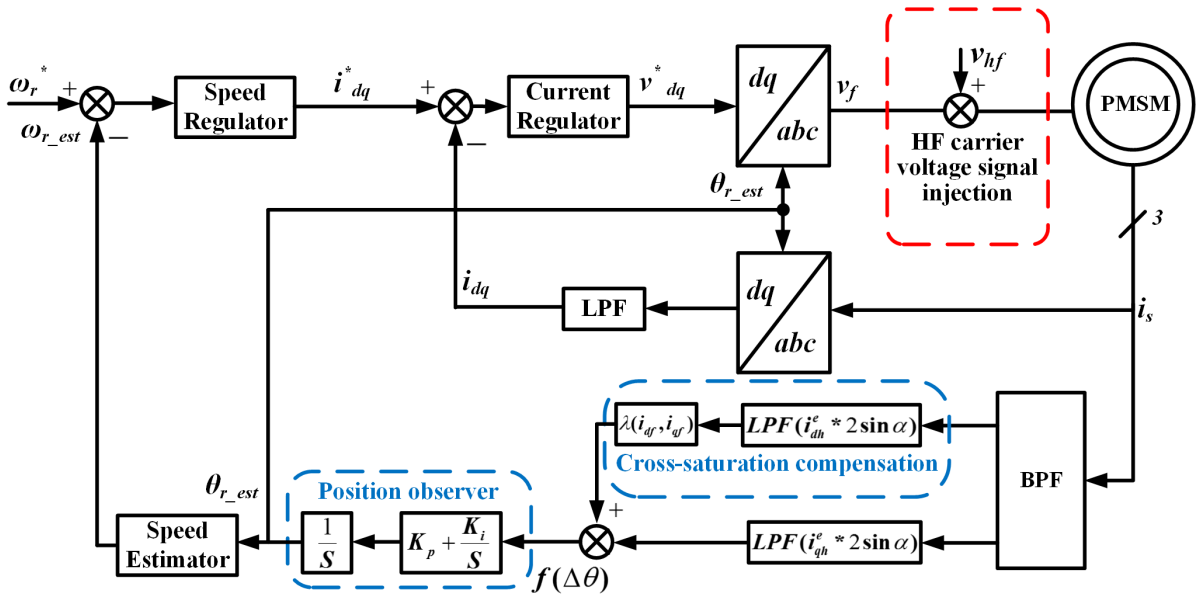

Fig. 3.4 Block diagram of pulsating carrier signal injection in *d*-axis based sensorless control [GON11].

It should be mentioned that the abovementioned analyses and expressions are related to single three-phase PMSM. For the dual three-phase PMSM, the high-frequency pulsating carrier voltage signals are injected into the two stator winding sets independently, and the same analysis for single three-phase PMSM is applied.

3.3.2. Rotating Carrier Signal Injection Technique

A balanced three-phase carrier voltage is injected into the $\alpha\beta$-reference frame for a high-frequency rotating carrier voltage injection approach. This is done to form a rotating excitation which is superimposed on the fundamental excitation [ZHU11] [JAN03] [OVR04] [JAN04] as illustrated in Fig. 3.5. The information of the rotor position can then be extracted from the position-dependent modulated current response.

The balanced rotating carrier voltage vector is injected into the $\alpha\beta$-reference frame as

$$\begin{bmatrix} v_{\alpha h} \\ v_{\beta h} \end{bmatrix} = V_c \begin{bmatrix} \cos\alpha \\ \sin\alpha \end{bmatrix}, \text{ where } \alpha = \omega_c t + \varphi \tag{3.18}$$

where φ, ω_c, and V_c denote the initial phase angle, the angular speed, and the amplitude of the injected high-frequency rotating carrier voltage, respectively.

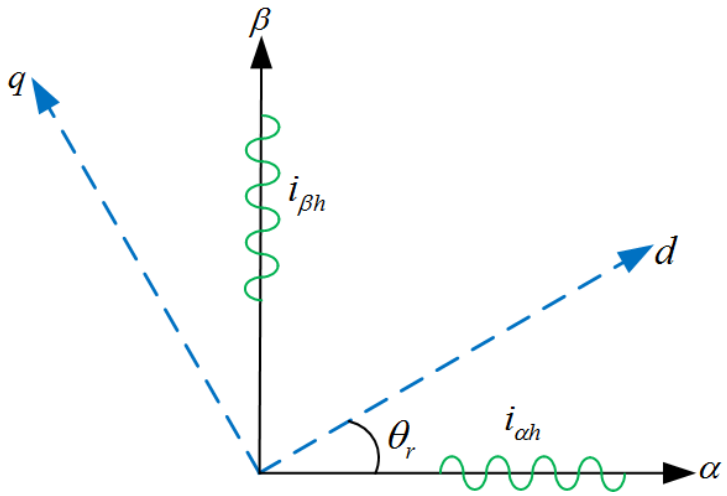

Fig. 3.5. Rotating signal injection.

The differential high-frequency current response in the $\alpha\beta$-reference frame is given by

$$p\begin{bmatrix} i_{\alpha h} \\ i_{\beta h} \end{bmatrix} = V_c \begin{bmatrix} \frac{1}{L_p} + \frac{1}{L_n}\cos(2\theta_r + \theta_m) & \frac{1}{L_n}\sin(2\theta_r + \theta_m) \\ \frac{1}{L_n}\sin(2\theta_r + \theta_m) & \frac{1}{L_p} - \frac{1}{L_n}\cos(2\theta_r + \theta_m) \end{bmatrix} \begin{bmatrix} \cos\alpha \\ \sin\alpha \end{bmatrix} \tag{3.19}$$

The resultant position-dependant carrier current response in the $\alpha\beta$-reference frame can then be expressed as

$$\begin{bmatrix} i_{\alpha h} \\ i_{\beta h} \end{bmatrix} = \frac{V_c}{\omega_c} \begin{bmatrix} \frac{1}{L_p} + \frac{1}{L_n}\cos(2\theta_r + \theta_m) & \frac{1}{L_n}\sin(2\theta_r + \theta_m) \\ \frac{1}{L_n}\sin(2\theta_r + \theta_m) & \frac{1}{L_p} - \frac{1}{L_n}\cos(2\theta_r + \theta_m) \end{bmatrix} \begin{bmatrix} \sin\alpha \\ -\cos\alpha \end{bmatrix} \tag{3.20}$$

$$= \begin{bmatrix} I_p \cos(\alpha - \pi/2) \\ I_p \sin(\alpha - \pi/2) \end{bmatrix} + \begin{bmatrix} I_n \cos(-\alpha + 2\theta_r + \theta_m + \pi/2) \\ I_n \sin(-\alpha + 2\theta_r + \theta_m + \pi/2) \end{bmatrix}$$

where θ_m, L_p and L_n are defined in (3.7) , while I_p and I_n are defined in (3.13).

The carrier current response in the $\alpha\beta$-reference frame can be given as (3.21) by using a complex vector form.

$$i_h = I_p\ e^{j(\alpha-\pi/2)} + I_n\ e^{j(-\alpha+2\theta_r+\theta_m+\pi/2)} \tag{3.21}$$

In summary, the high-frequency rotating carrier injection can be viewed as follows:

- There are two components in the carrier current, i.e. positive- and negative-sequence components. The negative component includes the information of rotor position in its phase angle and the positive-sequence component has the same rotated speed as the injected carrier voltage vector. The rotor position information can be extracted from the negative-sequence component.
- The spectra of the positive- and negative-sequence carrier currents are asymmetric, unlike the symmetrical spectrum of the carrier current response for a pulsating carrier signal injection. The magnitudes of the positive- and negative-sequence carrier currents are both proportional to the ratio of (V_c/ω_c), and machine parameter-dependent.

The negative-sequence carrier current can be extracted from the total carrier current response by employing a synchronous reference frame filter (SRFF) [DEG98] [RAC10] [GAR07], which includes the information of rotor position. SRFF utilizes the frame transformation to transform the fundamental current to DC. With the aid of a low pass filter, this DC component can then be obtained without phase lag. The fundamental current can be obtained by applying the reverse transformation. The positive-negative current can be derived by employing the same procedure with the phase angle of the injected carrier voltage. By subtracting the positive-sequence current from the total carrier current response, it is possible to obtain the negative-sequence current. By employing the signal demodulation together with SRFF, Fig. 3.6, the negative-sequence current can be obtained as

$$i_n = I_n\ e^{j(-\alpha+2\theta_r+\theta_m+\pi/2)} \tag{3.22}$$

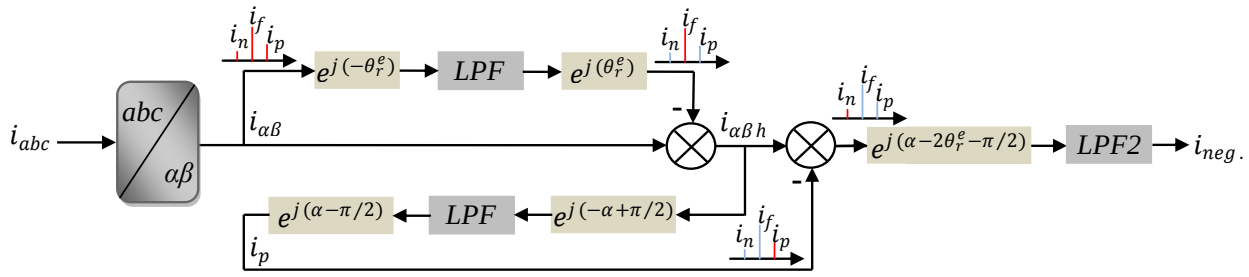

Fig. 3.6. Demodulation process for carrier current for rotating injection [GON11].

Then, in the synchronous reference frame, i_{neg} with the estimated negative-sequence carrier frequency can be derived as

$$i_{neg} = I_n\ e^{j(-\alpha+2\theta_r+\theta_m+\pi/2)}\ e^{j(\alpha-2\theta_{re}-\pi/2)} = I_n\ e^{j(2\Delta\theta+\theta_m)} = I_n\ e^{j(\theta_{neg})} \tag{3.23}$$

where θ_{neg} is the angular offset of the negative-sequence carrier current. Expression (3.23) can be re-written as

$$\begin{bmatrix} i_{neg-d} \\ i_{neg-q} \end{bmatrix} = \begin{bmatrix} I_n \cos(2\Delta\theta_r + \theta_m) \\ I_n \sin(2\Delta\theta_r + \theta_m) \end{bmatrix} \tag{3.24}$$

The q-axis carrier current is commonly utilized as the input signal $f(\Delta\theta)$ to the rotor position observer [JAN95] [DEG98], and it can be expressed as

$$f(\Delta\theta) = i_{neg-q} = I_n \sin(2\Delta\theta + \theta_m) \tag{3.25}$$

It is similar to that of conventional pulsating injection, and it is expected that a position estimation error would have occurred due to cross-saturation effect ($-\theta_m/2$) and also for the rotating injection. The phase angle is modified as (3.26) in [GON11] to compensate for such error.

$$\alpha^* = \alpha + \theta_m \tag{3.26}$$

And the carrier current response is then expressed as

$$i = i_f + I_p\ e^{j(\alpha+\theta_m-\pi/2)} + I_n\ e^{j(-\alpha+2\theta_r+\pi/2)} \tag{3.27}$$

In this way, it can be found that the cross-saturation angle (θ_m) has been shifted from the negative-sequence current to the positive-sequence current.

It is therefore expected that the rotor position can be estimated accurately from the negative-sequence carrier current, and (3.24) can be updated as

$$\begin{bmatrix} i_{neg-d} \\ i_{neg-q} \end{bmatrix} = \begin{bmatrix} I_n \cos(2\Delta\theta_r) \\ I_n \sin(2\Delta\theta_r) \end{bmatrix} \tag{3.28}$$

and the updated input signal $f(\Delta\theta)$ to the rotor position observer is expressed as

$$f(\Delta\theta) = i_{neg-q} = I_n \sin(2\Delta\theta) \tag{3.29}$$

The complete schematic diagram for the sensorless control method based on rotating carrier voltage injection including the cross-saturation effect compensation is depicted in Fig. 3.7.

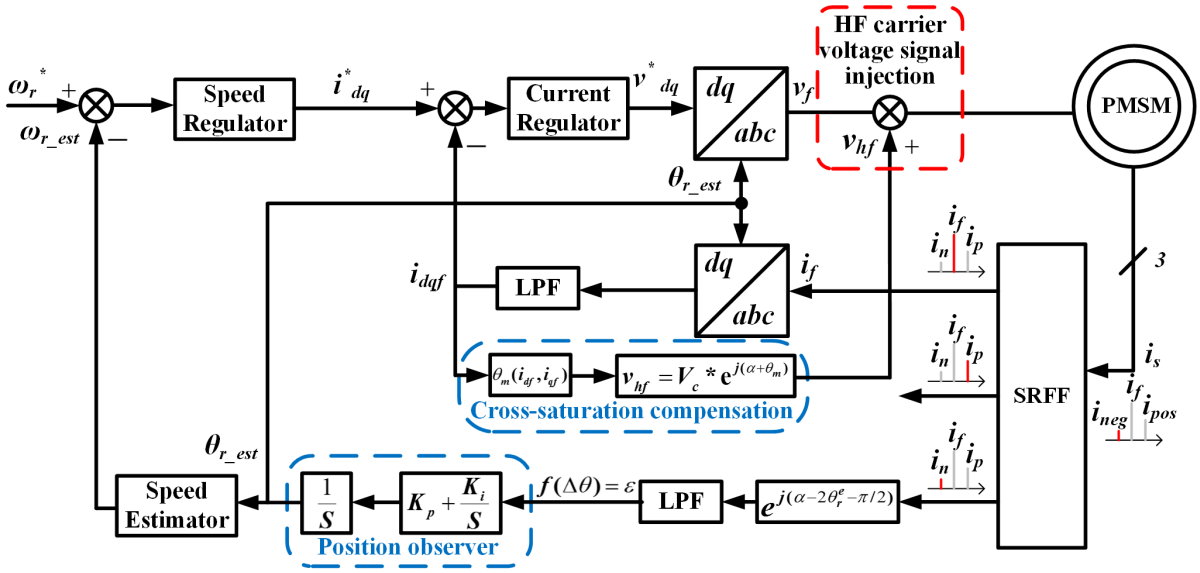

Fig. 3.7 Block diagram of rotating carrier signal injection in stationary reference frame based sensorless control [GON11].

It should be mentioned that the abovementioned analyses and expressions are related to single three-phase PMSM. For the dual three-phase PMSM, the high-frequency rotating carrier voltage signals are injected into the two stator winding set independently, and the same analysis for single three-phase PMSM is applied.

3.3.3. Rotor Position Observer

The position tracking observer is much more popular than the arc-tangent function ($\tan^{-1}$) calculation [TES03] for rotor position estimation, because it gives good immunity to disturbance harmonics while still keeping the dynamic performance of position tracking. Some non-linear controllers, such as bang-bang controllers, can be employed by the position observer [JAN04] in order to enhance the dynamic characteristics.

The signal $f(\Delta\theta)$ is considered as input signal to the rotor position observer for sensorless control methods based on pulsating and rotating injections. The schematic diagram of the rotor position observer, including PI regular, is shown in Fig. 3.8.

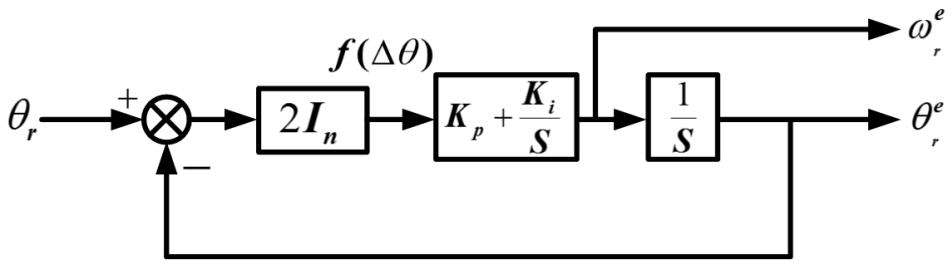

Fig. 3.8. Schematic diagram of rotor position observer.

The expression of the closed-loop transfer function between the estimated and actual information of rotor position, according to Fig 3.8, can be given as

$$\frac{\theta_r^e}{\theta_r} = \frac{2I_n k_p s + 2I_n k_i}{s^2 + 2I_n k_p s + 2I_n k_i} \tag{3.30}$$

From (3.7) and (3.13), it can be found that I_n is load-dependant. Thus, the PI gains, i.e. k_p and k_i, should be varied on-line with I_n to preserve a constant bandwidth. In practical implementation, for simplicity, such gains can be chosen based on the typical value of I_n at no-load condition.

3.3.4. Evaluation of Test Machine Saliency Level

Prior to applying the sensorless control methods based on high-frequency carrier signal injection based, the investigation of the machine saliency level is essentially required. The machine saliency relates to the variation of the inductance and the machine load condition. Usually, anisotropy ratio scheme [GUG06], saliency ration method [YAN11], and feasible region strategy

[BIA07] are utilized to evaluate the level of machine saliency. However, such methods require the machine parameters, i.e. incremental inductances, and they are suitable for in theoretical analysis rather than practical application. On the other hand, a high-frequency impedance measurements which does not require the machine parameters are introduced in [JAN03]. Although it avoids the requirement of machine parameter, it leads to more computational load on the processor due to complicated calculations of the impedance. Therefore, with considering the limitations of the mentioned methods, a simplified experimental method has been introduced in [GON11] to construct a saliency circle, in which the full machine saliency information can be detected. In this thesis, the simplified experimental method is employed in order to investigate the machine saliency level of the test machine. With the help of an encoder (position sensor) to provide the actual rotor position, the rotor is locked at zero position (θ_r=0). After that, a high-frequency pulsating voltage signal as expressed in (3.31) is then injected in the estimated *dq* synchronous reference frame. As illustrated in Fig. 3.9, the estimated synchronous reference frame has $\Delta\theta$ phase angle difference from the actual synchronous reference frame. The injected signal rotates at fixed speed (2Hz) in clockwise direction. The injected carrier voltage has an amplitude of 8V and a frequency of 550Hz for the prototype machine. These machine's specifications are listed in Appendix II. The carrier current response in the estimated *dq* synchronous reference frame can be obtained as (3.32).

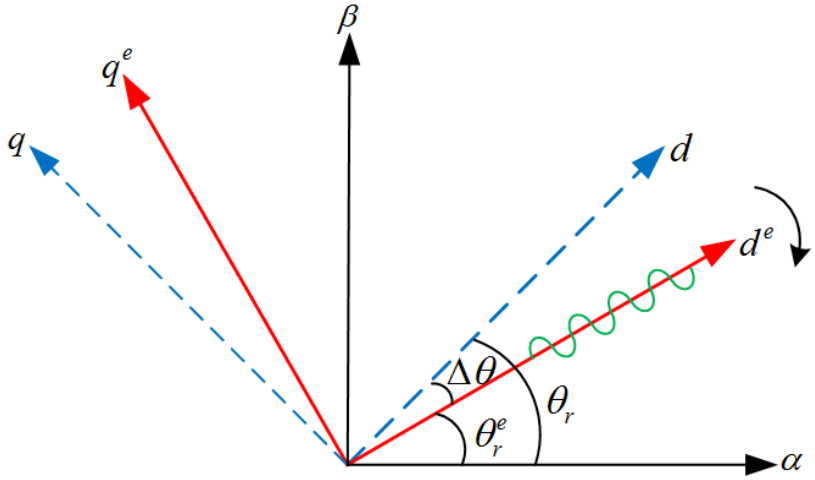

Fig. 3.9. Actual and estimated synchronous reference frames.

$$\begin{bmatrix} v_{dh}^{e} \\ v_{qh}^{e} \end{bmatrix} = V_c \begin{bmatrix} \cos\alpha \\ 0 \end{bmatrix}, \text{ where } \alpha = \omega_c t + \varphi \tag{3.31}$$

$$\begin{bmatrix} i_{dh}^{e} \\ i_{qh}^{e} \end{bmatrix} = \begin{bmatrix} I_p + I_n \cos(2\Delta\theta + \theta_m) \\ I_n \sin(2\Delta\theta + \theta_m) \end{bmatrix} \sin(\alpha) \tag{3.32}$$

where $\Delta\theta = \theta_r - \theta_r^e$.

The carrier current response in the estimated *dq* synchronous reference frame without fundamental excitation, i.e. I_d = 0 A and I_q = 0A, is measured, as illustrated in Fig. 3.10. It should be noted that the high-frequency *d*- and *q*-axis carrier current responses have the same phase angle with different amplitudes. These amplitudes are modulated by position difference between estimated and real *dq* reference frames, i.e. $\Delta\theta$. By employing the synchronous detection techniques [MAD95] [RAC10] to demodulate the position-dependant amplitude from the carrier current response, as such, the amplitude can be derived as

$$\begin{bmatrix} |i_{dh}^{e}| \\ |i_{qh}^{e}| \end{bmatrix} = LPF\left(\begin{bmatrix} i_{dh}^{e} \\ i_{qh}^{e} \end{bmatrix} 2\sin\alpha\right) = \begin{bmatrix} I_p + I_n \cos(2\Delta\theta + \theta_m) \\ I_n \sin(2\Delta\theta + \theta_m) \end{bmatrix} \tag{3.33}$$

With the aid of synchronous detection techniques, the measured carrier currents amplitudes are shown in Fig. 3.11. When the position difference between the actual and estimated position is 0 degree or 180 degrees, the estimated *d*-axis for carrier signal injection is aligned with the real *d*-axis. Consequently, the *d*-axis current amplitude reaches the maximum value, whilst the amplitude of *q*-axis current is close to zero. In this case, the cross-saturation angle θ_m is almost negligible without fundamental excitation according to (3.33).

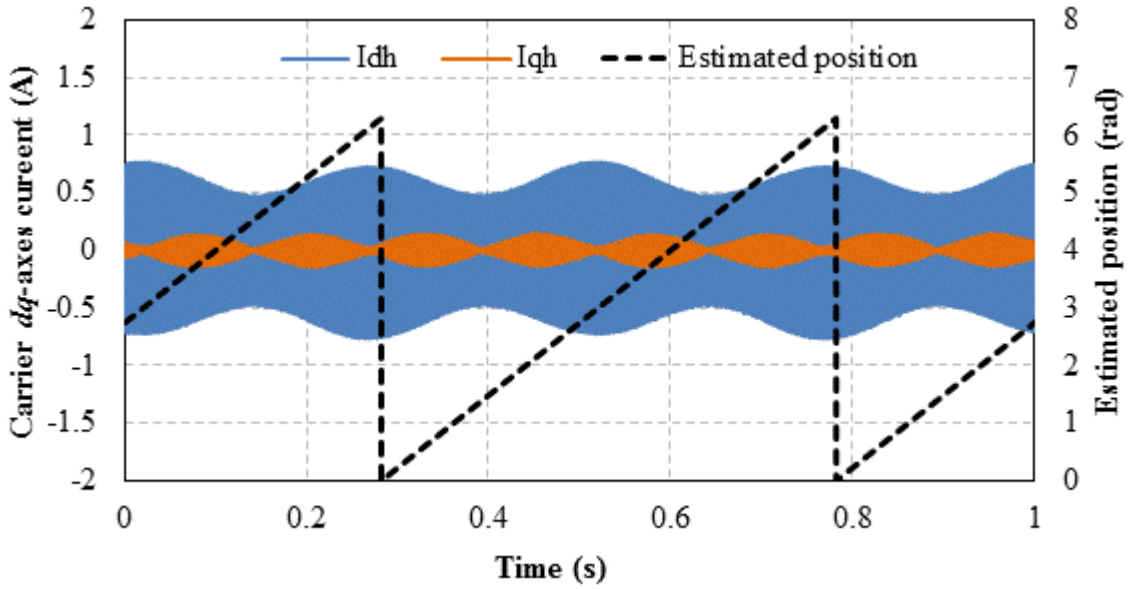

Fig. 3.10. Measurement of carrier currents in estimated *dq*-axis frame, (I_d=0A, I_q=0A).

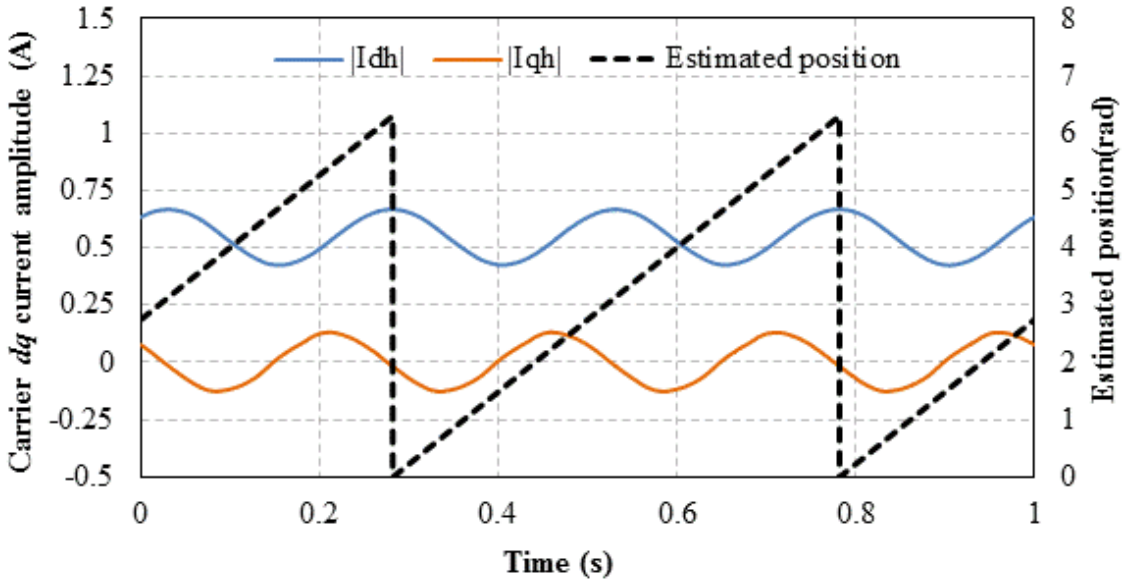

Fig. 3.11. Carrier currents amplitudes in estimated *dq*-axis reference frame, (I_d=0A, I_q=0A).

When the variations of the measured carrier current amplitudes without and with full load are combined together in Fig. 3.12, the formed circle is specified as the machine saliency circle. The circle clearly shows the machine saliency information. The centre location of the machine saliency circle is defined by I_p, and its radius depends on I_n which denotes the level of the machine saliency. Furthermore, at different load conditions, the radius I_n has a significant change due to the inductances variations versus the fundamental excitation, and I_p , i.e. the offset, is also affected by the variation of inductances. If the radius of the machine saliency circle, i.e. I_n, is long enough, the machine is appropriate for sensorless control methods based on high-frequency carrier signal injection.

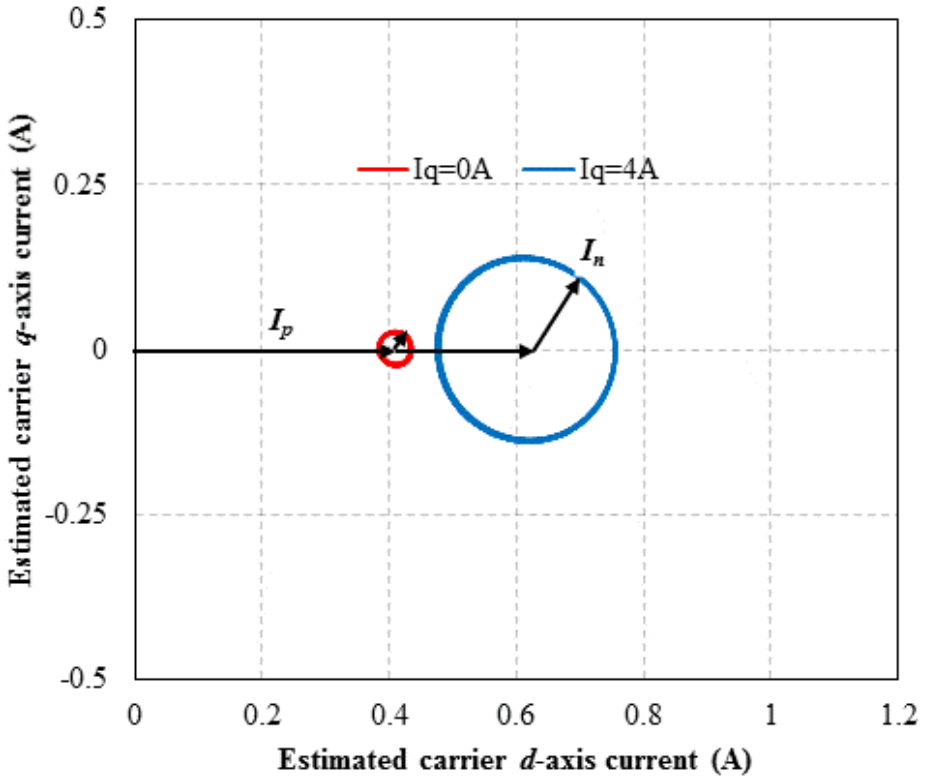

Fig. 3.12 Current loci without and with full load, machine saliency circles.

3.3.5. Influence of Cross-Saturation

With different load conditions, an error of rotor position estimation would occur because of the magnetic saturation caused by variation of load. The cross saturation angle is close to zero, and as mentioned in the previous subsection, it can be neglected when I_q=0. The amplitudes of the carrier current responses are measured as depicted in Fig. 3.13 and Fig. 3.14 by applying different fundamental q-axis currents. It can be seen clearly that the cross-saturation angle θ_m is occurred and significantly affected by the load current I_q. In order to investigate the influence of cross-saturation, the cross-saturation angle θ_m is measured in sensored operation, i.e. using an encoder, with different q-axis currents, Fig. 3.15. As it has been found, the cross-saturation angle θ_m is approximately proportional to the q-axis current, $\theta_m = K_r * I_q$, and can easily be compensated by utilizing the compensation scheme introduced in [ZHU07].

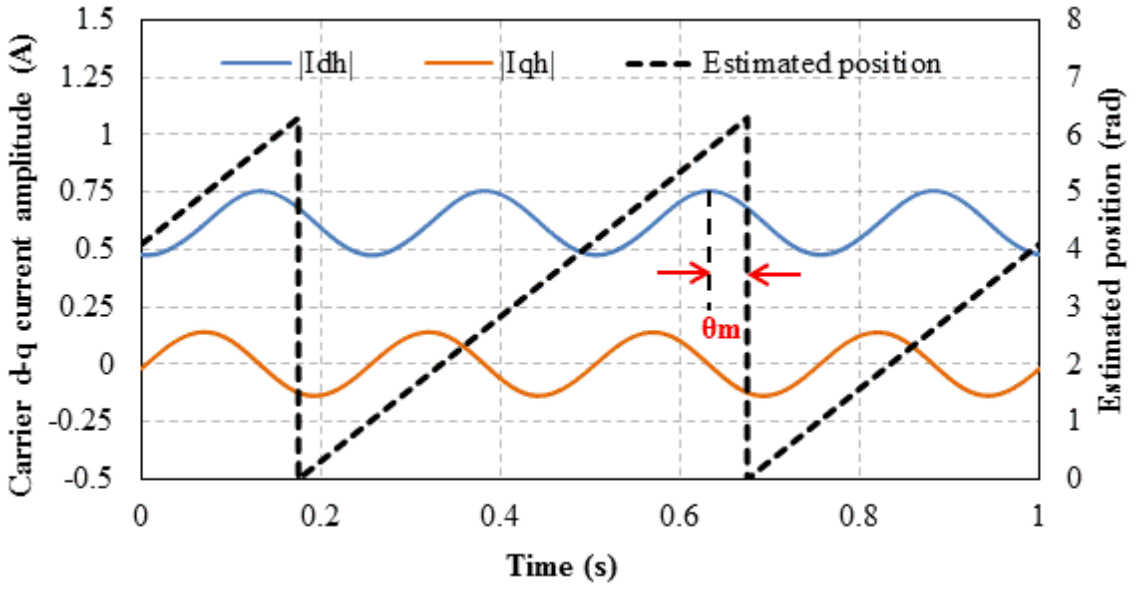

Fig. 3.13. Carrier currents amplitudes in estimated *dq*-axis reference frame, (I_d=0A, I_q=4A).

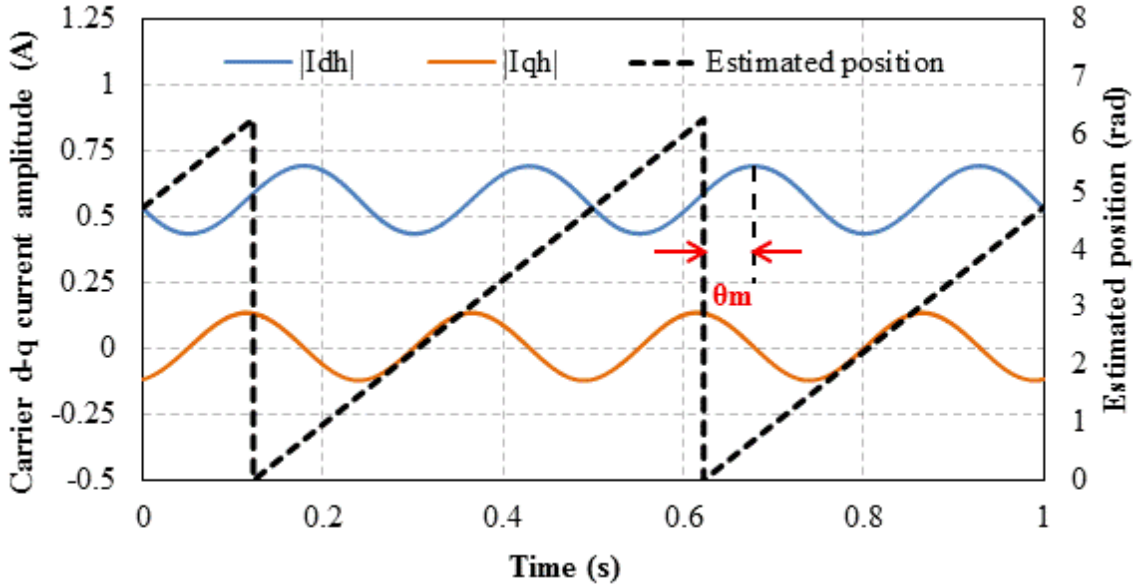

Fig. 3.14. Carrier currents amplitudes in estimated *dq*-axis reference frame, (I_d=0A, I_q=-4A).

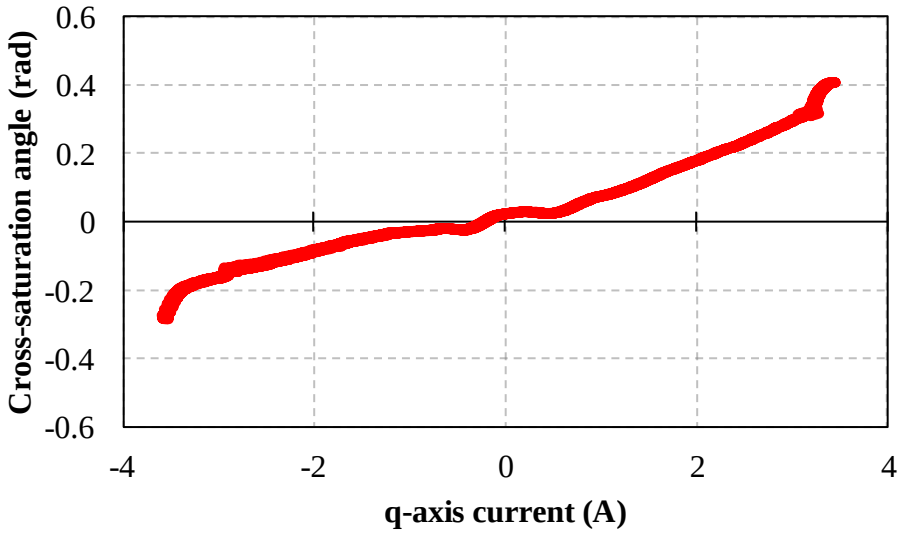

Fig. 3.15. Angle of Cross-saturation measured in sensored operation with different *q*-axis currents.

3.4. Sensorless Control Performance for Pulsating Carrier Signal Injection

In order to validate the effectiveness of sensorless control performance, the pulsating carrier signal injection method is applied to the single and dual three-phase prototype PMSMs. The machine saliency components for positive and negative carrier signals responses in the estimated rotor frame can be utilized to detect the rotor position information. A high-frequency voltage with amplitude of 8 V and carrier frequency of 550Hz is injected in the estimated *dq* reference frame (*d*-axis), and the performance of the rotor position estimation using the *q*-axis carrier current response is investigated under steady-state and dynamic conditions.

3.4.1. Estimation of Rotor Position in Steady and Dynamic States

A. Sensorless Control Performance for Single Three-Phase PMSM

For the single three-phase PMSM, the steady-state test for the pulsating carrier signal injection method is carried out at the condition of 30rpm rotor speed with *q*-axis current of about 2 A. The comparison of estimated rotor position and actual position, without and with compensation of cross-saturation effect, is illustrated in Fig.3.16 and Fig.3.17, respectively, together with the estimation error. It can clearly be seen that the estimated rotor position exhibits good position tracking performance with considering the cross-saturation compensation.

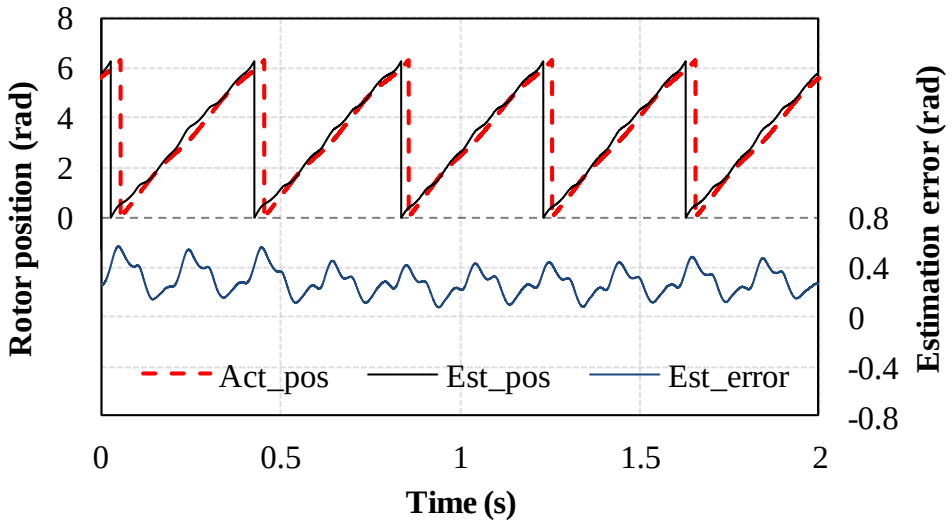

Fig. 3.16. Steady-state performance without cross-saturation compensation, I_q=2A, 30rpm.

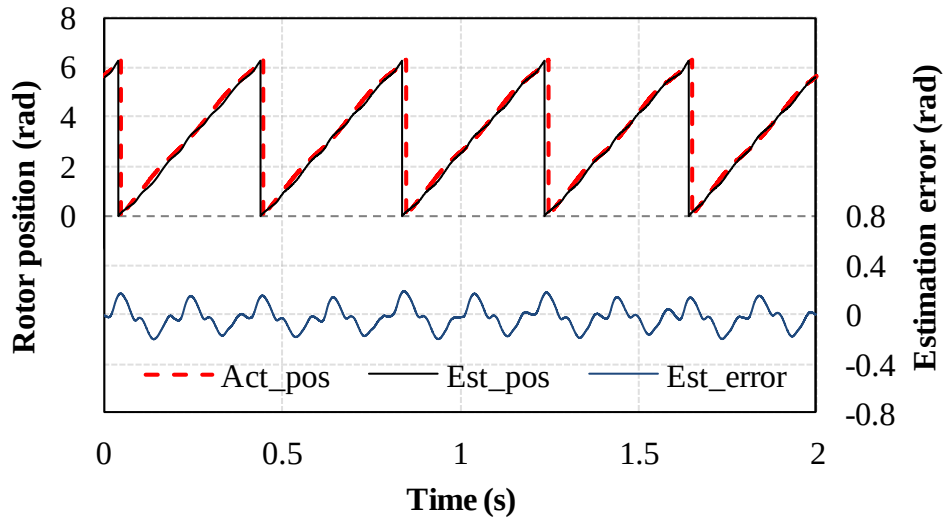

Fig. 3.17. Steady-state performance with cross-saturation compensation, I_q=2A, 30rpm.

The experiments for the dynamic performance are carried out when the rotor initial speed is zero and step changed to 30rpm and then to 60rpm. Fig. 3.18 (a) shows the speed response, and Fig. 3.18 (b) shows the q-axis current. The estimated and actual rotor positions as well as the estimation error, are illustrated in and Fig. 3.18 (c). The results show a decent dynamic performance. Furthermore, in order to validate the robustness and accuracy of the pulsating carrier signal injection method in terms of the sensitivity to the injection frequency, the peak-to-peak position estimation error with different carrier frequency injections at 30 rpm and q-axis current of 2 A is depicted in Fig. 3.19. It can clearly be observed that the estimation error becomes a bit higher in case of high injection frequency due to the digital sampling delay [KOC09] [MOG13].

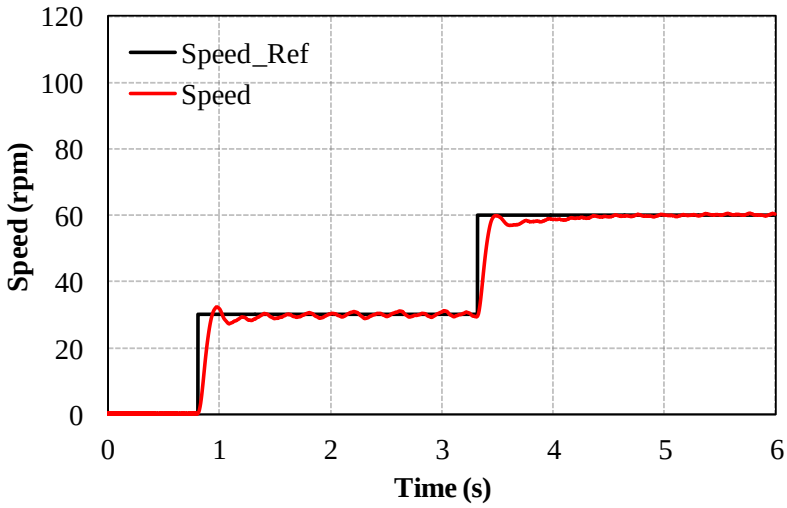

(a) Reference speed and actual rotor speed

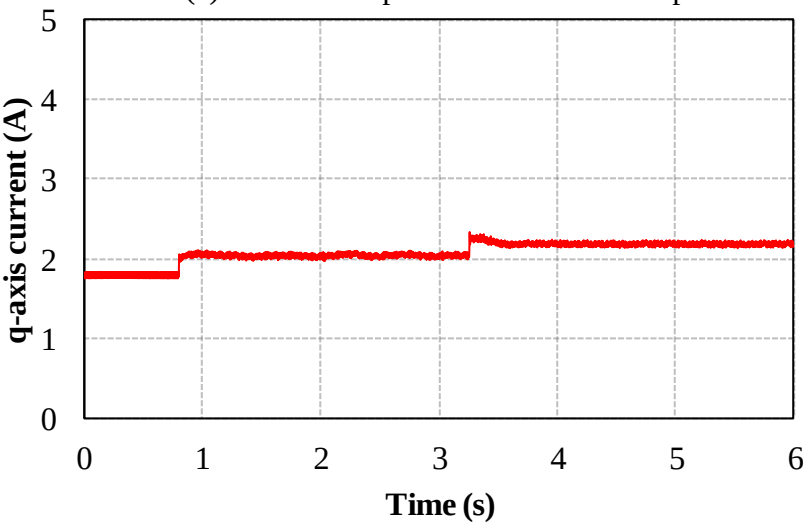

(b) q-axis current

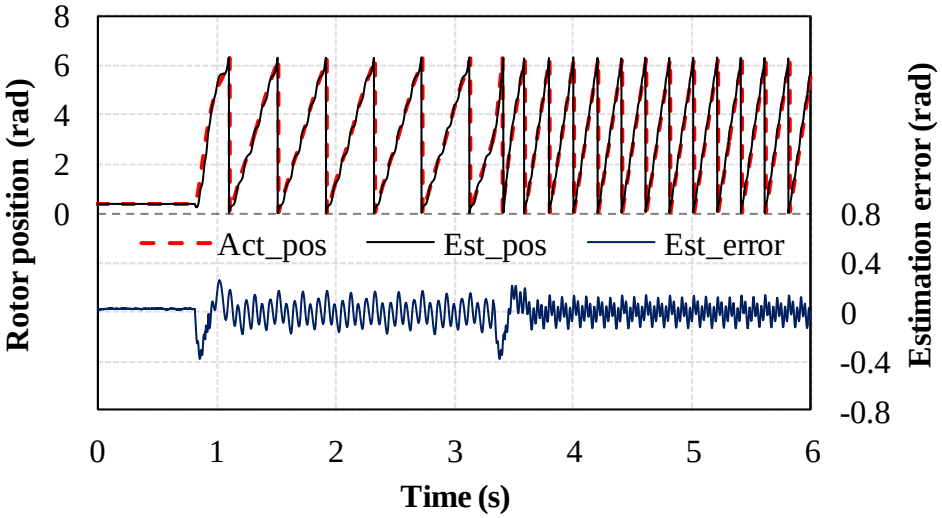

(c) Rotor position estimation performance

Fig. 3.18. Dynamic performance under step change in rotor speed, I_q=2A, 0-30-60rpm.

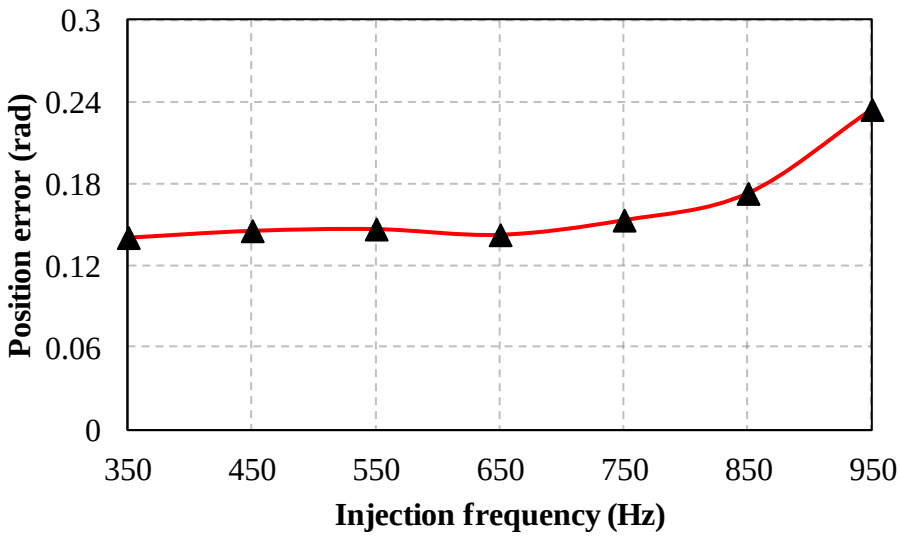

Fig. 3.19 Peak-to-peak position estimation error with different frequency injections, I_q=2A, 30 rpm.

B. Sensorless Control Performance for Dual Three-Phase PMSM

Generally, the models of the dual three-phase PMSMs can be classified into two different models as; double *dq* model which the two stator winding sets are controlled separately [BOJ03], and vector space decomposition model (VSD) where the two stator winding sets are mutually decoupled [ZHA95]. The two models are well explained in Chapter 1. In this section, the pulsating carrier signal injection method is extended to be applied to dual three-phase machine, and the sensorless control performances under steady-state and dynamic conditions are examined for both models (i.e. double *dq* model, and VSD model).

1. Double *dq* Model

For this model, the *d*-axis pulsating carrier voltage signal with amplitude of 8 V and carrier frequency of 550Hz is injected on both stator winding sets independently. By applying the *d*-axis pulsating carrier injection technique on both winding sets independently, the comparison of estimated and actual rotor position under steady-state condition, without/with compensation of cross-saturation effect are illustrated in Fig.3.20 and Fig.3.21, respectively. Furthermore, the dynamic-state performance when the rotor mechanical initial speed is zero and step change to 30rpm and then to 60rpm, is illustrated in Fig. 3.22. It can be found that the rotor position estimation performances for both the steady-state and dynamic conditions show good position tracking with considering the cross-saturation effect compensation.

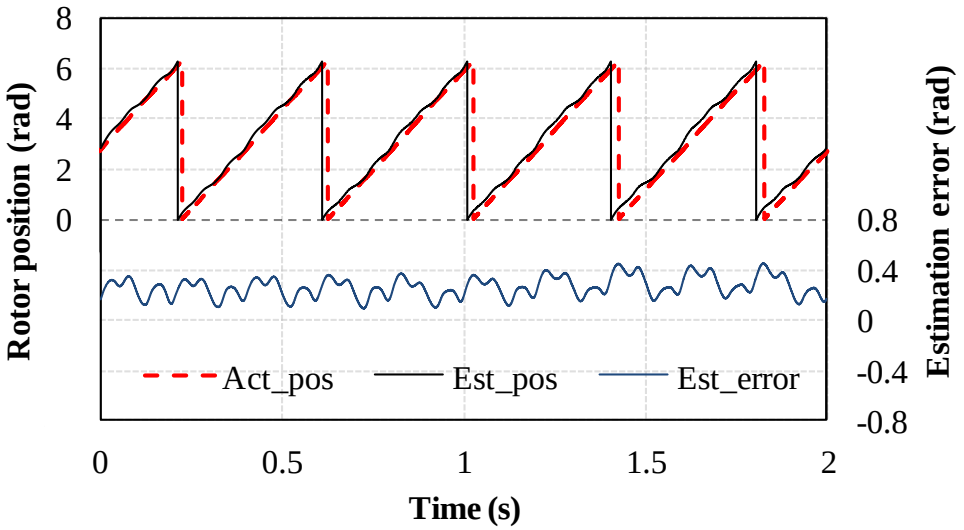

Fig. 3.20. Steady-state performance without cross-saturation compensation, I_q=2A, 30rpm.

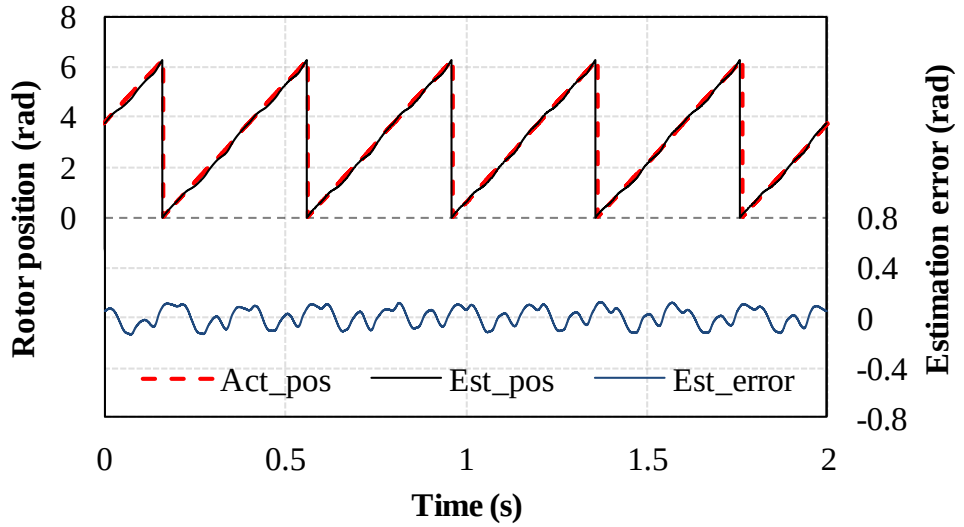

Fig. 3.21. Steady-state performance with cross-saturation compensation, I_q=2A, 30rpm.

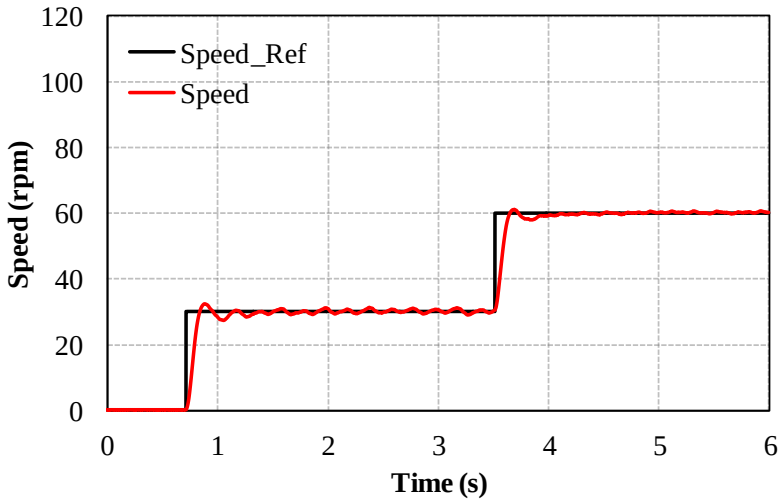

(a) Reference speed and actual rotor speed

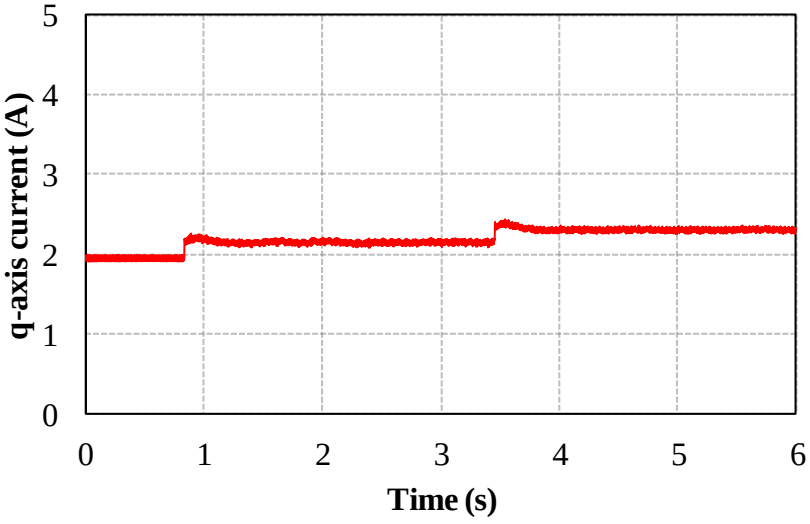

(b) q-axis current

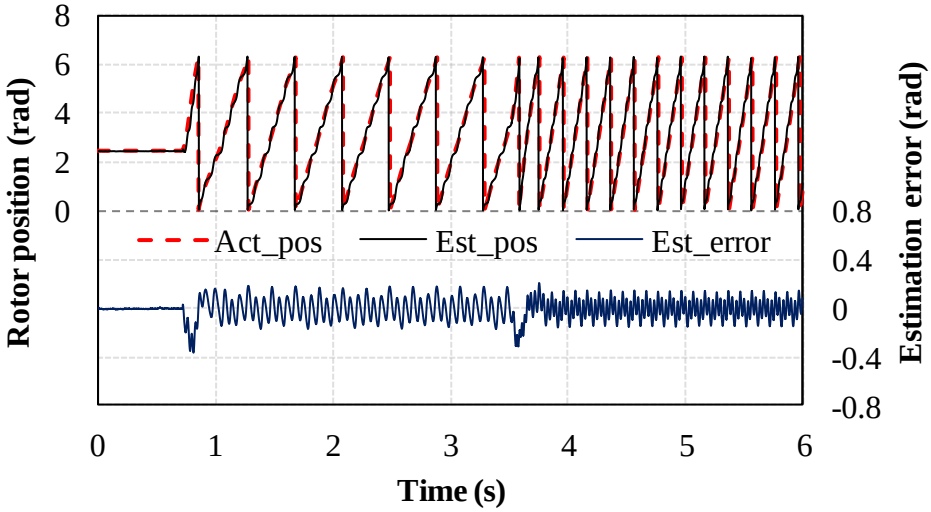

(c) Rotor position estimation performance

Fig. 3.22. Dynamic performance under step change in rotor speed, I_q=2A, 0-30-60rpm.

2. Vector Space Decomposition (VSD) Model

The model based on VSD is decomposed into three orthogonal subspaces; $\alpha\beta$-subspace, z_1z_2-subspace, and o_1o_2-subspace. Since only the $\alpha\beta$-subspace is related to electromechanical energy conversion [ZHA95] as explained in Chapter 1, the *d*-axis pulsating carrier voltage signal with amplitude of 8 V and carrier frequency of 550Hz is injected on this subspace after it is transformed to *dq* rotating reference frame. Then, the actual and estimated rotor position together with position estimation error with compensation of cross-saturation effect is obtained as illustrated in Fig. 3.23. Additionally, the dynamic sensorless control performance including the rotor speed response is depicted in Fig. 3.24. It should be noted that the position estimation error as well as the estimation error oscillation are decreased when injecting high-frequency signal with the aid of vector space decomposition modelling approach that is because the mutual coupling between the two winding sets is eliminated since the decoupling between two winding sets is considered in the transformation of this approach, while it is not considered in the double *dq* modelling approach [ZHA95]. Also, it shows outstanding dynamic performance with fast transient response. Furthermore, the peak-to-peak estimation error among different frequency injections with q-axis current of 2A and speed at 30rpmis shown in Fig. 3.25 to confirm the rotor estimation accuracy against different carrier frequency injections. From Fig. 3.25, less estimation error sensitivity can be observed with different frequency injections.

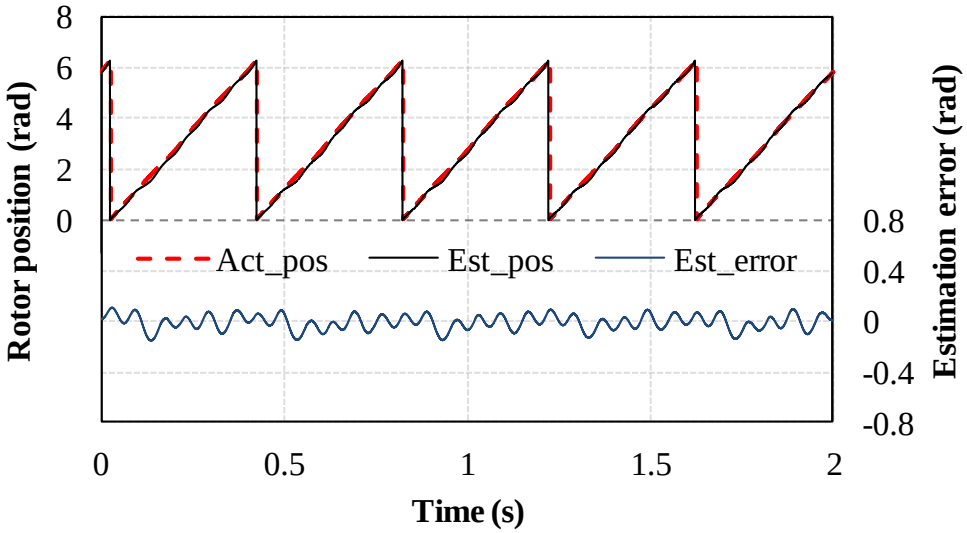

Fig. 3.23. Steady-state performance with cross-saturation compensation, I_q=2A, 30rpm.

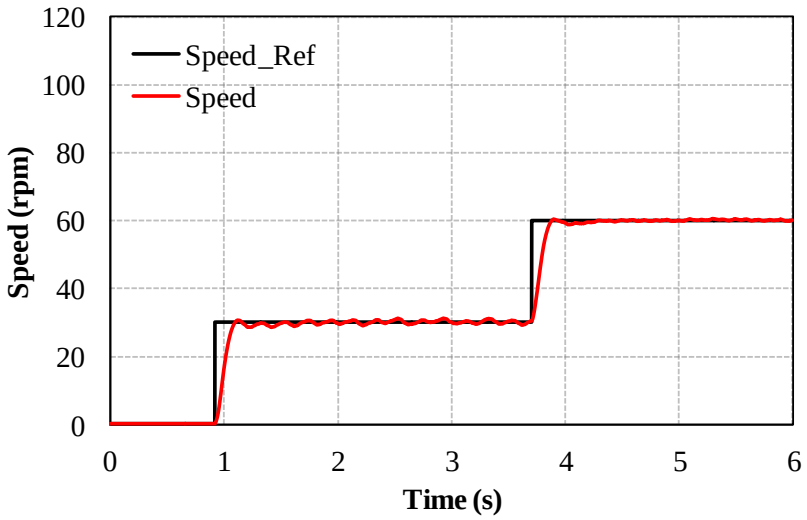

(a) Reference speed and actual rotor speed

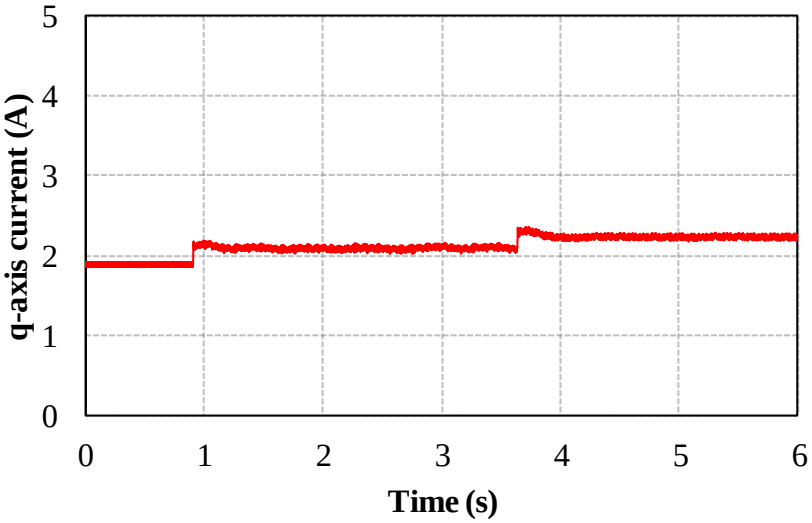

(b) q-axis current

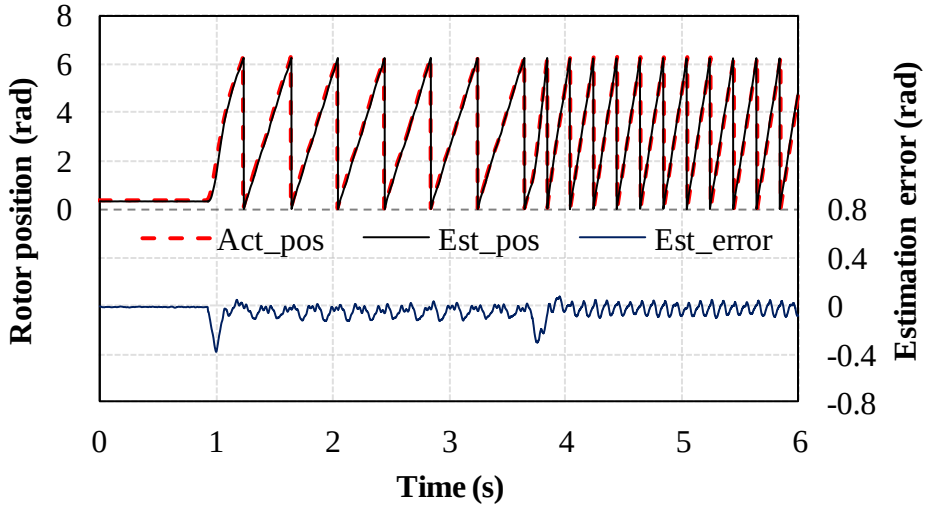

(c) Rotor position estimation performance

Fig. 3.24. Dynamic performance under step change in rotor speed, I_q=2A, 0-30-60rpm.

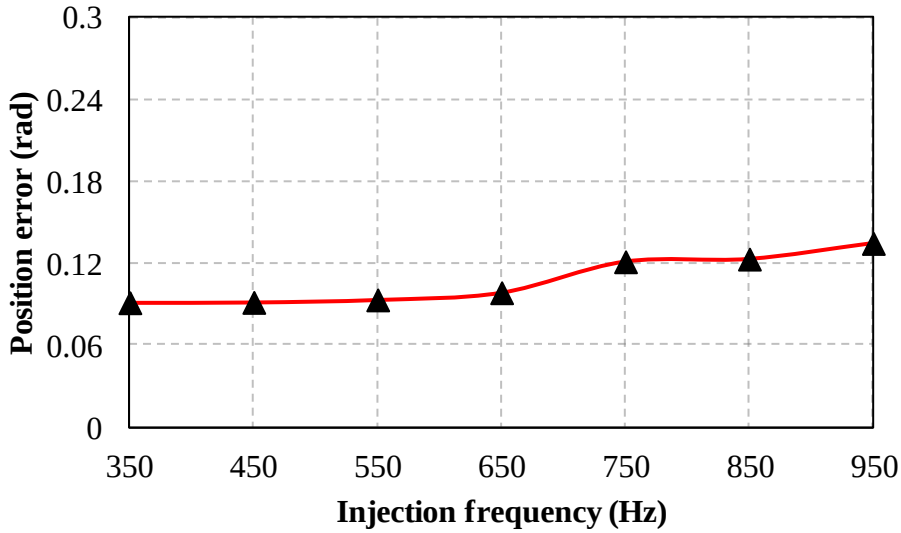

Fig. 3.25. Peak-to-peak position estimation error with different frequency injections, I_q=2A, 30 rpm.

3.5. Sensorless Control Performance for Rotating Carrier Signal Injection

The high-frequency rotating signal injection approach is applied to the single and dual three-phase prototype PMSMs. The position-dependant negative carrier current response is employed to detect the information of rotor position. A high-frequency voltage with amplitude of 8 V and carrier frequency of 550Hz is injected in the $\alpha\beta$ stationary reference frame, and the sensorless control performance employing the negative carrier current response is investigated under steady-state and dynamic conditions.

3.5.1. Estimation of Rotor Position in Steady and Dynamic States

A. Sensorless Control Performance for Single Three-Phase PMSM

With a constant speed at 30 rpm and *q*-axis current of about 2 A, the steady-state performances of rotor position estimation without and with compensation of cross-saturation effect are illustrated in Fig.3.26 and Fig.3.27, respectively, together with the estimation error. A good position tracking performance of the estimated rotor position is observed when considering the compensation of cross-saturation effect. Moreover, the dynamic performance is shown in Fig. 3.28, where the rotor speed response is shown in Fig. 3.28 (a), the q-axis current is shown in Fig. 3.28 (b), and the rotor position estimation performance under speed step change (0-30-60rpm) is depicted in Fig. 3.28 (c). Large oscillation in the estimation error exists due to the machine multiple saliencies effect as reported in [XU15].

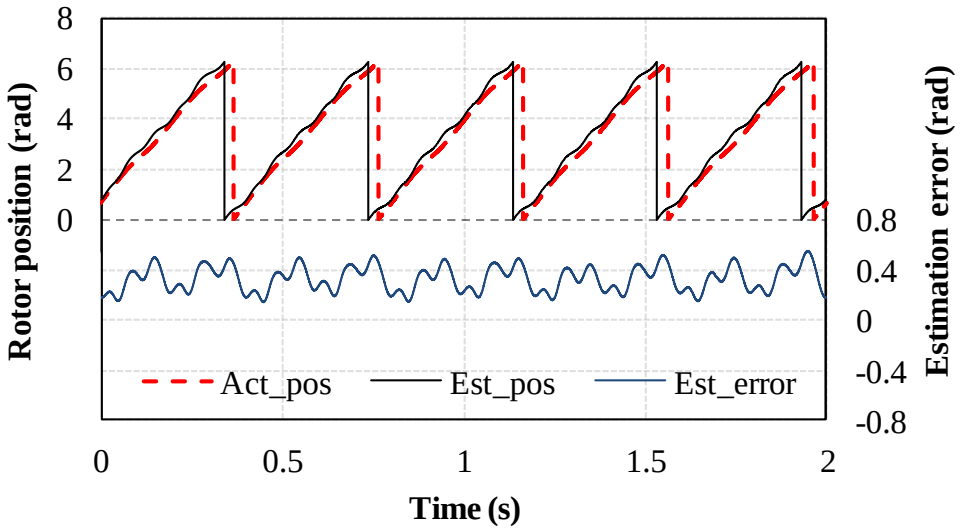

Fig. 3.26. Steady-state performance without cross-saturation compensation, I_q=2A, 30 rpm.

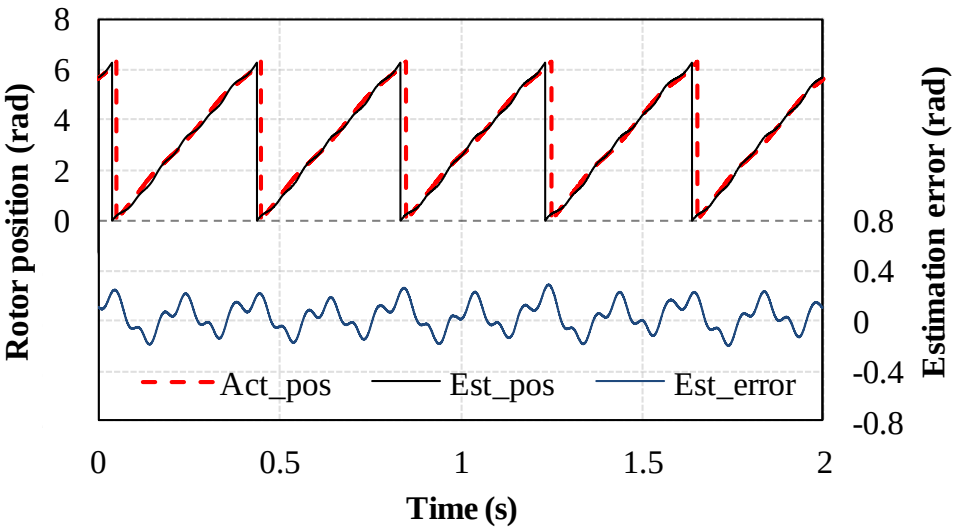

Fig. 3.27. Steady-state performance with cross-saturation compensation, I_q=2A, 30 rpm.

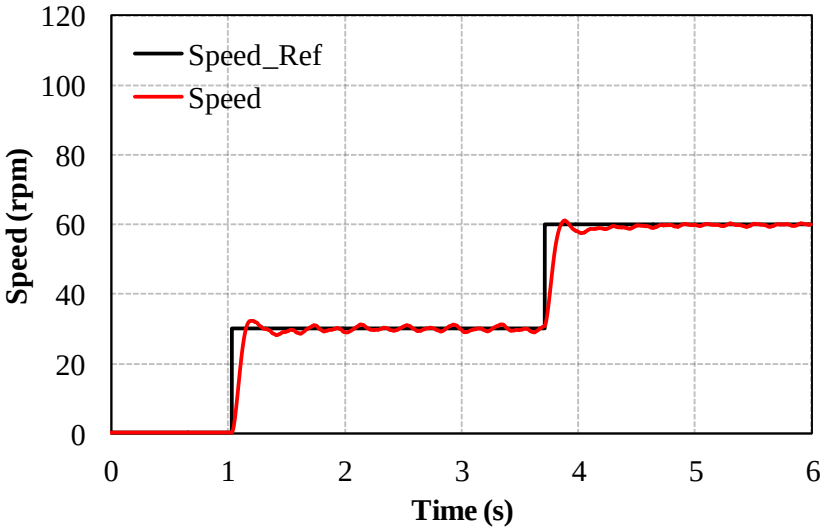

(a) Reference speed and actual rotor speed

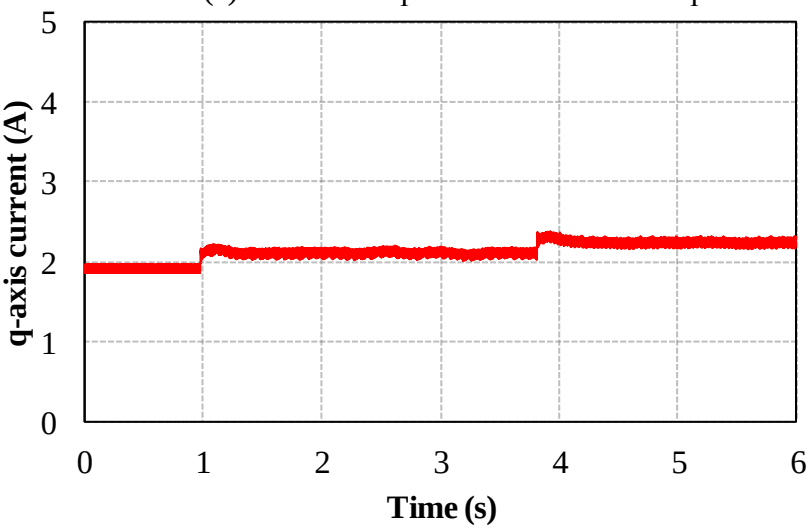

(b) q-axis current

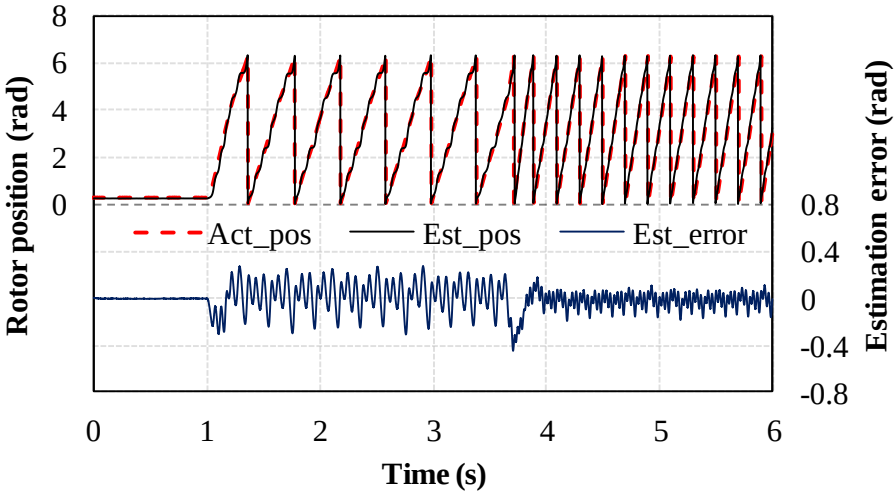

(c) Rotor position estimation performance

Fig. 3.28. Dynamic performance under step change in rotor speed, I_q=2A, 0-30-60rpm.

Additionally, the peak-to-peak estimation error at 30 rpm and q-axis current of 2 A for the rotating carrier signal injection method to demonstrate the sensitivity of the rotor position estimation accuracy to different frequency injections is illustrated in Fig. 3.29. It can be seen that the estimation error for the rotating carrier signal injection method is more sensitive to the carrier frequency since the signal processing introduces phase shifts to the saliency position [XU15].

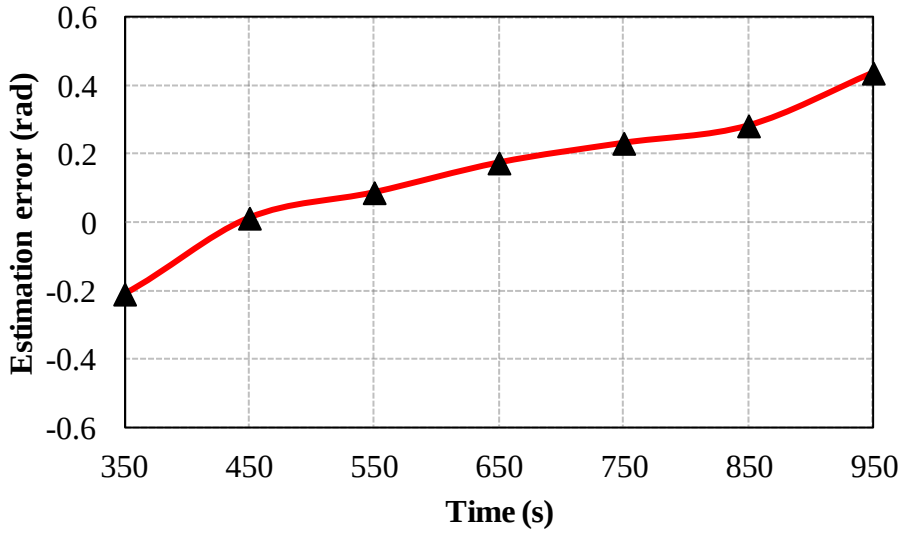

Fig. 3.29. Peak-to-peak position estimation error with different frequency injections, I_q=2A, 30 rpm.

B. Sensorless Control Performance for Dual Three-Phase PMSM

The rotating carrier signal injection method is extended to dual three-phase machine, and the sensorless control performances under steady-state and dynamic conditions are carried out for double *dq* model, and VSD model.

1. Double *dq* Model

With the aid of the double *dq* model, injection of two independent high-frequency rotating voltage signals with amplitude of 8 V and carrier frequency of 550Hz are implemented into both stator winding sets. Then, the performances of rotor position estimation without/with cross-saturation effect compensation under steady-state condition are demonstrated in Fig.3.30 and Fig.3.31, respectively. Furthermore, when the rotor mechanical initial speed is zero and step change to 30rpm and then to 60rpm, the dynamic-state performance is shown in Fig. 3.32. For both the steady-state and dynamic conditions, a good position tracking can be obtained with considering the cross-saturation effect compensation.

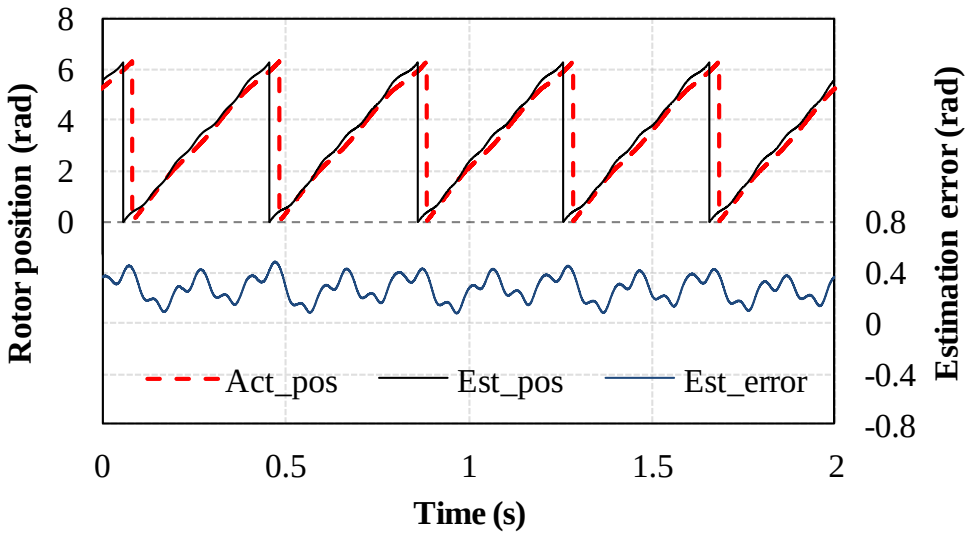

Fig. 3.30. Steady-state performance without cross-saturation compensation, I_q=2A, 30 rpm.

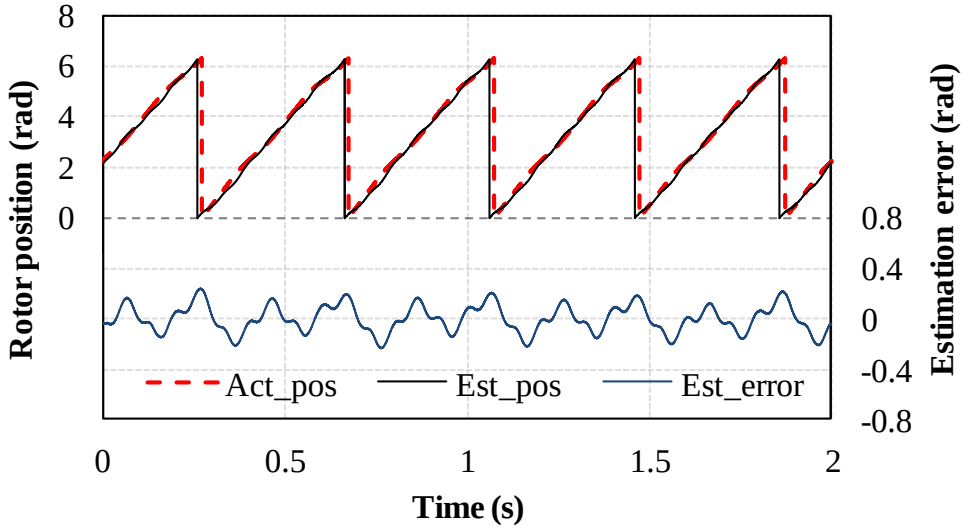

Fig. 3.31. Steady-state performance with cross-saturation compensation, I_q=2A, 30 rpm.

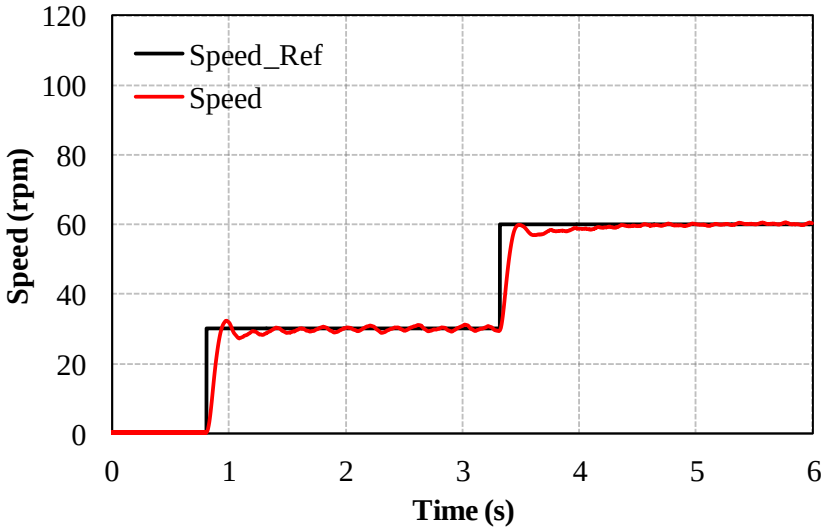

(a) Reference speed and actual rotor speed

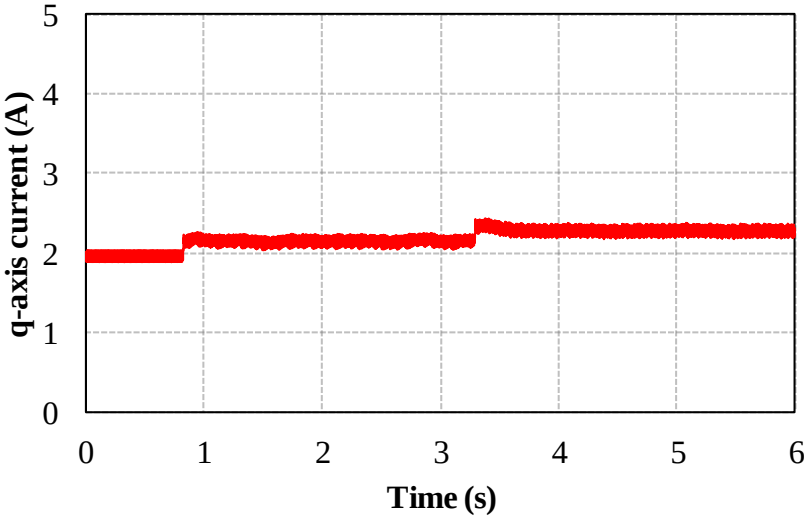

(b) q-axis current

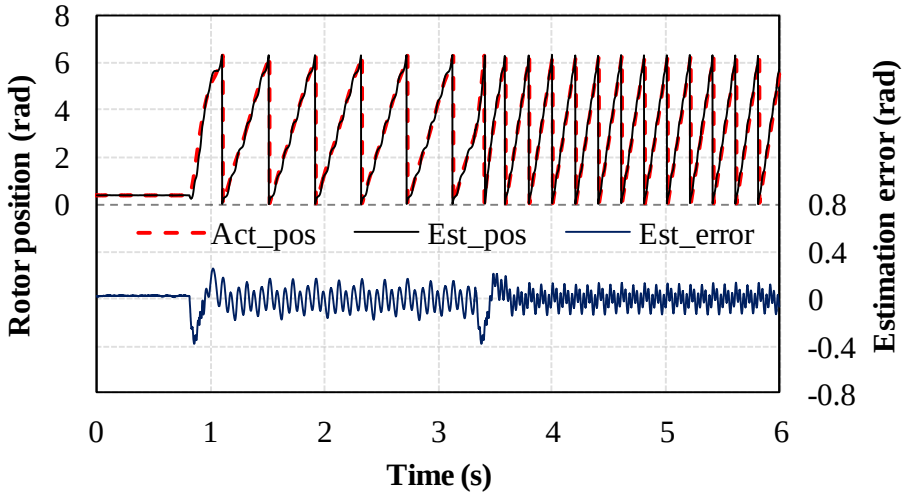

(c) Rotor position estimation performance

Fig. 3.32. Dynamic performance under step change in rotor speed, I_q=2A, 0-30-60rpm.

2. Vector Space Decomposition (VSD)

For VSD model, the rotating carrier voltage signal with amplitude of 8 V and carrier frequency of 550Hz is injected into $\alpha\beta$-subspace. At the steady-state condition, the comparison of the actual and estimated rotor position with compensation of cross-saturation is illustrated in Fig. 3.33 together with position estimation error. Then, the dynamic sensorless control performance is shown in Fig. 3.34, where the rotor speed reference is given as 0-30-60 rpm. It is worth noting that the estimation error oscillation is decreased when the vector space decomposition modelling approach is employed due to the mutual decoupling in this approach. From Fig. 3.34, an outstanding dynamic performance with fast transient can be observed. However, the peak-to-peak estimation error with different frequency injections is still sensitive to carrier frequency injections compared with the pulsating carrier signal injection method employing VSD approach, Fig. 35. This is due to the phase shifts to the saliency position introduced in the signal processing.

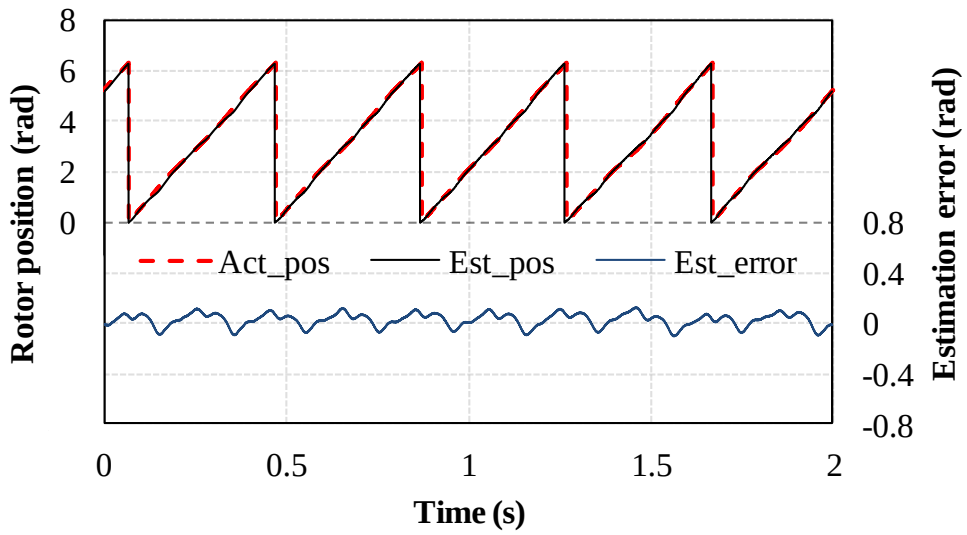

Fig. 3.33. Steady-state performance with cross-saturation compensation, I_q=2A, 30 rpm.

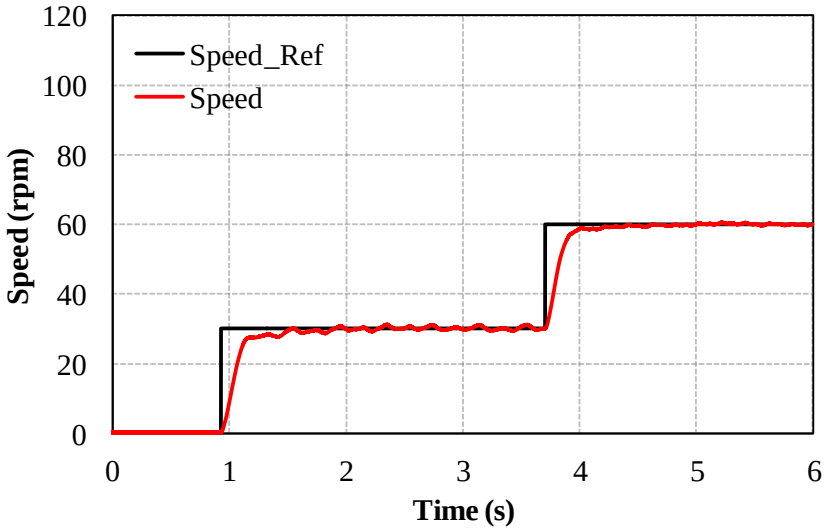

(a) Reference speed and actual rotor speed

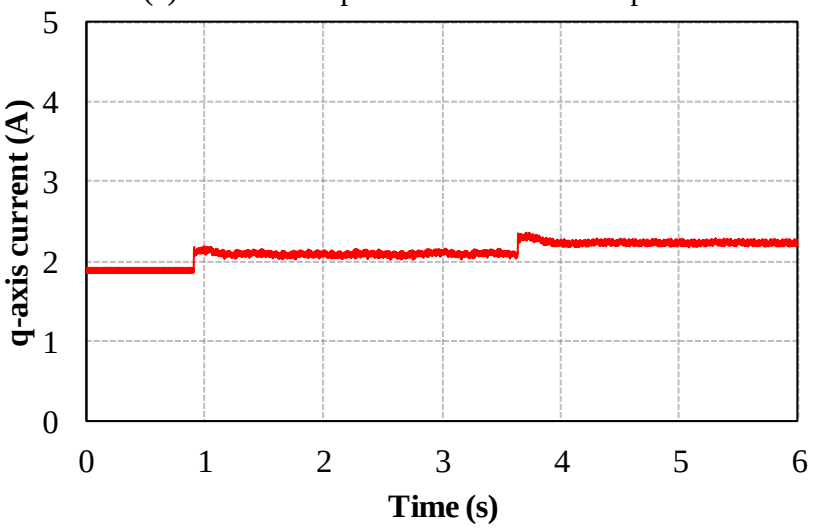

(b) q-axis current

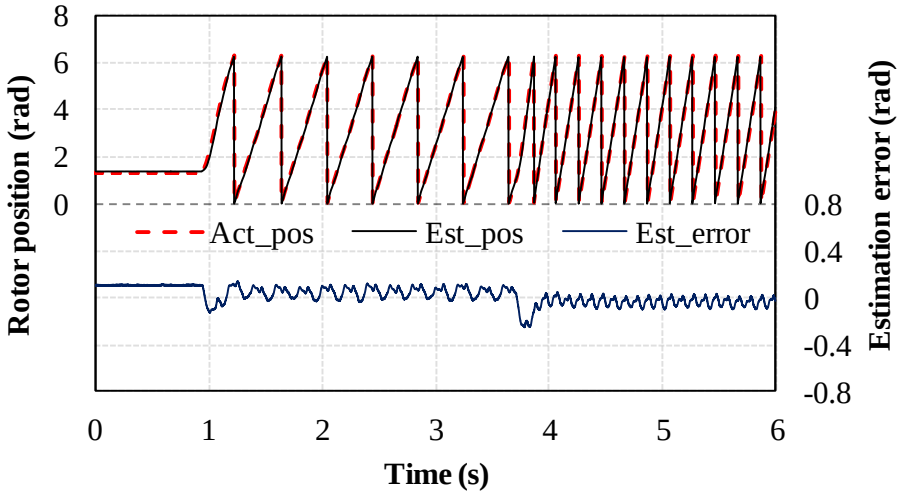

(c) Rotor position estimation performance

Fig. 3.34. Dynamic performance under step change in rotor speed, I_q=2A, 0-30-60rpm.

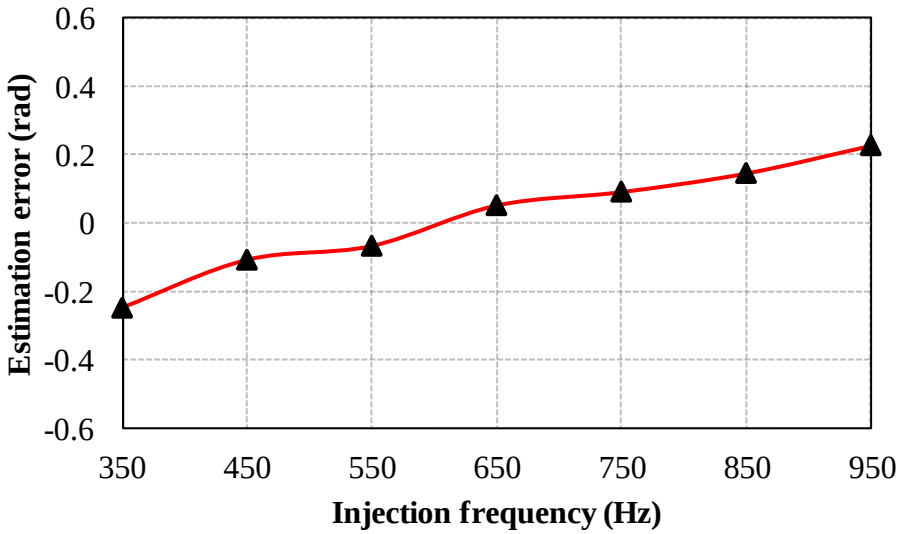

Fig. 3.35. Peak-to-peak position estimation error with different frequency injections, I_q=2A, 30 rpm.

3.6. Comparison of Sensorless Control Techniques Based on Carrier Signal Injection

The classical sensorless control strategies based on high-frequency carrier signals injections, i.e. pulsating injection, and rotating injection are applied to single and dual three-phase PMSMs to investigate the sensorless control performance under steady-state and dynamic conditions, and the performances of both techniques for single and dual three-phase PMSMs are summarized in Table 3.1.

TABLE 3.1

Comparison of Sensorless Control Methods Based on Carrier Signals Injections for Single and Dual Three-Phase PMSMs

	Pulsating (3-phase PMSM)	Rotating (3-phase PMSM)	Pulsating (DTP-PMSM, dq Model)	Pulsating (DTP-PMSM, VSD)	Rotating (DTP-PMSM, dq Model)	Rotating (DTP-PMSM, VSD)
Reference frame	Estimated synchronous	Stationary	Two estimated synchronous	Estimated synchronous	Two stationary	Stationary
Carrier voltage injec.	Pulsating carrier voltage	Rotating carrier voltage	Two independent pulsating carrier voltages	Pulsating carrier voltage	Two independent rotating carrier voltages	Rotating carrier voltage
Carrier current	Amplitude-modulated	Phase-modulated	Amplitude-modulated	Amplitude-modulated	Phase-modulated	Phase-modulated
Cross-saturation angle	$-\theta_m / 2$	$-\theta_m / 2$	$-\theta_m / 2$	$-\theta_m / 2$	$-\theta_m / 2$	$-\theta_m / 2$
Oscillation error	Medium	Medium	Medium	Low	Medium	Low
Load effect	Sensitive	Sensitive	Sensitive	Sensitive	Sensitive	Sensitive
Steady-state performance	Good	Medium	Good	Very Good	Medium	Very Good
Dynamic performance	Good	Medium	Good	Very Good	Medium	Very Good

3.7. Summary

This chapter discusses in details the commonly used conventional sensorless control strategies based on high-frequency carrier signals injections, i.e. pulsating high-frequency carrier voltage signal injection into the estimated synchronous rotating reference frame, and rotating high-frequency carrier voltage signal injection into the stationary reference frame. These techniques are applied to single and dual three-phase PMSMs to investigate the sensorless control performance under steady-state and dynamic conditions.

Firstly, the machine saliency level variation with the load for the test machine is measured experimentally, and it has been found that the saliency level is suitable for sensorless control techniques based on high-frequency carrier signals injections. Furthermore, the influence of the cross-saturation on the estimation of rotor position is analysed.

In terms of the accuracy rotor position estimation for both single and dual three-phase PMSMs, it has been concluded that the oscillation on the rotor position estimation error for dual three-phase PMSM employing VSD modelling approach is significantly reduced for both pulsation and rotating injections compared to that of single three-phase PMSM and dual three-phase PMSM employing double *dq* modelling approach. This is due to the mutual coupling between the two winding sets being eliminated in VSD approach.

It is worth mentioning that the peak-to-peak estimation error for the pulsating injection is less sensitive to the carrier frequency compared to that of rotating injection since the pulsating injection is not affected by the phase shifts introduced in the signal processing.

The rotor position estimation for the high-frequency carrier signal injection based sensorless control methods generally depend on the carrier signal response, i.e. carrier current response or zero-sequence carrier voltage response. In this chapter, the performances of the rotor position estimation for both injection methods are investigated for single and dual three-phase PMSMs based on the carrier current response. On the other hand, the performances of the rotor position estimation based on the zero-sequence carrier voltage will be investigated in the following chapters, i.e. Chapters 4 and 5.

CHAPTER 4

IMPROVED ROTOR POSITION ESTIMATION BY PULSATING CARRIER SIGNAL INJECTION UTILIZING ZERO-SEQUENCE CARRIER VOLTAGE FOR DTP-PMSM

4.1. Introduction

Generally, the carrier signal injection based sensorless control methods inject either high frequency voltage or current signals (normally voltage) into the fundamental excitation of the machine, and utilize the corresponding signals, i.e. carrier current response or zero-sequence carrier voltage, to extract the rotor position information. The sensorless control methods of high-frequency carrier signal injections introduced in Chapter 3 utilize the carrier current response to extract the rotor position information. In this chapter, the zero-sequence carrier voltage is utilized based on pulsating high-frequency injection strategy to estimate the rotor position. In [GAR07]-[BRI04], it has been demonstrated that both carrier current signal and zero-sequence carrier voltage signal can be used to obtain the rotor position for rotating voltage carrier signal injection based sensorless control strategy. Furthermore, the zero-sequence carrier voltage for pulsating carrier signal injection can also be used to extract the rotor position information [XU15]-[XU16]. Compared to the carrier current signal, the zero-sequence carrier voltage signal has the advantage of lower total harmonic distortion (THD), and less sensitivity to the distortion of injected carrier voltage caused by the current regulator, PWM strategy, and inverter nonlinearity [GAR07]. Therefore, by employing the zero-sequence carrier voltage signal, significant enhancement of the system bandwidth and the position estimation accuracy can be achieved, which contributes to the improvement of stability of system [GAR07].

In literature, the zero-sequence carrier voltage sensing methods for single three-phase machines based on both rotating and pulsating carrier signal injection have been studied in [GAR07], [BRI04], [BRI05], [CON00], [CON06], and [XU15]-[XU16]. However, the pulsating carrier signal injection utilizing zero-sequence voltage method has demonstrated that the position estimation performance is degraded with large oscillation in the estimation error. These oscillations occur due to the large undesirable harmonic components in carrier responses, i.e. the 6^{th} harmonic, which is caused by multiple saliencies including primary saliency [XU15]-[XU16],

and [REI08]. Such an issue can be solved by employing a look-up table based multiple saliency decoupling compensation method [BRI05]. However, the implementation of this method takes memory of the controller and requires time-consuming offline measurements. Additionally, a nonlinear adaptive model based on the neural network is introduced for multiple saliency decoupling compensation [REI08], but it requires intensive measurements and has complex structure.

The aforementioned problem can also be found on the DTP-PMSM when the pulsating carrier signal injection utilizing zero-sequence voltage method is employed. Fortunately, DTP-PMSM with two isolated neutral points has the merit of having additional degrees of freedom with two independent high frequency injection into the two stator winding sets. The phase angle between the two injected high frequency signals can be changed, which permits the possibility of solving such an issue. Thus, the aforementioned harmonic components can be potentially suppressed in DTP-PMSM drives by a modified pulsating injection with zero-sequence voltage method in which an optimum phase shift between the two injected high frequency carrier signals is applied. This is investigated in this chapter.

In this chapter, the pulsating carrier signal injection with zero-sequence voltage method is firstly utilized for position estimation of a single three-phase PMSM to show the influence of the undesirable 6^{th} harmonic component in carrier response which has been demonstrated in [XU15], [XU16]. To solve the same issue which occurs in DTP-PMSM drives, an improved sensorless control method of pulsating injection using zero-sequence carrier voltage is proposed. An optimum phase shift between two injected high frequency carrier signals is applied to suppress the undesirable harmonic components, and then the position estimation accuracy can be enhanced. A new measurement method using only one voltage sensor placed between the two isolated neutral points is also proposed, which simplifies the measurement of zero-sequence voltage. The effectiveness of proposed method will be confirmed by several experiments implemented on dSPACE platform using the prototype DTP-PMSM.

4.2. Pulsating Signal Injection Using Zero-Sequence Voltage for Single Three-Phase PMSM

Carrier-signal-based sensorless methods inject a high-frequency excitation signal, normally voltage, which interacts with the machine saliencies to produce specific frequency components in measurable electrical variables such as carrier current response or zero-sequence carrier voltage [BRI04]. Then, such measurable variables can be used to estimate the rotor position. For zero-sequence carrier voltage method, when a balanced and symmetrical high-frequency carrier-signal voltage is applied to the stator windings, the zero-sequence carrier voltage is produced [BRI05]. It can be utilized for rotor position estimation. The use of zero-sequence carrier voltage has several advantages. Its magnitude does not depend on the frequency of the injected carrier signal which enables the use of higher carrier-signal frequencies [BRI05] and [XU16], reducing the associated torque ripple and acoustic noise. Moreover, the harmonics in the carrier-signal voltage due to the non-ideal behavior of the inverter can be easily decoupled from the zero-sequence carrier voltage to increase the robustness and the position estimation accuracy [BRI04]-[BRI05].

4.2.1. Modelling of Single Three-Phase PMSM

To illustrate the sensorless control performance of pulsating carrier signal injection employing zero-sequence voltage for both single and dual three-phase PMSMs, the sensorless performance of single three-phase PMSM is firstly investigated to highlight the problems of oscillating position estimation error.

In general, the modeling of the high-frequency injection techniques utilizing zero-sequence carrier voltage is performed in the natural reference frame [BRI04] and [BRI05]. However, in [BRI04] and [BRI05], the phase mutual-inductance has not been considered in the model. Thus, the phase mutual-inductance is considered in this chapter for both single, [XU16], and dual three-phase PMSMs models.

Under the assumptions that back-EMF and resistive voltage drop are negligible and the PM machine can be seen as pure inductive load at low speed and high carrier frequency, the voltage equations for single three-phase PMSM can be expressed as (4.1) [BRI05] [XU16].

$$\begin{bmatrix} v_{an1} \\ v_{bn1} \\ v_{cn1} \end{bmatrix} = \begin{bmatrix} L_{aa} & M_{ab} & M_{ac} \\ M_{ba} & L_{bb} & M_{bc} \\ M_{ca} & M_{cb} & L_{cc} \end{bmatrix} \begin{bmatrix} di_a / dt \\ di_b / dt \\ di_c / dt \end{bmatrix} \tag{4.1}$$

where v_{an1}, v_{bn1}, and v_{cn1}, and i_a, i_b, and i_c, are phase voltages and currents, respectively, whileL_{aa}, L_{bb}, L_{cc}, M_{ab} (M_{ba}), M_{ac} (M_{ca}), and M_{bc} (M_{cb}) denote the three phase incremental self- and mutual-inductances, respectively.

Generally, the three-phase inductances can be expressed as

$$\begin{cases} L_{aa} = L_0 - L_2 \cos(2\theta_r) \\ L_{bb} = L_0 - L_2 \cos(2\theta_r + 2\pi/3) \\ L_{cc} = L_0 - L_2 \cos(2\theta_r - 2\pi/3) \end{cases} \tag{4.2}$$

$$\begin{cases} M_{ab} = M_{ba} = M_0 - M_2 \cos(2\theta_r - 2\pi/3) \\ M_{bc} = M_{cb} = M_0 - M_2 \cos(2\theta_r) \\ M_{ca} = M_{ac} = M_0 - M_2 \cos(2\theta_r + 2\pi/3) \end{cases}$$

where L_0, M_0, L_2, and M_2 are referred as the amplitudes of dc and second harmonic of phase self- and mutual-inductances, respectively, while θ_r is the actual rotor position.

When the pulsating carrier signal is injected into the estimated d-q-axis synchronous reference frame as two superposition rotating carrier voltage with opposite direction, the injected voltages of three-phases are given as

$$v_a = V_c \cos(\omega_c t)\cos(\theta_r^e) \tag{4.3}$$

$$v_b = V_c \cos(\omega_c t)\cos(\theta_r^e - 2\pi/3) \tag{4.4}$$

$$v_c = V_c \cos(\omega_c t)\cos(\theta_r^e + 2\pi/3) \tag{4.5}$$

where θ_r^e represents the estimated rotor position, while V_c and ω_c are the carrier voltage and frequency, respectively. The pulsating injection in the estimated reference frame is depicted in Fig. 4.1.

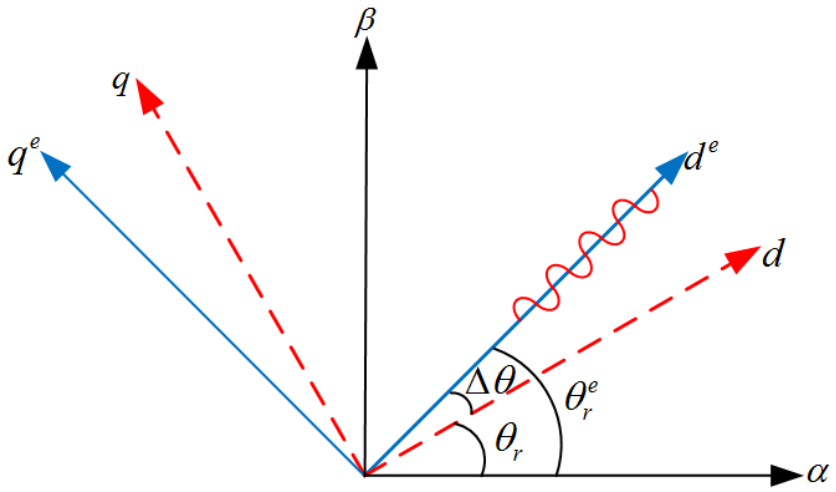

Fig. 4.1. High frequency d-axis pulsating voltage signal injection.

Then, the resultant zero-sequence carrier voltage for single three-phase PMSM can be expressed as [XU16]

$$\begin{aligned} v_{0sn1} = & \frac{V_C\left(L_0 - M_0\right)\left(L_2 - M_2\right)}{2L_0^{\,2} + 2M_0^{\,2} - 2M_2^{\,2} - 4L_0M_0 - 2L_2M_2 - \dfrac{L_2^{\,2}}{2}} \\ & \times \cos(\omega_C t)\cos(2\theta_r + \theta_r^e) \\ & - \frac{V_C}{2}\frac{\left(L_2 - 2M_2\right)\left(L_2 - M_2\right)}{2L_0^{\,2} + 2M_0^{\,2} - 2M_2^{\,2} - 4L_0M_0 - 2L_2M_2 - \dfrac{L_2^{\,2}}{2}} \\ & \times \cos(\omega_C t)\cos(-4\theta_r + \theta_r^e) \end{aligned} \tag{4.6}$$

For the prototype PM machine, the incremental self- and mutual-inductances can be obtained by finite element (FE) simulation as illustrated in Fig. 4.2 together with the spectrum of the self-inductance.

From Fig. 4.2, since $(L_0 - M_0)$ is much larger than $(L_2 - 2M_2)/2$, the second term of zero-sequence carrier voltage in (4.6) can be neglected, and the first term can be employed for rotor position information as (4.7) [BRI05], [XU16].

$$v_{0sn1} = \frac{V_C (L_0 - M_0)(L_2 - M_2)}{2L_0^{\,2} + 2M_0^{\,2} - 2M_2^{\,2} - 4L_0M_0 - 2L_2M_2 - \frac{L_2^{\,2}}{2}} \times \cos(\omega_C t)\cos(2\theta_r + \theta_r^e)$$

$$= \frac{V_C}{2} \frac{(L_0 - M_0)(L_2 - M_2)}{2L_0^{\,2} + 2M_0^{\,2} - 2M_2^{\,2} - 4L_0M_0 - 2L_2M_2 - \frac{L_2^{\,2}}{2}} \times \left[\cos(\omega_C t + 2\theta_r + \theta_r^e) + \cos(\omega_C t - 2\theta_r - \theta_r^e)\right] \quad (4.7)$$

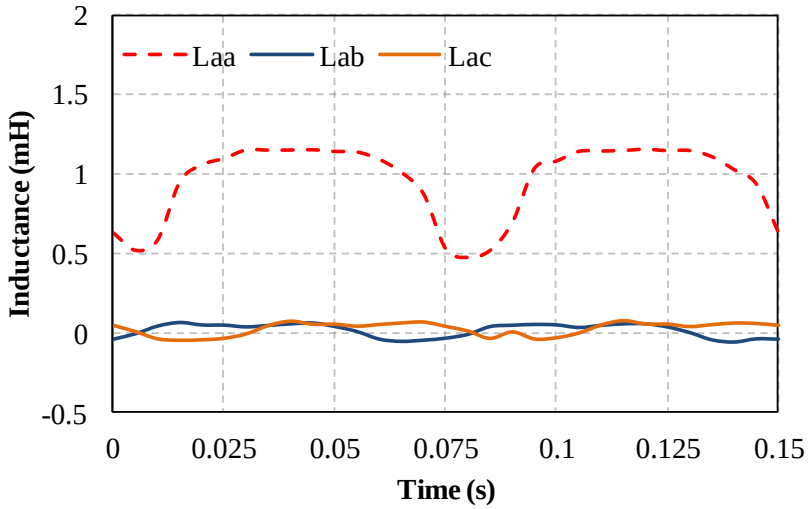

(a) Incremental self- and mutual-inductances

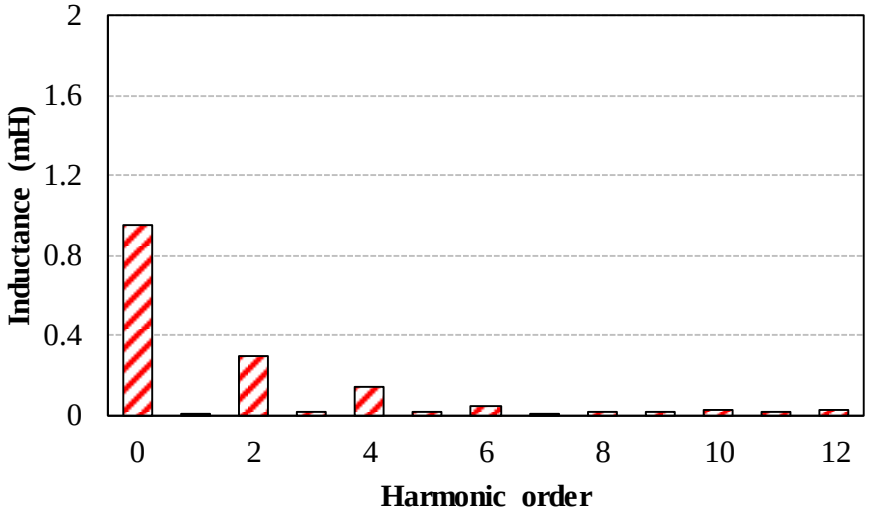

(b) Spectrum of self-inductance

Fig. 4.2. Incremental self- and mutual-inductances of phase A by FE simulation, and spectrum of self-inductance.

The zero-sequence voltage in (4.7) includes two high frequency components at $f_c \pm 3f_e$, one can be used for rotor position estimation (f_c+3f_e), and the second component, i.e. (f_c-3f_e), would negatively affect the estimation performance due to its large amplitude, as will be shown experimentally.

The demodulation signal of the zero-sequence carrier voltage is obtained by (4.8), and the schematic diagram of demodulation process of corresponding signal is illustrated in Fig. 4.3.

$$\begin{aligned} V_{0sn1} &= LPF\left(v_{0sn1}(4\sin(\omega_c t - 3\theta_r^e))\right) \\ &= \frac{V_C}{2}\frac{(L_0 - M_0)(L_2 - M_2)}{2L_0^{\,2} + 2M_0^{\,2} - 2M_2^{\,2} - 4L_0M_0 - 2L_2M_2 - \frac{L_2^{\,2}}{2}} \\ &\quad \times\left(\sin(2\Delta\theta) + \sin(2\theta_e + 4\theta_r^e)\right) \end{aligned} \tag{4.8}$$

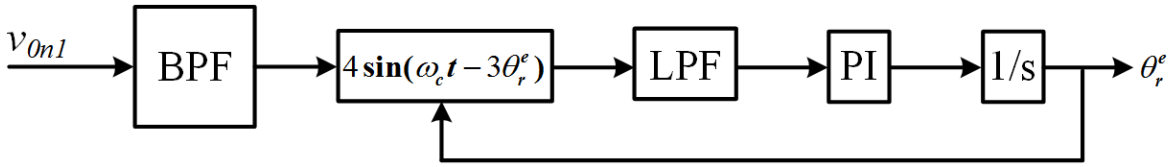

Fig. 4.3. Block diagram of zero-sequence carrier signal process with pulsating injection.

It can be seen from (4.8) that, under the steady-state condition, i.e. $\theta_r \approx \theta_r^e$, large amplitude of the undesirable 6th harmonic component exists, which significantly deteriorates the sensorless control performance [XU16].

4.2.2. Analysis of Zero-Sequence Carrier voltage Response

A high frequency pulsating voltage signal (V_c=8V, f_c=500Hz) is injected into the estimated reference frame with 50% of the full load, and the rotor position is estimated from the measured zero-sequence carrier voltage. The phase current is shown in Fig. 4.4. It exhibits large distortions due to large amplitude of undesirable component in the estimation error. Fig. 4.5 shows the spectrum of the measured zero-sequence carrier voltage for the single three-phase PMSM, (f_e=2.5Hz). The zero-sequence carrier voltage frequency components are essentially at $f_c \pm 3f_e$, i.e. the 197th and the 203rd. The component at f_c+3f_e can be used for position estimation. In contrast, the high frequency component at f_c-3f_e can affect the estimation performance because of its large amplitude. Such oscillation can considerably deteriorate the position estimation and then lead to

unstable sensorless control performance.

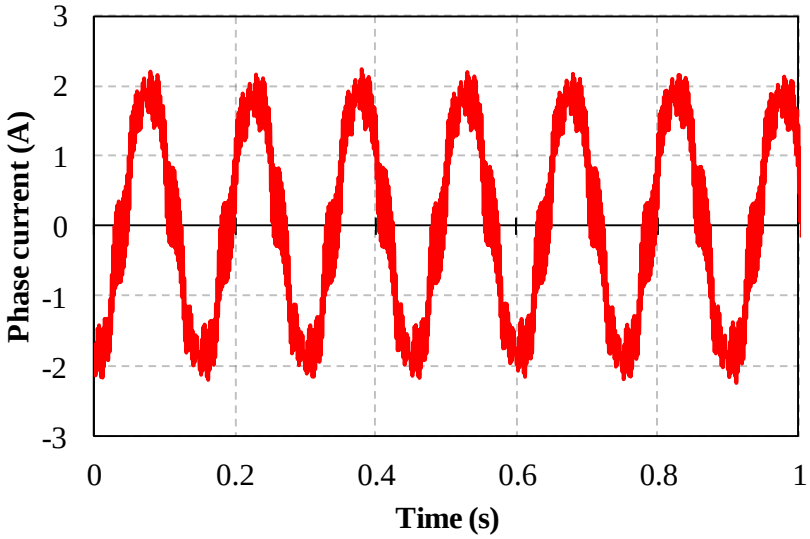

Fig. 4.4. Phase current, f_c=500Hz, V_c=8V, 30rpm.

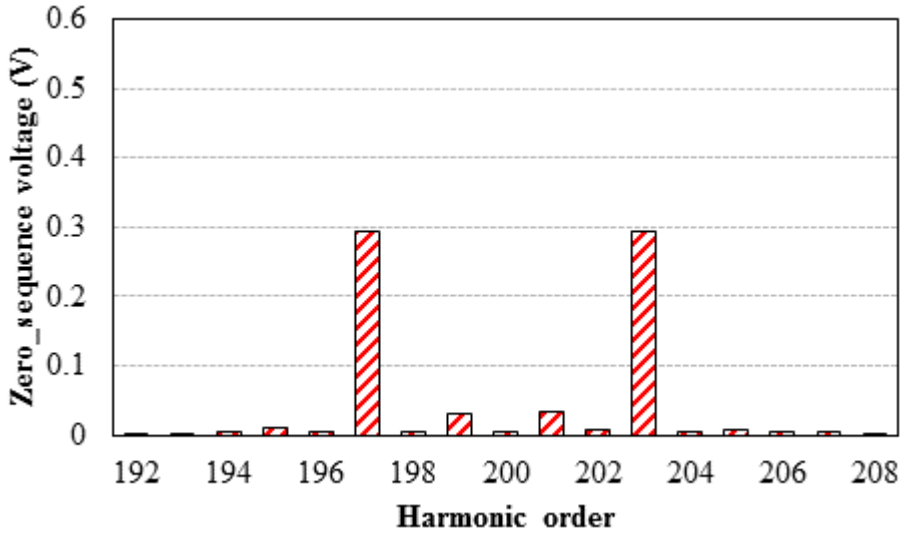

Fig. 4.5. Spectrum of measured zero-sequence carrier voltage, three-phase PMSM, 30rpm.

4.2.3. Performance of Rotor Position Estimation

The measured zero-sequence carrier voltage is then utilized for rotor position estimation. Comparison of the estimated and the actual rotor positions is shown in Fig. 4.6, together with the position estimation error. From Fig. 4.6, it is obvious that large oscillation in the position estimation error occurs due to the large amplitude of undesirable 6th harmonic component at

steady-state condition. Such oscillation can considerably deteriorate the position estimation and then lead to unstable sensorless control performance.

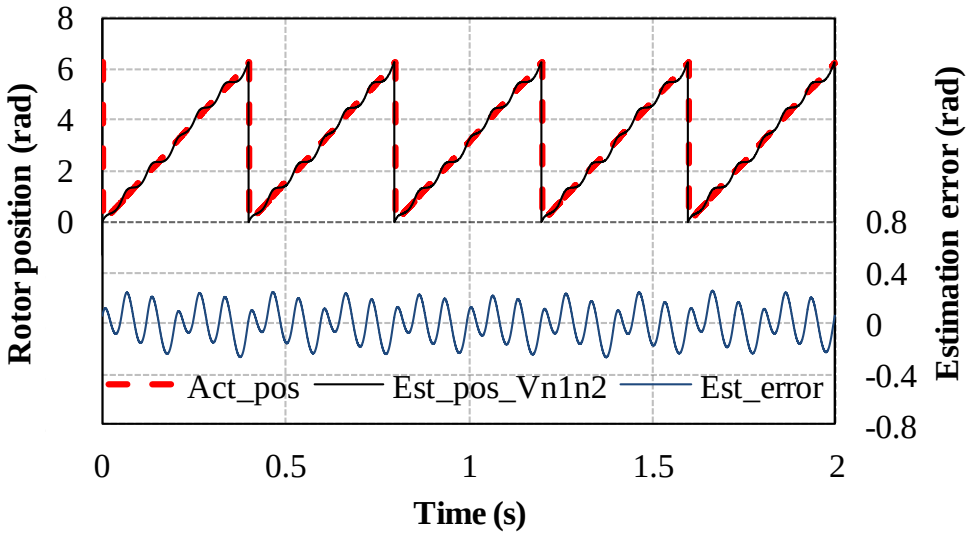

Fig. 4.6. Rotor position estimation in steady-state of three-phase PMSM, 30rpm.

4.3. Proposed Pulsating Signal Injection Using Zero-Sequence Voltage for Dual Three-Phase (DTP) PMSM

As mentioned above, the pulsating carrier signal injection with zero-sequence voltage based sensorless control method for single three-phase exhibits large oscillation in the position estimation error due to large amplitude of the undesirable 6^{th} harmonic component in zero-sequence carrier voltage signal. Fortunately, for DTP-PMSM, it is possible to suppress such harmonic components by employing an optimum phase shift between two injected signals, due to its additional degree of freedom with high frequency injection into two independent stator winding sets. Hence, the rotor position estimation can be improved accordingly as will be analyzed, which is the main target of this chapter.

4.3.1. New Zero-Sequence Carrier Voltage Measurement Method

Usually, the resultant zero-sequence carrier voltage is measured based on one of the most two common measurement methods, i.e. measurement using phase-to-neutral-voltages as shown in Fig. 4.7 [BRI04], or measurement using the auxiliary resistor network [BRI05], Fig. 4.8.

For the first method in the case of DTP-PMSM, the three phase-to-neutral voltages of each winding set are measured individually. The advantage of this method is that the zero-sequence components presented in the phase voltages are automatically decoupled [BRI04]. Moreover, the measured zero-sequence voltage includes the components that are produced by the interaction between the machine saliency and the carrier signal excitation [BRI04]. However, it increases the cost of system since six voltage sensors are required. Alternatively, the second method has demonstrated an effective measurement of the zero-sequence voltage for single three-phase machine [BRI05]. The zero-sequence voltage can be measured by connecting a balanced three-phase resistor network in parallel with the motor terminals [BRI05]. For DTP-PMSM, two three-phase resistor networks are required, one for each winding set, which makes the measurement very complicated. Thus, this chapter proposes a new zero-sequence carrier voltage measurement, in which one voltage sensor is placed between the two isolated neutral points, i.e. v_{0sn1n2}, as shown in Fig. 4.9. This method can measure the zero-sequence carrier voltage response induced from the interaction between the high frequency signal excitation for both winding sets and the machine saliency. Compared to the aforementioned measurement methods, this method is simple in structure, and easy to implement. Hence, the zero-sequence carrier voltage signals presented hereafter are obtained by new measurement method.

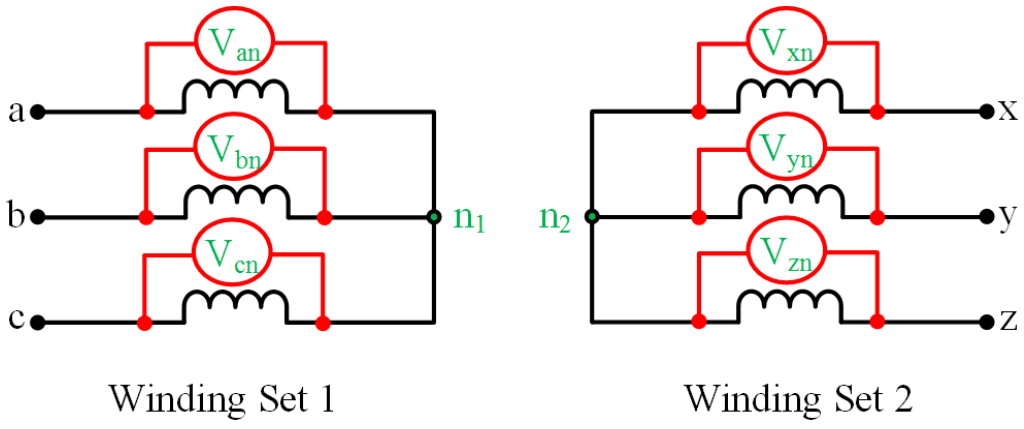

Fig. 4.7. Measurement of zero-sequence voltage using phase-to-neutral voltages.

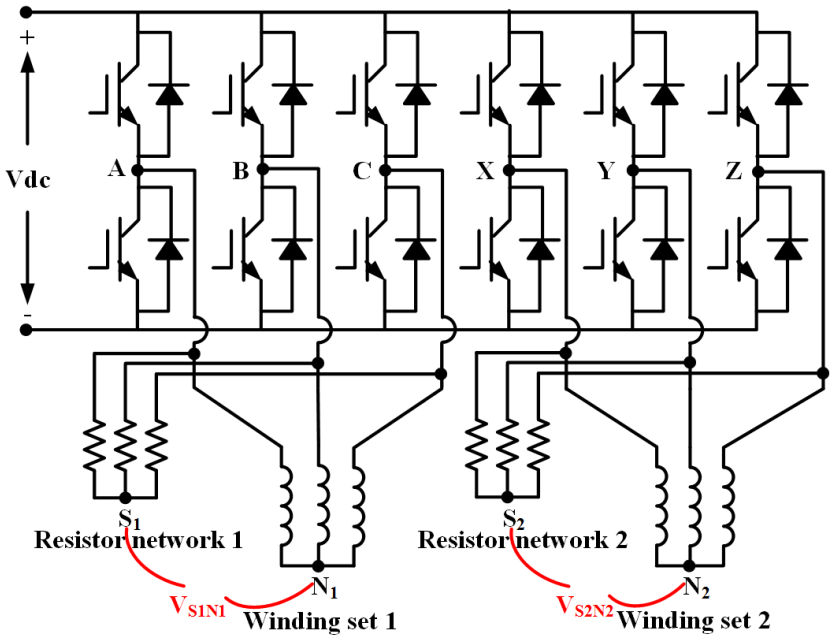

Fig. 4.8. Measurement of zero-sequence voltage using auxiliary resistor network.

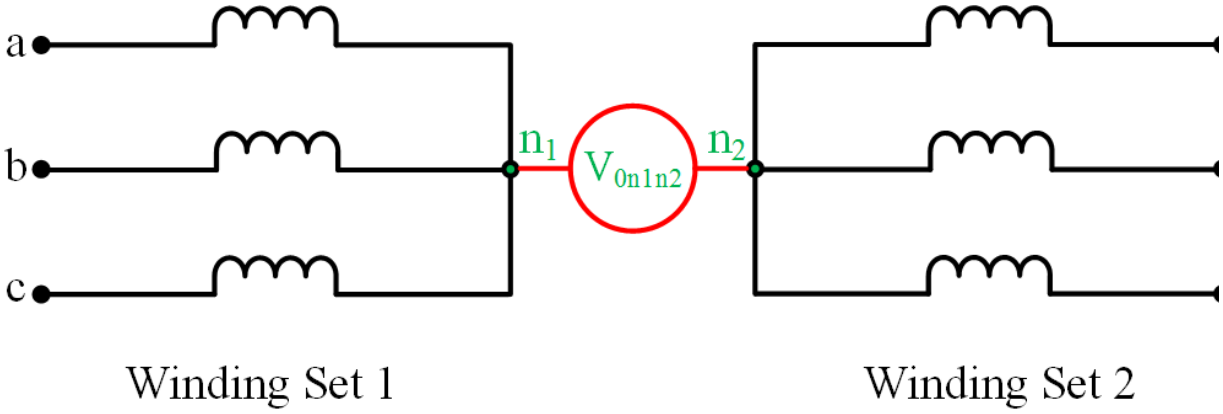

Fig. 4.9. New measurement method of zero-sequence voltage between two neutral points.

4.3.2. Modelling of Dual Three-Phase PMSM

For DTP-PMSM having two Y-connected winding sets with two isolated neutral points, the voltage equations for the first winding set are exactly the same as those of single three-phase PMSM (4.1), whilst the voltage equations for the second winding set are expressed as

$$\begin{bmatrix} v_{xn2} \\ v_{yn2} \\ v_{zn2} \end{bmatrix} = \begin{bmatrix} L_{xx} & M_{xy} & M_{xz} \\ M_{yx} & L_{yy} & M_{yz} \\ M_{zx} & M_{zy} & L_{zz} \end{bmatrix} \begin{bmatrix} di_x / dt \\ di_y / dt \\ di_z / dt \end{bmatrix} \tag{4.9}$$

The three-phase inductances of the second winding set can be expressed as

$$\begin{cases} L_{xx} = L_0 - L_2 \cos(2\theta_r - 2\pi/6) \\ L_{yy} = L_0 - L_2 \cos(2\theta_r - 10\pi/6) \\ L_{zz} = L_0 - L_2 \cos(2\theta_r + 6\pi/6) \end{cases} \tag{4.10}$$

$$\begin{cases} M_{xy} = M_{yx} = M_0 - M_2 \cos(2\theta_r + 6\pi/6) \\ M_{yz} = M_{zy} = M_0 - M_2 \cos(2\theta_r - 10\pi/6) \\ M_{zx} = M_{xz} = M_0 - M_2 \cos(2\theta_r - 2\pi/6) \end{cases}$$

where v_{xn2}, v_{yn2}, and v_{zn2}, and i_x, i_y, and i_z, are referred as phase voltages and currents of the second winding set, respectively. L_{xx}, L_{yy}, L_{zz}, M_{xy} (M_{yx}), M_{xz} (M_{zx}), and M_{yz} (M_{zy}) are the three phase incremental self- and mutual-inductances of the second winding set, respectively.

Assuming that two independent high-frequency carrier signals are injected into the estimated synchronous reference frames for both winding sets, the injected voltages of the first winding set are expressed as (4.3)-(4.5), and the expressions of the injected voltages of the second winding set are given by

$$v_x = V_c \cos(\omega_c t)\cos(\theta_r^e - \pi/6) \tag{4.11}$$

$$v_y = V_c \cos(\omega_c t)\cos(\theta_r^e - 5\pi/6) \tag{4.12}$$

$$v_z = V_c \cos(\omega_c t)\cos(\theta_r^e + 3\pi/6) \tag{4.13}$$

With (4.1)-(4.5) and (4.9)-(4.13), the resultant zero-sequence carrier voltages for both winding sets of DTP-PMSM, by neglecting the second term of zero-sequence voltage similar to the case of single three-phase PMSM, i.e. (4.7), can be obtained as

$$v_{0sn1} = \frac{V_C\left(L_0 - M_0\right)\left(L_2 - M_2\right)}{2L_0{}^2 + 2M_0{}^2 - 2M_2{}^2 - 4L_0M_0 - 2L_2M_2 - \frac{L_2{}^2}{2}} \times \cos(\omega_C t)\cos(2\theta_r + \theta_r^e) \tag{4.14}$$

$$v_{0sn2} = \frac{V_C\left(L_0 - M_0\right)\left(L_2 - M_2\right)}{2L_0{}^2 + 2M_0{}^2 - 2M_2{}^2 - 4L_0M_0 - 2L_2M_2 - \frac{L_2{}^2}{2}} \times \cos(\omega_C t)\cos(2\theta_r + \theta_r^e - 3\pi/6) \tag{4.15}$$

Thus, the resultant zero-sequence carrier voltage between the two isolated neutral points of DTP-PMSM can be given as

$$\begin{aligned} v_{0sn1n2} &= v_{0sn1} - v_{0sn2} \\ &= \frac{-\sqrt{2}\ V_C\left(L_0 - M_0\right)\left(L_2 - M_2\right)}{2L_0{}^2 + 2M_0{}^2 - 2M_2{}^2 - 4L_0M_0 - 2L_2M_2 - \frac{L_2{}^2}{2}} \\ &\quad \times \cos(\omega_C t)\cos(2\theta_r + \theta_r^e - 3\pi/4) \end{aligned} \tag{4.16}$$

Similar to the case of single three-phase, for simplicity, the corresponding demodulated zero-sequence carrier voltage, V_{0sn1n2}, is expressed as (4.17).

$$\begin{aligned} V_{0sn1n2} &= LPF\left(v_{0sn1n2}(4\sin(\omega_c t - 3\theta_r^e))\right) \\ &= \frac{-\sqrt{2}\ V_C\left(L_0 - M_0\right)\left(L_2 - M_2\right)}{2L_0{}^2 + 2M_0{}^2 - 2M_2{}^2 - 4L_0M_0 - 2L_2M_2 - \frac{L_2{}^2}{2}} \\ &\quad \times\left(\sin(2\Delta\theta - \frac{3\pi}{4}) + \sin(2\theta_r + 4\theta_r^e - \frac{3\pi}{4})\right) \end{aligned} \tag{4.17}$$

From (4.17), it can be seen that the 6th harmonic component with large amplitudes also exists under the steady-state condition just like the case of single three-phase PMSM, which deteriorates the position estimation performance significantly. Therefore, a modified method which fully utilizes the additional degrees of freedom in DTP-PMSM drives to improve the position estimation performance is required.

The expression of zero-sequence carrier voltage between the two isolated neutral points,

taking into account a phase shift in the injected signal of the second winding set, is given by

$$
\begin{aligned}
v_{0sn1n2\_h} &= v_{0s1} - v_{0s2} \\
v_{0sn1n2\_h} &= \left[\begin{array}{c} \dfrac{V_C \left(L_0 - M_0\right)\left(L_2 - M_2\right)}{2L_0{}^2 + 2M_0{}^2 - 2M_2{}^2 - 4L_0M_0 - 2L_2M_2 - \dfrac{L_2{}^2}{2}} \\ \times \cos(\omega_c \, \mathrm{t}) \cos(2\theta_r + \theta_r^e) \end{array} \right] \\
&\quad - \left[\begin{array}{c} \dfrac{V_C \left(L_0 - M_0\right)\left(L_2 - M_2\right)}{2L_0{}^2 + 2M_0{}^2 - 2M_2{}^2 - 4L_0M_0 - 2L_2M_2 - \dfrac{L_2{}^2}{2}} \\ \times \cos(\omega_c \, \mathrm{t} - \varphi) \cos(2\theta_r + \theta_r^e - \dfrac{3\pi}{6}) \end{array} \right] \\
&= -\frac{V_C \left(L_0 - M_0\right)\left(L_2 - M_2\right)}{2L_0{}^2 + 2M_0{}^2 - 2M_2{}^2 - 4L_0M_0 - 2L_2M_2 - \dfrac{L_2{}^2}{2}} \\
&\quad \times \left[\begin{array}{l} \sin(\omega_c t + 2\theta_r + \theta_r^e - \dfrac{\pi}{4} - \dfrac{\varphi}{2}) \sin(\dfrac{\pi}{4} + \dfrac{\varphi}{2}) \\ + \sin(\omega_c t - 2\theta_r - \theta_r^e + \dfrac{\pi}{4} - \dfrac{\varphi}{2}) \sin(-\dfrac{\pi}{4} + \dfrac{\varphi}{2}) \end{array} \right]
\end{aligned}
\tag{4.18}
$$

where φ is the phase shift between the two injected high frequency signals. From (4.18), it can be clearly seen that the zero-sequence voltage involves two high frequency components at $f_c \pm 3f_e$, and the high frequency components at $f_c - 3f_e$ can deteriorate the position estimation performance where undesirable 6th harmonic in the estimation error occur. In order to eliminate/suppress the undesirable 6th harmonic in the estimation error, an optimum phase shift is required. It is worth noting that when the phase shift between the two high frequency signals injected into the two sets of three-phase windings is $\varphi = \pi/2$, the second term, which causes large oscillation in the estimation error, can be eliminated as undesirable components at $f_c - 3f_e$ equal to zero. Meanwhile, the first term at high frequency of $f_c + 3f_e$ that is used for position estimations maximized. Therefore, with the optimum phase shift, $\pi/2$, the zero-sequence carrier voltage becomes (4.19).

$$
\begin{aligned}
v_{0sn1n2\_h} &= -\frac{V_C\left(L_0 - M_0\right)\left(L_2 - M_2\right)}{2L_0{}^2 + 2M_0{}^2 - 2M_2{}^2 - 4L_0M_0 - 2L_2M_2 - \frac{L_2{}^2}{2}} \\
&\quad \times \sin(\omega_c\ \mathrm{t} + 2\theta_r + \theta_r^e - \frac{\pi}{2}) \\
&= \frac{V_C\left(L_0 - M_0\right)\left(L_2 - M_2\right)}{2L_0{}^2 + 2M_0{}^2 - 2M_2{}^2 - 4L_0M_0 - 2L_2M_2 - \frac{L_2{}^2}{2}} \\
&\quad \times \cos(\omega_c\ \mathrm{t} + 2\theta_r + \theta_r^e)
\end{aligned}
\tag{4.19}
$$

From (4.19), it can be clearly seen that the zero-sequence carrier voltage expression is simplified with one term only when applying the optimum phase shift in the injected carrier signal of second winding set. Furthermore, the undesirable 6th harmonic component does not exist for the position tracking observer. Thus, it is expected that the improved pulsating injection with zero-sequence carrier voltage for DTP-PMSM can achieve high accuracy of rotor position estimation, as will be shown in the next subsections.

The demodulation process for the zero-sequence carrier voltage, by considering the optimum phase angle shift, v_{0sn1n2_h}, is given by (4.20), and the schematic diagram of signal process is similar to that in Fig. 4.3.

$$
\begin{aligned}
V_{0sn1n2\_h} &= LPF\left(v_{0sn1n2}(4\sin(\omega_c t - 3\theta_r^e))\right) \\
&= \frac{V_C\left(L_0 - M_0\right)\left(L_2 - M_2\right)}{2L_0{}^2 + 2M_0{}^2 - 2M_2{}^2 - 4L_0M_0 - 2L_2M_2 - \frac{L_2{}^2}{2}} \sin(2\Delta\theta)
\end{aligned}
\tag{4.20}
$$

4.3.3. Experimental Results and Analysis for DTP-PMSM

The experimental test rig consists of a two three-phase voltage source inverter (VSI), a dSPACE (DS1005) digital controller, a DC power supply, a prototype dual three-phase (DTP) permanent magnet synchronous machine (PMSM), and coupled with a DC motor for loading. One voltage sensor as well as the access to the two isolated neutral points of dual three-phase machine are required to measure the zero-sequence carrier voltage. The overall sensorless control system is shown in Fig.4.10. Besides, the sampling frequency is set to10 kHz, while the DC-link voltage is 40V.

A high frequency pulsating voltage signal with an amplitude of V_c=8V, and carrier frequency of f_c=500Hz is injected into the estimated reference frames for both winding sets of DTP-PMSM independently with 50% of the full load to investigate the sensorless control performance of pulsating injection using zero-sequence voltage under steady-state and dynamic conditions. The phase currents without and with considering the optimum phase shift between the injected signals are illustrated in Fig. 4.11 and Fig. 4.12, respectively. It can be clearly seen that the phase current without optimum phase shift exhibits distortion compared to the phase current with the optimum phase shift. With optimum phase shift, the phase current becomes more sinusoidal with less distortions. Then, the rotor position is estimated from the measured zero-sequence carrier voltage. Moreover, the rotor speed during the steady-state condition set as 30 rpm (f_e=2.5Hz).

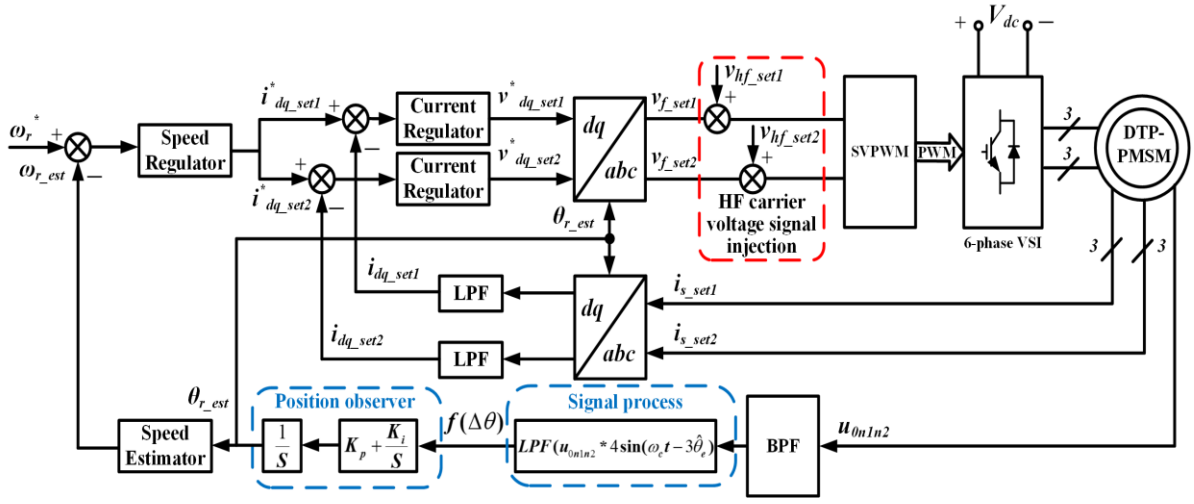

Fig. 4.10. Overall control system.

A. Steady-State Performance

The spectra of measured zero-sequence carrier voltage between the two isolated neutral points with employing different phase shifts are illustrated in Fig. 4.13 (a). For precise comparison, the spectra of measured zero-sequence carrier voltage without/with optimum phase shift (90 degrees) are compared in Fig. 4.13 (b). It can be clearly seen that the undesirable high frequency components of the 197th order, which cause oscillation in the estimation error, is significantly suppressed when applying 90 degrees phase angle shift between the two injected signals among different phase shifts. Figs. 4.14-4.15 show the comparisons of estimated and actual rotor positions

as well as the estimation error without/with optimum phase shift, respectively. Apparently, without phase shift, the position estimation performance for DTP-PMSM, can exhibit large oscillation in the estimation error similar to that of single three-phase PMSM, Fig. 4.14, due to the large amplitude of the undesirable harmonic component in zero-sequence carrier voltage, i.e. the 197th, as shown in Fig. 4.13 (b).

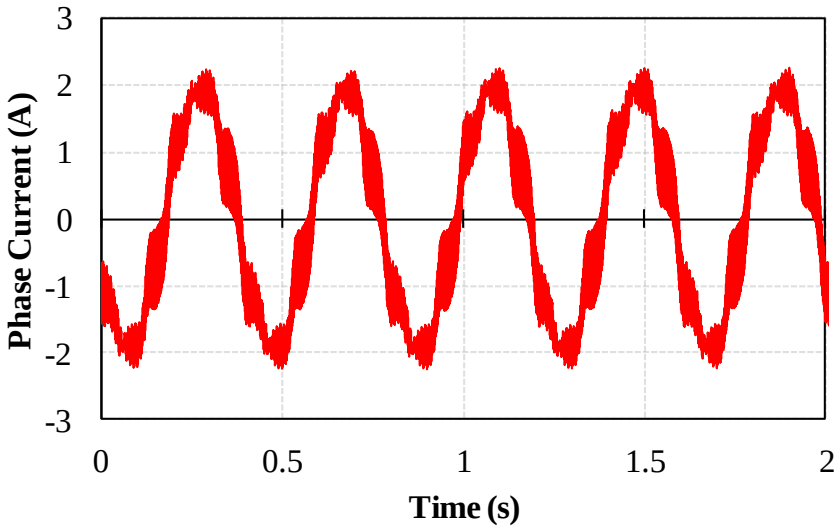

Fig. 4.11. Phase current without optimum phase shift, f_c=500Hz, V_c=8V, 30rpm.

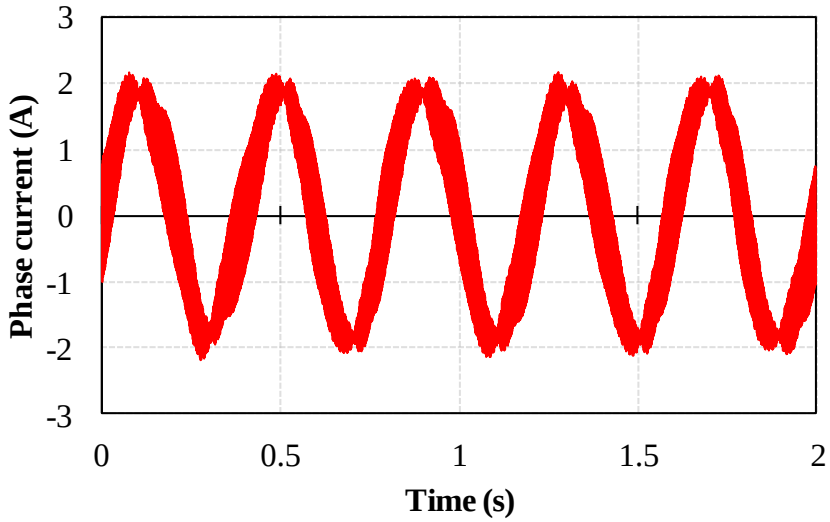

Fig. 4.12. Phase current with optimum phase shift, f_c=500Hz, V_c=8V, 30rpm.

Thanks to the existence of additional degrees of freedom in DTP-PMSM drives, by applying an optimum phase shift between the injected high frequency carrier signals, the 197th frequency component of zero-sequence voltage is significantly suppressed. Meanwhile, the 203rd frequency component, which is utilized for rotor position estimation in this chapter, is maximized, Fig. 4.13 (b). As a result, when employing the optimum phase shift between the two injected high frequency signals, the rotor position estimation is notably improved, Fig.4.15.

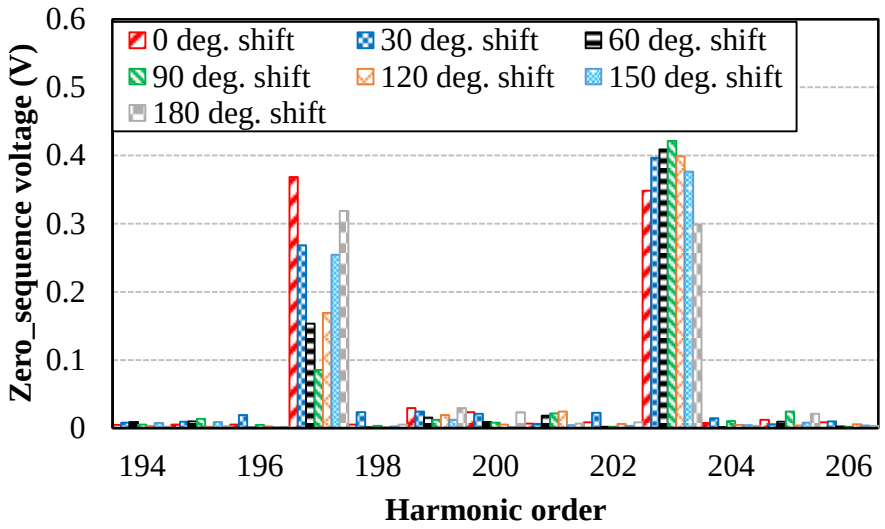

(a) with different phase shifts

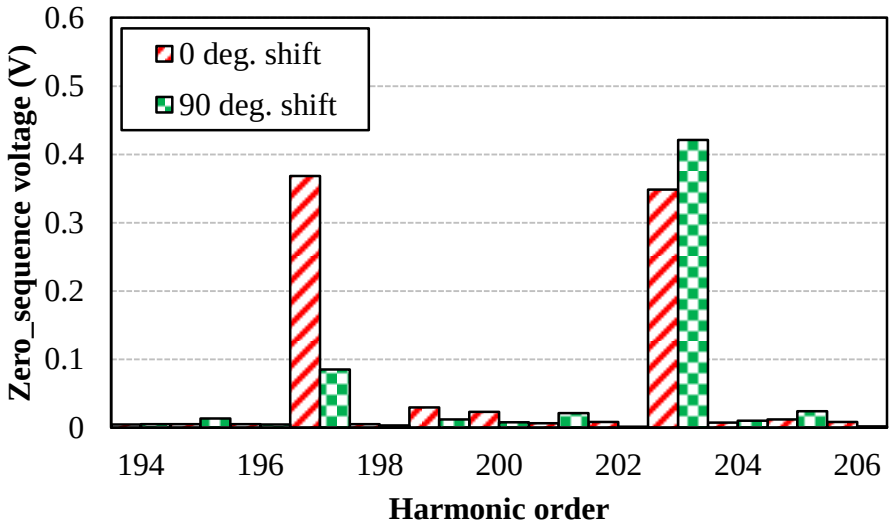

(b) without/with optimum phase shifts

Fig. 4.13. Spectra of measured zero-sequence carrier voltages with different phase shifts.

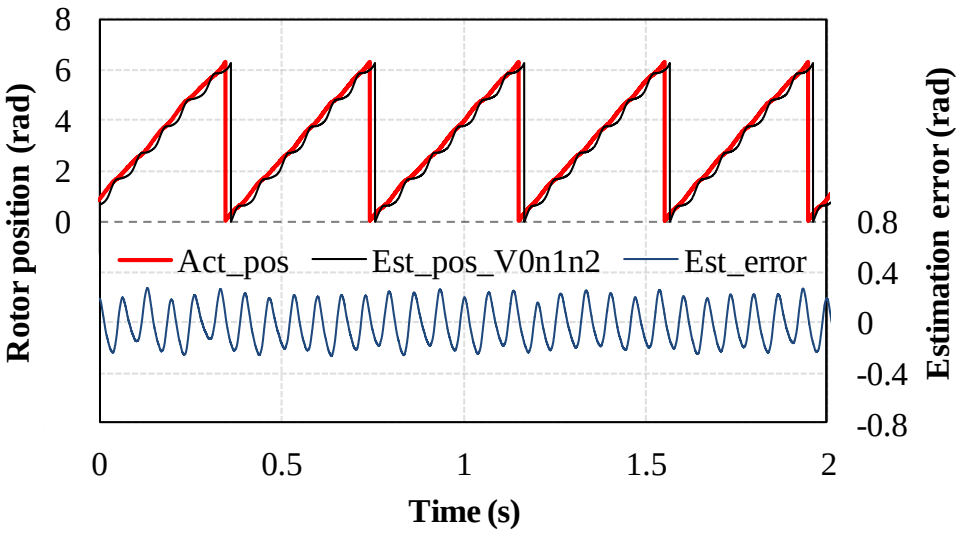

Fig. 4.14. Rotor position estimation of DTP-PMSM without phase shift, 30rpm.

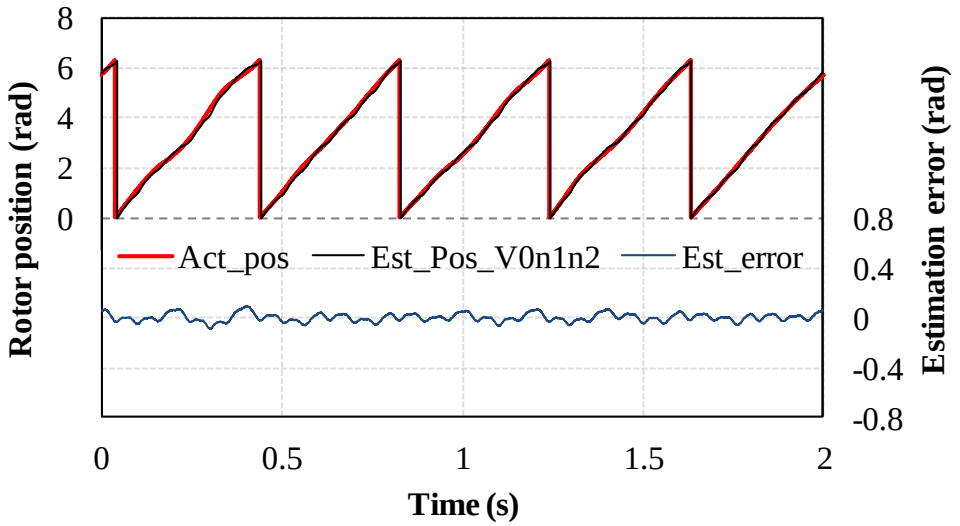

Fig. 4.15. Rotor position estimation of DTP-PMSM with optimum phase shift, 30rpm.

Furthermore, in order to verify the modified pulsating carrier signal injection with zero-sequence carrier voltage method, the rotor position estimation for ultra-low speed operation, 6rpm, is provided as illustrated in Fig. 4.16. It can be seen that with ultra-low speed operation, the oscillations in the estimation error are slightly increased. This is due to that with the same position observer bandwidth, the frequency of the additional harmonic components becomes smaller with the decrease of rotor speed, which results in the increased oscillations in the estimation error.

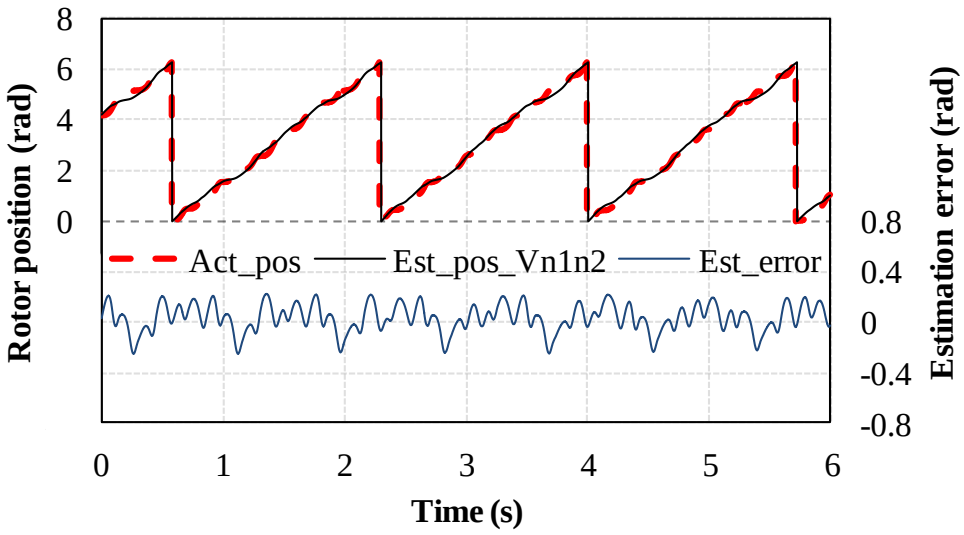

Fig. 4.16. Rotor position estimation with optimum phase shift for ultra-low speed, 6rpm.

To further confirm less oscillating estimation errors among different injection frequencies of the modified method, the peak-peak estimation errors without/with optimum phase angle are shown in Fig. 4.17. It can be clearly seen that the oscillating errors without optimum phase angle is much larger compared to that with optimum phase shift. It should be noted that K_p and K_i of the PI regulator in the position observer are kept the same for fair comparison.

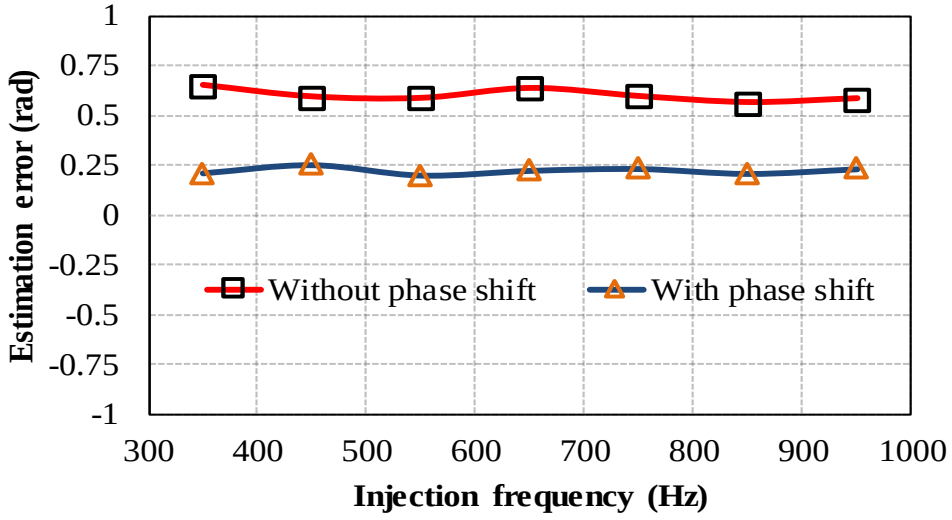

Fig. 4.17. Peak-to-peak estimation errors with different injection frequencies.

B. Dynamic Performance

In order to further validate the effectiveness of improved zero-sequence voltage method based on pulsating injection with the optimum phase shift, the dynamic performance test is carried out when the rotor speed reference is zero and step change to 30rpm and then 60rpm as shown in Fig. 4.18. It should be mentioned that the injected carrier signals of steady-state and dynamic conditions are the same. Good tracking for estimated position with fast dynamic response can be observed at different speed range including standstill.

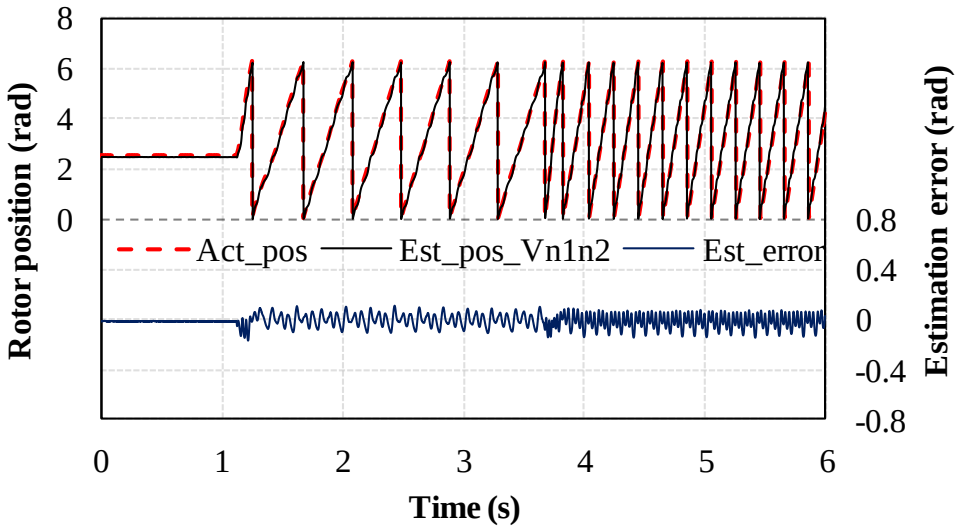

(a) Rotor position estimation performance

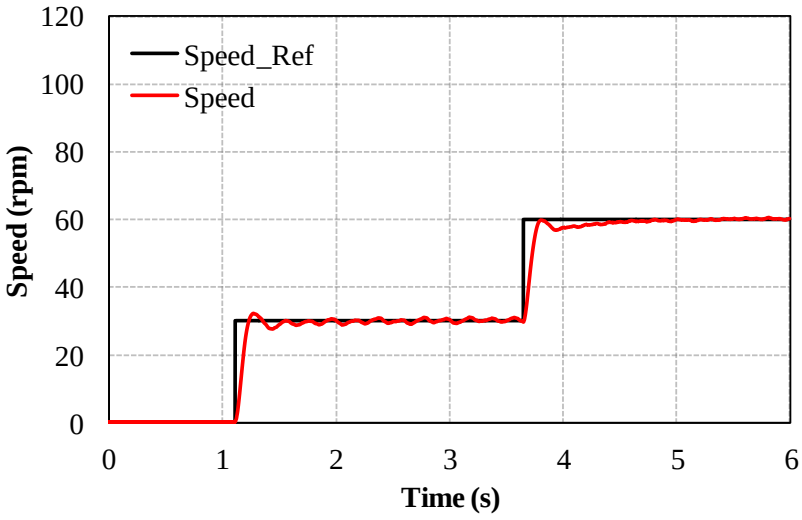

(b) Reference speed and actual rotor speed

Fig. 4.18. Dynamic performance under step change in speed, 0-30-60rpm.

Also, the step load test is implemented for the modified method as shown in Fig.4.19. It shows good position estimation tracking performance when q-axis current is rapidly increased from 0.2 to 2.5 A. It can be concluded that the modified method shows outstanding steady-state and dynamic performances when applied to the prototype DTP-PMSM.

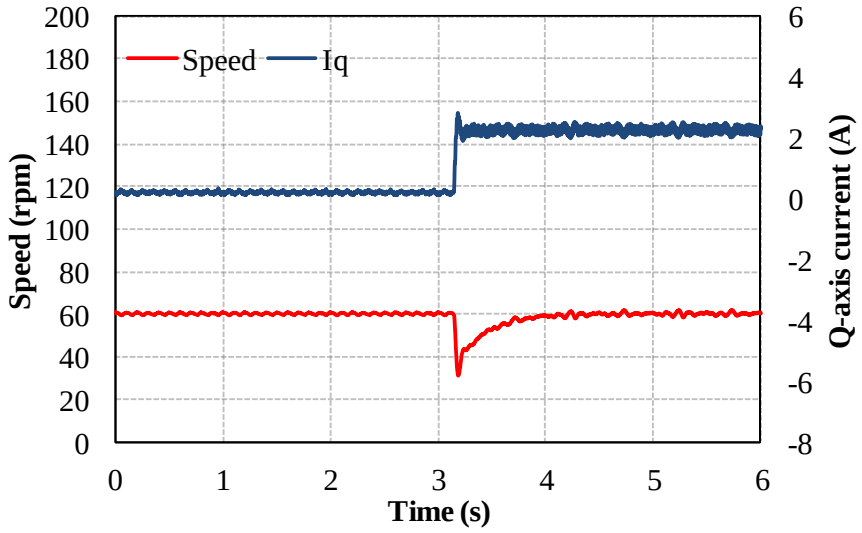

(a) Rotor speed and q-axis current

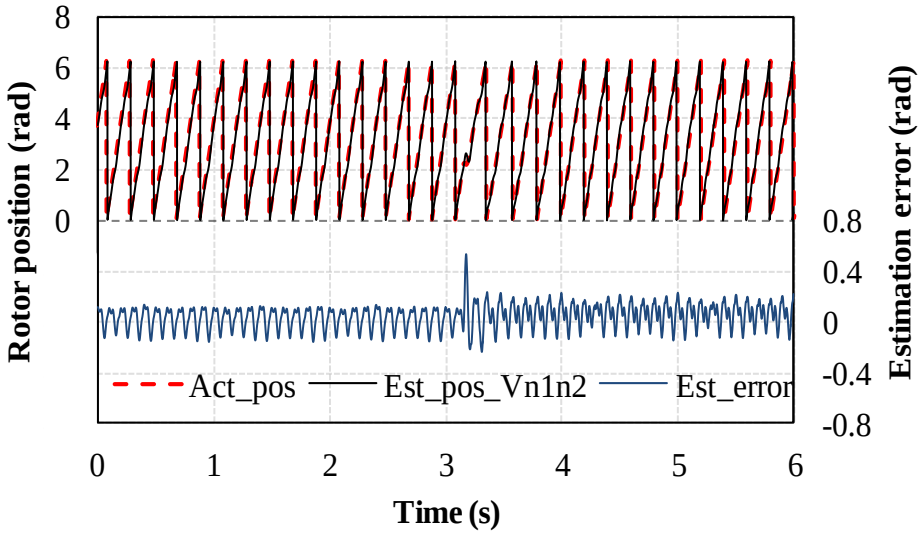

(b) Rotor position estimation performance

Fig. 4.19. Dynamic performance under step load change.

4.4. Summary

This chapter investigates the sensorless control method based on the pulsating carrier signal injection utilizing zero-sequence voltage for DTP-PMSM drives. A new simple method of zero-sequence voltage measurement is presented first by using one voltage sensor between two isolated neutral points of both windings sets. Then, an improved pulsating injection based sensorless control method employing zero-sequence carrier voltage is proposed where undesirable 6^{th} harmonic components can be suppressed by applying an optimum phase shift, i.e. 90 degrees, between the two independent high frequency injected signals. Consequently, the position estimation accuracy is enhanced. The experimental results validate the effectiveness of proposed method under steady-state and dynamic conditions, and they are in consistent with theoretical analysis.

CHAPTER 5

IMPROVED ROTOR POSITION ESTIMATION BY ROTATING CARRIER SIGNAL INJECTION UTILIZING ZERO-SEQUENCE CARRIER VOLTAGE FOR DTP-PMSM

5.1. Introduction

Similar to the concept in Chapter 4, this chapter investigates the sensorless control performance of rotating high-frequency carrier signal injection method utilizing the zero-sequence carrier voltage response for single and dual three-phase PMSMs.

For rotating carrier signal injection method, it has been proved that the rotor position can be estimated by using both the negative sequence carrier current signal and the zero-sequence carrier voltage signal [GAR07] [BRI04]. The zero-sequence carrier voltage exhibits low total harmonic distortion (THD), and shows less sensitivity to the distortion of the injected carrier signal compared to carrier current response [GAR07]. Furthermore, it has been found that the system bandwidth and rotor position estimation accuracy can be significantly enhanced when utilizing zero-sequence carrier voltage [GAR07] [BRI04] [BRI05] [CON06] [CON00], [XU16]. However, for the single three phase machine with rotating signal injection, undesirable 6^{th} harmonic estimation error occurs due to the additional saliency components in the zero-sequence carrier voltage [BRI05]. To compensate the undesirable 6^{th} harmonic estimation error, a look-up table based multiple saliency decoupling compensation strategy [BRI05], and a nonlinear adaptive model based on structured neural network [REI08] can be employed. However, the existing compensation methods have complex structures or require intensive off-line measurements.

In contrast, as mentioned in Chapter 4, the DTP-PMSM has advantage of additional degree of freedom with high frequency injection based sensorless control since it consists of two separated winding sets with two isolated neutral points, where the phase angle difference between the two injected high frequency signals can be changed. Therefore, in this chapter, an optimum phase angle difference between the two winding injection carrier signals will be utilized to suppress the oscillating position errors.

In this chapter, firstly, the rotating carrier signal injection using zero-sequence voltage method is employed for position estimation of a single three-phase PMSM. Then, the oscillating position error due to the additional saliency components effect is analyzed. Subsequently, the sensorless control performance of rotating injection utilizing zero-sequence carrier voltage for DTP-PMSM is investigated. It should be mentioned that the simplified zero-sequence voltage measurement method which is employed in Chapter 4 is also utilized for this chapter. Consequently, an improved sensorless control method of rotating injection with zero-sequence carrier voltage sensing is proposed, where an optimum phase angle shift between the two injected high-frequency carrier signals is applied for suppressing the undesirable harmonic components, which leads to an improvement of position estimation accuracy. Finally, the experimental results confirm the effectiveness of the proposed method implemented on the prototype DTP-PMSM using a dSPACE platform.

5.2. Rotating Signal Injection Using Zero-Sequence Voltage for Single Three-Phase PMSM

5.2.1. Modelling of Single Three-Phase PMSM

The sensorless performance of rotating carrier signal injection utilizing zero-sequence carrier voltage method for single three-phase PMSM is firstly investigated to show the issues of oscillating position estimation error caused by additional high frequency components in the demodulation of zero-sequence carrier voltage.

Generally, the high-frequency carrier signal injection models employing the zero-sequence carrier voltage are applied on the natural reference frame [BRI04]-[BRI05], and thus the specific information about the self- and mutual-inductances of the machine is required. In this chapter, the self- and mutual-inductances are considered in the models for both single [XU16], and dual three-phase PMSMs.

At low speed and high carrier frequency, the back-EMF and resistive voltage drop can be neglected and the PM machine can be seen as pure inductive load. Then, the expressions of single three-phase PMSM voltages are given as [BRI05]

$$\begin{bmatrix} v_{an1} \\ v_{bn1} \\ v_{cn1} \end{bmatrix} = \begin{bmatrix} L_{aa} & M_{ab} & M_{ac} \\ M_{ba} & L_{bb} & M_{bc} \\ M_{ca} & M_{cb} & L_{cc} \end{bmatrix} \begin{bmatrix} di_a / dt \\ di_b / dt \\ di_c / dt \end{bmatrix} \tag{5.1}$$

where L_{aa}, L_{bb}, L_{cc}, M_{ab} (M_{ba}), M_{ac} (M_{ca}), and M_{bc} (M_{cb}) denote the three phase incremental self- and mutual-inductances, respectively, while v_{an1}, v_{bn1}, and v_{cn1}, and i_a, i_b, and i_c, are referred as phase voltages and currents, respectively.

Generally, the expressions of the three-phase inductances are given as

$$\begin{cases} L_{aa} = L_0 - L_2 \cos(2\theta_r) \\ L_{bb} = L_0 - L_2 \cos(2\theta_r + 2\pi/3) \\ L_{cc} = L_0 - L_2 \cos(2\theta_r - 2\pi/3) \end{cases} \tag{5.2}$$

$$\begin{cases} M_{ab} = M_{ba} = M_0 - M_2 \cos(2\theta_r - 2\pi/3) \\ M_{bc} = M_{cb} = M_0 - M_2 \cos(2\theta_r) \\ M_{ca} = M_{ac} = M_0 - M_2 \cos(2\theta_r + 2\pi/3) \end{cases}$$

where θ_r is the actual rotor position, and L_0, M_0, L_2, and M_2 represent the amplitudes of dc and second harmonics of phase self- and mutual-inductances, respectively.

For three-phase Star-connected winding,

$$\frac{di_a}{dt} + \frac{di_b}{dt} + \frac{di_c}{dt} = 0 \tag{5.3}$$

From (5.1)-(5.4), the zero-sequence voltage can be directly obtained as

$$v_{0s1} = \frac{1}{3}(v_{an1} + v_{bn1} + v_{cn1}) \tag{5.4}$$

When rotating carrier signal is injected into machine, the injected voltages of three-phases can be expressed as

$$v_a = V_c \cos(\omega_c t) \tag{5.5}$$

$$v_b = V_c \cos(\omega_c t - 2\pi/3) \tag{5.6}$$

$$v_c = V_c \cos(\omega_c t + 2\pi/3) \tag{5.7}$$

where ω_c and V_c are the carrier frequency and voltage, respectively. The rotating high-frequency injection in $\alpha\beta$-reference frame is illustrated in Fig. 5.1.

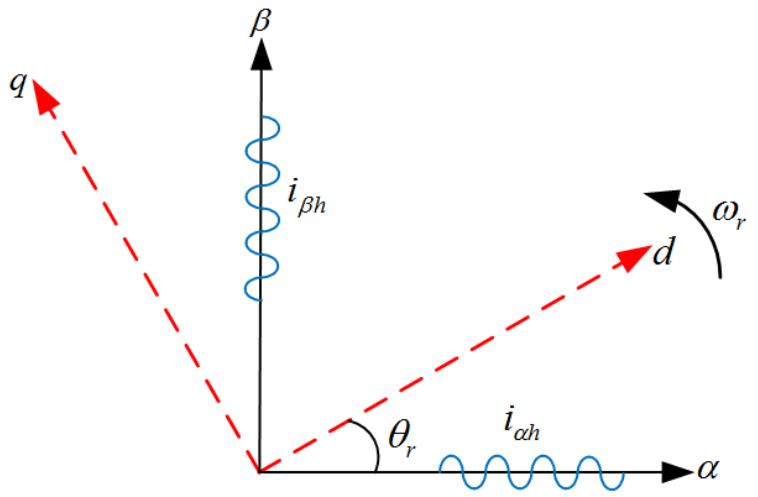

Fig. 5.1. High frequency rotating voltage signal injection.

With (5.1)-(5.7), the resultant zero-sequence carrier voltage for single three-phase PMSM is derived as (5.8).

$$v_{0sn1} = V_{o1}\cos(\omega_c t + 2\theta_e) - V_{o2}\cos(\omega_c t - 4\theta_e)$$

$$v_{0sn1} = \frac{V_C\left(L_0 - M_0\right)\left(L_2 - M_2\right)}{2L_0^{\,2} + 2M_0^{\,2} - 2M_2^{\,2} - 4L_0M_0 - 2L_2M_2 - \frac{L_2^{\,2}}{2}}\cos(\omega_C t + 2\theta_r) \tag{5.8}$$

$$-\frac{V_C}{2}\frac{\left(L_2 - 2M_2\right)\left(L_2 - M_2\right)}{2L_0^{\,2} + 2M_0^{\,2} - 2M_2^{\,2} - 4L_0M_0 - 2L_2M_2 - \frac{L_2^{\,2}}{2}}\cos(\omega_C t - 4\theta_r)$$

In (5.8), it can be seen that the zero-sequence carrier voltage includes two high frequency components at f_c+2f_e and f_c-4f_e, respectively, where f_c is the carrier frequency, while f_e is the fundamental frequency. Normally, the first term of the zero-sequence carrier voltage in (5.8) is utilized for rotor position estimation [GAR07] [BRI04] [BRI05], and the second term is undesirable harmonic component which leads to oscillation in the estimated position.

Furthermore, it should be noted that the signal amplitude of the first term is not related to the injected frequency compared to that of negative sequence current which is inversely proportional to the injected frequency. Thus, for zero-sequence carrier voltage method, high frequency injection can be employed which contributes to high system bandwidths and improves the system stability consequently.

5.2.2. Analysis of Zero-Sequence Carrier Voltage Response

A high frequency rotating voltage signal with amplitude of 8V and frequency of 500Hz is injected into the stationary reference frame with 50% of the full load, and by utilizing the measured zero-sequence carrier voltage, the rotor position is estimated. The phase current is shown in Fig. 5.2. Large distortions can be found in the phase current due to large amplitude of undesirable harmonic components in the position estimation error.

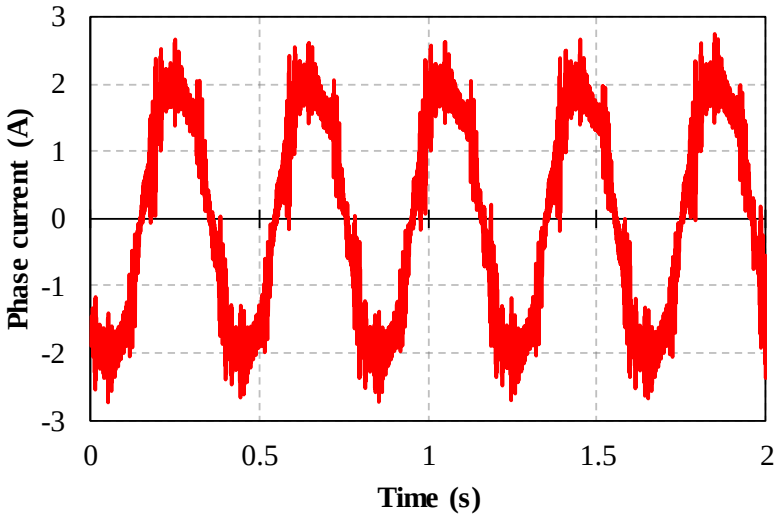

Fig. 5.2. Phase current, f_c=500Hz, V_c=8V, 30rpm.

The spectra of the measured zero-sequence carrier voltage for single three-phase PMSM is shown in Fig. 5.3. It can be clearly seen that the frequency components of zero-sequence carrier voltage with rotating signal injection are mainly at f_c+2f_e and f_c-4f_e, i.e. the 202nd and the 196th. The high frequency components at f_c+2f_e are used for position estimation, while the other components at f_c-4f_e cause oscillation in the estimated position because of its large amplitude.

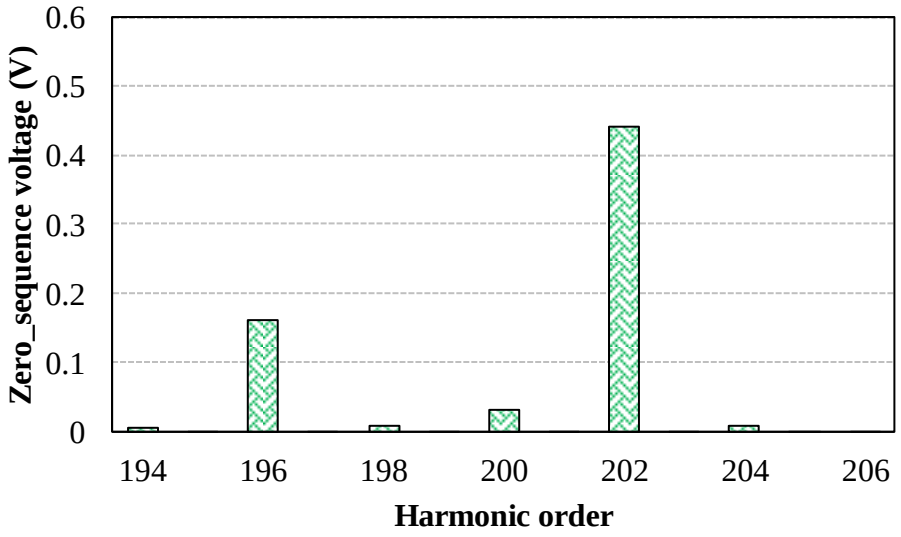

Fig. 5.3. Spectra of measured zero-sequence carrier voltage, three-phase PMSM, 30rpm.

5.2.3. Performance of Rotor Position Estimation

The zero-sequence carrier voltage response is utilized in order to estimate the rotor position. Fig. 5.4 illustrates the comparison of estimated and actual rotor positions, together with the position estimation error.

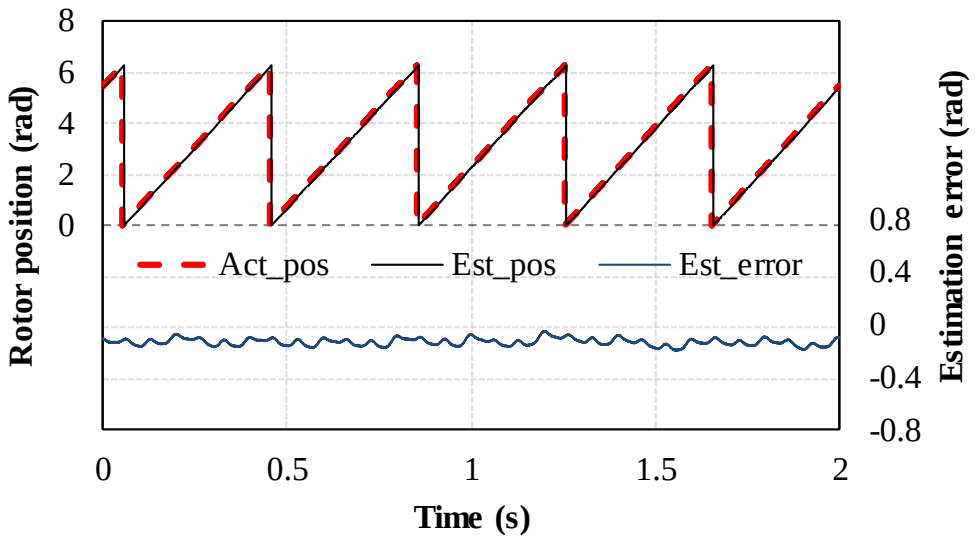

Fig. 5.4. Rotor position estimation in steady-state of single three-phase PMSM, 30rpm.

From Fig. 5.4, it can be found that the 6th harmonic position estimation error and offset due to large undesirable harmonic components, i.e. the 196th, caused by additional saliency effects. Such 6th harmonic estimation error can deteriorate the rotor position estimation which results in unstable sensorless control performance. Thus, due to the merits of dual three-phase machine in terms of independent high frequency injection for both winding sets, it is employed to overcome such oscillations in the estimation error as shown in details in the next subsection.

5.3. Proposed Rotating Signal Injection Using Zero-Sequence Voltage for Dual Three-Phase PMSM

As mentioned earlier, the rotating carrier signal injection utilizing zero-sequence voltage based sensorless control for single three-phase PMSM shows the 6th harmonic estimation error due to the undesirable harmonic components in the demodulated zero-sequence carrier voltage. To overcome such an issue, the existing methods require time-consuming offline measurements and complex structures [BRI05], [REI08].

On the other hand, for DTP-PMSM drives, it is possible to suppress the undesirable harmonic components since it has advantage of additional degrees of freedom with high frequency injection

in two separated stator winding sets. This can be achieved by applying an optimum phase shift between the two injected high-frequency signals. Then, the rotor position estimation will be improved accordingly.

Thus, in this chapter, the main purpose is to suppress the undesirable harmonic components of zero-sequence carrier voltage as much as possible. By adopting dual three-phase PMSM configuration, the oscillations in the position estimation error can be reduced by considering an optimum phase shift between the injected high-frequency carrier signals, as will be analyzed in the following section.

5.3.1. Modelling of Dual Three-Phase PMSM

In the case of DTP-PMSM with two separated stator winding sets spatially shifted by 30 electrical degrees with two isolated neutral points, the phase voltage equations for the first winding set are the same to the expressions of single three-phase PMSM in (5.1), while the phase voltages for the second winding set are expressed as

$$\begin{bmatrix} v_{xn2} \\ v_{yn2} \\ v_{zn2} \end{bmatrix} = \begin{bmatrix} L_{xx} & M_{xy} & M_{xz} \\ M_{yx} & L_{yy} & M_{yz} \\ M_{zx} & M_{zy} & L_{zz} \end{bmatrix} \begin{bmatrix} di_x / dt \\ di_y / dt \\ di_z / dt \end{bmatrix}. \tag{5.9}$$

The expressions of three-phase inductances for the second winding set are given by

$$\begin{cases} L_{xx} = L_0 - L_2 \cos(2\theta_r - 2\pi/6) \\ L_{yy} = L_0 - L_2 \cos(2\theta_r - 10\pi/6) \\ L_{zz} = L_0 - L_2 \cos(2\theta_r + 6\pi/6) \end{cases}$$

$$\begin{cases} M_{xy} = M_{yx} = M_0 - M_2 \cos(2\theta_r + 6\pi/6) \\ M_{yz} = M_{zy} = M_0 - M_2 \cos(2\theta_r - 10\pi/6) \\ M_{zx} = M_{xz} = M_0 - M_2 \cos(2\theta_r - 2\pi/6) \end{cases} \tag{5.10}$$

where L_{xx}, L_{yy}, L_{zz}, M_{xy} (M_{yx}), M_{xz} (M_{zx}), and M_{yz} (M_{zy}) denote the three phase incremental self- and mutual-inductances of the second stator winding set, respectively. v_{xn2}, v_{yn2}, and v_{zn2}, and i_x, i_y, and i_z, represent the phase voltages and currents of the second stator winding set, respectively.

For the second star-connected three-phase winding set,

$$\frac{di_x}{dt}+\frac{di_y}{dt}+\frac{di_z}{dt}=0 \tag{5.11}$$

Then, by using (5.9)-(5.11), the zero-sequence voltage for the second winding can be calculated as

$$v_{0s2}=\frac{1}{3}(v_{xn2}+v_{yn2}+v_{zn2}) \tag{5.12}$$

Assuming that the balanced rotating carrier voltage is injected into two winding sets of DTP-PMSM independently, the injected carrier voltages of the first set are the same as the single three-phase, i.e. (5.5)-(5.7), and the injected voltages of the second three-phase winding are expressed as

$$v_x=V_c\cos(\omega_c t) \tag{5.13}$$

$$v_y=V_c\cos(\omega_c t-2\pi/3) \tag{5.14}$$

$$v_z=V_c\cos(\omega_c t+2\pi/3) \tag{5.15}$$

Using (5.1)-(5.15), the resultant zero-sequence carrier voltages for both winding sets can be obtained as

$$v_{0sn1} = \frac{V_C\left(L_0 - M_0\right)\left(L_2 - M_2\right)}{2L_0^{\,2} + 2M_0^{\,2} - 2M_2^{\,2} - 4L_0M_0 - 2L_2M_2 - \frac{L_2^{\,2}}{2}} \times \cos(\omega_C t + 2\theta_r)$$
$$- \frac{V_C}{2}\frac{\left(L_2 - 2M_2\right)\left(L_2 - M_2\right)}{2L_0^{\,2} + 2M_0^{\,2} - 2M_2^{\,2} - 4L_0M_0 - 2L_2M_2 - \frac{L_2^{\,2}}{2}} \times \cos(\omega_C t - 4\theta_r) \tag{5.16}$$

$$v_{0sn2} = \frac{V_C\left(L_0 - M_0\right)\left(L_2 - M_2\right)}{2L_0^{\,2} + 2M_0^{\,2} - 2M_2^{\,2} - 4L_0M_0 - 2L_2M_2 - \frac{L_2^{\,2}}{2}} \times \cos(\omega_C t + 2\theta_r + 5\pi/3)$$
$$- \frac{V_C}{2}\frac{\left(L_2 - 2M_2\right)\left(L_2 - M_2\right)}{2L_0^{\,2} + 2M_0^{\,2} - 2M_2^{\,2} - 4L_0M_0 - 2L_2M_2 - \frac{L_2^{\,2}}{2}} \times \cos(\omega_C t - 4\theta_r + 2\pi/3) \tag{5.17}$$

Generally, the measurement of zero-sequence carrier voltage is obtained based on two common measurement methods, i.e. one method utilizing phase-to-neutral-voltages [BRI04], and another method employing auxiliary resistor network [BRI05]. For DTP-PMSM, the new measurement method introduced in Chapter 4 is also utilized in this chapter.

The zero-sequence carrier voltage between the two isolated neutral points, i.e. $v_{0sn1n2} = v_{0sn1} - v_{0sn2}$, is given by

$$
\begin{aligned}
v_{0sn1n2} = & \frac{V_C \left(L_0 - M_0\right)\left(L_2 - M_2\right)}{2L_0{}^2 + 2M_0{}^2 - 2M_2{}^2 - 4L_0M_0 - 2L_2M_2 - \frac{L_2{}^2}{2}} \\
& \times \sin(\omega_C t + 2\theta_r + 5\pi/6) \\
& - \frac{\sqrt{3}\, V_C}{2} \frac{\left(L_2 - 2M_2\right)\left(L_2 - M_2\right)}{2L_0{}^2 + 2M_0{}^2 - 2M_2{}^2 - 4L_0M_0 - 2L_2M_2 - \frac{L_2{}^2}{2}} \cdot \\
& \times \sin(\omega_C t - 4\theta_r + 2\pi/6)
\end{aligned}
\tag{5.18}
$$

From (5.18), it can be seen that the zero-sequence carrier voltage includes two high frequency components at f_c+2f_e and f_c-4f_e, respectively, similar to the case of single three-phase PMSM.

By considering a phase shift in the injected signal of the second winding set, the zero-sequence carrier voltage between the two isolated neutral points, can be expressed as

$$
\begin{aligned}
v_{0sn1n2} &= v_{0sn1} - v_{0sn2} \\
v_{0sn1n2} &= \begin{bmatrix} \dfrac{V_C\left(L_0 - M_0\right)\left(L_2 - M_2\right)}{2L_0{}^2 + 2M_0{}^2 - 2M_2{}^2 - 4L_0M_0 - 2L_2M_2 - \dfrac{L_2{}^2}{2}} \\ \times\cos(\omega_c t + 2\theta_r) \\ -\dfrac{V_C}{2}\dfrac{\left(L_2 - 2M_2\right)\left(L_2 - M_2\right)}{2L_0{}^2 + 2M_0{}^2 - 2M_2{}^2 - 4L_0M_0 - 2L_2M_2 - \dfrac{L_2{}^2}{2}} \\ \times\cos(\omega_c t - 4\theta_r) \end{bmatrix} \\
&\quad - \begin{bmatrix} \dfrac{V_C\left(L_0 - M_0\right)\left(L_2 - M_2\right)}{2L_0{}^2 + 2M_0{}^2 - 2M_2{}^2 - 4L_0M_0 - 2L_2M_2 - \dfrac{L_2{}^2}{2}} \\ \times\cos(\omega_c t + 2\theta_r + 5\pi/3 - \varphi) \\ -\dfrac{V_C}{2}\dfrac{\left(L_2 - 2M_2\right)\left(L_2 - M_2\right)}{2L_0{}^2 + 2M_0{}^2 - 2M_2{}^2 - 4L_0M_0 - 2L_2M_2 - \dfrac{L_2{}^2}{2}} \\ \times\cos(\omega_c t - 4\theta_r + 2\pi/3 - \varphi) \end{bmatrix} \\
&= -\frac{2\ V_C\left(L_0 - M_0\right)\left(L_2 - M_2\right)}{2L_0{}^2 + 2M_0{}^2 - 2M_2{}^2 - 4L_0M_0 - 2L_2M_2 - \dfrac{L_2{}^2}{2}} \\
&\quad \times\sin(\omega_c t + 2\theta_r + 5\pi/6 - \varphi/2)\sin(-5\pi/6 + \varphi/2) \\
&\quad + \frac{V_C}{2}\frac{2\ \left(L_2 - 2M_2\right)\left(L_2 - M_2\right)}{2L_0{}^2 + 2M_0{}^2 - 2M_2{}^2 - 4L_0M_0 - 2L_2M_2 - \dfrac{L_2{}^2}{2}} \\
&\quad \times\sin(\omega_c t - 4\theta_r + 2\pi/6 - \varphi/2)\sin(-2\pi/6 + \varphi/2)
\end{aligned}
\tag{5.19}
$$

where φ is the phase shift in the injected high frequency carrier signal. An optimum phase shift is required in order to eliminate/suppress the undesirable harmonic components, i.e. high frequency components at f_c-$4f_e$, which leads to an improved rotor position estimation. From (5.19), it is found that the second term, which causes oscillation in the position estimation error, can be

suppressed/eliminated when the phase shift between the two injected high frequency signals is $\varphi = 2\pi/3$, as the undesirable harmonic components at f_c-$4f_e$ equals to zero. Meanwhile, the amplitude of the high frequency components at f_c+$2f_e$, which is used for position estimation, is maximized. Thus, $2\pi/3$ is the optimum phase shift in order to eliminate/suppress such oscillation in the estimation error, as will be shown experimentally. Then, the zero-sequence carrier voltage with considering the optimum phase shift becomes

$$\begin{aligned} v_{0sn1n2} &= \frac{2\,V_C\left(L_0 - M_0\right)\left(L_2 - M_2\right)}{2L_0^{\,2} + 2M_0^{\,2} - 2M_2^{\,2} - 4L_0M_0 - 2L_2M_2 - \dfrac{L_2^{\,2}}{2}} \\ &\quad \times \sin(\omega_c t + 2\theta_r + 3\pi/6) \\ &= -\frac{2\,V_C\left(L_0 - M_0\right)\left(L_2 - M_2\right)}{2L_0^{\,2} + 2M_0^{\,2} - 2M_2^{\,2} - 4L_0M_0 - 2L_2M_2 - \dfrac{L_2^{\,2}}{2}} \\ &\quad \times \cos(\omega_c t + 2\theta_r) \end{aligned} \tag{5.20}$$

From (5.20), when considering the optimum phase shift in the injected carrier signal of the second winding set, it is obvious that the zero-sequence carrier voltage is simplified with one term only. Furthermore, large amplitude of the undesirable harmonic component that causes oscillating estimation error does not exist for the position tracking observer. Consequently, it is expected that a high rotor position estimation accuracy can be achieved with the modified rotating signal injection employing zero-sequence carrier voltage for DTP-PMSM, as will be shown experimentally in the next section.

Fig. 5.5 shows the block diagram of signal demodulation process, and position tracking observer utilizing zero-sequence voltage. The zero-sequence carrier voltage is demodulated to form a DC signal to be proportional to the error, and then such error can be fed into the position observer that updates the estimated rotor position in order to force the error to zero [XU15].

Furthermore, the expression of the demodulated zero-sequence carrier voltage, with applying the optimum phase shift, is given by

$$\begin{aligned} V_{0sn1n2} &= LPF\left(v_{0sn1n2}\times\cos(\omega_c t)\right)\sin(2\theta_r^e) \\ &\quad -LPF\left(v_{0sn1n2}\times\sin(\omega_c t)\right)\cos(2\theta_r^e) \\ &= -\frac{V_C\left(L_0-M_0\right)\left(L_2-M_2\right)}{2L_0^{\,2}+2M_0^{\,2}-2M_2^{\,2}-4L_0M_0-2L_2M_2-\frac{L_2^{\,2}}{2}}\sin(2\Delta\theta_e) \end{aligned} \tag{5.21}$$

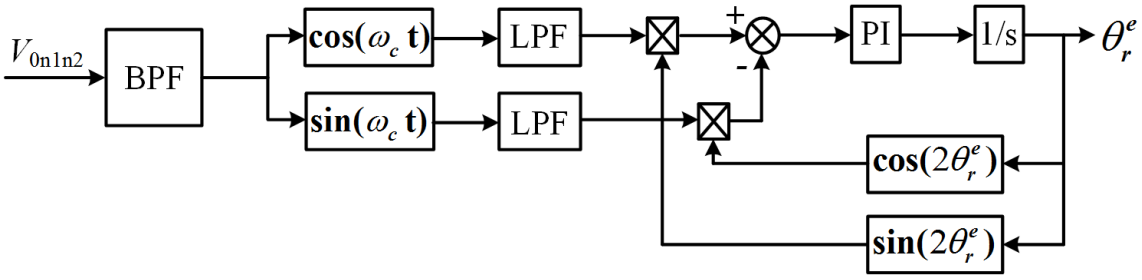

Fig. 5.5. Block diagram of zero-sequence carrier signal process with rotating injection.

5.3.2. Experimental Results and Analysis for DTP-PMSM

The experiments are implemented on a dSPACE DS1005 digital controller to validate the improved rotating carrier signal injection using zero-sequence voltage. The overall sensorless control system is shown in Fig. 5.6. The experimental test rig involves DC power supply, a prototype DTP-PMSM and coupled with a DC motor for loading, and a six-phase voltage source inverter (VSI). The DC-link voltage is set to 40V, whereas the pulse width modulation (PWM) switching frequency is 10 kHz. The specifications of the prototype machine are shown in Appendix II. Besides, the parameters of all PI regulators, and the cut-off frequencies of LPFs for whole control system shown in Fig. 5.6 are listed in Table 5.1.

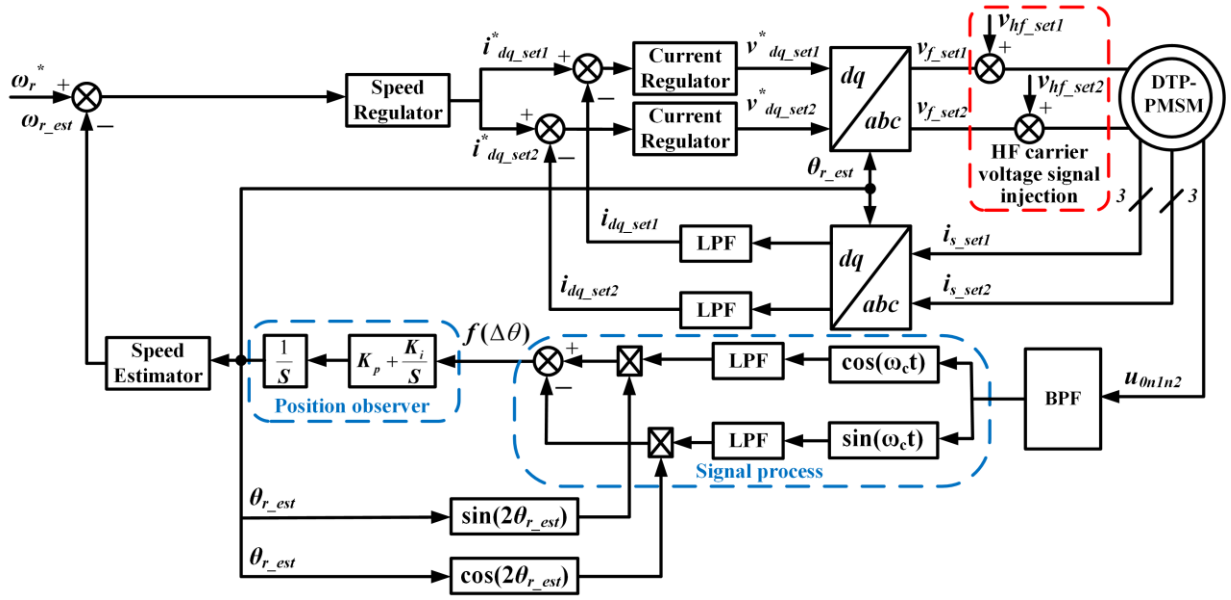

Fig. 5.6. Overall control system.

In order to investigate the sensorless control performance of proposed method under steady-state and dynamic conditions for DTP-PMSM, a balanced high frequency rotating voltage signal with amplitude of 8V and frequency of 500Hz is injected into the stationary reference frame for both three-phase winding sets independently.

Then, the measured zero-sequence carrier voltage is used to estimate the rotor position. During the steady-state condition, the rotor speed is set as 30 rpm (f_e=2.5Hz). The phase currents without and with the optimum phase angle between the injected high-frequency carrier signals are illustrated in Fig. 5.7 and Fig. 5.8, respectively. It can be seen that the phase current without the optimum phase angle shows significant distortion due to the large oscillation in the position estimation error. By considering the optimum phase angle, the phase current becomes more sinusoidal with less distortions since the oscillation in the position estimation error is significantly reduced.

TABLE 5.1

PARAMETERS OF PI REGULATORS AND LOW PASS FILTERS

Parameters	Values
Proportional gain of PI in *dq* frame (set1 and set2)	30
Integral gain of PI in *dq* frame (set1 and set2)	1000
Proportional gain of PI in position observer	200
Integral gain of PI in position observer	1000
Cut-off frequency of LPFs in *dq* frame (set1 and set2)	100 Hz
Cut-off frequency of LPFs in position observer	50 Hz

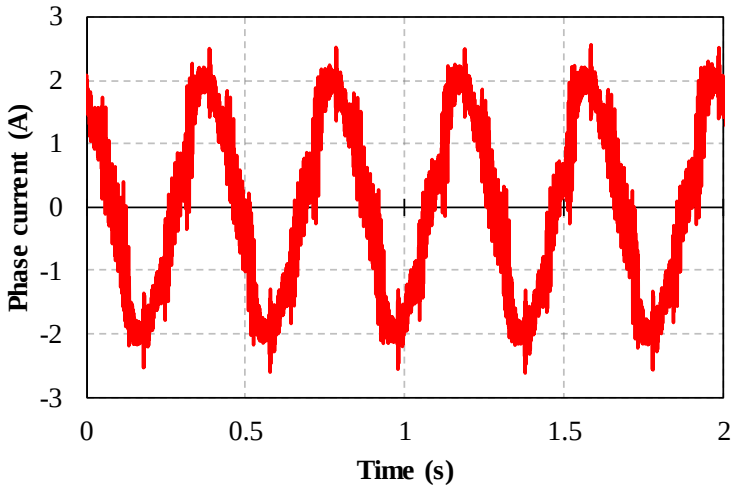

Fig. 5.7. Phase current without optimum phase shift, f_c=500Hz, V_c=8V, 30rpm.

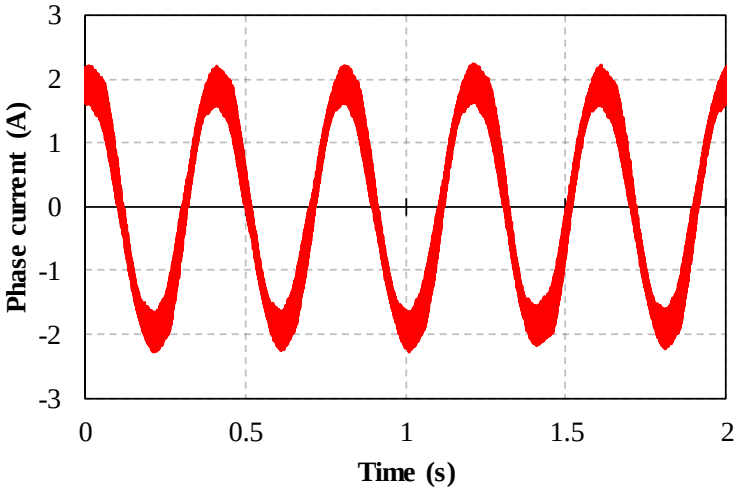

Fig. 5.8. Phase current with optimum phase shift, f_c=500Hz, V_c=8V, 30rpm.

The steady-state and dynamic performances of the improved rotating high-frequency carrier signal injection employing zero-sequence voltage method are provided next with comprehensive analysis.

A. Steady-State Performance

Fig. 5.9 (a) shows the spectra of measured zero-sequence carrier voltage by applying different phase shifts, and the spectra of measured zero-sequence voltage without/with optimum phase shift ($2\pi/3$) are compared in Fig. 5.9 (b). Then, the comparisons of estimated and actual rotor positions without/ with optimum phase shift are shown in Figs. 5.10 and 5.11, respectively. From Fig. 5.9, it can be seen that high frequency components of measured zero-sequence carrier voltage are mainly at f_c+2f_e and f_c-4f_e (202^{nd} and 196^{th}), respectively. The high frequency components at 202^{nd} is used for position estimation, while the component at the 196^{th} is undesirable harmonic components and causes large oscillation in the estimated rotor position. However, it can be found that such undesirable harmonic components can be significantly suppressed to minimum amplitude when considering 120 degrees phase shift among different phase shifts. For position estimation performance, it can be clearly observed that the estimated rotor position without applying the optimum phase shift (120 degrees) exhibits oscillating position estimation due to the undesirable high frequency components at the 196^{th}, Fig. 5.10. On the other hand, the oscillation in the estimated position has been reduced when implementing the optimum phase shift in the injected signal of the second three-phase winding set thanks to the existence of additional degrees of freedom in DTP-PMSM drives. As a result, the rotor position estimation accuracy is enhanced with good tracking as shown in Fig. 5.11.

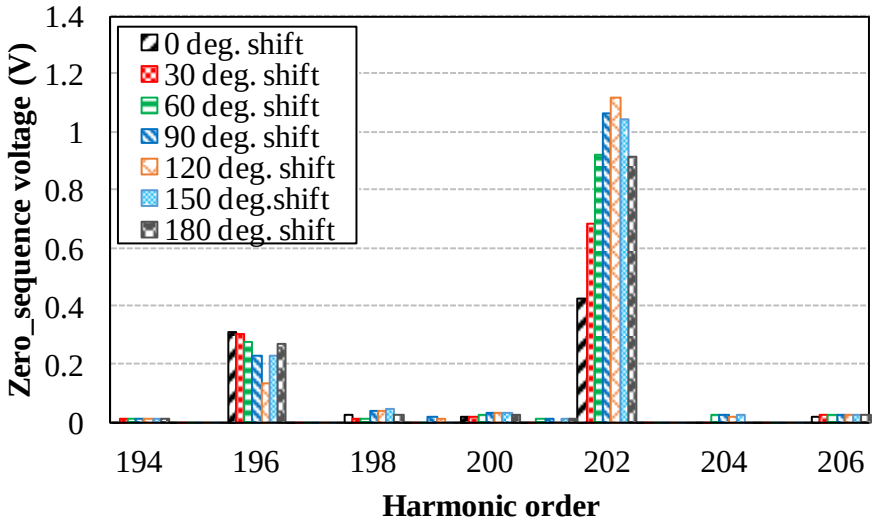

(a) With different phase shifts

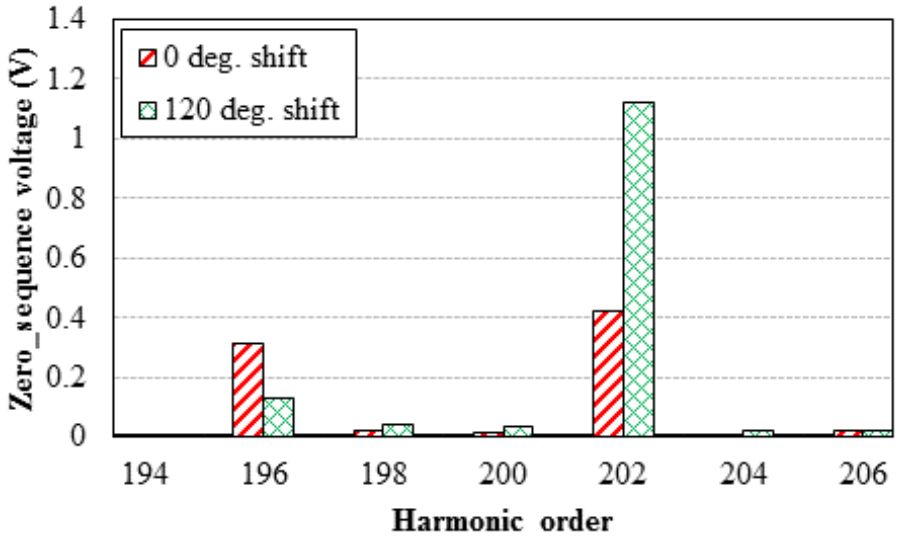

(b) Without/with optimum phase shift

Fig. 5.9. Spectra of measured zero-sequence carrier voltage, 30rpm.

Furthermore, to verify the improved method, the rotor position estimation for ultra-low speed operation, 6rpm, is examined and its performance is shown in Fig. 5.12. It can be seen that slight increase in the oscillations in the estimation error can be observed with ultra-low speed operation. This is due to that with the same position observer bandwidth, the frequency of the additional harmonic components becomes smaller with the decrease of rotor speed, which results in the increased oscillations in the estimation error.

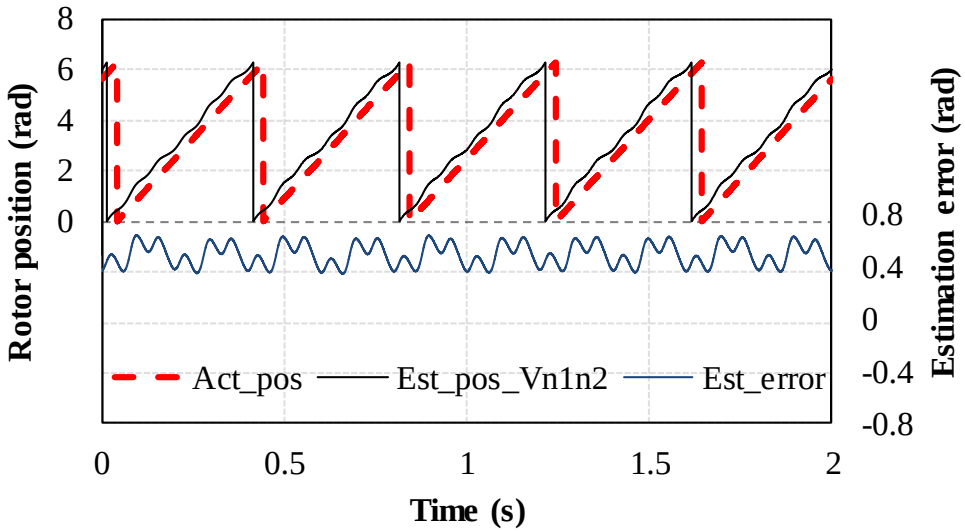

Fig. 5.10. Rotor position estimation of DTP-PMSM without optimum phase shift, 30rpm.

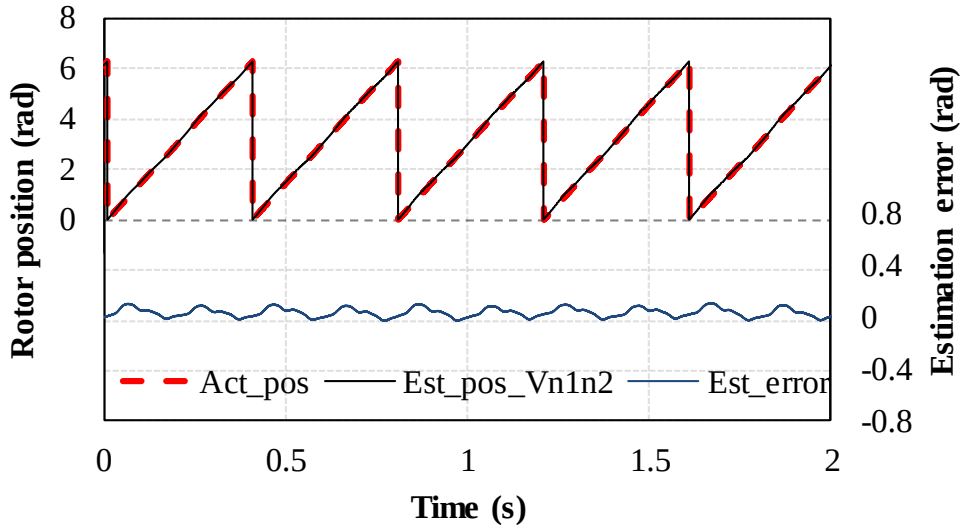

Fig. 5.11. Rotor position estimation of DTP-PMSM with optimum phase shift, 30rpm.

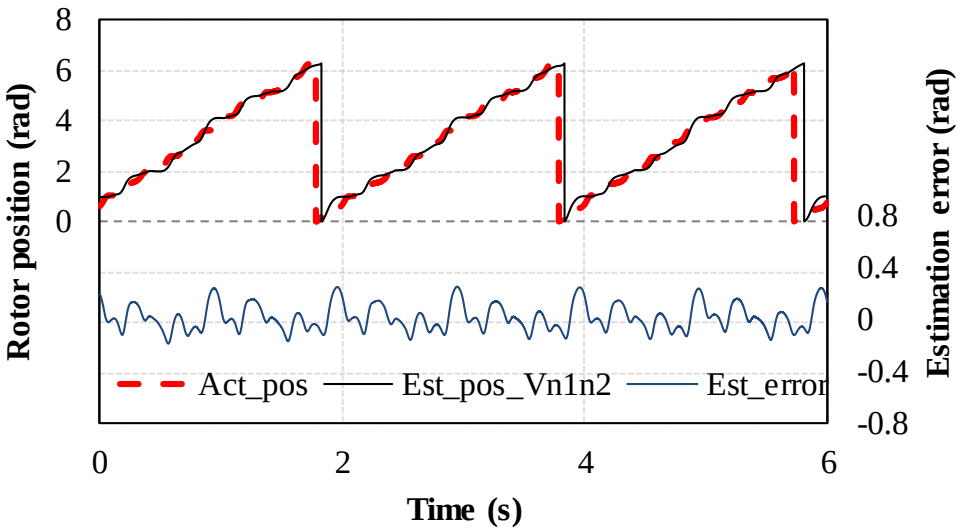

Fig. 5.12. Rotor position estimation with optimum phase shift at ultra-low speed, 6rpm.

Besides, the peak-to-peak position estimation errors for different phase shifts in the injected high frequency signal of the second winding set are illustrated in Fig. 5.13. It can be clearly seen that the smallest peak-to-peak estimation error can be found when employing 120 degrees shift.

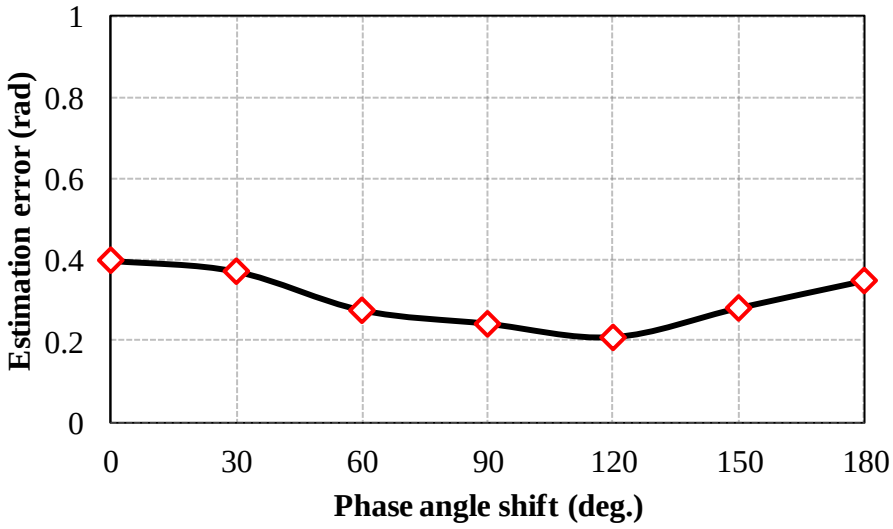

Fig. 5.13. Peak-to-peak estimation errors vs different phase shifts, 30rpm.

B. Dynamic Performance

To further verify the effectiveness of the modified rotating carrier signal injection utilizing zero-sequence voltage method, when applying the optimum phase shift (120 degrees), the dynamic performance is shown in Fig. 5.14 when the rotor speed reference is zero and step change to 30rpm and then to 60 rpm.

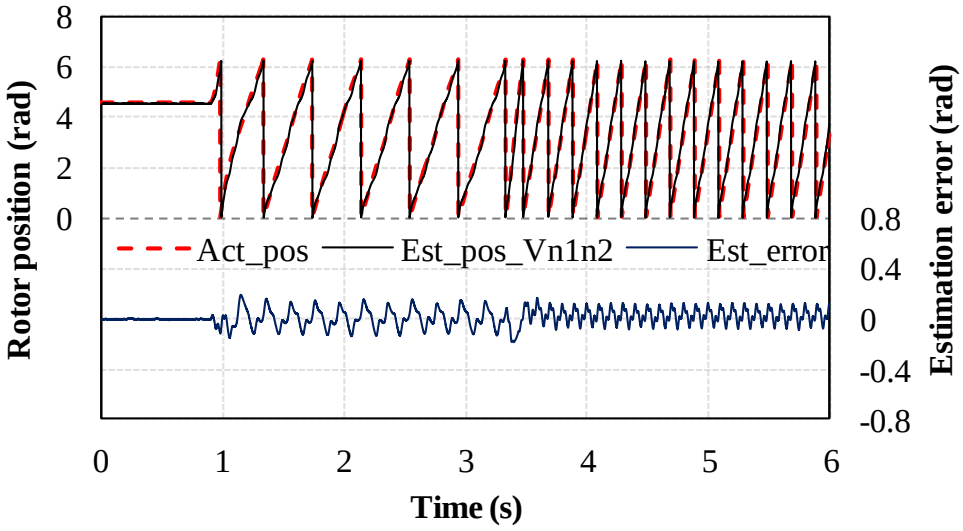

(a) Rotor position estimation

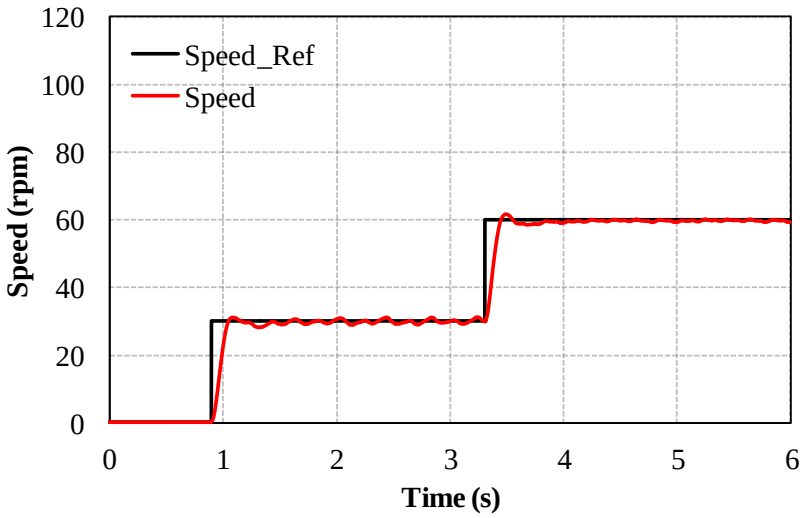

(b) Speed response

Fig. 5.14. Dynamic performance under step change in speed, 0-30-60rpm.

From Fig. 5.14, the estimated rotor position can track the actual rotor position very well, and fast dynamic response can be observed at different speed range. By considering the optimum phase shift, it can be shown that the rotating carrier signal injection employing zero-sequence carrier voltage method for DTP-PMSM demonstrates exceptionally good steady-state and dynamic performances. Additionally, the step load test is implemented for the improved method as illustrated in Fig. 5.15.

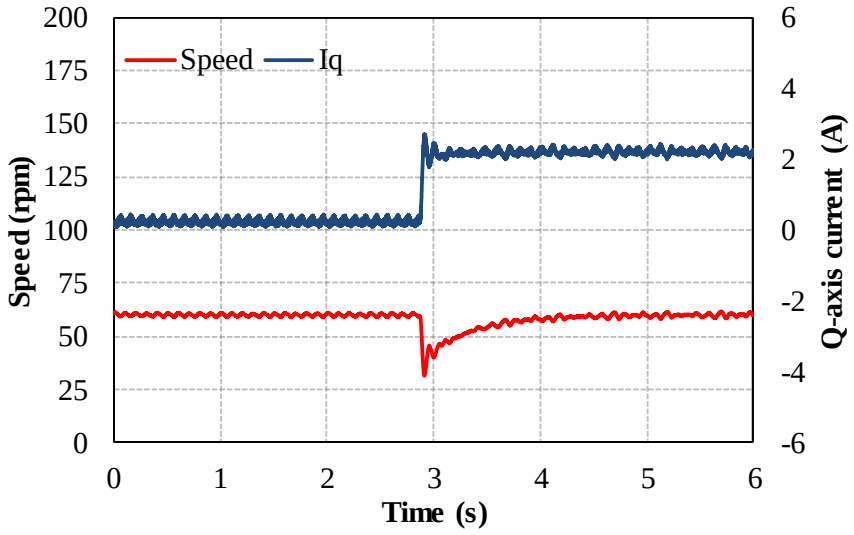

(a) Rotor speed and q-axis current

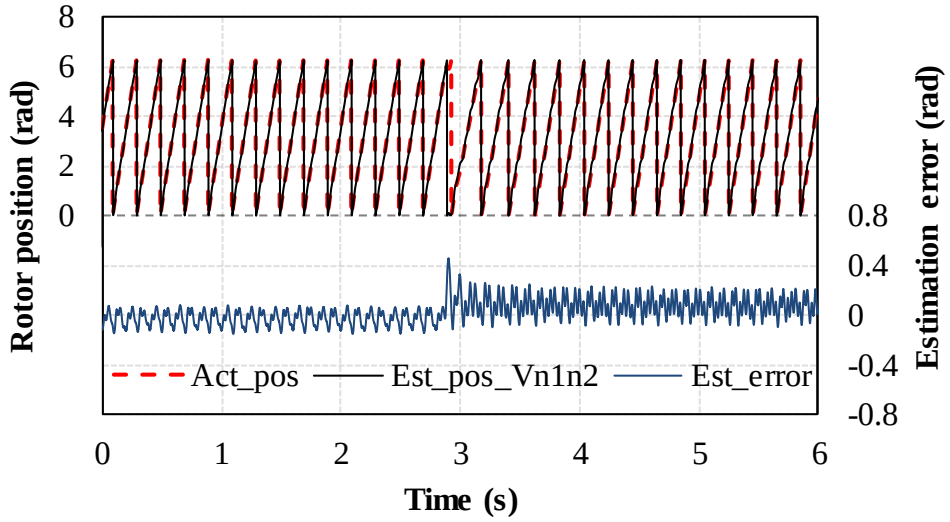

(b) Rotor position estimation performance

Fig. 5.15. Dynamic performance under step load change.

It shows good position estimation tracking performance when *q*-axis current is rapidly increased from 0.2 to 2 A. It can be concluded that outstanding steady-state and dynamic performances can be achieved when the improved method is employed.

5.4. Summary

This chapter investigates the rotor position estimation accuracy for PMSM drives based on rotating carrier signal injection by employing a zero-sequence voltage based sensorless control strategy. For single three-phase PMSM, undesirable 6^{th} harmonic estimation error occurs due to the additional saliency components in the zero-sequence carrier voltage.

In the case of DTP-PMSM, an improved rotating carrier signal injection using zero-sequence voltage based sensorless control method is proposed which can suppress the oscillating position estimation error by employing the optimum phase shift, i.e. 120 degrees, thanks to the existence of additional degrees of freedom in DTP-PMSM drives. This results in improvement of rotor position estimation accuracy. The experimental results verify the outstanding overall performance of the proposed method for DTP-PMSM.

CHAPTER 6

SENSORLESS CONTROL OF DUAL THREE-PHASE PMSM OVER WIDE-SPEED RANGE OF OPERATION INCLUDING STANDSTILL

6.1. Introduction

Due to the drawbacks of high-frequency carrier signal injection strategies in the high-speed range operation such as extra losses, transient disturbances, torque ripple, additional current harmonics, and noise produced from the injection carrier voltage, the high-frequency carrier signal injection techniques usually considered to be suitable at zero speed and low speed operation. On the other hand, the fundamental model based sensorless control methods would be effectively failing to estimate the information of rotor position at low speed. Such methods show a decent performance at high-speed region [SIL02].

Although PWM excitation based sensorless methods could be regarded as an achievable approach for the wide speed range operation, the sensor, which is required to measure the current derivative, is considered as an obstruction to their practical implementations. On the other hand, several combination methods have been addressed in [HA99] [SCH94] [CAP01] [SIL06]. However, these combination methods have not taken into account the smooth transition between different methods except the latter one and it is used for single three-phase PMSM. Such a method has not been applied to dual three-phase PMSM.

Therefore, it is desirable to combine the advantages of high-frequency carrier signal injection strategies at low speed operation, and the lower losses and simplicity of fundamental model based sensorless control to achieve high performance of rotor position estimation for dual three-phase PMSM. This combination should consider the smooth transition between various techniques without deteriorating the dynamic performance. In this chapter, the flux-linkage observer method introduced in Chapter 2 is combined with all high-frequency carrier signal injection methods presented in Chapters 3, 4 and 5 to evaluate the effectiveness of the rotor position estimation at whole speed region for dual three-phase PMSM. To achieve smooth transition between the combined methods, a function similar to hysteresis is applied for certain speed range with optimum weighted gains for both estimated positions without having complex structure and consuming time for computation.

6.2. Principle of Sensorless Control Methods for Low- and High-Speed Ranges

In this section, the principles of fundamental based model sensorless control method, and the high-frequency carrier signal injection techniques are briefly discussed as follows.

A. Flux-Linkage Observer Based Sensorless Control Method

A simple model could be utilised to obtain the rotor position by calculating the vector of the flux-linkage produced by the permanent magnet (PM). For rotor flux-linkage observer, the magnetic excitation flux, i.e. the rotor flux-linkage, can be calculated by subtracting the voltage drop on the inductance from the stator flux-linkage vector in the stationary reference frame as given below [WU91] [SHE02].

In $\alpha\beta$ reference frame, the stator voltage vector is given by

$$\bar{V}_{s\alpha\beta} = p\bar{\psi}_{s\alpha\beta} + R_s\bar{I}_{s\alpha\beta} \tag{6.1}$$

and by integrating the respective back-EMF, the stator flux-linkage vector in the stationary reference is given by

$$\bar{\psi}_{s\alpha\beta} = \int \left(\bar{V}_{s\alpha\beta} - R_s\bar{I}_{s\alpha\beta}\right)\, dt \tag{6.2}$$

Then, the flux-linkage vector produced by PM ($\bar{\psi}_{r\alpha\beta}$) is expressed as

$$\bar{\psi}_{r\alpha\beta} = \bar{\psi}_{s\alpha\beta} - L_s\bar{I}_{s\alpha\beta} \tag{6.3}$$

where $V_{s\alpha\beta}$, $\psi_{s\alpha\beta}$, $I_{s\alpha\beta}$ denote the stator voltage, flux-linkage and current vectors in $\alpha\beta$ reference frame, respectively. R_s represents the stator resistance, and p is referred to as the differential operator, while the stator self-inductance is denoted by L_s.

Generally, for surface-mounted permanent magnet synchronous machine (SPMSM) which is utilized in this investigation, $L_\alpha = L_\beta = L_s$. Thus, the rotor fluxes for SPMSM in α — and β – axes can be expressed as [SON09] [XU14]

$$\psi_{r\alpha} = \int \left(v_\alpha - R_s i_\alpha\right)\, dt - L_s i_\alpha \tag{6.4}$$

$$\psi_{r\beta} = \int \left(v_\beta - R_s i_\beta\right)\, dt - L_s i_\beta \tag{6.5}$$

Hence, the rotor position can be estimated

$$\theta_r^e = arctan\left(\frac{\psi_{r\beta}}{\psi_{r\alpha}}\right) \tag{6.6}$$

where θ_r is electrical rotor position.

Due to the lack of sufficient back-EMF induced in the stator winding at low speed region, it is well known that this method break down at low speeds. For full details about the principle of the flux-linkage observer, see Chapter 2, Section 2.2. On the other hand, the machine-saliency-based methods is preferred to be implemented at low-speed region which demonstrate an outstanding performance at standstill and low-speed range. These methods rely on the machine saliency resulted from either geometric rotor saliency or saliency resulting from the magnetic-saturation. The most commonly used methods of the continuous carrier signal injection are; a pulsating signal injection [COR98] [AIH99] [JAN03] [LI09b] [GON11b], and a rotating sinusoidal signal injection [JAN95] [GON11b]. Such methods are briefly described below.

B. High-Frequency Pulsating Signal Injection Based Sensorless Control Method

In the case of pulsating carrier voltage injection strategy, a high-frequency pulsating carrier voltage is injected into *d*-axis or *q*-axis in the estimated *dq*-synchronous reference frame. In this investigation, the carrier voltage is injected into *d*-axis of the estimated reference frame, and it is expressed as (6.7). A super-position of rotating carrier vectors in opposite direction can describe this injection as illustrated in Fig. 6.1. Then, the rotor position can be estimated by minimizing the amplitude of the modulated carrier current response which is orthogonal to the injection axis, Chapter 3, or it can be extracted from zero-sequence carrier voltage, Chapter 4. For more information regarding to rotor position estimation using carrier current response, refer to Chapter 3, subsection 3.3.1. For rotor position estimation utilizing zero-sequence carrier voltage based on pulsating injection method, see Chapter 4.

$$\begin{bmatrix} v_{dh}^e \\ v_{qh}^e \end{bmatrix} = V_c \begin{bmatrix} \cos\alpha \\ 0 \end{bmatrix}, \text{ where } \alpha = \omega_c t + \varphi \tag{6.7}$$

where V_c, ω_c and φ are defined as the amplitude, angular speed, and the initial phase angle of the injected high-frequency pulsating voltage, respectively.

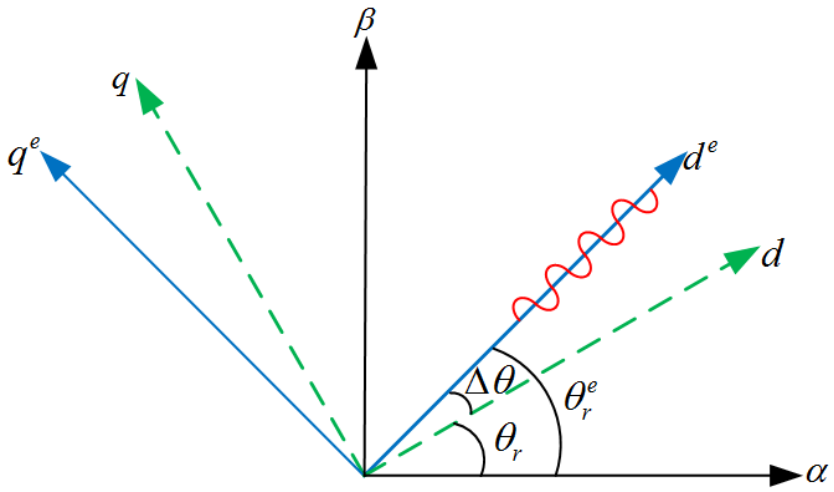

Fig. 6.1. Pulsating carrier signal injection.

C. High-Frequency Rotating Signal Injection Based Sensorless Control Method

For rotating voltage injection method, a three-phase balanced carrier voltage is injected into $\alpha\beta$-reference frame to compose a rotating excitation superimposed on fundamental excitation [ZHU11] [JAN04] as shown in Fig. 6.2. The injected rotating carrier voltage vector into the stationary reference frame is given as (6.8). Then, the information of rotor position could be obtained either from the position-dependant modulated current response, Chapter 3, or from the zero-sequence carrier voltage, Chapter 5. For more details about the rotor position estimation employing carrier current response, see Chapter 3, subsection 3.3.2, whilst Chapter 5 discusses the rotor position estimation using zero-sequence carrier voltage based on rotating injection method.

$$\begin{bmatrix} v_{\alpha h} \\ v_{\beta h} \end{bmatrix} = V_c \begin{bmatrix} \cos\alpha \\ \sin\alpha \end{bmatrix}, \text{ where } \alpha = \omega_c t + \varphi \tag{6.8}$$

where φ, V_c, and ω_c represent the initial phase angle, the amplitude, and the angular speed of the injected rotating carrier voltage, respectively.

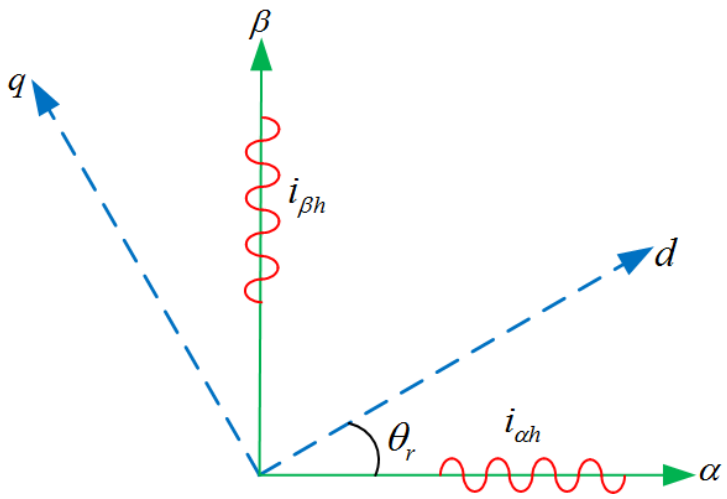

Fig. 6.2. Rotating carrier signal injection.

6.3. Sensorless Control Structure Combining High-Frequency Carrier Signal Injection Methods with Flux-Linkage Observer

To extend the sensorless control performance over wide speed range for dual three-phase PMSM, a combination of two sensorless control strategies is introduced in this chapter to avoid the obstacles of high-frequency carrier signal injection techniques at high speed. The combined sensorless control method includes the flux-linkage observer based sensorless control strategy and high-frequency carrier signal injection techniques. In this chapter, the investigation carried out with four different high-frequency carrier signal injection methods which are combined with the flux-linkage observer, namely pulsating injection using carrier current response, rotating injection utilizing carrier current response, pulsating injection using zero-sequence carrier voltage response, and rotating injection employing zero-sequence carrier voltage response. At low-speed range, the high-frequency carrier signal injection methods are utilized for rotor position estimation, while the flux-linkage observer is employed to estimate the rotor position at high-speed range. A smooth transition between the two combined methods is required. Between the low-speed range and high-speed range, there is an area to change the algorithm of the position estimator. It should be changed smoothly to ensure the system stability, and also high dynamic performance.

To achieve smooth transition between the combined methods, a function similar to hysteresis is applied for certain speed range with optimum weighted gains for both estimated positions as expressed in (6.9), where the high frequency injection method can work for zero- to low-speed

range, and for high-speed range, the flux-linkage observer method will take over.

$$\theta_r^e = k \times \theta_{r\_hf}^e + (1-k) \times \theta_{r\_fo}^e \tag{6.9}$$

where θ_r^e is referred to as final estimated rotor position, $\theta_{r\_hf}^e$ denotes the estimated rotor position of high-frequency carrier signal injection method, while the estimated rotor position of the flux-linkage observer is represented by $\theta_{r\_fo}^e$, and *k* is the weighting gain which can be calculated as

$$k = \begin{cases} 1 & \text{if } \omega_{prev.} < \omega_{low} \\ \dfrac{1}{\omega_{low} - \omega_{high}} (\omega_{prev.} - \omega_{high}) & \text{if } \omega_{low} < \omega_{prev.} < \omega_{high} \\ 0 & \text{if } \omega_{prev.} > \omega_{high} \end{cases} \tag{6.10}$$

where $\omega_{prev.}$ is the speed of the previous step, ω_{low} referred to as low-speed border of the area, and the high-speed border of the area is denoted by ω_{high}.

It is worth mentioning that the injection of the high-frequency signal should be gradually reduced until it reaches zero to reduce the adverse effects of the injected signal to the system when the speed is higher than the high-speed border.

6.4. Performance of Rotor Position Estimation with Different Combinations

In order to verify the combined sensorless control method, experimental tests are carried out on prototype dual three-phase PMSM whose specifications are listed in Appendix II, with the aid of dSPACE platform. Besides, the sampling frequency is set to 10 kHz, while the DC-link voltage is 40V. In the experimental tests, the low-speed border ω_{low} is chosen as 60 rpm, and the high-speed border is chosen as 150 rpm. The overall sensorless control system is illustrated in Fig. 6.3.

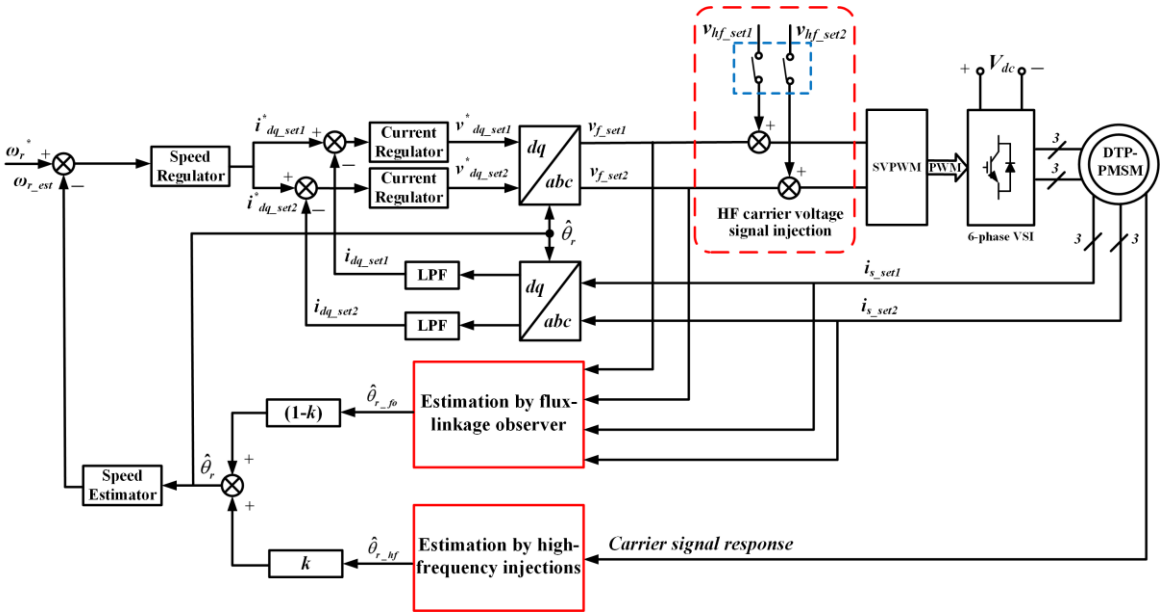

Fig. 6.3. Overall sensorless control system.

In low-speed range, a high frequency voltage signal (V_c=8V, f_c=500Hz) is injected into the into the system. It will disappear when the machine runs in high-speed range, and the estimator of the flux-linkage observer starts to work. The performances of rotor position estimation with different combinations for dual three-phase PMSM are investigated, and shown as follows.

A. Rotor Position Estimation By Utilizing Pulsating Injection Combined with Flux-Linkage Observer

In this case, the flux-linkage observer is combined with the conventional pulsating injection using carrier current response. The flux-linkage observer is introduced in Chapter 2, whilst the conventional pulsating injection using carrier current response is presented in Chapter 3, section 3.3.1. When the rotor initial speed is zero and step changed to 80 rpm and then to 250rpm, the rotor speed response is shown in Fig. 6.4 (a), and the comparison of the actual and estimated rotor positions together with the estimation error are illustrated in Fig. 6.4 (b).

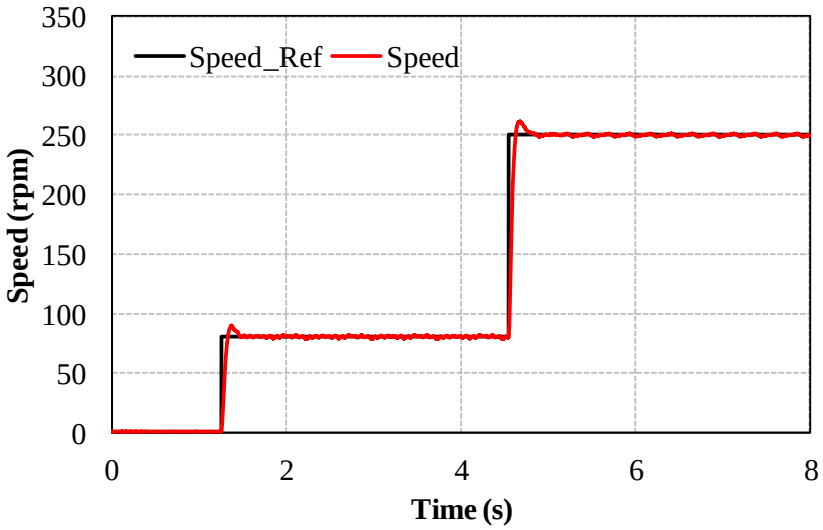

(a) Speed response

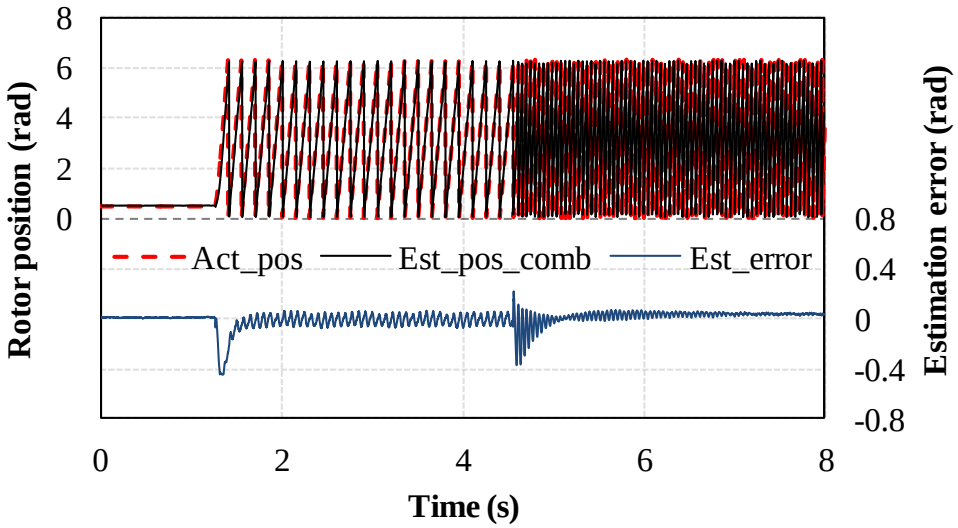

(b) Rotor position estimation

Fig. 6.4. Sensorless control performance from low- to high-speed range, 0-80-250 rpm.

Furthermore, the performance of the combined method is shown in Fig. 6.5 when the speed changes from -50 rpm to 200 rpm. Both results show good position tracking with a smooth transition between the two sensorless control methods.

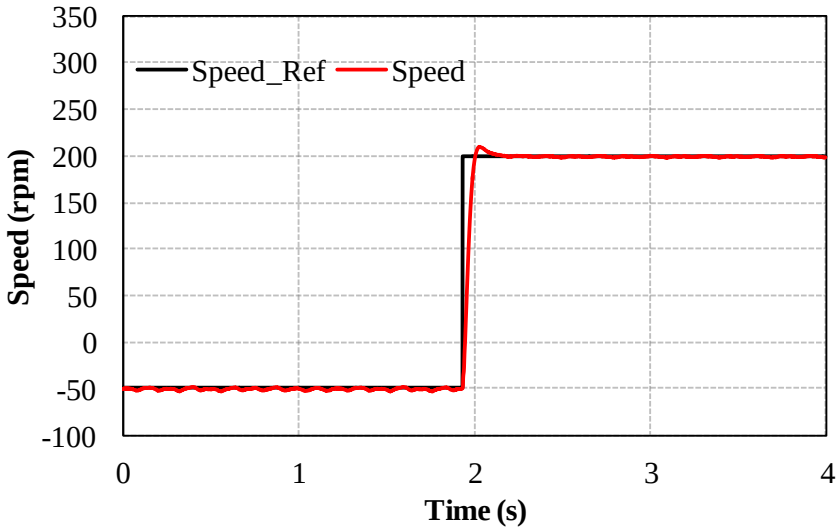

(a) Position estimation

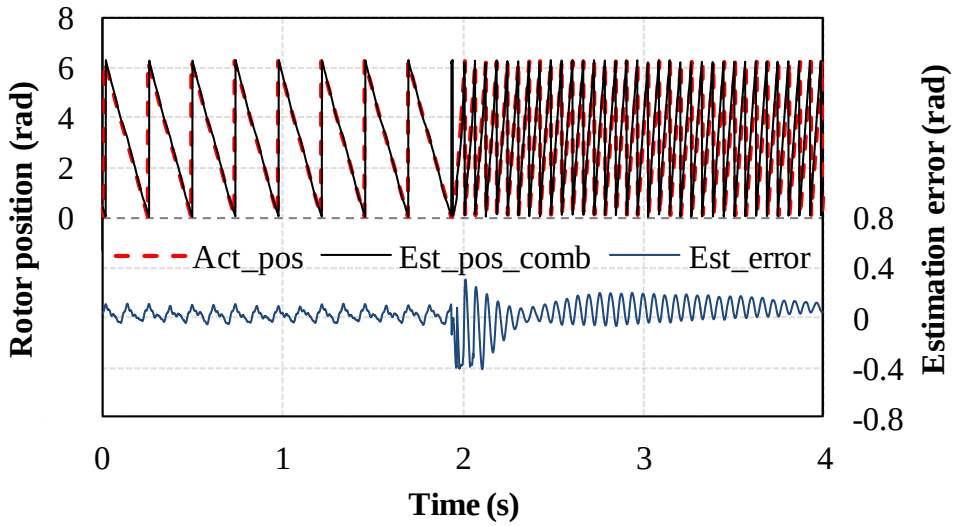

(b) Speed response

Fig. 6.5. Sensorless control performance from low- to high-speed range, -50-200 rpm.

B. Rotor Position Estimation By Utilizing Rotating High-Frequency Injection Combined with Flux-Linkage Observer

Here, the flux-linkage observer is combined with the conventional rotating injection using carrier current response. The conventional rotating injection using carrier current response is addressed in Chapter 3, section 3.3.2. The sensorless control performances of this combination under two different speed step changes are shown in Fig. 6.6 and Fig. 6.7, respectively, where Fig. 6.6 shows the sensorless control performance under speed step change (0-80-250rpm), and the

sensorless control performance when the speed step change as (-50 to 200 rpm) is illustrated in Fig. 6.7. It can be found that large oscillation in the estimation error at low-speed, and this is can be explained by the machine multiple saliencies effects [XU15]. However, a smooth transition between the low-speed and high-speed operation region can be observed.

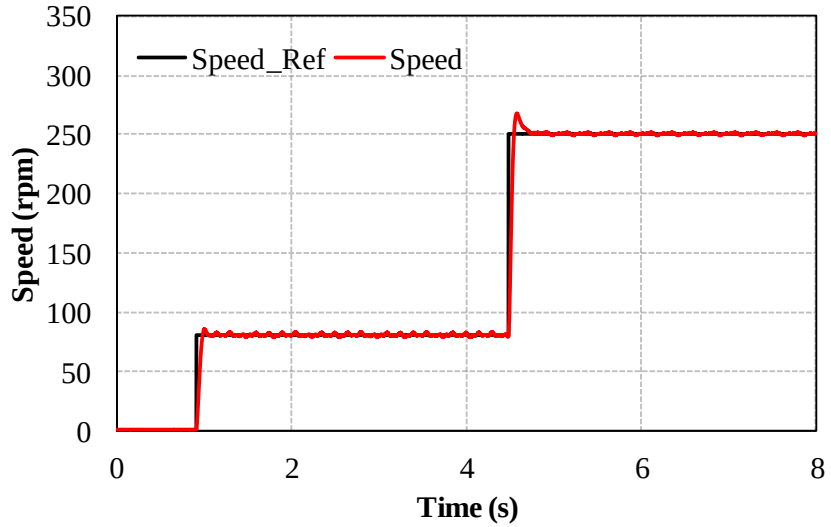

(a) Speed response

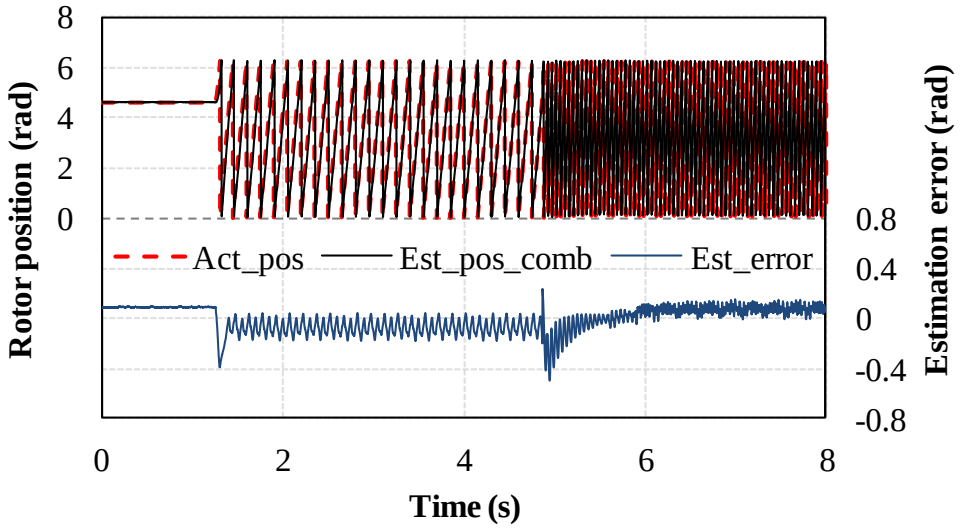

(b) Rotor position estimation

Fig. 6.6 Sensorless control performance from low- to high-speed range, 0-80-250 rpm.

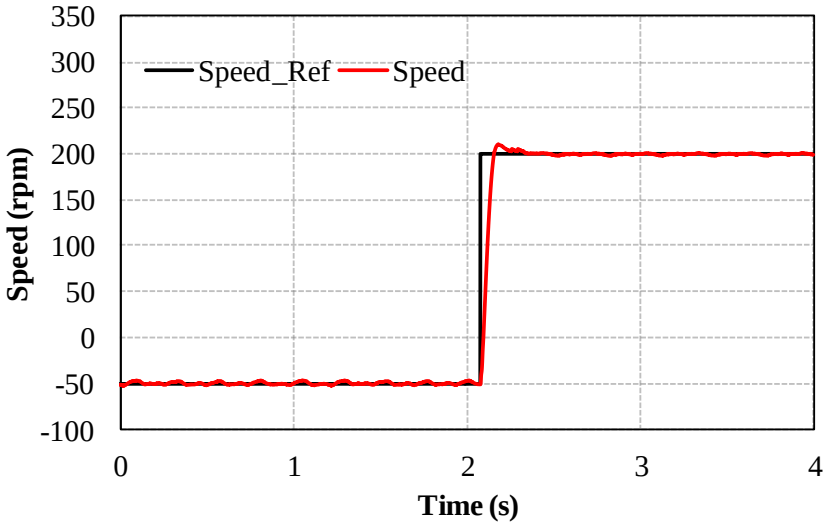

(a) Speed response

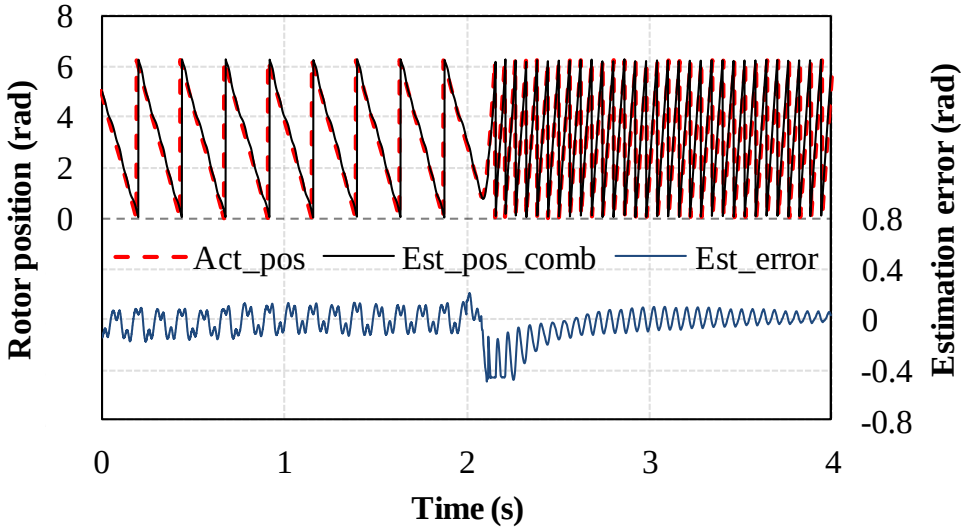

(b) Rotor position estimation

Fig. 6.7 Sensorless control performance from low- to high-speed range, -50-200 rpm.

C. Rotor Position Estimation By Utilizing Pulsating High-Frequency Injection Employing Zero-Sequence Voltage Combined with Flux-Linkage Observer

For this combination sensorless control method, the flux-linkage observer is combined with the pulsating injection employing zero-sequence carrier voltage. The pulsating injection with zero-sequence carrier voltage is introduced in Chapter 4. Fig. 6.8 shows the sensorless control performance where the rotor speed reference is given as 0-80-250 rpm. Moreover, when the rotor speed is step changed from -50 rpm to 200 rpm, the sensorless control performance is illustrated

in Fig. 6.9. It can be clearly seen that an outstanding rotor position estimation performance can be observed with smooth transition when the speed is switched from low-speed range to high-speed range.

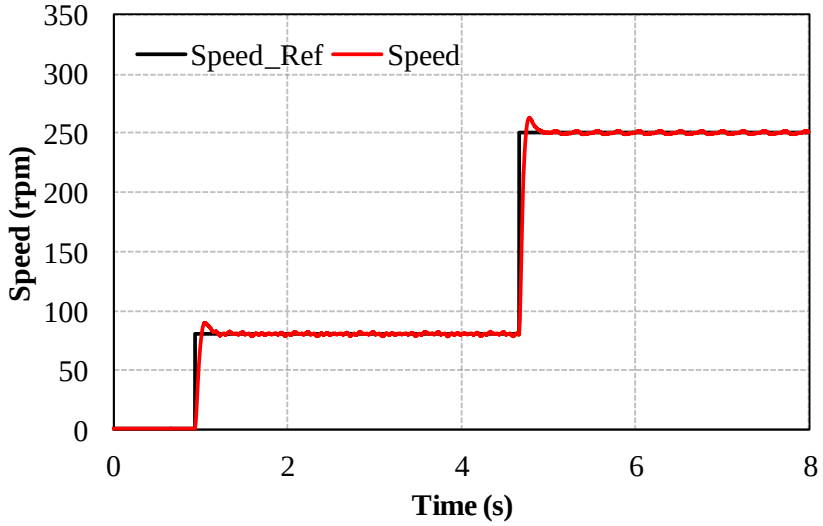

(a) Speed response

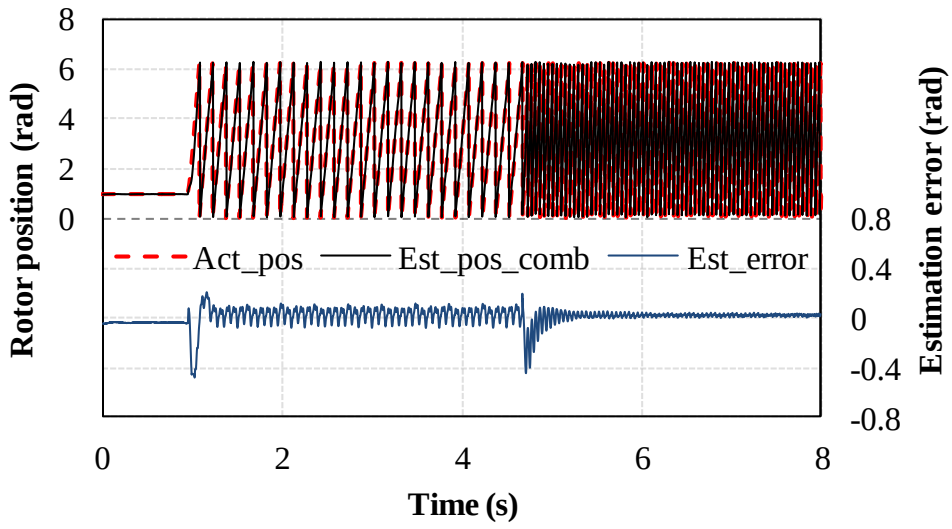

(b) Rotor position estimation

Fig. 6.8. Sensorless control performance from low- to high-speed range, 0-80-250 rpm.

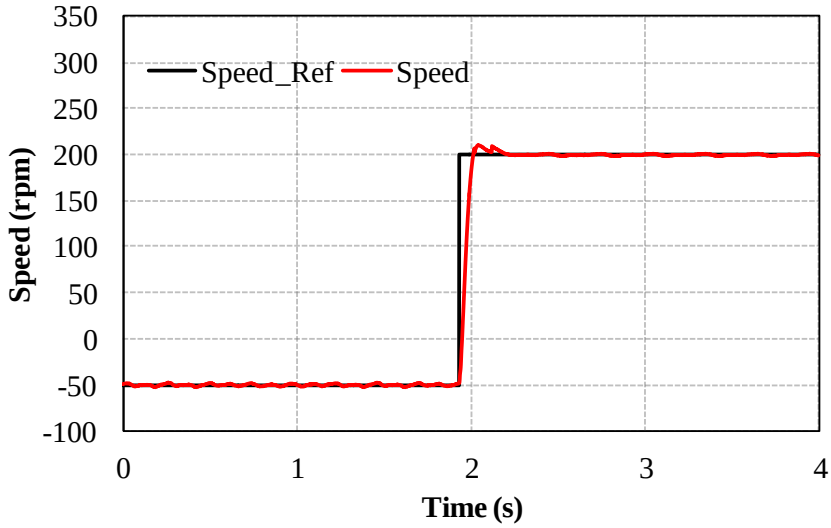

(a) Speed response

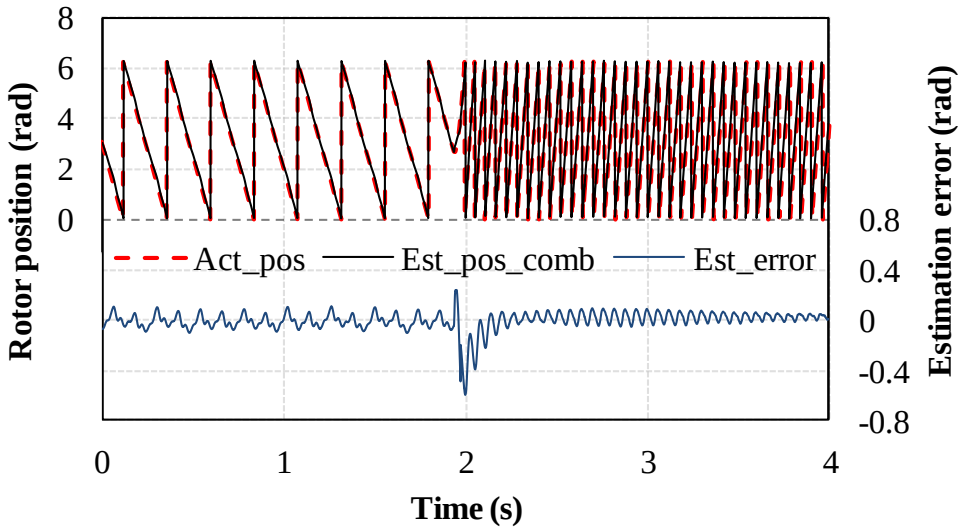

(b) Rotor position estimation

Fig. 6.9. Sensorless control performance from low- to high-speed range, -50-200 rpm.

D. Rotor Position Estimation By Utilizing Rotating High-Frequency Injection Employing Zero-Sequence Voltage Combined with Flux-Linkage Observer

In this combined sensorless control method, the flux-linkage observer is combined with the rotating injection utilizing zero-sequence carrier voltage. The rotating injection employing zero-sequence carrier voltage to estimate the rotor position is presented in Chapter 5. The dynamic sensorless control performance of this method is illustrated in Fig. 6.10, where the rotor speed reference is zero and step change to 80rpm and then to 250rpm, and then when the rotor speed

reference is given as (-50-200rpm), the sensorless control performance is illustrated in Fig. 6.11. It can be found that the performances of rotor position estimation for both conditions exhibit good position tracking with considering a smooth transition between different speed ranges.

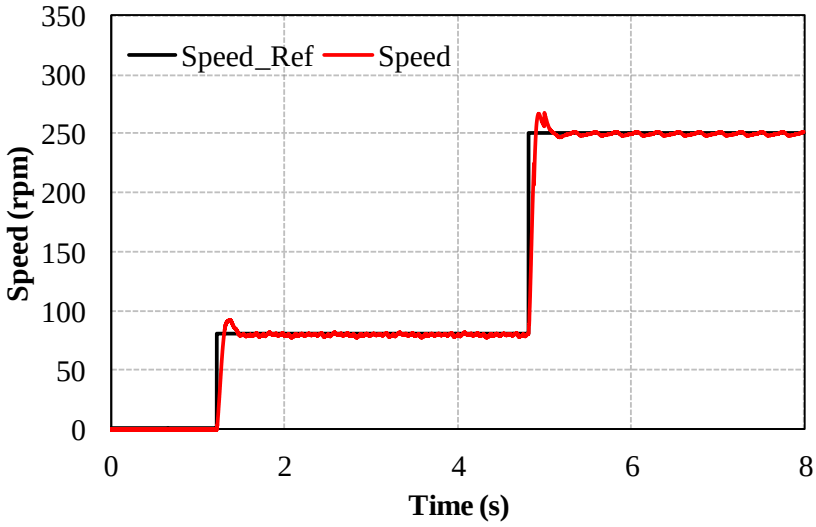

(a) Speed response

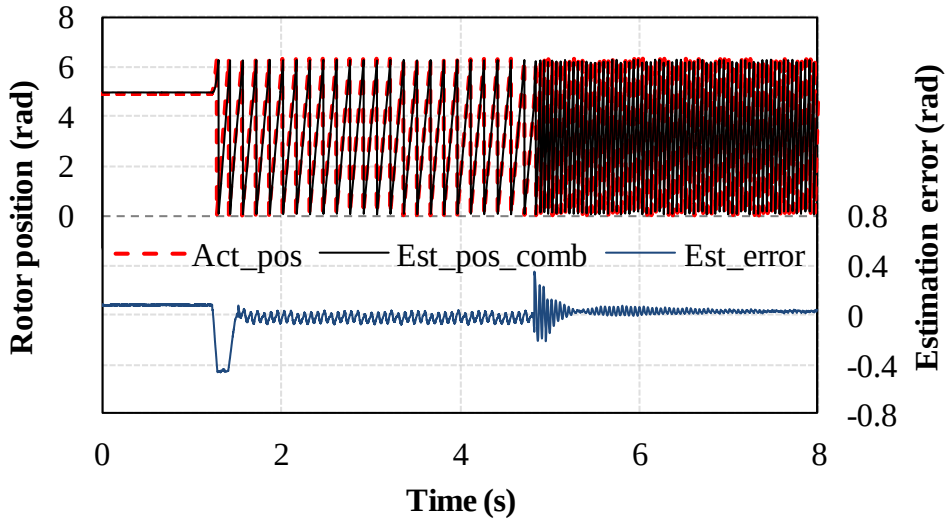

(b) Rotor position estimation

Fig. 6.10. Sensorless control performance from low- to high-speed range, 0-80-250 rpm.

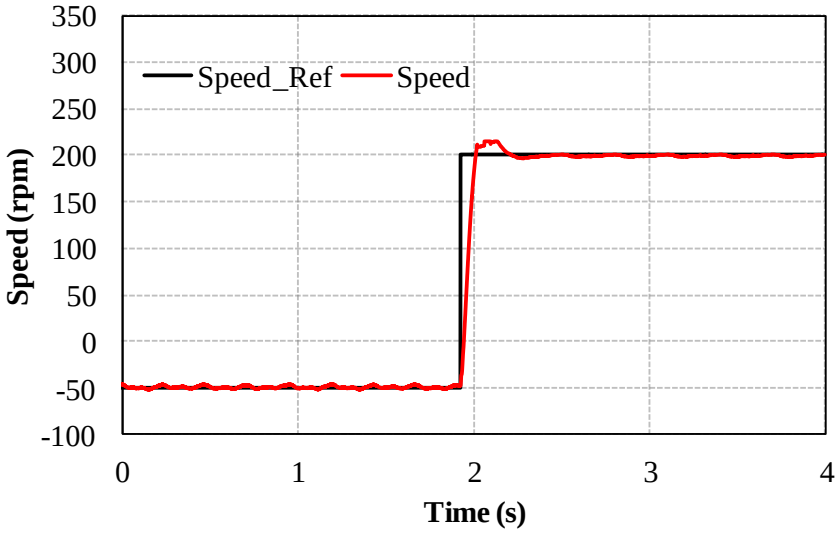

(a) Speed response

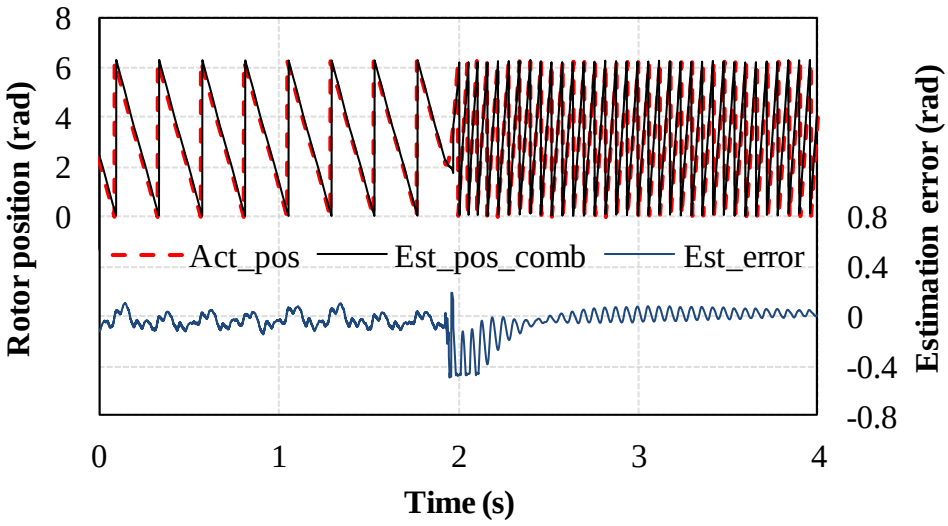

(b) Rotor position estimation

Fig. 6.11. Sensorless control performance from low- to high-speed range, -50-200 rpm.

6.5. Summary

In this chapter, combination of sensorless control strategies to derive the estimated rotor position at full speed range with smooth transition between the low-speed and high-speed ranges have been introduced. The combined sensorless control method includes the flux-linkage observer technique and four different high-frequency carrier signal injection methods, namely pulsating injection utilizing carrier current response, rotating injection employing carrier current response, pulsating injection using zero-sequence carrier voltage response, and rotating injection utilizing zero-sequence carrier voltage response. These techniques are applied to dual three-phase PMSM to investigate the sensorless control performance under different speed ranges.

The rotor position is estimated by employing the high-frequency carrier signal injections methods at low-speed range, while the flux-linkage observer method is utilized to estimate the rotor position at high-speed range. A function similar to hysteresis is applied for certain speed range with optimum weighted gains for both estimated positions to achieve a smooth transition between the combined methods.

From the experimental results, it has been found that a smooth transition from the high-frequency carrier signal injections methods at low speeds to the flux-linkage observer strategy at higher speeds are achieved, and the system stability is ensured.

CHAPTER 7

GENERAL CONCLUSIONS AND DISCUSSION

This thesis focuses on the sensorless control of single and dual three-phase PMSM drives to improve the rotor position estimation in different sensorless control methods covering the low- and high-speed ranges, including the sensorless control based on flux-linkage observer (FO) scheme and extended Kalman filter (EKF) scheme in high speed region, and sensorless control methods based on high-frequency voltage injection at zero speed and in low speed region.

7.1. Sensorless Control Based on Flux-Linkage Observer and Simplified EKF for Single and Dual Three-Phase PMSMs

To achieve high performance control of PMSMs, accurate rotor position information is required, which can be obtained from high-resolution sensors, e.g. encoders and resolvers. However, such sensors may not only increase the system size and cost but also impair robustness and reliability of the system. Therefore, various sensorless control techniques have been developed, and they can be classified into two groups: methods based on machine saliency, and methods based on fundamental model.

The former approaches have been demonstrated that they are capable of providing high performance sensorless control at low-speed and standstill operating regions. In contrast, the methods based on fundamental model can provide superior performance in medium- and high-speed ranges where the machine model can be accurately established.

The main idea of sensorless control strategies based on the fundamental model is the estimation of the back electromotive force (back-EMF) or the flux-linkage, which involve the information of rotor position, according to the machine model. Hence, the rotor position estimation could be accomplished via open-loop calculation, or closed-loop observer such as flux-linkage observer (FO), or directly obtained from the machine model utilizing adaptive observers like an extended Kalman filter (EKF). The most common method is the integration of back-EMF which is stator flux-linkage observer but such method is very sensitive to machine parameters, and machine variables. Alternatively, EKF algorithm can directly estimate the rotor position from the machine model. The EKF is a full-order stochastic observer for the recursive optimum state estimation of a nonlinear dynamic system in real time, which shows good position and speed

estimation performance. However, it requires relatively complex matrix computations, which make it challenging to be implemented in practice. On the other hand, a simplified EKF algorithm has been developed to be combined with a back-EMF estimator for accurate speed estimation.

Ideally, both of the FO and EKF approaches exhibit decent speed and rotor position estimation performance. However, in most of the industrial applications, some issues such as distorted back-EMF and current harmonics could more or less affect the sensorless control performance for both strategies.

Thus, based on the detailed discussion on both commonly used fundamental-model-based sensorless control methods, i.e. FO and simplified EKF, the influence of harmonics in back-EMF and currents on rotor position and speed estimation accuracy for both FO and EKF is investigated for single and dual three-phase PMSMs. It has been demonstrated that the performance of conventional FO based sensorless control would be deteriorated when the single three-phase PMSM suffers from distorted back-EMF. In order to overcome such issue, a simplified EKF with high-noise rejection ability has been adopted which provides a higher rotor position estimation accuracy. Furthermore, the switching-table-based direct torque control (ST-DTC) for DTP-PMSM, which inherently involves non-sinusoidal stator currents in addition to the distorted back-EMF, is taken as a case to investigate the effect of current harmonics on sensorless control performance.

By employing the FO and simplified EKF based sensorless vector control of single three-phase PMSM, it can be concluded that the rotor position estimation accuracy is less affected by the back-EMF harmonics when the simplified EKF method is utilized since it is less sensitive to such noises.

Then, when the influence of non-sinusoidal stator currents together with back-EMF harmonics has been investigated for the conventional and modified ST-DTC of DTP-PMSM, it has been indicated that the simplified EKF shows better accuracy of rotor position and speed estimation in both the conventional and modified ST-DTC strategies. In addition, its steady-state performance shows a slight superiority over that based on FO, in terms of flux and torque ripples, and THD of phase currents. For the dynamic performance, the estimated speed of simplified EKF shows less phase lag and fluctuations compared to that of FO. The comparison of both sensorless control strategies, i.e. FO and simplified EKF, is shown in Table 7.1.

TABLE 7.1

COMPARISON OF CONVENTIONAL FLUX-LINKAGE OBSERVER AND SIMPLIFIED EKF BASED SENSORLESS CONTROL

	Conventional flux-linkage observer	Simplified EKF
Applicability	SPM/IPM (with extended active flux)	SPM/IPM
Sensitivity to parameters	High	Medium
Sensitivity to back-EMF harmonics	High	Low
Sensitivity to current harmonics	High	Low
Signal-to-noise ratio	Medium	High
Steady-state operation	Good	Good
Dynamic-state operation	Medium	Good

7.2. Sensorless Control Based on High-Frequency Carrier Signal Injection for Single and Dual Three-Phase PMSMs

Since the methods based on fundamental model can only operate at high speed region because of the lack of sufficient back-EMF at low speed region, the machine-saliency based sensorless control techniques such as continuous carrier voltage signal injection methods are usually employed to overcome such an issue at low speed. The continuous carrier voltage signal injection strategies can be categorized into two major methods: pulsating carrier signal injection in the estimated reference frame, and rotating carrier signal injection in the stationary reference frame.

The saliency of the machine resulted from geometric anisotropy of the machine or magnetic saturation is a necessary requirement for the sensorless control strategies based on machine-saliency, which are well improved in numerous industrial applications due to their effectiveness of sensorless control performance at zero speed and in low-speed range. Normally, a high-frequency carrier voltage signals (rotating or pulsating) is persistently superimposed into the fundamental excitation. From the interaction of the injected voltage with the spatial saliency of the machine, a rotor position-dependent carrier signals responses are produced, i.e. carrier current response and zero-sequence carrier voltage. Then, the rotor position could be extracted from either the carrier current response or zero-sequence carrier voltage response by using a tracking position observer.

Besides, in terms of the selection of high-frequency injected voltage, higher position estimation error may occur when a low magnitude of injected carrier voltage is selected. Therefore, the higher magnitude of injected carrier voltage is preferred with considering carrier signal demodulation and the bandwidth of position observer. The injected carrier voltage amplitude is a compromise between the signal-to-noise ratio (SNR) of the carrier signals responses and the employing of DC bus voltage. It is reasonable that 30% of the total available DC bus voltage could be utilized for carrier signal injection. Furthermore, the carrier frequency of the injected carrier voltage is normally selected as 1/50 ~1/10 PWM frequency.

According to the detailed discussion on commonly used the sensorless control strategies based on high-frequency signal injection in Chapter 3, i.e. high-frequency pulsating carrier voltage injection into the estimated synchronous rotating reference frame, and rotating carrier voltage injection into the stationary reference frame. These techniques with utilizing the carrier current response are applied to single and dual three-phase PMSMs to investigate the sensorless control performances under steady-state and dynamic conditions. In case of DTP-PMSM, the high-frequency carrier signal injection methods are investigated for two modelling, i.e. double *dq* model, and vector space decomposition (VSD) model. Prior to applying the sensorless control strategies based on high-frequency carrier signal injection, the level of machine saliency variation with the load for the test machine is measured experimentally, and it has been found that the saliency level is appropriate to implement the sensorless control strategies based on high-frequency carrier signal injection. Furthermore, the influence of the cross-saturation on the rotor position estimation is analysed, and the simple compensation method of such effect is considered in this thesis.

In terms of rotor position estimation accuracy from the position-dependant carrier current response for both single and dual three-phase PMSMs, it has been concluded that the oscillation on the rotor position estimation error for dual three-phase PMSM employing VSD modelling approach is significantly reduced for both pulsation and rotating injections compared to that of single three-phase PMSM and dual three-phase PMSM employing double *dq* modelling approach. This is due to the mutual coupling between the two winding sets is eliminated in VSD approach.

The comparison of the pulsating and rotating carrier signals injections strategies employing carrier current response for single and dual three-phase PMSMs is summarized in Table 7.2.

TABLE 7.2 (TABLE 3.1)

COMPARISON OF CARRIER SIGNAL INJECTION METHODS FOR SINGLE AND DUAL THREE-PHASE PMSMs

	Pulsating (Three-phase PMSM)	Rotating (Three-phase PMSM)	Pulsating (DTP-PMSM, double dq Model)	Pulsating (DTP-PMSM, VSD)	Rotating (DTP-PMSM, double dq Model)	Rotating (DTP-PMSM, VSD)
Reference frame	Estimated synchronous	Stationary	Two estimated synchronous	Estimated synchronous	Two stationary	Stationary
Carrier voltage injection	Pulsating carrier voltage	Rotating carrier voltage	Two independent pulsating carrier voltages	Pulsating carrier voltage	Two independent rotating carrier voltages	Rotating carrier voltage
Carrier current	Amplitude-modulated	Phase-modulated	Amplitude-modulated	Amplitude-modulated	Phase-modulated	Phase-modulated
Cross-saturation angle	$-\theta_m / 2$	$-\theta_m / 2$	$-\theta_m / 2$	$-\theta_m / 2$	$-\theta_m / 2$	$-\theta_m / 2$
Oscillation error	Medium	Medium	Medium	Low	Medium	Low
Load effect	Sensitive	Sensitive	Sensitive	Sensitive	Sensitive	Sensitive
Steady-state	Good	Medium	Good	Very Good	Medium	Very Good
Dynamic-state operation	Good	Medium	Good	Very Good	Medium	Very Good
Sensitivity of error to injection frequency	Low	High	Low	Low	High	High

Furthermore, the zero-sequence carrier voltage can also be utilized to extract the rotor position information when applying the pulsating and rotating carrier signal injections strategies. Owing to the fact that the rotor position can be estimated by using zero-sequence carrier voltage, the sensorless control performances of both pulsating and rotating carrier signal injection methods employing zero-sequence voltage are investigated for single and dual three-phase PMSMs in Chapters 4 and 5, respectively. Compared to the carrier current signal, the zero-sequence carrier voltage signal has the advantage of lower total harmonic distortion (THD), and less sensitivity to the distortion of injected carrier voltage caused by the current regulator, PWM strategy, and inverter nonlinearity. Therefore, by utilizing the zero-sequence carrier voltage signal, the system bandwidth is significantly enhanced, and higher accuracy of position estimation can be achieved, which contributes to the improvement of stability of system. However, undesirable 6^{th} harmonic estimation error occurs for single three-phase PMSM with pulsating and rotating signals injections due to undesirable harmonic components in the zero-sequence carrier voltage. Such undesirable harmonic components are caused by multiple saliencies including primary saliency. To solve such issue, the existing methods require time-consuming offline measurements and complex structures.

As for the case of DTP-PMSM drives, thanks to the existence of additional degrees of freedom with independent high-frequency injected signals since it consists of two separated winding sets with two isolated neutral points, where the phase angle difference between the two injected high-frequency signals can be changed. Therefore, by applying the optimum phase shift angle between the injected signals, modified pulsating and rotating carrier signal injections methods employing zero-sequence voltage based sensorless control strategies are proposed to suppress the 6^{th} harmonic position errors. Besides, a new simple measurement method of zero-sequence carrier voltage is proposed where one voltage sensor is placed between the two isolated neutral points. The proposed methods can achieve the improved rotor position estimation accuracy with low computational burden. The experimental results verify the outstanding overall performance of the proposed methods for DTP-PMSM.

The comparison of the conventional pulsating and rotating carrier signals injection techniques utilizing carrier current response, and the techniques employing zero-sequence carrier voltage for DTP-PMSM is summarized in Table 7.3.

TABLE 7.3

COPMARISON OF PULSATING AND ROTATING CARRIER SIGNALS INJECTIONS TECHNIQUES FOR DTP-PMSM

	Pulsating injection-carrier current	Pulsating injection-zero-seq. voltage	Rotating injection-carrier current	Rotating injection-zero-seq. voltage
Implementation	Easy	Medium	Easy	Medium
Carrier signal response	Amplitude-modulated	Amplitude-modulated	Phase-modulated	Phase-modulated
Bandwidth	Medium	High	Medium	High
Sensitivity to distortion	High	Low	High	Low
Requirement of A/D resolution	High	Low	High	Low
Stability	Reduced	Very stable	Reduced	Very stable
Signal delays	Insensitive	Insensitive	Sensitive	Sensitive
Carrier signal demodulation	Simple	Simple	Complex	Complex
Cross-coupling saturation	Same	Same	Same	Same
Accuracy	High	High	Medium	High
Dynamic performance	Good	Good	Medium	Good

7.3. Sensorless Control for Dual Three-Phase PMSM Over Wide-Speed Range

The high-frequency carrier signal injection techniques have the drawbacks of extra losses, transient disturbances, torque ripple, additional current harmonics, and noise resulting from the carrier voltage injection in the high-speed range operation. Consequently, they fail to work in high speed region. Therefore, it is desirable to combine the advantages of high-frequency carrier signal injection techniques at low speed operation, and the lower losses and simplicity of fundamental model based sensorless control to achieve high performance of rotor position estimation. Such combinations have been addressed in literature for single three-phase machines only. Based on the detailed discussions on the high-frequency carrier signal injection methods and fundamental-model-based sensorless control strategies introduced in Chapters 2, 3, 4, and 5, the combined sensorless control methods are investigated for dual three-phase PMSM to achieve high performance of rotor position estimation with smooth transition between the low-speed range and the high-speed range.

The rotor position is estimated by employing the high-frequency carrier signal injections methods at low-speed range, while the flux-linkage observer method is utilized to estimate the rotor position in high-speed range. From the experimental results, it has been found that a smooth transition from the high-frequency carrier signal injections methods at low speeds to the flux-linkage observer strategy at higher speeds are achieved, and the system stability is ensured.

7.4. Future Work

This thesis covers different sensorless control techniques for single and dual three-phase PMSMs drives to improve the rotor position estimation over both the low- and high-speed ranges. However, some areas of research need to be further investigated. These areas are listed below as follows:

- Investigation on sensorless control performance for dual three-phase PMSM when the two stator winding are unbalanced. For instance, unbalance back-EMFs due to winding turn error, which causes unbalanced impedance of the two stator winding sets.
- Usually, the performances of the sinusoidal waveform injection techniques introduced in Chapters 3, 4, and 5 are insufficient for some applications, since the bandwidths of rotor position estimation are limited. Such limitation are restricted by the LPFs which are applied in the demodulation of the carrier signals responses. Also, the frequency of injected voltage cannot be too high to form a proper sinusoidal high-frequency injected voltage due to the limitation of PWM frequency. In order to enhance the rotor position estimation bandwidth, square waveform carrier signal injection method is preferred since the requirement of LPFs for demodulation is eliminated, and the dynamic performance can be remarkably enhanced. Such method is only applied for single three-phase machines. Therefore, it is worthy to investigate the sensorless control performance of square waveform carrier signal injection strategy utilizing both the carrier current response, and zero-sequence carrier voltage for dual three-phase machine.

REFERENCES

[ACA06] P. P. Acamley, and J. F. Watson, "Review of position-sensorless operation of brushless permanent-magnet machines," *IEEE Trans. Ind. Electron.*, vol. 53, no. 2, pp. 352-362, Apr. 2006.

[ACC12] A. Accetta, M. Cirrincione, M. Pucci, and G. Vitale, "Sensorless control of PMSM fractional horsepower drives by signal injection and neural adaptive-band filtering," *IEEE Trans. Ind. Electron*., vol. 59, no. 3, pp. 1355-1366, Mar. 2012.

[AIH99] T. Aihara, A. Toba, T. Yanase, A. Mashimo, and K. Endo, "Sensorless torque control of salient-pole synchronous motor at zero-speed operation," *IEEE Trans. Power Electronics*, vol. 14, no. 1, pp. 202-208, 1999.

[ALM14] A. H. Almarhoon, and Z. Q. Zhu, "Influence of back-EMF and current harmonics on position estimation accuracy of permanent magnet synchronous machine," *17th International Conference on Electrical Machines and Systems*, *ICEMS2014*, pp.2728-2733, Oct. 2014.

[ALN13] E. Al-nabi, B. Wu, N. R. Zargari, and V. Sood, "Sensorless control of CSC-fed IPM machine for zero- and low-speed operations using pulsating HFI method," *IEEE Trans. Ind. Electron.*, vol. 60, no. 5, pp. 1711–1723, May 2013.

[AND08] G. D. Andreescu, C. I. Pitic, F. Blaabjerg, and I. Boldea, "Combined-flux observer with signal injection enhancement for wide speed range sensorless direct torque control of IPMSM drives," *IEEE Trans. Energy Convers.*, vol. 23, no. 2, pp. 393–402, Jun. 2008.

[BAE03] B.-H. Bae, S.-K. Sul, J.-H. Kwon, and J.-S. Byeon, "Implementation of sensorless vector control for super-high-speed PMSM of turbo- compressor," *IEEE Trans. Ind. Appl.*, vol. 39, no. 3, pp.811-818, May/Jun., 2003.

[BAN16] F. Baneira, A. G. Yepes, O. Lopez, and J. Doval-Gandoy, "Estimation method of stator winding temperature for dual three-phase machines based on DC-signal injection," *IEEE Trans. Power Electron.*, vol. 31, no. 7, pp. 5141-5148, Jul. 2016.

[BAR10a] M. Barcaro, N. Bianchi, and F. Magnussen, "Faulty operations of a PM fractional-slot machine with a dual three-phase winding," *IEEE Trans. Ind. Appl.*, vol. 58, no. 9, pp. 3825-3832, 2010.

[BAR10b] M. Barcaro, N. Bianchi, and F. Magnussen, "Analysis and tests of a dual three-phase 12-slot 10-pole permanent-magnet motor," *IEEE Trans. Ind. Appl.*, vol. 46, no. 6, pp. 2355-2362, 2010.

[BAR12] M. Barcaro, A. Faggion, N. Bianchi, S. Bolognani, "Sensorless rotor position detection capability of a dual three-phase fractional-slot IPM machine," *IEEE Trans. Ind. Appl.*, vol. 48, no. 6, pp. 2086-2078, 2012.

[BIA07] N. Bianchi and S. Bolognami, "Influence of rotor geometry of an IPM motor on sensorless control feasibility," *IEEE Trans. Ind. Appl.*, vol. 43, no. 1, pp.87-96, 2007.

[BIA08] N. Bianchi, S. Bolognani, J.-H. Jang, and S.-K. Sul, "Advantages of inset PM machines for zero-speed sensorless position detection," *IEEE Trans. Ind. Appl.*, vol. 44, no. 4, pp. 1190-1198, Aug. 2008.

[BOG06] A. Boglietti, R. Boji, A. Cavagnino, and Tenconi, "Effiecincy analysis of PWM inverter fed three-phase and dual three-phase induction machines," *IEEE Industry Applications Conference 2006*, vol. 1, 2006, pp. 434-440.

[BOJ03] R. Bojoi, M. Lazzari, F. Profumo, and A. Tenconi, "Digital field-oriented control for dual three-phase induction motor drives," *IEEE Trans. Ind. Appl.*, vol. 39, no. 3, pp. 752-760, May/Jun. 2003.

[BOJ05] R. Bojoi, F. Farina, G. Griva, F. Profumo, and A. Tenconi, "Direct torque control for dual three-phase induction motor drives," *IEEE Trans. Ind. Appl.*, vol. 41, no. 6, pp. 1627-1636, Nov./Dec. 2005.

[BOJ06] R. Bojoi, E. Levi, F. Farina, A. Tenconi, and F. Profumo, "Dual three-phase induction motor drive with digital current control in the stationary reference frame," *IEE Proc.-Electr. Power Appl.*, vol. 153, no. 1, pp. 129-139, Jan. 2006.

[BOL09] I. Boldea, M. C. Paicu, G. D. Andreescu, and F. Blaabjerg, "Active flux DTFC-SVM sensorless control of IPMSM," *IEEE Trans. Energy Conversion*, vol. 24, no. 2, pp. 314-322, Mar./Apr. 2009.

[BOL11] S. Bolognani, S. Calligaro, R. Petrella, and M. Sterpellone, "Sensorless control for IPMSM using PWM excitation, analytical developments and implementation issues," *Symposium on Sensorless Control of Electrical Drives (SLED2011)*, 2011, pp. 64-73.

[BRI04] F. Briz, M. W. Degner, P. García, and R. D. Lorenz, "Comparison of saliency-based sensorless control techniques for AC machines," *IEEE Trans. Ind. Appl.*, vol. 40, no. 4, pp. 1107–1115, Jul./Aug. 2004.

[BRI05] F. Briz, M. W. Degner, P. García, and J. M. Guerrero, "Rotor position estimation of AC machines using the zero sequence carrier signal voltage," *IEEE Trans. Ind. Appl.*, vol. 41, no. 6, pp. 1637–1646, Nov./Dec. 2005.

[CAP01] E. Capecchi, P. Gulielmi, M. Pastorelli, and A. Vagati, "Position-sensorless control of transverse-laminated synchronous reluctance motor," *IEEE Trans. Industry Applications*, vol. 37, no. 6, pp. 1768-1776, 2001.

[CAR06] C. Caruana, G. M. Asher, and M. Summer, "Performance of HF signal injection techniques for zer-low-frequency vector control of induction machines under sensorless conditions," *IEEE Trans. Ind. Electron.*, vol. 53, no. 1, pp. 225–238, Feb. 2006.

[CHE00] Z. Chen, M. Tomita, S. Ichikawa, S. Doki, and S. Okuma, "Sensorless control of interior permanent magnet synchronous motor by estimation of an extended electromotive force," *Industry Applications Conference*, vol. 3, 2000, pp. 1814-1819.

[CHE03] Z. Chen, M. Tomita, S. Koki, and S. Okuma, "An extended electromotive force model for sensorless control of interior permanent-magnet synchronous motors," *IEEE Trans. Ind. Electron.*, vol. 50, no. 2, pp. 288-295, 2003.

[CHE14] Z. Chen, J.B. Gao, F.X. Wang, Z.X. Ma, Z.B. Zhang, and R. Kennel, "Sensorless control for SPMSM with concentrated windings using multi-signal injection method," *IEEE Trans. Ind. Electron.*, vol.61, no.12, pp.6624-6634, Dec. 2014.

[CHE14] H. S. Che, E. Levi, M. Jones, W. P. Hew, and N. Abd Rahim, "Current Control Methods for an Asymmetrical Six-Phase Induction Motor Drive," *IEEE Trans. Power Electron.*, vol. 29, no. 1, pp. 407-417, Jan 2014.

[CHE99] Y. S. Chen, "Motor topologies and control strategies for permanent magnet brushless AC drives," PhD Thesis Submitted to University of Sheffield, UK, 1999.

[CHI09] S. Chi, Z. Zhang, and L. Xu, "Sliding-mode sensorless control of direct-drive PM synchronous motors for washing machine applications," *IEEE Trans. Ind. Appl.*, vol. 45, no. 2, pp. 582–590, Mar./Apr. 2009.

[CHI09] S. Chi, Z. Zhang, and L. Xu, "Sliding-mode sensorless control of direct-drive PM synchronous motors for washing machine applications," *IEEE Trans. Ind. Appl.*, vol. 45, no. 2, pp.582-590, 2009.

[CON00] A. Consoli, G. Scarcella, and A. Testa, "A new zero-frequency flux position detection approach for direct-field-oriented-control drives," *IEEE Trans. Ind. Appl.*, vol. 36, no. 3, pp. 797–804, May./Jun. 2000.

[CON06] A. Consoli, G. Scarcella, G. Bottiglieri, and A. Testa, "Harmonic analysis of voltage zero-sequence-based encoderless techniques," *IEEE Trans. Ind. Appl.*, vol. 42, no. 6, pp. 1548–1557, Nov./Dec. 2006.

[COR98] M. J. Corley and R. D. Lorenz, "Rotor position and velocity estimation for a salient-pole permanent magnet synchronous machine at standstill and high speed," *IEEE Trans. Industry Applications*, vol. 34, no. 4, pp.784-789, 1998.

[CUP10] F. Cupertino, P. Giangrande, L. Salatore, and G. Pellegrino, "Model based design of sensorless control scheme for permanent magnet motors using signal injection," *IEEE Energy Conversion Congress and Exposition (ECCE2010)*, 2010, pp. 3139-3146.

[DEG98] M. W. Degner, and R. D. Lorenz, "Using multiple saliencies for the estimation of flux, position, and velocity in AC machines," *IEEE Trans. Ind. Appl.*, vol. 34, no. 5, pp. 1097-1104, 1998.

[DEP88] M. Depenbrock, "Direct self-control (dsc) of inverter-fed induction machine," *IEEE Trans. Power Electron.*, vol. 3, no. 4, pp. 420-429, Oct. 1988.

[DSP10] Dspace, "Hardware installation and configuration reference,", Release 6.6, May 2010.

[DUR11] M. J. Duran, J. Prieto, F. Barrero, S. Toral, "Predictive current control of dual three-phase drives using restrained search techniques," *IEEE Trans. Ind. Electron.*, vol. 58, no. 8, pp. 3253-3263, Aug. 2011.

[DWA08] S. Dwari, and L. Parsa, "Open-circuit fault tolerant control of five-phase permanent magnet motors with third-harmonic back-EMF," *34th Annual Conference of IEEE on Industrial Electronics*, *IECON 2008*, 2008, pp. 3114-3119.

[FAE09] M. Faeq, and D. Ishak, "A new scheme sensorless control of BLDC motor using software PLL and third harmonic back-EMF," *IEEE Industrial Electronics and Applications*, *ISIEA*, 2009, pp. 861-865.

[FAR06] F. Farina, R. Bojoi, A. Tenconi, and F. Profumo, "Direct torque control with full order stator flux observer for dual-three phase induction motor drives," *IEEJ Trans. Ind. Appl*., vol. 126, no. 4, pp. 412-419, 2006.

[FOO09a] G. Foo, and M. F. Rahman, "Direct torque and flux control of an IPM synchronous motor drive using a back stepping approach," *IET Electric. Power Appl*., vol. 3, no. 5, pp. 413-421, 2009.

[FOO10] G. Foo, and M. F. Rahman, "Sensorless sliding-mode MTPA control of an IPM synchronous motor drive using a sliding-mode observer and HF signal injection," *IEEE Trans. Ind. Electron.*, vol. 57, no. 4, pp. 1270–1278, Apr. 2010.

[FOO10] G. FOO, and M. F. Rahman, "Sensorless sliding-mode MTPA control of IPM synchronous motor drive using a sliding-mode observer and HF signal injection," *IEEE Trans. Ind. Electron*., vol. 57, no. 4, pp. 1270-1278, 2010.

[FUE11] E. Fuentes, and R. Kennel, "Sensorless-predictive torque control of the PMSM using a reduced order extended kalman filter," *Symposium on Sensorless Control for Electrical Drives*, 2011, pp. 123-128.

[FUR92] T. Furuhashi, S. Sangwongwanich, and S. Okuma, "A position and velocity sensorless control for brushless DC motors using an adaptive sliding mode observer," *IEEE Trans. Ind. Electron*., vol. 39, no. 2, pp. 89-95, 1992.

[GAB13] F. Gabriel, F. De Belie, X. Neyt, and P. Lataire, "High-frequency issues using rotating voltage injections intended for position self-sensing," *IEEE Trans. Ind. Electron.*, vol. 60, no. 12, pp. 5447–5457, Dec. 2013.

[GAD10] S. M. Gadoue, D. Giaouris, and J. W. Finch, "MRAS sensorlesss vector control of an induction motor using new sliding-mode and fuzzy-logic adaption mechanisms," *IEEE Trans. Energy Conversion*, vol. 25, no. 2, pp. 394-402, 2010.

[GAO07] Q. Gao, G. M. Asher, M. Sumner, and P. Makys, "Position estimation of AC machines over a wide frequency range based on space vector PWM excitation," *IEEE Trans. Ind. Appl.*, vol. 43, no. 4, pp. 1001-1011, 2007.

[GAO11] L. L. Gao, J. E. Fletcher, L. B. Zheng, "Low-speed control improvements for a two-level five-phase inverter-fed induction machine using classic direct torque control," *IEEE Trans. Ind. Electron.*, vol. 58, no. 7, pp. 2744-2754, Jul. 2011.

[GAR07] P. Garcia, F. Briz, M. W. Degner, and D. Diaz-Reigosa, "Accuracy, bandwidth, and stability limits of carrier-signal- injection- based sensorless control methods*," IEEE Trans. Ind. Appl.*, vol. 43, no. 4, pp. 990–1000, Jul./Aug. 2007.

[GON11] L. M. Gong, "Carrier signal injection based sensorless control of permanent magnet brushless AC machines," PhD Thesis Submitted to University of Sheffield, UK, 2011.

[GON11a] L. M. Gong, and Z. Q. Zhu, "A novel method for compensating inverter nonlinearity effects in carrier signal injection-based sensorless control from positive-sequence carrier current distortion," *IEEE Trans. Ind. Appl.*, vol. 47, no. 3, pp. 1283-1292, 2011.

[GON11b] L. M. Gong and Z. Q. Zhu, "Improved rotating carrier signal injection method for sensorless control of PM brushless AC motors, accounting for cross-saturation effect," *Power Electronics and ECCE Asia (ICPE & ECCE)*, pp. 1132-1139, 2011.

[GRE12] R. Gregor, and J. Rodas, "Speed sensorless control of dual three-phase induction machine based on a luenberger observer for rotor current estimation," *Annual Conference of IEEE on Industrial Electronics, IECON 2012*, 2012, pp. 3653-3658.

[GUE05] J. M. Guerrero, M. Leetmaa, F. Briz, A. Zamarron, and R. D. Lorenz, "Inverter nonlinearity effects in high-frequency signal-injection-based sensorless control methods," *IEEE Trans. Ind. Appl.*, vol. 41, no. 2, pp. 618-626, 2005.

[GUG06] P. Guglielmi, M. Pastorelli, and A. Vagaati, "Cross-saturation effects in IPM motor and related impact on sensorless control," *IEEE Trans. Ind. Appl.*, vol. 42, no. 6, pp. 1516-1522, 2006.

[HA00] J. I. Ha, and S. K. Sul, "Physical understanding of high-frequency injection method to sensorless drives of an induction machine," *Conference of IEEE Industry Applications*, 2000, pp. 1802-1808.

[HA08] J. I. Ha, "Analysis of inherent magnetic position sensors in symmetric AC machines for zero or low speed senssorless drives," *IEEE Trans. Magn.*, vol. 44, no. 2, pp. 4689-4696, Dec. 2008.

[HA99] J.-I. Ha, S.-J. Kang, and S.-K. Sul, "Position-controlled synchronous reluctance motor without rotational transducer," *IEEE Trans. Industry Applications*, vol. 35, no. 6, pp. 1393-1398, 1999.

[HAR00] L. Harnefors, and H. P. Nee, "A general Algorithm for speed and position estimation of AC motors," *IEEE Trans. Ind. Electron.*, vol. 47, no. 1, pp. 77-83, 2000.

[HAR96] L. Harnefors, "Speed estimation from noisy resolver signals," *Sixth International Conference on Power Electronics and Variable Speed Drives*, pp.279-282, 23-25 Sept. 1996.

[HAT05] K. Hatua, and V. T. Ranganathan, "Direct torque control schemes for split-phase induction machine," *IEEE Trans. Ind. Appl.*, vol. 41, no. 5, pp. 1243-1254, Sept./Oct. 2005.

[HAT05] K. Hatua and V. T. Ranganathan, "Direct torque control schemes for split-phase induction machine," *Power Electronics, Machines and Drives (PEMD2012)*, 2012, pp. 1-6, Sep./Oct. 2005.

[HE09] Y. He, W. Hu, Y. Wang, J. Wu, and Z. Wang, "Speed and position sensorless control for dual-three-phase PMSM drives," *Twenty-fourth Annual IEEE Applied Power Electronics conference and Exposition (APEC)*, 2009, pp. 945-950.

[HE10] Y. He, Y. Wang, J. Wu, Y. Feng, and J. Liu, "A simple current sharing scheme for dual three-phase permanent-magnet synchronous motor drives," *in proc. 2010 Twenty-fifth Annual IEEE Applied Power Electronics conference and Exposition (APEC)* 2010, pp. 1093-1096.

[HOA12] K. D. Hoang, Z. Q. Zhu, and M. Foster, "Optimum look-up table for reduction of current harmonics in direct torque controlled dual three-phase permanent magnet brushless AC machine drives," *Power Electronics, Electrical Drives, Automation and Motion (SPEEDAM)* 2012, pp. 1-6.

[HOA15] K. D. Hoang, Y. Ren, Z. Zhu, and M. Foster, "Modified switching-table strategy for reduction of current harmonics in direct torque controlled dual-three-phase permanent magnet synchronous machine drives," *IET, Electr. Power Appl.*, vol. 9, no. 1, pp. 10-19, Jan. 2015.

[HOL05] J. Holtz, and J. Juliet, "Sensorless control of rotor position angle of induction motor with arbitrary stator windings," *IEEE Trans. Ind. Appl.*, vol. 41, no. 6, pp. 1675-1682, 2005.

[HOL06] J. Holtz, "Sensorless control of iinduction machines-with or without signal injection," *IEEE Trans. on Ind. Electron.*, vol. 53, no. 1 pp. 7-30, Feb. 2006.

[HOL98] J. Holtz, "Sensorless position control of induction motors-an emerging technology," *IEEE Trans. Ind. Electron.*, vol. 45, no. 6, pp. 840-852, 1998.

[HU98] J. Hu, and B. Wu, "New integration algorithms for estimating motor flux over a wide speed range," *IEEE Trans. power Electron*., vol. 13, no. 5, pp. 969-977, 1998.

[HUA11] Y. Hua, M. Sumner, G. Asher, Q. Gao, and K. Saleh, "Improved sensorless control of a permanent magnet machine using fundamental pulse width modulation excitation," *IET Electric. Power Appl.*, vol. 5, no. 4, pp. 359-370, 2011.

[ISH06] D. Ishak, Z. Q. Zhu, and D. Howe, "Comparison of PM brushless motors, having either all teeth or alternate teeth wound," *IEEE Trans. Energy Conversion*, vol. 21, no. 1, pp. 95-103, Mar. 2006.

[JAN03] J. H. Jang, S. K. Sul, J. I. Ha, K. Ide, and M. Sawamura, "Sensorless drive of surface-mounted permanent-magnet motor by high-frequency signal injection based on magnetic saliency," *IEEE Trans. Industry Applications*, vol. 39, no. 4, pp. 1031-1039, 2003.

[JAN04] J. H. Jang, J. I. Ha, M. Ohto, K. Ide, and S. K. Sul, "Analysis of permanent-magnet machine for sensorless control based on high-frequency signal injection," *IEEE Trans. Ind. Appl*., vol. 40, no. 6, pp. 1595-1604, Nov./Dec. 2004.

[JAN95] P.L. Jansen and R. D. Lorenz, "Transducerless position and velocity estimation in induction and salient AC machines," *IEEE Trans. Industry Applications*, vol. 31, no. 2, pp. 240-247, 1995.

[JOE05] Y. S. Jeong, R. D. Lorenz, T. M. Jahns, and S. K. Sul, "Initial rotor position estimation of an interior permanent-magnet synchronous machine using carrier-frequency injection methods," *IEEE Trans. Ind. Appl.*, vol. 41, no. 1, pp. 38-45, 2005.

[JON09] M. Jones, S. N. Vukosavic, D. Dujic, and E. Levi, "A Synchronous Current Control Scheme for Multiphase Induction Motor Drives," *IEEE Trans. Energy Conversion*, vol. 24, no. 4, pp. 860-868, Dec 2009.

[JUN15] S. Jung, and J.-I. Ha, "Analog filtering method for sensorless AC machine control with carrier-frequency signal injection," *IEEE Trans. Ind. Electron.*, vol. 62, no. 9, pp. 5348-5358, Sept. 2015.

[KAN10] J. Kang, "Sensorless control of permanent magnet motors," *Control Engineering*, vol. 57, no. 4, pp. 1-4, 2010.

[KAR12] J. Karttunen, S. Kallio, P. Peltoniemi, and O. Pyrhonen, "Dual three-phase permanent magnet synchronous machine supplied by two independent voltage source inverters," *in proc. IEEE International Symposium on Power Electronics, Electrical Drives, Automation and Motion (SPEEDAM),* pp. 741-747, Jun. 2012.

[KAR16] J. Karttunen, S. Kallio, P. Peltoniemi, and P. Silventonen, "Current harmonic compensation in dual three-phase PMSMs using a disturbance observer," *IEEE Trans. Ind. Electron.*, vol. 63, no. 1, pp. 583-594, Jan. 2016.

[KEL03] J. W. Kelly, E. G. Strangas, and J. M. Miller, "Multiphase space vector pulse width modulation," *IEEE Trans. Energy Conversion*, vol. 18, no. 2, pp. 259-264, Jun. 2003.

[KIM03] H. Kim, M.C. Harke, and R.D. Lorenz, "Sensorless control of interior permanent magnet machine drives with zero-phase lag position estimation," *IEEE Trans. Ind. Appl.*, vol. 39, no. 6, pp.1726-1733, Nov./Dec., 2003.

[KIM11] H. Kim, J. Son, and J. Lee, "A high-speed sliding-mode observer for the sensorless speed control of a PMSM," *IEEE Trans. Ind. Electron*., vol. 58, no. 9, pp. 4069-4077, sept. 2011.

[KOC09] H. W. De Kock, M. J. Kamper, and R. M. Kennel, "Anisotropy comparison of reluctance and PM synchronous machines for position sensorless control using HF carrier injection," *IEEE Trans. Power Electronics*, vol. 24, no. 8, pp. 1905-1913, 2009.

[KRE94] L. Kreindler, J. C. Moreira, A. Testa, and T. A. Lipo, "Direct field orientation controller using the stator phase voltage third harmonic," *IEEE Trans. Ind. Appl.*, vol. 30, no. 2, pp. 441-447, 1994.

[LEE11] K. Lee, I. Choy, J. Back, and J. Choi, "Disturbance observer based sensorless speed controller for PMSM with improved robustness against load torque variation," *IEEE power Electronics and ECCE Asia (ICPE and ECCE)*, 2011, pp. 2537-2543.

[LEI11] R. Leidhold, "Position sensorless control of PM synchronous motors based on zero-sequence carrier injection," *IEEE Trans. on Ind. Electron.*, vol. 58, no. 12 pp. 5371-5379, 2011.

[LEV08] E. Levi, "Multiphase electric machines for variable-speed applications," *IEEE Trans. Ind. Electron.*, vol. 55, no. 5, pp. 1893-1909, May 2008.

[LI07] Y. Li, Z. Q. Zhu, D. Howe, and C. M. Bingham, "Improved rotor position estimation in extended back-emf based sensorless PM brushless AC drives with magnetic saliency accounting for cross-coupling magnetic saturation," *IEEE International Electric Machines and Drives Conference, IEMDC 2007*, Antalya, Turkey, 2007, pp. 214-219.

[LI09a] Y. Li., "Sensorless control of permanent magnet brushless AC motors accounting for cross-coupling magnetic saturation," PhD Thesis Submitted to University of Sheffield, UK, 2009.

[LI09b] Y. Li, Z. Q. Zhu, D. Howe, and C. M. Bingham, "Improved rotor position estimation by signal injection in brushless AC motors, Accounting for Cross-Coupling Magnetic Saturation" *IEEE Trans. Industry Applications*, vol. 45, no. 5, pp. 1843-1850, 2009.

[LI11] G. J. Li, J. Ojeda, E. Hoang, and M. Gabsi, "Thermal-electromagnetic analysis of a fault-tolerant dual-star flux-switching permanent magnet motor for critical application," *IET Electric Power Applications*, vol. 5, no. 6, pp. 503-513, Jul. 2011.

[LIN03] M. Linke, R. Kennel, and J. Holtz, "Sensorless speed and position control of synchronous machines using alternating carrier injection," *Electric Machines and Drives Conference*, 2003, vol. 2, pp. 1211-121.

[LIN14] T. C. Lin, L. M. Gong, J. M. Liu, and Z. Q. Zhu, "Investigation of saliency in a switched-flux permanent-magnet machine using high-frequency signal injection," *IEEE Trans. Ind. Electron.*, vol. 61, no. 9, pp. 5094-5104, Spet. 2014.

[LIN15] T. C. Lin, and Z. Q. Zhu, "Sensorless operation capability of surface-mounted permanent-magnet machine based on high-frequency signal injection methods," *IEEE Trans. Ind. Appl.*, vol. 51, no. 3, pp. 2161-2171, May/Jun. 2015.

[LIN15b] T. C. Lin, and Z. Q. Zhu, "Sensorless operation capability of surface-mounted permanent-magnet machine based on high-frequency signal injection methods," *IEEE Trans. Ind. Appl.*, vol. 51, no. 3, pp. 2161-2171, May/Jun. 2015.

[LIP80] T. A. Lipo, "A d-q model for six-phase induction machines," *Proc. International Conference on Electrical Machines ICEM*, Athens, Greece, 1980, pp. 860-867.

[LIU06] Y. Liu, Z. Q. Zhu, and D. Howe, "Instantaneous torque estimation in sensorless direct-torque-controlled brushless DC motors," *IEEE Trans. Ind. Appl.*, vol. 42, no. 5, pp. 1275–1283, Sept./Oct. 2006.

[LIU14] J. M. Liu, and Z. Q. Zhu, "Novel sensorless control strategy with injection of high-frequency pulsating carrier signal into stationary reference frame," *IEEE Trans. Ind. Appl.*, vol. 50, no. 4, pp. 2574-2583, Jul. 2014.

[LIU15] J. M. Liu, and Z. Q. Zhu, "Rotor position estimation for dual-three-phase permanent magnet synchronous machine based on third harmonic back-EMF," *IEEE Symposium on Sensorless Control for Electrical Drives*, (*SLED2015*), 2015, pp. 1-8.

[LJU79] L. Ljung, "Asymptotic behavior of the extended Kalman filter as a parameter estimator for linear systems," *IEEE Trans. Auto. Control*, vol. 24, no. 1, pp. 36–50, Feb. 1979.

[LUO16] X. Luo, Q. Tang, A. Shen, and Q. Zhang, "PMSM sensorless control by injecting HF pulsating carrier signal into estimated fixed-frequency rotating reference frame," *IEEE Trans. Ind. Electron.*, vol. 63, no. 4, pp. 2294-2303, Apr. 2016.

[MAD95] A. Madani, J. P. Barbot, F. Colamartino, and C. Marchand, "Reduction of torque pulsations by inductance harmonics identification of a permanent-magnet synchronous machine,"*proceedings of the 4th IEEE Conference on Control Applications*, 1995, pp. 787-792.

[MAT96] N. Matsui, "Sensorless PM brushless DC motor drives," *IEEE Trans. Ind. Electron*., vol. 43, no. 2, pp. 300-308, 1996.

[MED15] S. Medjmadj, D. Diallo, M. Mostefai, C. Delpha, and A. Arias, "PMSM drive position estimation: contribution to the high-frequency injection voltage selection issue," *IEEE Trans. Energy Conversion*, vol. 30, no. 1, pp. 349-358, Mar. 2015.

[MOG13] M. A. G. Moghadam, and F. Tahaami, "Sesorless control of PMSMs with tolerance for delays and stator resistance uncertainties," *IEEE Trans. Power Electron.*, vol. 28, no. 3, pp. 1391-1399, Mar.2013.

[MOR02] S. Morimoto, K. Kawamoto, M. Sanada, and Y. Takeda, "Sensorless control strategy for salient-pole PMSM based on extended EMF in rotating reference frame," *IEEE Trans. Ind. Appl.*, vol. 38, no. 4, pp. 1054–1061, Jul./Aug. 2002.

[MOR92] J. Moreira, and T. A. Lipo, "Modelling saturated AC machines including air gap flux harmonic components ," *IEEE Trans. Ind. Appl.*, vol. 28, no. 2, pp. 343-349, 1992.

[MOR96] S. Morimoto, M. Sanada, and Y. Takeda, "Inverter-driven synchronous motors for constant power," *IEEE Trans. Ind. Appl.*, vol. 2, no. 6, pp. 18-24, 1996.

[OVR03] S. Ovrebo, and R. Nilsen, "New self-sensing scheme based on INFORM, heterodyning and Luenberger observer," *IEEE Conference on Electric Machines Drives, (IEMD'03)*, vol. 3, 2003, pp. 1819-1825.

[OVR04] S. Ovrebo, "Control of permanent magnet synchronous machines," PhD Thesis Submitted to Norwegian University of Science and Technology, Trondheim, 2004.

[PAC05] M. Pacas, and J. Weber, "Predictive direct torque control for the PM synchronous machine," *IEEE Trans. Ind. Electron.*, vol. 52, no. 5, pp. 1350-1356, Oct. 2005.

[PAR07] L. Parsa and H. A. Toliyat, "Sensorless direct torque control of five-phase interior permanent-magnet motor drives," *IEEE Trans. Ind. Appl.*, vol. 43, no. 4, pp. 952-959, Jul./Aug. 2007.

[PAU11] D. Paulus, P. Landsmann, and R. Kennel, "Sensorless field-oriented control for permanent magnet synchronous machines with an arbitrary injection scheme and direct angle calculation," *Symposium on Sensorless Control of Electrical Drives (SLED 2011)*, pp. 41-46, 2011.

[PII08] A. Piippo, M. Hinkkanen, and J. Luomi, "Analysis of an adaptive observer for sensorless control of interior permanent magnet synchronous motors," *IEEE Trans. Ind. Electron.*, vol. 55, no. 2, pp. 570–576, Feb. 2008.

[PRO92] F. Profumo, G. Griva, M. Pastorelli, J. Moreira and R. De. Doncker, "Universal field oriented controller based on air gap flux sensing via third harmonic stator voltage," *Conference of IEEE Industry Applications Society Annual Meeting*, 1992, pp. 515-523.

[RAC08] D. Raca, P. Garcia, D. Reigosa, F. Briz, and R. D. Lorenz, "A comparative analysis of pulsating vs. rotating vector carrier signal injection-based sensorless control," *Proc. Of IEEE Applied Power Electronics Conf. and Exposition (APEC'08)*, pp. 879-885, Feb. 2008.

[RAC10] D. Raca, P. Garcia, D. D. Reigosa, F. Briz, and R. D. Lorenz, "Carrier signal selection for sensorless control of PM synchronous machines at zero and very low speeds," *IEEE Trans. Ind. Appl.*, vol. 46, no.1, pp. 167-178, Jan./Feb. 2010.

[RAU10] R. Raute, C. Caruana, C.S. Staines, J. Cilia, M. Sumner, and G. M. Asher, "Sensorless control of induction machines at low and zero speeds by using PWM harmonics for rotor-bar slotting detection," *IEEE Trans. Ind. Appl.*, vol. 46, no. 5, pp. 1989-1998, 2010.

[REI08] D. Reigosa, P. Garcia, D. Raca, F. Briz, and R. D. Lorenz, "Measurement and adaptive decoupling of cross-saturation effects and secondary saliencies in sensorless-controlled IPM synchronous machines," *IEEE Trans. Ind. Appl.*, vol. 44, no. 6, pp. 1758–1767, 2008.

[REN15a] Y. Ren., and Z. Q. Zhu, “Reduction of both harmonic current and torque ripple for dual three-phase permanent-magnet synchronous machine using modified switching-table-based direct torque control,” *IEEE Trans. Ind. Electron.*, vol. 62, no. 11, pp. 6671-6683, Nov. 2015.

[REN15b] Y. Ren and Z. Q. Zhu, "Enhancement of Steady-State Performance in Direct-Torque-Controlled Dual Three-Phase Permanent-Magnet Synchronous Machine Drives With Modified Switching Table," *IEEE Trans. Ind. Electron*., vol. 62, no. 6, pp. 3338-3350, Jun. 2015.

[ROB02] E. Robeischl, M. Schroedl, and K. Salutt, “Improved INFORM-measurement sequence and evaluation for sensorless permanent magnet synchronous motor drives,” *the 10th International Conference on Power Electronics and Motion Control*, Croatia, 2002.

[ROB04] E. Robeischl, and M. Schroedl, “Optimized INFORM measurement sequence for sensorless PM synchronous motor drives with respect to minimum current distortion,” *IEEE Trans. Ind. Appl.*, vol. 40, no. 2, pp. 591-598, Mar./Apr. 2004.

[SCH94] M. Schroedl, and P. Weinmeier “Sensorless control of reluctance machines at arbitrary operating conditions including standstill,” *IEEE Trans. Power Electronics*, vol. 9, no. 2, pp. 225-231, 1994.

[SCH96] M. Schroedl, “Sensorless control of AC machines at low speeds and standstill based on INFORM method,” *IEEE-IAS Annual Meeting*, 1996, pp. 270-277.

[SEN95] T. Senjyu, T. Shimabukruo, and K. Uezato, “Vector control of permanent magnet synchronous motors without position and speed sensors,” *in Proc. IEEE PESC'95*, 1995, pp. 759-765.

[SER12] P. Sergeant, F. De Belie, and J. Melkebeek, “Rotor geometry design of interior PMSMs with and without flux barriers for more accurate sensorless control,” *IEEE Trans. Ind. Electron*., vol. 59, no. 6, pp. 2457-2465, Jun. 2012.

[SHE02] J. X. Shen, Z. Q. Zhu, and D. Howe, “Improved speed estimation in sensorless PM brushless AC drives,” *IEEE Trans. Ind. Appl.*, vol. 38, no. 4, Jul./Aug. 2002.

[SHE04] J.X. Shen, Z.Q. Zhu, and D. Howe, “Sensorless flux-weakening control of permanent-magnet brushless machines using third harmonic back EMF,” *IEEE Trans. Ind. Appl.*, vol. 40, no. 6, pp. 1629-1636, Nov./Dec. 2004.

[SHE06] J.X. Shen, and S. Iwasaki, “Sensorless control of ultrahigh-speed PM brushless motor using PLL and third harmonic back EMF,” *IEEE Trans. Ind. Electron.*, vol.53, no.2, pp.421-428, Apr. 2006.

[SHE06a] J. X. Shen, Z. Q. Zhu, and D. Howe, "Practical issues in sensorless control of PM brushless machines using third-harmonic back-EMF," *IEEE 15th International Conference on Power Electronics and Motion Control, IPEMC*2006, 2006, pp. 1-5.

[SHE06b] J. X. Shen, and S. Iwasaki, "Sensorless control of ultrahigh-speed PM brushless motor using PLL and third-harmonic back-EMF," *IEEE Trans. Ind. Electron*., vol. 53, no. 2, pp. 421-428, 2006.

[SIL02] C. Silva, G. M. Asher, M. Sumner, and K. J. Bradley, "Sensorless rotor position control in a surface mounted PM machine using HF voltage injection," *in Proc. EPE-PEMC'02*, Dubrovnik, Croatia, 2002.

[SIL06] C. Silva, G. M. Asher, and M. Sumner, "Carrier-signal selection for sensorless control of PM synchronous machines at zero and very low speeds," *IEEE Trans. Ind. Electron.*, vol. 53, no. 1, pp. 373-378, 2006.

[SON09] C. Song, Z. Zheng, and X. Longya, "Sliding-mode sensorless control of direct-drive PM synchronous motors for washing machine applications," *IEEE Trans. Industry Applications*, vol. 45, no. 2, pp.582-590, 2009.

[STA06] C. S. Staines, C. Caruana, G. M. Asher, and M. Sumner, "Sensorless control of induction machine at zero and low frequency using zero-sequence current," *IEEE Trans. Ind. Electron.*, vol. 53, no. 1, pp. 195-206, 2006.

[TAK86] I. Takahashi, and T. Noguchi, "A new quick-response and high efficiency control strategy of an induction motor," *IEEE Trans. Ind. Appl*., vol. IA-22, no. 5, pp. 820-827, 1986.

[TER01] B. Terzic, and M. Jadric, "Design and implementation of the extended Kalman filter for the speed and rotor position estimation of brushless DC motor," *IEEE Trans. Ind. Electron.*, vol. 48, no. 6, pp. 1065–1073, Dec. 2001.

[TES03] N. Teske, G. M. Asher, M. Sumner, and K. J. Bradley, "Analysis and suppression of high-frequency inverter modulation in sensorless position-controlled induction machine drive," *IEEE Trans. Ind. Appl.*, vol. 39, no. 1, pp. 10-18, 2003.

[TIA11] Tian S. W., Jian G. Z., You G. G, and Gang, L., "Simulation and experimental studies of permanent magnet synchronous motor control methods," *IEEE International Conference on Applied Superconductivity and Electromagnetic Devices*, Sydney, Australia, Dec., 2011.

[VAS03] P. Vas, "Sensorless vector and direct torque control," *Oxford University Press*, 2003.

[WAN10] H. Wang, M. Yang, L. Niu and D. Xu, "Current-loop bandwidth expansion strategy for permanent magnet synchronous motor drives," *the 5th IEEE Conference on Industrial Electronics and Applications*, (*ICIEA2010*), 2010, pp. 1340-1345.

[WAN12] Z. Wang, K. Lu, and F. Blaabjerg, "A simple startup strategy based on current regulation for Back-EMF-based sensorless control of PMSM," *IEEE Trans. on Power Electron.*, vol.27, no.8, pp.3817-3825, Aug. 2012.

[WU91] R. Wu, and G. R. Slemon, "A permanent magnet motor drive without a shaft sensor," *IEEE Trans. Ind. Appl.*, vol. 27, no. 5, pp.1005-1011, Sept./Oct. 1991.

[XU14] W. Xu, and R.D. Lorenz, "Reduced parameter sensitivity stator flux linkage observer in deadbeat-direct torque and flux control for IPMSMs," *IEEE Trans. Ind. Appl.*, vol. 50, no. 4,pp. 2626-2636, Jul./Aug. 2014.

[XU15] P. L. Xu and Z. Q. Zhu, "Comparison of carrier signal injection methods for sensorless control of PMSM drives," *IEEE Energy Conversion Congress and Exposition (ECCE)*, Montreal, 2015, pp. 5616-5623.

[XU16] P. L. Xu, and Z. Q. Zhu, "Novel carrier signal injection method using zero sequence voltage for sensorless control of PMSM drives," *IEEE Trans. Ind. Electron.*, vol. 63, no. 4, pp. 2053-2061, Apr. 2016.

[YAN11] S. C. Yang, T. Suzuki, R. D. Lorenz, and T. M. Jahns, "Surface permanent magnet synchronous machine design for saliency tracking self-sensing position estimation at zero and low speeds," *IEEE Trans. Ind. Appl.*, vol. 47, no. 5, pp. 2103-2116, 2011.

[YAN12a] S.-C. Yang, and R. Lorenz, "Surface permanent magnet synchronous machine self-sensing position estimation at low speed using eddy current reflected asymmetric resistance," *IEEE Trans. Power Electronics*, vol. 27, no. 5, pp. 2595-2604, 2012.

[YAN12b] S.-C. Yang, and R. Lorenz, "Comparison of resistance based and inductance based self-sensing control for Surface permanent magnet machines using high-frequency signal injection," *IEEE Trans. Ind. Electron.*, vol. 48, no. 3, pp. 977-986, Jun. 2012.

[YOO09] A. Yoo and S. K. Sul, "Design of flux observer robust to interior permanent-magnet synchronous motor flux variation," *IEEE Trans. Ind. Appl.*, vol. 45, no. 5, pp. 1670-1677, 2009.

[YOO11] Y. D. Yoon, S.-K. Sul, S. Morimoto, and K. Ide, "High-bandwidth sensorless algorithm for ac machines based on square-wave-type voltage injection," *IEEE Trans. Ind. Appl.*, vol. 47, no. 3, pp. 1361-1370, May. 2011.

[ZHA06] Z. Zhang, H. Xu, L. Xu, and L. E. Heilman, "Sensorless direct field oriented control of three-phase induction motor based on sliding-mode for washing machine drive applications," *IEEE Trans. Ind. Appl.*, vol. 42, no. 3, pp. 694-701, 2006.

[ZHA11] Y. C. Zhang, J. G. Zhu, W. Xu, and Y. G. Guo, "A simple method to reduce torque ripple in direct torque-controlled permanent-magnet synchronous motor by using vectors with variable amplitude and angle," *IEEE Trans. Ind. Electron.*, vol. 58, no. 7, pp. 2848-2859, 2011.

[ZHA13] S. Zhao, O. Wallmark, and M. Leksell, "Low-speed sensorless control with reduced copper losses for saturated PMSynRel Machines," *IEEE Trans. Energy Conversion*, vol. 28, no. 4, pp. 841-848, Dec. 2013.

[ZHA95] Y. Zhao, and T. A. Lipo, "Space vector pwm control of dual three-phase induction machine using vector space decomposition," *IEEE Trans. Ind. Appl.*, vol. 31, no. 5, pp. 1100-1109, Sept./Oct. 1995.

[ZHA95] Y. Zhao and T. A. Lipo, "Space vector PWM control of dual three-phase induction machine using vector space decomposition," *IEEE Trans. Ind. Appl.*, vol. 31, no. 5, pp. 1100-1109, Sep./Oct. 1995.

[ZHO97] L. Zhong, M. F. Rahman, W. Y. Hu, and C. M. Bingham, "Analysis of direct torque control in permanent magnet synchronous motor drives," *IEEE Trans. Power Electron.*, vol. 12, no. 3, pp. 528-536, 1997.

[ZHU07] Z. Q. Zhu, Y. LI, D. Howe, and C. M. Bingham, "Compensation for rotor position estimation error due to cross-coupling magnetic saturation in signal injection based sensorless control of PM brushless AC motors," *Proc. Int. Electric Machines and Drives Conference*, 2007, pp.208-213.

[ZHU11] Z. Q. Zhu, "Sensorless operation of permanent magnet brushless DC and AC drives-basic and novel machine design and control aspects," *8th International Conference on Power Electronics-ECCE Asia*, The Shilla Jeju, Jeju, Korea, May 30, 2011.

[ACA06] P. P. Acamley, and J. F. Watson, "Review of position-sensorless operation of brushless permanent-magnet machines," *IEEE Trans. Ind. Electron.*, vol. 53, no. 2, pp. 352-362, Apr. 2006.

[ACC12] A. Accetta, M. Cirrincione, M. Pucci, and G. Vitale, "Sensorless control of PMSM fractional horsepower drives by signal injection and neural adaptive-band filtering," *IEEE Trans. Ind. Electron*., vol. 59, no. 3, pp. 1355-1366, Mar. 2012.

[AIH99] T. Aihara, A. Toba, T. Yanase, A. Mashimo, and K. Endo, "Sensorless torque control of salient-pole synchronous motor at zero-speed operation," *IEEE Trans. Power Electronics*, vol. 14, no. 1, pp. 202-208, 1999.

[ALM14] A. H. Almarhoon, and Z. Q. Zhu, "Influence of back-EMF and current harmonics on position estimation accuracy of permanent magnet synchronous machine," *17th International Conference on Electrical Machines and Systems, ICEMS2014*, pp.2728-2733, Oct. 2014.

[ALN13] E. Al-nabi, B. Wu, N. R. Zargari, and V. Sood, "Sensorless control of CSC-fed IPM machine for zero- and low-speed operations using pulsating HFI method," *IEEE Trans. Ind. Electron.*, vol. 60, no. 5, pp. 1711–1723, May 2013.

[AND08] G. D. Andreescu, C. I. Pitic, F. Blaabjerg, and I. Boldea, "Combined-flux observer with signal injection enhancement for wide speed range sensorless direct torque control of IPMSM drives," *IEEE Trans. Energy Convers.*, vol. 23, no. 2, pp. 393–402, Jun. 2008.

[BAE03] B.-H. Bae, S.-K. Sul, J.-H. Kwon, and J.-S. Byeon, "Implementation of sensorless vector control for super-high-speed PMSM of turbo- compressor," *IEEE Trans. Ind. Appl.*, vol. 39, no. 3, pp.811-818, May/Jun., 2003.

[BAN16] F. Baneira, A. G. Yepes, O. Lopez, and J. Doval-Gandoy, "Estimation method of stator winding temperature for dual three-phase machines based on DC-signal injection," *IEEE Trans. Power Electron.*, vol. 31, no. 7, pp. 5141-5148, Jul. 2016.

[BAR10a] M. Barcaro, N. Bianchi, and F. Magnussen, "Faulty operations of a PM fractional-slot machine with a dual three-phase winding," *IEEE Trans. Ind. Appl.*, vol. 58, no. 9, pp. 3825-3832, 2010.

[BAR10b] M. Barcaro, N. Bianchi, and F. Magnussen, "Analysis and tests of a dual three-phase 12-slot 10-pole permanent-magnet motor," *IEEE Trans. Ind. Appl.*, vol. 46, no. 6, pp. 2355-2362, 2010.

[BAR12] M. Barcaro, A. Faggion, N. Bianchi, S. Bolognani, "Sensorless rotor position detection capability of a dual three-phase fractional-slot IPM machine," *IEEE Trans. Ind. Appl.*, vol. 48, no. 6, pp. 2086-2078, 2012.

[BIA07] N. Bianchi and S. Bolognami, "Influence of rotor geometry of an IPM motor on sensorless control feasibility," *IEEE Trans. Ind. Appl.*, vol. 43, no. 1, pp.87-96, 2007.

[BIA08] N. Bianchi, S. Bolognani, J.-H. Jang, and S.-K. Sul, "Advantages of inset PM machines for zero-speed sensorless position detection," *IEEE Trans. Ind. Appl.*, vol. 44, no. 4, pp. 1190-1198, Aug. 2008.

[BOG06] A. Boglietti, R. Boji, A. Cavagnino, and Tenconi, "Effiecincy analysis of PWM inverter fed three-phase and dual three-phase induction machines," *IEEE Industry Applications Conference 2006*, vol. 1, 2006, pp. 434-440.

[BOJ03] R. Bojoi, M. Lazzari, F. Profumo, and A. Tenconi, "Digital field-oriented control for dual three-phase induction motor drives," *IEEE Trans. Ind. Appl.*, vol. 39, no. 3, pp. 752-760, May/Jun. 2003.

[BOJ03a] R. Bojoi, F. Farina, M. Lazzari, F. Profumo, and A. Tenconi, "Analysis of the asymmetrical operation of dual three-phase induction machines," *Proc. IEEE Int. Electric Machines and Drives Conf. IEMDC*, Madison, WI, 2003, pp. 429–435.

[BOJ05] R. Bojoi, F. Farina, G. Griva, F. Profumo, and A. Tenconi, "Direct torque control for dual three-phase induction motor drives," *IEEE Trans. Ind. Appl*., vol. 41, no. 6, pp. 1627-1636, Nov./Dec. 2005.

[BOJ06] R. Bojoi, E. Levi, F. Farina, A. Tenconi, and F. Profumo, "Dual three-phase induction motor drive with digital current control in the stationary reference frame," *IEE Proc.-Electr. Power Appl.*, vol. 153, no. 1, pp. 129-139, Jan. 2006.

[BOL09] I. Boldea, M. C. Paicu, G. D. Andreescu, and F. Blaabjerg, "Active flux DTFC-SVM sensorless control of IPMSM," *IEEE Trans. Energy Conversion*, vol. 24, no. 2, pp. 314-322, Mar./Apr. 2009.

[BOL11] S. Bolognani, S. Calligaro, R. Petrella, and M. Sterpellone, "Sensorless control for IPMSM using PWM excitation, analytical developments and implementation issues," *Symposium on Sensorless Control of Electrical Drives (SLED2011)*, 2011, pp. 64-73.

[BRI04] F. Briz, M. W. Degner, P. García, and R. D. Lorenz, "Comparison of saliency-based sensorless control techniques for AC machines," *IEEE Trans. Ind. Appl.*, vol. 40, no. 4, pp. 1107–1115, Jul./Aug. 2004.

[BRI05] F. Briz, M. W. Degner, P. García, and J. M. Guerrero, "Rotor position estimation of AC machines using the zero sequence carrier signal voltage," *IEEE Trans. Ind. Appl.*, vol. 41, no. 6, pp. 1637–1646, Nov./Dec. 2005.

[CAP01] E. Capecchi, P. Gulielmi, M. Pastorelli, and A. Vagati, "Position-sensorless control of transverse-laminated synchronous reluctance motor," *IEEE Trans. Industry Applications*, vol. 37, no. 6, pp. 1768-1776, 2001.

[CAR06] C. Caruana, G. M. Asher, and M. Summer, "Performance of HF signal injection techniques for zer-low-frequency vector control of induction machines under sensorless conditions," *IEEE Trans. Ind. Electron.*, vol. 53, no. 1, pp. 225–238, Feb. 2006.

[CHE00] Z. Chen, M. Tomita, S. Ichikawa, S. Doki, and S. Okuma, "Sensorless control of interior permanent magnet synchronous motor by estimation of an extended electromotive force," *Industry Applications Conference*, vol. 3, 2000, pp. 1814-1819.

[CHE03] Z. Chen, M. Tomita, S. Koki, and S. Okuma, "An extended electromotive force model for sensorless control of interior permanent-magnet synchronous motors," *IEEE Trans. Ind. Electron.*, vol. 50, no. 2, pp. 288-295, 2003.

[CHE14] Z. Chen, J.B. Gao, F.X. Wang, Z.X. Ma, Z.B. Zhang, and R. Kennel, "Sensorless control for SPMSM with concentrated windings using multi-signal injection method," *IEEE Trans. Ind. Electron.*, vol.61, no.12, pp.6624-6634, Dec. 2014.

[CHE14] H. S. Che, E. Levi, M. Jones, W. P. Hew, and N. Abd Rahim, "Current Control Methods for an Asymmetrical Six-Phase Induction Motor Drive," *IEEE Trans. Power Electron.*, vol. 29, no. 1, pp. 407-417, Jan 2014.

[CHE99] Y. S. Chen, "Motor topologies and control strategies for permanent magnet brushless AC drives," PhD Thesis Submitted to University of Sheffield, UK, 1999.

[CHI09] S. Chi, Z. Zhang, and L. Xu, "Sliding-mode sensorless control of direct-drive PM synchronous motors for washing machine applications," *IEEE Trans. Ind. Appl.*, vol. 45, no. 2, pp. 582–590, Mar./Apr. 2009.

[CON00] A. Consoli, G. Scarcella, and A. Testa, "A new zero-frequency flux position detection approach for direct-field-oriented-control drives," *IEEE Trans. Ind. Appl.*, vol. 36, no. 3, pp. 797–804, May./Jun. 2000.

[CON06] A. Consoli, G. Scarcella, G. Bottiglieri, and A. Testa, "Harmonic analysis of voltage zero-sequence-based encoderless techniques," *IEEE Trans. Ind. Appl.*, vol. 42, no. 6, pp. 1548–1557, Nov./Dec. 2006.

[COR98] M. J. Corley and R. D. Lorenz, "Rotor position and velocity estimation for a salient-pole permanent magnet synchronous machine at standstill and high speed," *IEEE Trans. Industry Applications*, vol. 34, no. 4, pp.784-789, 1998.

[CUP10] F. Cupertino, P. Giangrande, L. Salatore, and G. Pellegrino, "Model based design of sensorless control scheme for permanent magnet motors using signal injection," *IEEE Energy Conversion Congress and Exposition (ECCE2010)*, 2010, pp. 3139-3146.

[DEG98] M. W. Degner, and R. D. Lorenz, "Using multiple saliencies for the estimation of flux, position, and velocity in AC machines," *IEEE Trans. Ind. Appl.*, vol. 34, no. 5, pp. 1097-1104, 1998.

[DEP88] M. Depenbrock, "Direct self-control (dsc) of inverter-fed induction machine," *IEEE Trans. Power Electron.*, vol. 3, no. 4, pp. 420-429, Oct. 1988.

[DSP10] Dspace, "Hardware installation and configuration reference,", Release 6.6, May 2010.

[DUR11] M. J. Duran, J. Prieto, F. Barrero, S. Toral, "Predictive current control of dual three-phase drives using restrained search techniques," *IEEE Trans. Ind. Electron.*, vol. 58, no. 8, pp. 3253-3263, Aug. 2011.

[DWA08] S. Dwari, and L. Parsa, "Open-circuit fault tolerant control of five-phase permanent magnet motors with third-harmonic back-EMF," *34th Annual Conference of IEEE on Industrial Electronics*, *IECON 2008*, 2008, pp. 3114-3119.

[FAE09] M. Faeq, and D. Ishak, "A new scheme sensorless control of BLDC motor using software PLL and third harmonic back-EMF," *IEEE Industrial Electronics and Applications*, *ISIEA*, 2009, pp. 861-865.

[FAR06] F. Farina, R. Bojoi, A. Tenconi, and F. Profumo, "Direct torque control with full order stator flux observer for dual-three phase induction motor drives," *IEEJ Trans. Ind. Appl*., vol. 126, no. 4, pp. 412-419, 2006.

[FOO09a] G. Foo, and M. F. Rahman, "Direct torque and flux control of an IPM synchronous motor drive using a back stepping approach," *IET Electric. Power Appl*., vol. 3, no. 5, pp. 413-421, 2009.

[FOO10] G. Foo, and M. F. Rahman, "Sensorless sliding-mode MTPA control of an IPM synchronous motor drive using a sliding-mode observer and HF signal injection," *IEEE Trans. Ind. Electron.*, vol. 57, no. 4, pp. 1270–1278, Apr. 2010.

[FOO10] G. FOO, and M. F. Rahman, "Sensorless sliding-mode MTPA control of IPM synchronous motor drive using a sliding-mode observer and HF signal injection," *IEEE Trans. Ind. Electron*., vol. 57, no. 4, pp. 1270-1278, 2010.

[FUE11] E. Fuentes, and R. Kennel, "Sensorless-predictive torque control of the PMSM using a reduced order extended kalman filter," *Symposium on Sensorless Control for Electrical Drives*, 2011, pp. 123-128.

[FUR92] T. Furuhashi, S. Sangwongwanich, and S. Okuma, "A position and velocity sensorless control for brushless DC motors using an adaptive sliding mode observer," *IEEE Trans. Ind. Electron*., vol. 39, no. 2, pp. 89-95, 1992.

[GAB13] F. Gabriel, F. De Belie, X. Neyt, and P. Lataire, "High-frequency issues using rotating voltage injections intended for position self-sensing," *IEEE Trans. Ind. Electron.*, vol. 60, no. 12, pp. 5447–5457, Dec. 2013.

[GAD10] S. M. Gadoue, D. Giaouris, and J. W. Finch, "MRAS sensorlesss vector control of an induction motor using new sliding-mode and fuzzy-logic adaption mechanisms," *IEEE Trans. Energy Conversion*, vol. 25, no. 2, pp. 394-402, 2010.

[GAO07] Q. Gao, G. M. Asher, M. Sumner, and P. Makys, "Position estimation of AC machines over a wide frequency range based on space vector PWM excitation," *IEEE Trans. Ind. Appl.*, vol. 43, no. 4, pp. 1001-1011, 2007.

[GAO11] L. L. Gao, J. E. Fletcher, L. B. Zheng, "Low-speed control improvements for a two-level five-phase inverter-fed induction machine using classic direct torque control," *IEEE Trans. Ind. Electron.*, vol. 58, no. 7, pp. 2744-2754, Jul. 2011.

[GAR07] P. Garcia, F. Briz, M. W. Degner, and D. Diaz-Reigosa, "Accuracy, bandwidth, and stability limits of carrier-signal- injection- based sensorless control methods*," IEEE Trans. Ind. Appl.*, vol. 43, no. 4, pp. 990–1000, Jul./Aug. 2007.

[GON11] L. M. Gong, "Carrier signal injection based sensorless control of permanent magnet brushless AC machines," PhD Thesis Submitted to University of Sheffield, UK, 2011.

[GON11a] L. M. Gong, and Z. Q. Zhu, "A novel method for compensating inverter nonlinearity effects in carrier signal injection-based sensorless control from positive-sequence carrier current distortion," *IEEE Trans. Ind. Appl.*, vol. 47, no. 3, pp. 1283-1292, 2011.

[GON11b] L. M. Gong and Z. Q. Zhu, "Improved rotating carrier signal injection method for sensorless control of PM brushless AC motors, accounting for cross-saturation effect," *Power Electronics and ECCE Asia (ICPE & ECCE)*, pp. 1132-1139, 2011.

[GOP93] S. ChiK. Gopakumar, Z. ZhangV. T. Ranganthan, and L. XuS. R. Bhat, "Sp-phase induction motor operation from PWM voltage source inverter," *IEEE Trans. Ind. Appl.*, vol. 4529, no. 25, pp.582927-932590, 20091993.

[GRE10] R. Gregor, and J. Rodas, "Speed sensorless control of dual three-phase induction motor drives," *IET Electric. Power Appl.*, vol. 4, no. 1, pp.26-34, 2010.

[GRE12] R. Gregor, and J. Rodas, "Speed sensorless control of dual three-phase induction machine based on a luenberger observer for rotor current estimation," *Annual Conference of IEEE on Industrial Electronics, IECON 2012*, 2012, pp. 3653-3658.

[GUE05] J. M. Guerrero, M. Leetmaa, F. Briz, A. Zamarron, and R. D. Lorenz, "Inverter nonlinearity effects in high-frequency signal-injection-based sensorless control methods," *IEEE Trans. Ind. Appl.*, vol. 41, no. 2, pp. 618-626, 2005.

[GUG06] P. Guglielmi, M. Pastorelli, and A. Vagaati, "Cross-saturation effects in IPM motor and related impact on sensorless control," *IEEE Trans. Ind. Appl.*, vol. 42, no. 6, pp. 1516-1522, 2006.

[HA00] J. I. Ha, and S. K. Sul, "Physical understanding of high-frequency injection method to sensorless drives of an induction machine," *Conference of IEEE Industry Applications*, 2000, pp. 1802-1808.

[HA08] J. I. Ha, "Analysis of inherent magnetic position sensors in symmetric AC machines for zero or low speed senssorless drives," *IEEE Trans. Magn.*, vol. 44, no. 2, pp. 4689-4696, Dec. 2008.

[HA99] J.-I. Ha, S.-J. Kang, and S.-K. Sul, "Position-controlled synchronous reluctance motor without rotational transducer," *IEEE Trans. Industry Applications*, vol. 35, no. 6, pp. 1393-1398, 1999.

[HAR00] L. Harnefors, and H. P. Nee, "A general Algorithm for speed and position estimation of AC motors," *IEEE Trans. Ind. Electron.*, vol. 47, no. 1, pp. 77-83, 2000.

[HAR96] L. Harnefors, "Speed estimation from noisy resolver signals," *Sixth International Conference on Power Electronics and Variable Speed Drives*, pp.279-282, 23-25 Sept. 1996.

[HAT05] K. Hatua, and V. T. Ranganathan, "Direct torque control schemes for split-phase induction machine," *IEEE Trans. Ind. Appl.*, vol. 41, no. 5, pp. 1243-1254, Sept./Oct. 2005.

[HAT05] K. Hatua and V. T. Ranganathan, "Direct torque control schemes for split-phase induction machine," *Power Electronics, Machines and Drives (PEMD2012)*, 2012, pp. 1-6, Sep./Oct. 2005.

[HE09] Y. He, W. Hu, Y. Wang, J. Wu, and Z. Wang, "Speed and position sensorless control for dual-three-phase PMSM drives," *Twenty-fourth Annual IEEE Applied Power Electronics conference and Exposition (APEC)*, 2009, pp. 945-950.

[HE10] Y. He, Y. Wang, J. Wu, Y. Feng, and J. Liu, "A simple current sharing scheme for dual three-phase permanent-magnet synchronous motor drives," *in proc. 2010 Twenty-fifth Annual IEEE Applied Power Electronics conference and Exposition (APEC)* 2010, pp. 1093-1096.

[HOA12] K. D. Hoang, Z. Q. Zhu, and M. Foster, "Optimum look-up table for reduction of current harmonics in direct torque controlled dual three-phase permanent magnet brushless AC machine drives," *Power Electronics, Electrical Drives, Automation and Motion (SPEEDAM)* 2012, pp. 1-6.

[HOA15] K. D. Hoang, Y. Ren, Z. Zhu, and M. Foster, "Modified switching-table strategy for reduction of current harmonics in direct torque controlled dual-three-phase permanent magnet synchronous machine drives," *IET, Electr. Power Appl.*, vol. 9, no. 1, pp. 10-19, Jan. 2015.

[HOL05] J. Holtz, and J. Juliet, "Sensorless control of rotor position angle of induction motor with arbitrary stator windings," *IEEE Trans. Ind. Appl.*, vol. 41, no. 6, pp. 1675-1682, 2005.

[HOL06] J. Holtz, "Sensorless control of iinduction machines-with or without signal injection," *IEEE Trans. on Ind. Electron.*, vol. 53, no. 1 pp. 7-30, Feb. 2006.

[HOL98] J. Holtz, "Sensorless position control of induction motors-an emerging technology," *IEEE Trans. Ind. Electron.*, vol. 45, no. 6, pp. 840-852, 1998.

[HU98] J. Hu, and B. Wu, "New integration algorithms for estimating motor flux over a wide speed range," *IEEE Trans. power Electron*., vol. 13, no. 5, pp. 969-977, 1998.

[HUA11] Y. Hua, M. Sumner, G. Asher, Q. Gao, and K. Saleh, "Improved sensorless control of a permanent magnet machine using fundamental pulse width modulation excitation," *IET Electric. Power Appl.*, vol. 5, no. 4, pp. 359-370, 2011.

[ISH06] D. Ishak, Z. Q. Zhu, and D. Howe, "Comparison of PM brushless motors, having either all teeth or alternate teeth wound," *IEEE Trans. Energy Conversion*, vol. 21, no. 1, pp. 95-103, Mar. 2006.

[JAN03] J. H. Jang, S. K. Sul, J. I. Ha, K. Ide, and M. Sawamura, "Sensorless drive of surface-mounted permanent-magnet motor by high-frequency signal injection based on magnetic saliency," *IEEE Trans. Industry Applications*, vol. 39, no. 4, pp. 1031-1039, 2003.

[JAN04] J. H. Jang, J. I. Ha, M. Ohto, K. Ide, and S. K. Sul, "Analysis of permanent-magnet machine for sensorless control based on high-frequency signal injection," *IEEE Trans. Ind. Appl*., vol. 40, no. 6, pp. 1595-1604, Nov./Dec. 2004.

[JAN95] P.L. Jansen and R. D. Lorenz, "Transducerless position and velocity estimation in induction and salient AC machines," *IEEE Trans. Industry Applications*, vol. 31, no. 2, pp. 240-247, 1995.

[JOE05] Y. S. Jeong, R. D. Lorenz, T. M. Jahns, and S. K. Sul, "Initial rotor position estimation of an interior permanent-magnet synchronous machine using carrier-frequency injection methods," *IEEE Trans. Ind. Appl.*, vol. 41, no. 1, pp. 38-45, 2005.

[JON09] M. Jones, S. N. Vukosavic, D. Dujic, and E. Levi, "A Synchronous Current Control Scheme for Multiphase Induction Motor Drives," *IEEE Trans. Energy Conversion*, vol. 24, no. 4, pp. 860-868, Dec 2009.

[JUN15] S. Jung, and J.-I. Ha, "Analog filtering method for sensorless AC machine control with carrier-frequency signal injection," *IEEE Trans. Ind. Electron.*, vol. 62, no. 9, pp. 5348-5358, Sept. 2015.

[KAN10] J. Kang, "Sensorless control of permanent magnet motors," *Control Engineering*, vol. 57, no. 4, pp. 1-4, 2010.

[KAR12] J. Karttunen, S. Kallio, P. Peltoniemi, and O. Pyrhonen, "Dual three-phase permanent magnet synchronous machine supplied by two independent voltage source inverters," *in proc. IEEE International Symposium on Power Electronics, Electrical Drives, Automation and Motion (SPEEDAM),* pp. 741-747, Jun. 2012.

[KAR16] J. Karttunen, S. Kallio, P. Peltoniemi, and P. Silventonen, "Current harmonic compensation in dual three-phase PMSMs using a disturbance observer," *IEEE Trans. Ind. Electron.*, vol. 63, no. 1, pp. 583-594, Jan. 2016.

[KEL03] J. W. Kelly, E. G. Strangas, and J. M. Miller, "Multiphase space vector pulse width modulation," *IEEE Trans. Energy Conversion*, vol. 18, no. 2, pp. 259-264, Jun. 2003.

[KIM03] H. Kim, M.C. Harke, and R.D. Lorenz, "Sensorless control of interior permanent magnet machine drives with zero-phase lag position estimation," *IEEE Trans. Ind. Appl.*, vol. 39, no. 6, pp.1726-1733, Nov./Dec., 2003.

[KIM11] H. Kim, J. Son, and J. Lee, "A high-speed sliding-mode observer for the sensorless speed control of a PMSM," *IEEE Trans. Ind. Electron*., vol. 58, no. 9, pp. 4069-4077, sept. 2011.

[KLI83] E. A. Klingshirn, "High phase order induction motors - part I-description and theoretical considerations," *IEEE Trans. Power Apparatus and Systems*, vol. PAS-102, no. 1, pp. 47-53, Jan. 1983.

[KOC09] H. W. De Kock, M. J. Kamper, and R. M. Kennel, "Anisotropy comparison of reluctance and PM synchronous machines for position sensorless control using HF carrier injection," *IEEE Trans. Power Electronics*, vol. 24, no. 8, pp. 1905-1913, 2009.

[KRE94] L. Kreindler, J. C. Moreira, A. Testa, and T. A. Lipo, "Direct field orientation controller using the stator phase voltage third harmonic," *IEEE Trans. Ind. Appl.*, vol. 30, no. 2, pp. 441-447, 1994.

[LEE11] K. Lee, I. Choy, J. Back, and J. Choi, "Disturbance observer based sensorless speed controller for PMSM with improved robustness against load torque variation," *IEEE power Electronics and ECCE Asia (ICPE and ECCE)*, 2011, pp. 2537-2543.

[LEI11] R. Leidhold, "Position sensorless control of PM synchronous motors based on zero-sequence carrier injection," *IEEE Trans. on Ind. Electron.*, vol. 58, no. 12 pp. 5371-5379, 2011.

[LEV07] E. Levi, R. Bojoi, F. Profumo, H. A. Toliyat, and S. Williamson, "Multiphase induction motor drives - a technology status review," *IET Electr. Power Appl.*, vol. 1, no. 4, pp. 489-516, Jul 2007.

[LEV08] E. Levi, "Multiphase electric machines for variable-speed applications," *IEEE Trans. Ind. Electron.*, vol. 55, no. 5, pp. 1893-1909, May 2008.

[LI07] Y. Li, Z. Q. Zhu, D. Howe, and C. M. Bingham, "Improved rotor position estimation in extended back-emf based sensorless PM brushless AC drives with magnetic saliency accounting for cross-coupling magnetic saturation," *IEEE International Electric Machines and Drives Conference, IEMDC 2007*, Antalya, Turkey, 2007, pp. 214-219.

[LI09a] Y. Li., "Sensorless control of permanent magnet brushless AC motors accounting for cross-coupling magnetic saturation," PhD Thesis Submitted to University of Sheffield, UK, 2009.

[LI09b] Y. Li, Z. Q. Zhu, D. Howe, and C. M. Bingham, "Improved rotor position estimation by signal injection in brushless AC motors, Accounting for Cross-Coupling Magnetic Saturation" *IEEE Trans. Industry Applications*, vol. 45, no. 5, pp. 1843-1850, 2009.

[LI11] G. J. Li, J. Ojeda, E. Hoang, and M. Gabsi, "Thermal-electromagnetic analysis of a fault-tolerant dual-star flux-switching permanent magnet motor for critical application," *IET Electric Power Applications*, vol. 5, no. 6, pp. 503-513, Jul. 2011.

[LIN03] M. Linke, R. Kennel, and J. Holtz, "Sensorless speed and position control of synchronous machines using alternating carrier injection," *Electric Machines and Drives Conference*, 2003, vol. 2, pp. 1211-121.

[LIN14] T. C. Lin, L. M. Gong, J. M. Liu, and Z. Q. Zhu, "Investigation of saliency in a switched-flux permanent-magnet machine using high-frequency signal injection," *IEEE Trans. Ind. Electron.*, vol. 61, no. 9, pp. 5094-5104, Spet. 2014.

[LIN15] T. C. Lin, and Z. Q. Zhu, "Sensorless operation capability of surface-mounted permanent-magnet machine based on high-frequency signal injection methods," *IEEE Trans. Ind. Appl.*, vol. 51, no. 3, pp. 2161-2171, May/Jun. 2015.

[LIN15b] T. C. Lin, and Z. Q. Zhu, "Sensorless operation capability of surface-mounted permanent-magnet machine based on high-frequency signal injection methods," *IEEE Trans. Ind. Appl.*, vol. 51, no. 3, pp. 2161-2171, May/Jun. 2015.

[LIP80] T. A. Lipo, "A d-q model for six-phase induction machines," *Proc. International Conference on Electrical Machines ICEM*, Athens, Greece, 1980, pp. 860-867.

[LIU06] Y. Liu, Z. Q. Zhu, and D. Howe, "Instantaneous torque estimation in sensorless direct-torque-controlled brushless DC motors," *IEEE Trans. Ind. Appl.*, vol. 42, no. 5, pp. 1275–1283, Sept./Oct. 2006.

[LIU14] J. M. Liu, and Z. Q. Zhu, "Novel sensorless control strategy with injection of high-frequency pulsating carrier signal into stationary reference frame," *IEEE Trans. Ind. Appl.*, vol. 50, no. 4, pp. 2574-2583, Jul. 2014.

[LIU15] J. M. Liu, and Z. Q. Zhu, "Rotor position estimation for dual-three-phase permanent magnet synchronous machine based on third harmonic back-EMF," *IEEE Symposium on Sensorless Control for Electrical Drives*, (*SLED2015*), 2015, pp. 1-8.

[LJU79] L. Ljung, "Asymptotic behavior of the extended Kalman filter as a parameter estimator for linear systems," *IEEE Trans. Auto. Control*, vol. 24, no. 1, pp. 36–50, Feb. 1979.

[LUO16] X. Luo, Q. Tang, A. Shen, and Q. Zhang, "PMSM sensorless control by injecting HF pulsating carrier signal into estimated fixed-frequency rotating reference frame," *IEEE Trans. Ind. Electron.*, vol. 63, no. 4, pp. 2294-2303, Apr. 2016.

[LYR02] R. O. C. Lyra, and T. A. Lipo, "Torque density improvement in a six-phase induction motor with third harmonic current injection," *IEEE Trans. Ind. Appl.*, vol. 38, no. 5, pp. 1351-1360, Oct. 2002.

[MAD95] A. Madani, J. P. Barbot, F. Colamartino, and C. Marchand, "Reduction of torque pulsations by inductance harmonics identification of a permanent-magnet synchronous machine,"*proceedings of the 4th IEEE Conference on Control Applications*, 1995, pp. 787-792.

[MAT96] N. Matsui, "Sensorless PM brushless DC motor drives," *IEEE Trans. Ind. Electron.*, vol. 43, no. 2, pp. 300-308, 1996.

[MED15] S. Medjmadj, D. Diallo, M. Mostefai, C. Delpha, and A. Arias, "PMSM drive position estimation: contribution to the high-frequency injection voltage selection issue," *IEEE Trans. Energy Conversion*, vol. 30, no. 1, pp. 349-358, Mar. 2015.

[MOG13] M. A. G. Moghadam, and F. Tahaami, "Sesorless control of PMSMs with tolerance for delays and stator resistance uncertainties," *IEEE Trans. Power Electron.*, vol. 28, no. 3, pp. 1391-1399, Mar.2013.

[MOR02] S. Morimoto, K. Kawamoto, M. Sanada, and Y. Takeda, "Sensorless control strategy for salient-pole PMSM based on extended EMF in rotating reference frame," *IEEE Trans. Ind. Appl.*, vol. 38, no. 4, pp. 1054–1061, Jul./Aug. 2002.

[MOR92] J. Moreira, and T. A. Lipo, "Modelling saturated AC machines including air gap flux harmonic components ," *IEEE Trans. Ind. Appl.*, vol. 28, no. 2, pp. 343-349, 1992.

[MOR96] S. Morimoto, M. Sanada, and Y. Takeda, "Inverter-driven synchronous motors for constant power," *IEEE Trans. Ind. Appl.*, vol. 2, no. 6, pp. 18-24, 1996.

[NEL74] R. H. Nelson, and P. C. Krause, "Induction machine analysis for arbitrary displacement between multiple winding sets," *IEEE Trans. Power Apparatus and Systems*, vol. 93, no. 3, pp. 841-848, 1974.

[OVR03] S. Ovrebo, and R. Nilsen, "New self-sensing scheme based on INFORM, heterodyning and Luenberger observer," *IEEE Conference on Electric Machines Drives, (IEMD'03)*, vol. 3, 2003, pp. 1819-1825.

[OVR04] S. Ovrebo, "Control of permanent magnet synchronous machines," PhD Thesis Submitted to Norwegian University of Science and Technology, Trondheim, 2004.

[PAC05] M. Pacas, and J. Weber, "Predictive direct torque control for the PM synchronous machine," *IEEE Trans. Ind. Electron.*, vol. 52, no. 5, pp. 1350-1356, Oct. 2005.

[PAR07] L. Parsa and H. A. Toliyat, "Sensorless direct torque control of five-phase interior permanent-magnet motor drives," *IEEE Trans. Ind. Appl.*, vol. 43, no. 4, pp. 952-959, Jul./Aug. 2007.

[PAU11] D. Paulus, P. Landsmann, and R. Kennel, "Sensorless field-oriented control for permanent magnet synchronous machines with an arbitrary injection scheme and direct angle calculation," *Symposium on Sensorless Control of Electrical Drives (SLED 2011)*, pp. 41-46, 2011.

[PII08] A. Piippo, M. Hinkkanen, and J. Luomi, "Analysis of an adaptive observer for sensorless control of interior permanent magnet synchronous motors," *IEEE Trans. Ind. Electron.*, vol. 55, no. 2, pp. 570–576, Feb. 2008.

[PRO92] F. Profumo, G. Griva, M. Pastorelli, J. Moreira and R. De. Doncker, "Universal field oriented controller based on air gap flux sensing via third harmonic stator voltage," *Conference of IEEE Industry Applications Society Annual Meeting*, 1992, pp. 515-523.

[RAC08] D. Raca, P. Garcia, D. Reigosa, F. Briz, and R. D. Lorenz, "A comparative analysis of pulsating vs. rotating vector carrier signal injection-based sensorless control," *Proc. Of IEEE Applied Power Electronics Conf. and Exposition (APEC'08)*, pp. 879-885, Feb. 2008.

[RAC10] D. Raca, P. Garcia, D. D. Reigosa, F. Briz, and R. D. Lorenz, "Carrier signal selection for sensorless control of PM synchronous machines at zero and very low speeds," *IEEE Trans. Ind. Appl.*, vol. 46, no.1, pp. 167-178, Jan./Feb. 2010.

[RAU10] R. Raute, C. Caruana, C.S. Staines, J. Cilia, M. Sumner, and G. M. Asher, "Sensorless control of induction machines at low and zero speeds by using PWM harmonics for rotor-bar slotting detection," *IEEE Trans. Ind. Appl.*, vol. 46, no. 5, pp. 1989-1998, 2010.

[REI08] D. Reigosa, P. Garcia, D. Raca, F. Briz, and R. D. Lorenz, "Measurement and adaptive decoupling of cross-saturation effects and secondary saliencies in sensorless-controlled IPM synchronous machines," *IEEE Trans. Ind. Appl.*, vol. 44, no. 6, pp. 1758–1767, 2008.

[REN15a] Y. Ren., and Z. Q. Zhu, "Reduction of both harmonic current and torque ripple for dual three-phase permanent-magnet synchronous machine using modified switching-table-based direct torque control," *IEEE Trans. Ind. Electron.*, vol. 62, no. 11, pp. 6671-6683, Nov. 2015.

[REN15b] Y. Ren and Z. Q. Zhu, "Enhancement of Steady-State Performance in Direct-Torque-Controlled Dual Three-Phase Permanent-Magnet Synchronous Machine Drives With Modified Switching Table," *IEEE Trans. Ind. Electron.*, vol. 62, no. 6, pp. 3338-3350, Jun. 2015.

[ROB02] E. Robeischl, M. Schroedl, and K. Salutt, "Improved INFORM-measurement sequence and evaluation for sensorless permanent magnet synchronous motor drives," *the 10th International Conference on Power Electronics and Motion Control*, Croatia, 2002.

[ROB04] E. Robeischl, and M. Schroedl, "Optimized INFORM measurement sequence for sensorless PM synchronous motor drives with respect to minimum current distortion," *IEEE Trans. Ind. Appl.*, vol. 40, no. 2, pp. 591-598, Mar./Apr. 2004.

[SCH94] M. Schroedl, and P. Weinmeier "Sensorless control of reluctance machines at arbitrary operating conditions including standstill," *IEEE Trans. Power Electronics*, vol. 9, no. 2, pp. 225-231, 1994.

[SCH96] M. Schroedl, "Sensorless control of AC machines at low speeds and standstill based on INFORM method," *IEEE-IAS Annual Meeting*, 1996, pp. 270-277.

[SEN95] T. Senjyu, T. Shimabukruo, and K. Uezato, "Vector control of permanent magnet synchronous motors without position and speed sensors," *in Proc. IEEE PESC'95*, 1995, pp. 759-765.

[SER12] P. Sergeant, F. De Belie, and J. Melkebeek, "Rotor geometry design of interior PMSMs with and without flux barriers for more accurate sensorless control," *IEEE Trans. Ind. Electron*., vol. 59, no. 6, pp. 2457-2465, Jun. 2012.

[SHE02] J. X. Shen, Z. Q. Zhu, and D. Howe, "Improved speed estimation in sensorless PM brushless AC drives," *IEEE Trans. Ind. Appl.*, vol. 38, no. 4, Jul./Aug. 2002.

[SHE04] J.X. Shen, Z.Q. Zhu, and D. Howe, "Sensorless flux-weakening control of permanent-magnet brushless machines using third harmonic back EMF," *IEEE Trans. Ind. Appl.*, vol. 40, no. 6, pp. 1629-1636, Nov./Dec. 2004.

[SHE06] J.X. Shen, and S. Iwasaki, "Sensorless control of ultrahigh-speed PM brushless motor using PLL and third harmonic back EMF," *IEEE Trans. Ind. Electron.*, vol.53, no.2, pp.421-428, Apr. 2006.

[SHE06a] J. X. Shen, Z. Q. Zhu, and D. Howe, "Practical issues in sensorless control of PM brushless machines using third-harmonic back-EMF," *IEEE 15th International Conference on Power Electronics and Motion Control*, *IPEMC*2006, 2006, pp. 1-5.

[SHE06b] J. X. Shen, and S. Iwasaki, "Sensorless control of ultrahigh-speed PM brushless motor using PLL and third-harmonic back-EMF," *IEEE Trans. Ind. Electron*., vol. 53, no. 2, pp. 421-428, 2006.

[SIL02] C. Silva, G. M. Asher, M. Sumner, and K. J. Bradley, "Sensorless rotor position control in a surface mounted PM machine using HF voltage injection," *in Proc. EPE-PEMC'02*, Dubrovnik, Croatia, 2002.

[SIL06] C. Silva, G. M. Asher, and M. Sumner, "Carrier-signal selection for sensorless control of PM synchronous machines at zero and very low speeds," *IEEE Trans. Ind. Electron.*, vol. 53, no. 1, pp. 373-378, 2006.

[SON09] C. Song, Z. Zheng, and X. Longya, "Sliding-mode sensorless control of direct-drive PM synchronous motors for washing machine applications," *IEEE Trans. Industry Applications*, vol. 45, no. 2, pp.582-590, 2009.

[STA06] C. S. Staines, C. Caruana, G. M. Asher, and M. Sumner, "Sensorless control of induction machine at zero and low frequency using zero-sequence current," *IEEE Trans. Ind. Electron.*, vol. 53, no. 1, pp. 195-206, 2006.

[TAK86] I. Takahashi, and T. Noguchi, "A new quick-response and high efficiency control strategy of an induction motor," *IEEE Trans. Ind. Appl*., vol. IA-22, no. 5, pp. 820-827, 1986.

[TER01] B. Terzic, and M. Jadric, "Design and implementation of the extended Kalman filter for the speed and rotor position estimation of brushless DC motor," *IEEE Trans. Ind. Electron.*, vol. 48, no. 6, pp. 1065–1073, Dec. 2001.

[TES03] N. Teske, G. M. Asher, M. Sumner, and K. J. Bradley, "Analysis and suppression of high-frequency inverter modulation in sensorless position-controlled induction machine drive," *IEEE Trans. Ind. Appl.*, vol. 39, no. 1, pp. 10-18, 2003.

[TIA11] Tian S. W., Jian G. Z., You G. G, and Gang, L., "Simulation and experimental studies of permanent magnet synchronous motor control methods," *IEEE International Conference on Applied Superconductivity and Electromagnetic Devices*, Sydney, Australia, Dec., 2011.

[VAS03] P. Vas, "Sensorless vector and direct torque control," *Oxford University Press*, 2003.

[WAN10] H. Wang, M. Yang, L. Niu and D. Xu, "Current-loop bandwidth expansion strategy for permanent magnet synchronous motor drives," *the 5th IEEE Conference on Industrial Electronics and Applications*, (*ICIEA2010*), 2010, pp. 1340-1345.

[WAN12] Z. Wang, K. Lu, and F. Blaabjerg, "A simple startup strategy based on current regulation for Back-EMF-based sensorless control of PMSM," *IEEE Trans. on Power Electron.*, vol.27, no.8, pp.3817-3825, Aug. 2012.

[WU91] R. Wu, and G. R. Slemon, "A permanent magnet motor drive without a shaft sensor," *IEEE Trans. Ind. Appl.*, vol. 27, no. 5, pp.1005-1011, Sept./Oct. 1991.

[XU14] W. Xu, and R.D. Lorenz, "Reduced parameter sensitivity stator flux linkage observer in deadbeat-direct torque and flux control for IPMSMs," *IEEE Trans. Ind. Appl*., vol. 50, no. 4,pp. 2626-2636, Jul./Aug. 2014.

[XU15] P. L. Xu and Z. Q. Zhu, "Comparison of carrier signal injection methods for sensorless control of PMSM drives," *IEEE Energy Conversion Congress and Exposition (ECCE)*, Montreal, 2015, pp. 5616-5623.

[XU16] P. L. Xu, and Z. Q. Zhu, "Novel carrier signal injection method using zero sequence voltage for sensorless control of PMSM drives," *IEEE Trans. Ind. Electron.*, vol. 63, no. 4, pp. 2053-2061, Apr. 2016.

[YAN11] S. C. Yang, T. Suzuki, R. D. Lorenz, and T. M. Jahns, "Surface permanent magnet synchronous machine design for saliency tracking self-sensing position estimation at zero and low speeds," *IEEE Trans. Ind. Appl.*, vol. 47, no. 5, pp. 2103-2116, 2011.

[YAN12a] S.-C. Yang, and R. Lorenz, "Surface permanent magnet synchronous machine self-sensing position estimation at low speed using eddy current reflected asymmetric resistance," *IEEE Trans. Power Electronics*, vol. 27, no. 5, pp. 2595-2604, 2012.

[YAN12b] S.-C. Yang, and R. Lorenz, "Comparison of resistance based and inductance based self-sensing control for Surface permanent magnet machines using high-frequency signal injection," *IEEE Trans. Ind. Electron.*, vol. 48, no. 3, pp. 977-986, Jun. 2012.

[YOO09] A. Yoo and S. K. Sul, "Design of flux observer robust to interior permanent-magnet synchronous motor flux variation," *IEEE Trans. Ind. Appl.*, vol. 45, no. 5, pp. 1670-1677, 2009.

[YOO11] Y. D. Yoon, S.-K. Sul, S. Morimoto, and K. Ide, "High-bandwidth sensorless algorithm for ac machines based on square-wave-type voltage injection," *IEEE Trans. Ind. Appl.*, vol. 47, no. 3, pp. 1361-1370, May. 2011.

[ZHA06] Z. Zhang, H. Xu, L. Xu, and L. E. Heilman, "Sensorless direct field oriented control of three-phase induction motor based on sliding-mode for washing machine drive applications," *IEEE Trans. Ind. Appl.*, vol. 42, no. 3, pp. 694-701, 2006.

[ZHA11] Y. C. Zhang, J. G. Zhu, W. Xu, and Y. G. Guo, "A simple method to reduce torque ripple in direct torque-controlled permanent-magnet synchronous motor by using vectors with variable amplitude and angle," *IEEE Trans. Ind. Electron.*, vol. 58, no. 7, pp. 2848-2859, 2011.

[ZHA13] S. Zhao, O. Wallmark, and M. Leksell, “Low-speed sensorless control with reduced copper losses for saturated PMSynRel Machines,” *IEEE Trans. Energy Conversion*, vol. 28, no. 4, pp. 841-848, Dec. 2013.

[ZHA95] Y. Zhao, and T. A. Lipo, “Space vector pwm control of dual three-phase induction machine using vector space decomposition,” *IEEE Trans. Ind. Appl.*, vol. 31, no. 5, pp. 1100-1109, Sept./Oct. 1995.

[ZHA95] Y. Zhao and T. A. Lipo, "Space vector PWM control of dual three-phase induction machine using vector space decomposition," *IEEE Trans. Ind. Appl.*, vol. 31, no. 5, pp. 1100-1109, Sep./Oct. 1995.

[ZHO97] L. Zhong, M. F. Rahman, W. Y. Hu, and C. M. Bingham, “Analysis of direct torque control in permanent magnet synchronous motor drives,” *IEEE Trans. Power Electron.*, vol. 12, no. 3, pp. 528-536, 1997.

[ZHU07] Z. Q. Zhu, Y. LI, D. Howe, and C. M. Bingham, “Compensation for rotor position estimation error due to cross-coupling magnetic saturation in signal injection based sensorless control of PM brushless AC motors,” *Proc. Int. Electric Machines and Drives Conference*, 2007, pp.208-213.

[ZHU11] Z. Q. Zhu, “Sensorless operation of permanent magnet brushless DC and AC drives-basic and novel machine design and control aspects,” *8th International Conference on Power Electronics-ECCE Asia*, The Shilla Jeju, Jeju, Korea, May 30, 2011.

APPENDICES

Appendix I: Experimental Drive System and Permanent Magnet Synchronous Machines

AI.1. Introduction

This chapter describes the hardware of experimental platform which is constructed depending on a dSPACE control system and interfaced with Matlab/Simulink model. The experimental platform is utilized for implementation of the developed sensorless control methods for single and dual three-phase PM machines. It should be noted that both systems, i.e. single and dual three-phase systems, utilise the same platform of experimental drive. Two sets of three-phase inverter, which is supplied by a DC power, is utilized for both machine drives where only one set is enabled when implementing the control of single three-phase system.

Furthermore, a brief description about dSPACE (DS1006) control system is given in this chapter. The detailed setup of the entire experiments for the control of the testing system is depicted in Fig. AI.1.

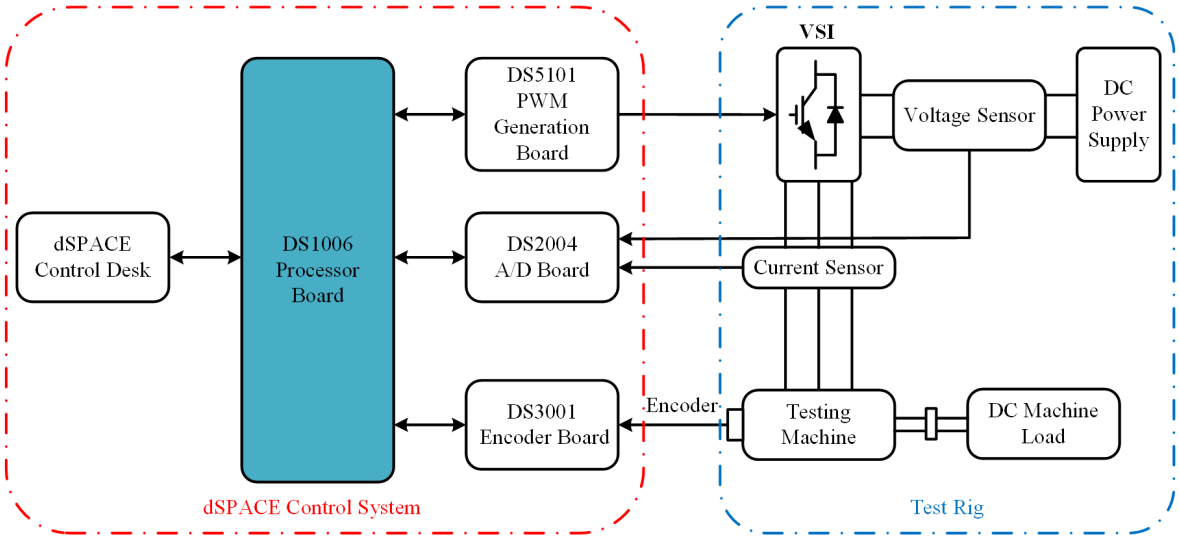

Fig. AI.1. Overview of the experimental system setup.

AI.2. dSPACE Control System and Software Setting

The dSPACE control system employed in this thesis includes many hardware boards with built in software such as processor board (DS1006), A/D conversion board (DS2004), encoder board (DS3001), and PWM generation board (DS5101). All these hardware boards are briefly described in the following subsections [DSP10].

The dSPACE hardware is connected by an optical fibre cable to a host PC in order to transmit the real time data. The data waveforms provided in the Matlab/Simulink could be monitored and captured by the control desk of dSPACE which makes it easy to analyse the experimental performance.

AI.2.1. Processor Board (DS1006)

The main processing unit in the dSPACE modular hardware is the processor board. This board is designed for complicated and processing-intensive models in real time applications that require enormous computing power. This board is based on a 2.4GHz multicore Opteron ™ processor. In addition, it can give real-time power calculation of the Opteron TM processor to the modular system, and can also provide an interface to the host PC and I/O boards. The processor (DS1006) can access to all I/O boards of dSPACE through PHS-bus. Furthermore, the data can be transferred via DS911 Giga-link module by utilizing the multiprocessing cable. The real time application can be run on one or more multi-core DS1006 boards. The single multi-core board includes a 512 KB L2 on-chip cache per core, and a 6 MB L3 cache. Also, for interchanging data with the host PC, each core has a 128 MB global memory, and it has a 1 GB local memory for executing the real time models. The overview of processor (DS1006) board is shown in Fig. AI.2.

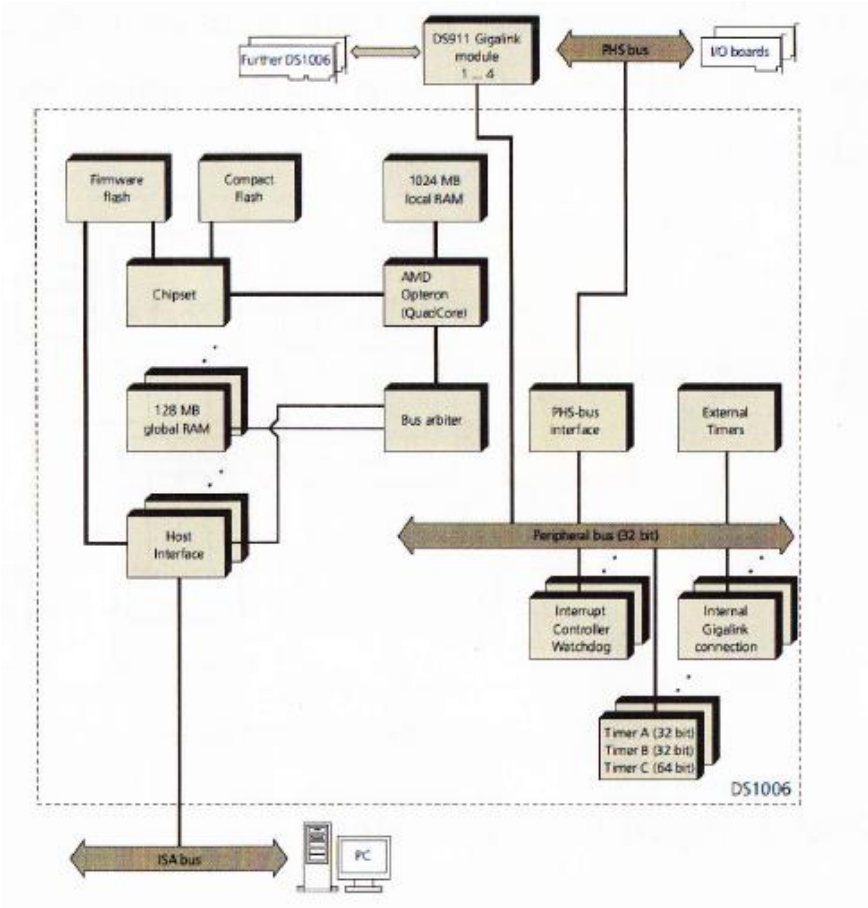

Fig. AI.2. Overview of processor (DS1006) board [DSP10]

AI.2.2. A/D Conversion Board (DS2004)

For the control system employed in this PhD research work, a high speed A/D conversion board DS2004 is utilized in the dSPACE modular system in which the analogue input signals are digitized at high sampling rates. The DS2004 board includes independent 16-bit A/D conversion channels, and each channel is equipped with differential inputs to achieve the requirement for digitizing the analogue input signals. The conversion time per channel is 800 ns. Actually, the DS2004 board can provide various hardware and software based trigger mechanisms in addition to data buffers for burst transfer. Due to the extensive trigger functions and measurement modes plus 4 external trigger inputs, the conversion of both whole sample bursts and single measurement values can be enabled in this A/D conversion board.

The burst mode of DS2004 can provide two approaches of converting measurement values:

- Continuous sample mode approach: when one burst of conversions finishes, the next burst starts automatically.
- Triggered sample mode approach: a burst of conversions could be started by a trigger event or software.

The DS2004 board can buffer up to 16384 analogue values in each channel, and then they can be transferred to the processor board as a burst. Thus, the communication overhead can be reduced as the overall system performance can be significantly improved.

AI.2.3. PWM Generation Board (DS5101)

The flexibility and PWM resolution are highly required in the machine drive control. The Digital Waveform Output Board (DS5101) is specifically designed in order to generate complex, high-speed digital signals at high resolution. A multitude of signals at various frequencies, including pulse-width modulation waveforms and incremental encoder signals can be generated by the DS5101 board. The main area of deployment of this board is hardware-in-the-loop simulation in automotive applications such as simulating sensors or controlling actuators.

Any TTL pulse patterns up to 16 channels can be autonomously generated with high accuracy by the DS5101 board. With fast time resolution of 25 ns, the toughest requirement can be achieved. The DS5101 board shows outstanding programmability and flexibility due its ability to change the widths of the pulse in the real time synthesized with different interrupt and trigger mechanisms.

In general, the output of the board can be classified into different PWM signal generations as generation single-phase PWM Signal (PWM1), generation three-phase PWM Signal (PWM3), and generation of three-phase PWM Signal with Inverted and Non-Inverted outputs (PWM6). Usually, the PWM6 is employed for machine drive control. The two sets of PWM6 could be applied for controlling a dual three-phase machine or two three-phase machines. One set only is utilized to control the single three-phase machine, while two sets are used to control the dual three-phase machine.

AI.2.4. Encoder Board (DS3001)

The DS3001 incremental encoder interface board is specifically designed for providing a precise position measurement with sensors obtaining digital information. In this thesis, this board is used for proving the rotor position information for the machine drive control after receiving the digital information from the sensor mounted on the motor shaft. The mounted sensor is utilized to obtain the actual rotor position for the control system, where the measured information of rotor position is used for park transformation.

The DS3001 board includes five parallel input channels, each channel can provide everything required to connect an incremental encoder, and process its output signals: differential or single-ended inputs for the encoder's two phase lines, an index input, and a regulated encoder power supply with sense lines. Such signals could be either single-ended (TTL) or differential (RS433).

Additionally, the input encoder lines range is from -2^{21} to 2^{21}. Thereafter, the position angle in radian could be obtained by DS3001 Simulink model from the scaled output signal as given by

$$\theta_r = 2^{21} \times \frac{2\pi}{encoder-lines} \times scaled-output \tag{AI.1}$$

For the incremental encoder used in this study with the resolution of 2048PPR, the rotor position could be calculated as

$$\theta_r = 2^{21} \times \frac{2\pi}{2048} \times scaled-output \tag{AI.2}$$

Then, by differentiating the rotor position angle, the rotor speed can be obtained as

$$\omega_r = \frac{\theta_r(\mathrm{k}) - \theta_r(\mathrm{k}-1)}{T_s} \tag{AI.3}$$

AI.3. Experimental Rig for Testing Control Strategies Employed in the Research

A permanent magnet synchronous machine is utilized for the experimental investigation to develop the sensorless control techniques. The testing machine employed in all chapters of the thesis is a dual three-phase PMSM, and it is also employed as a single three-phase PMSM in the way of either connecting the two stator winding sets in series or enabling one stator winding set only.

The test rig is based on a 230W dual three-phase prototype PMSM. The specifications and parameters of the testing machine are listed in Table AI.1. The cross-section of this 12/10 PMSM and its winding configuration are shown in Fig. AI.3. It is worth mentioning that the original design of this motor is a single three-phase PMSM, and alternative winding structure has been applied to form a dual three-phase PMSM [ISH06]. Unlike the traditional three-phase PMSM, each phase is formed by two coils connected in series. Phases A1, B1, and C1 are connected in star connection to form the first stator winding set, whilst phases A2, B2, and C2 are connected in star connection to form the second winding set. Furthermore, there is a 30 electrical degrees phase angle spatially shifted between the two stator winding sets.

The experimental setup involves a dSPACE (DS1005) digital controller, a dual three-phase inverter, a DC power supply and a prototype of dual three-phase PMSM. Additionally, an adjustable resistor is connected with a permanent magnet DC motor which is utilized for loading, and the DC motor is coupled with the prototype DTP-PMSM. The experimental rig of the testing machine is shown in Fig. AI.4.

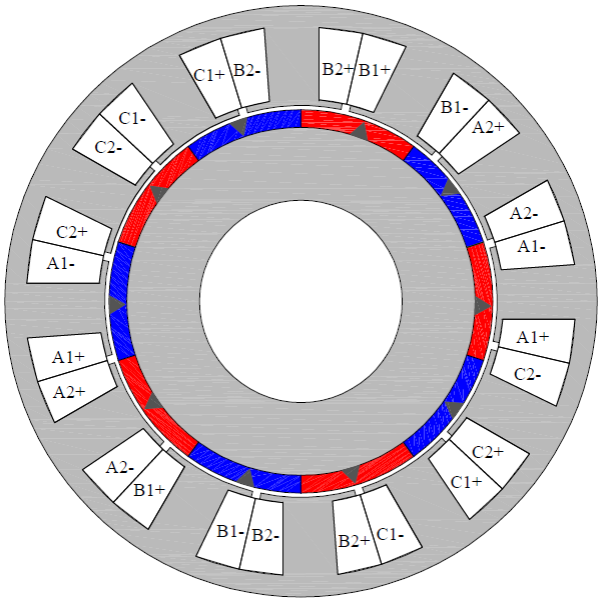

(a) Cross-section

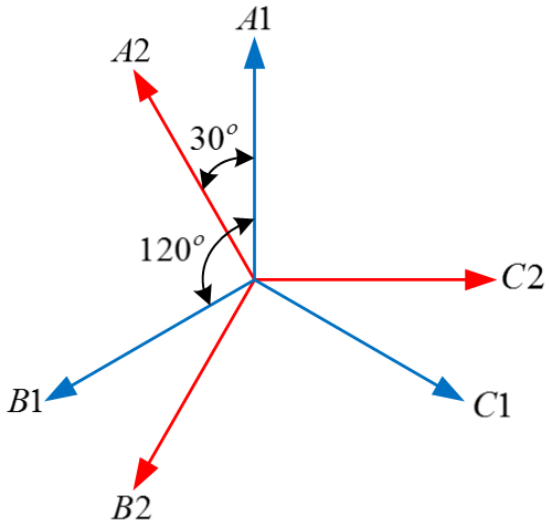

(b) Phase vector

Fig. AI.3. Cross-section and winding configuration in addition to phase vector of the testing machine.

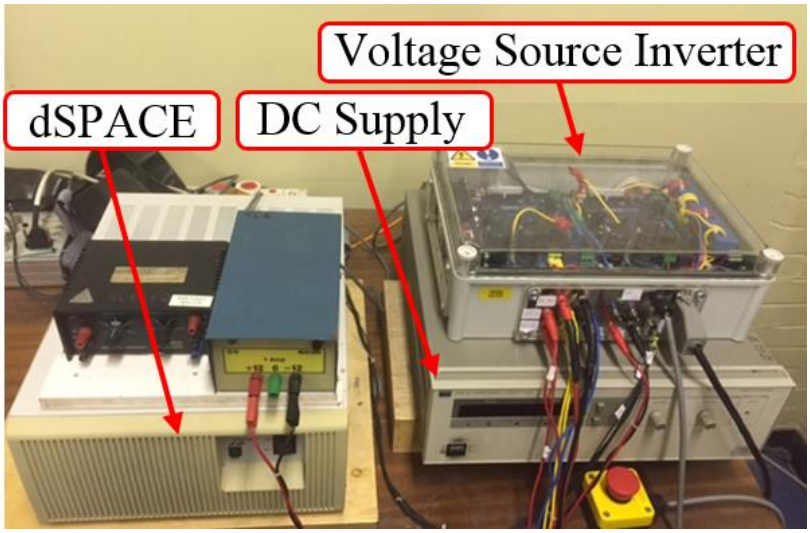

(a) Drive System of the machine

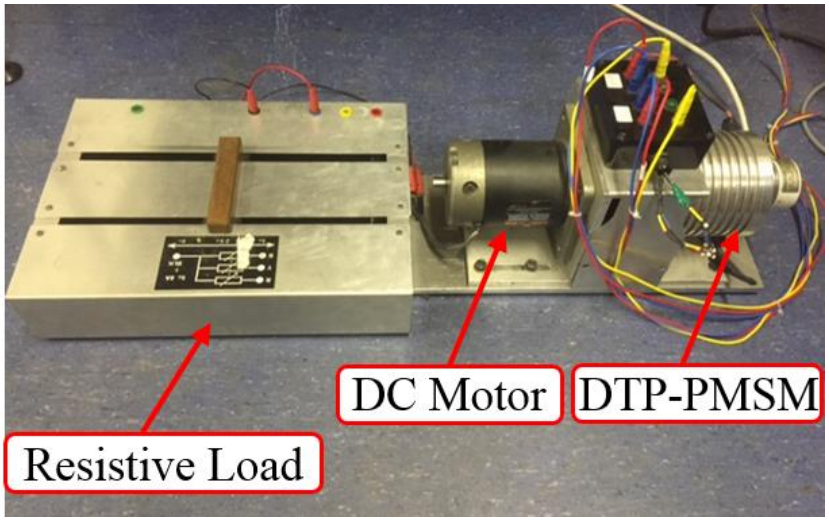

(b) Prototype dual three-phase PMSM and load

Fig. AI.4. Experimental rig of the testing machine.

TABLE AI.1

SPECIFICATIONS AND PARAMETERS OF TESTING MACHINE

Parameters	Values
Rated torque	5.5 Nm
Rated phase current (RMS)	4 A
Rated power	230 W
Rated speed	400
Permanent flux-linkage	0.0734 Wb
d-axis inductance	1.675 mH
q-axis inductance	2.125 mH
Stator resistance	1.1 Ω
DC-bus voltage	40V
Number of pole pairs	5

In Fig. AI.4, the DTP-PMSM drive is based on STEVAL-IHM027V1 with a power of 1 KW for each inverter. For the power module of the power board (STGIPS10K60A), the maximum voltage and current are 600 V and 10 A, respectively, and such a power module is designed by STMicroelectronics Ltd. It has the feature to be convenient with single three-phase AC supply from a range of 90 to 220 V, or DC supply from a range of 125 to 350 V. Furthermore, the gate drive signals can be transferred from the DS5101 Digital Waveform Output Board to the power inverter by utilizing an interface board. Then, the phase current and DC voltage can be measured, and then feedback such measured signals to (DS2004) High-Speed A/D Board.

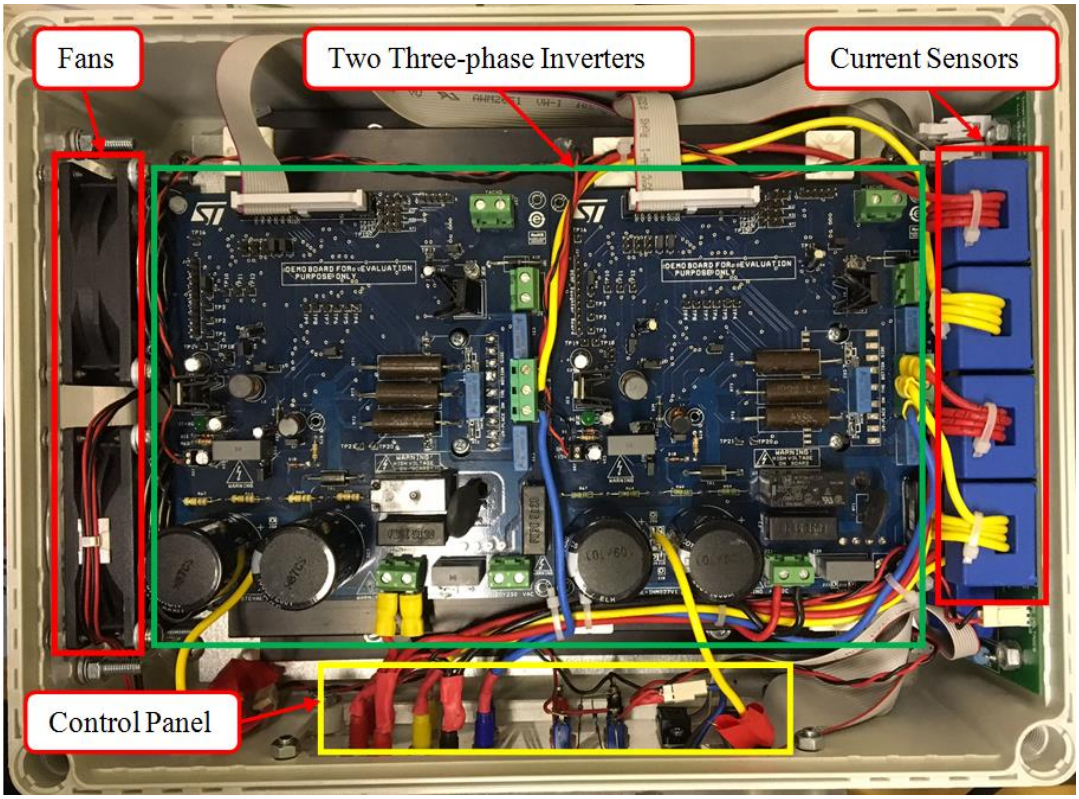

Fig. AI.5. Six-phase power inverter.

AI.3.1. Rotor Position Alignment for Encoder

An incremental encoder is used to obtain the actual position of the rotor for the testing machine in the overall control system. In order to detect the rotor position information, the incremental encoder board (DS3001) is employed. However, the zero-position alignment of the rotor position encoder to the magnet axis (*d*-axis), as illustrated in Fig. AI.6, is required. For initial position alignment, the three-phase back-EMF is typically a good reference. To achieve such alignment, the testing motor is spun by load machine connected to a DC power supply for rotation. Then, the three-phase back-EMF could be measured from the terminals of motor winding, and the rotor position can be adjusted from the dSPACE control desk. The rotor position information for the testing motor is well aligned as shown in Fig. AI.7.

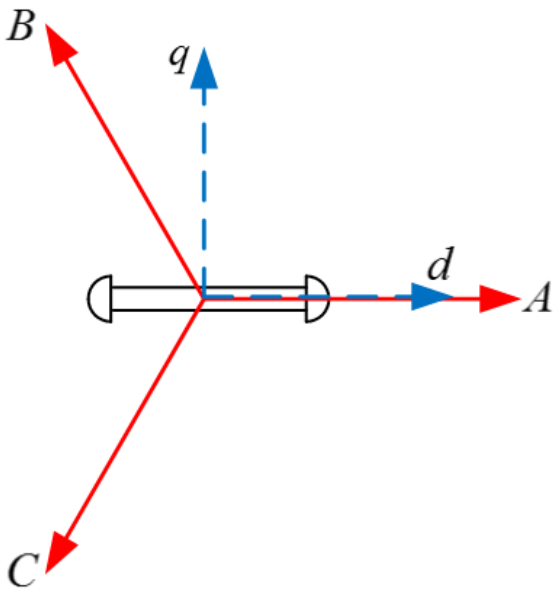

Fig. AI.6. Alignment for rotor position.

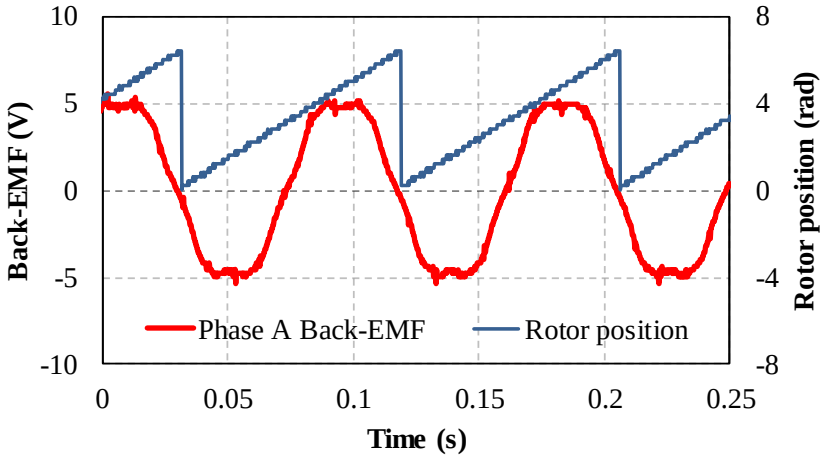

Fig. AI.7. Aligned actual rotor position with phase back-EMF.

AI.4. Conclusions

The experimental setup based on dSPACE control system together with the hardware platform and software interface for the control of single and dual three-phase PM machines are briefly introduced in this chapter. The parameters for the testing PM machine employed in this research study are also introduced. Different sensorless control strategies are applied to this machine as shown in details in the main chapters.

Appendix II: Specification of Prototype Machine

Testing Machine I: Dual three-phase PMSM

Parameters	Values
Rated power	240 W
Rated torque	5.5 Nm
Rated speed	400 rpm
DC Supply voltage	40 V
Number of slots	12
Number of poles	10
Radius of stator outer	50 mm
Radius of stator inner	28.5 mm
Radius of rotor outer	27.5 mm
Slot opening	2 mm
Axial length	50 mm
Tooth body width	7.1 mm
Yoke height	3.7 mm
Magnet thickness	3 mm
Airgap length	1 mm
Number of series turns per phase	132
Magnet remanence	1.2 T
α-axis and β-axis inductance	2.142 mH
z_1-axis and z_2-axis inductance	0.875 mH
Stator resistance	1.096 Ω
Permanent magnet flux	0.0734Wb

Appendix III: Publications during PhD Research Work

- **Best Paper Award**

The following paper has been selected for best paper award in *the 17th Int. Conf. on Electrical Machines and Systems, ICEMS2014, 22-25 Oct. 2014, Hangzhou, China:*

A. H. Almarhoon, and Z. Q. Zhu, "Influence of back-EMF and current harmonics on position estimation accuracy of permanent magnet synchronous machine," The 17th *Int. Conf. on Electrical Machines and Systems*, ICEMS2014, 22-25 Oct. 2014, Hangzhou, China.

Its modified version has been published in COMPEL: The International Journal for Computation and Mathematics in Electrical and Electronic Engineering.

- **Journal Papers**

[1]. A. H. Almarhoon, Y. Ren, and Z. Q. Zhu, "Influence of back-EMF and current harmonics on sensorless control performance of single and dual three-phase permanent magnet synchronous machines," *COMPEL: The International Journal for Computation and Mathematics in Electrical and Electronic Engineering*, vol.35, no.2, pp. 744-763, 2016.

[2]. Ali H. Almarhoon, Z. Q. Zhu, and P. L. Xu, "Improved rotor position estimation accuracy by rotating carrier signal injection utilizing zero-sequence carrier voltage for dual three-phase PMSM," *IEEE Trans. Ind. Electron*., in press.

[3]. Ali H. Almarhoon, Z. Q. Zhu, and P. L. Xu, "Improved pulsating carrier signal injection based sensorless control strategy using zero-sequence carrier voltage for DTP-PMSM," *IEEE Trans. on Energy Conversion*, in revision process.

- **Conference Papers**

[1]. A. H. Almarhoon, and Z. Q. Zhu, "Influence of back-EMF and current harmonics on position estimation accuracy of permanent magnet synchronous machine," The 17th *Int. Conf. on Electrical Machines and Systems*, ICEMS2014, 22-25 Oct. 2014, Hangzhou, China.

[2]. A. H. Almarhoon, Y. Ren, and Z. Q. Zhu, "Sensorless switching-table-based direct torque control for dual three-phase PMSM drives," The 17th *Int. Conf. on Electrical Machines and Systems*, ICEMS2014, 22-25 Oct. 2014, Hangzhou, China.